

LISTA PORTOFOLIU LUCRARI STIINTIFICE

Conf dr. Manea Rosana Mihaela

1. A Rare Case of Single Coronary Artery: Getting to the Heart of the Matter, Autors: Popa, Ramona Mihaela, Pantea, Rebecca, Macasoi, Petrisor, Manea, Rosana Mihaela, Journal of the Belgian Society of Radiology, 12.10.2023
[https://doi: 10.5334/jbsr.3122](https://doi.org/10.5334/jbsr.3122)
2. Analysis of breast cancer subtypes and their correlations with receptors and ultrasound G Sechel, LM Rogozea, NA Roman, D Ciurescu, ME Cocuz, RM Manea, Romanian Journal of Morphology and Embryology 62 (1), 269, 2021/1, doi [10.47162/RJME.62.1.28](https://doi.org/10.47162/RJME.62.1.28)
<https://www.ncbi.nlm.nih.gov/pmc/articles/PMC8597389/>
3. Aplicatii ale masuratorilor grosimii intima/media carotidei pentru prognozarea hipertensiunii esentiale la copii, Rosana Manea, Bianca Elena Popovici, Carmen Daniela Neculoiu, Dan Minea, Alina Calin- Revista de chimie, volumul 2018, Iunie
https://d1wqtxts1xzle7.cloudfront.net/65937424/54_20MANEA_20R_206_2018-libre.pdf?1615201410=&response-content-disposition=inline%3B+filename
4. Biomolecular Screening of *Pimpinella anisum* L. for Antioxidant and Anticholinesterase Activity in Mice Brain, Authors: Mushtaq, Aamir, Habib, Fatima, Manea, Rosana, Anwar, Rukhsana, (Gohar, Umar Farooq, Zia-Ul-Haq, Muhammad, Ahmad, Mobasher, Gavris, Claudia Mihaela, Chicea, Liana, MOLECULES,
<https://doi.org/10.3390/molecules28052217>
5. Clear Cell Renal Cell Carcinoma: Local Recurrence and Bilateral Adrenal Metastases-A Case Report, EM Popa, R Manea, RE Birla-Coroiu, Journal of the Belgian Society of Radiology 106 (1), 06 May 2022, <http://doi.org/10.5334/jbsr.2772>,
<https://jbsr.be/articles/10.5334/jbsr.2772/>
6. Giant Thoracic Aortic Aneurysm Rupture in a Patient with Extensive Atherosclerotic Disease, Autors: Popa, Ramona Mihaela, Andrei-Constantin, Chirita, Manea, Rosana Mihaela, Journal of the Belgian Society of Radiology, 08.08.20214
[https://doi: 10.5334/jbsr.3314](https://doi.org/10.5334/jbsr.3314)
7. Pharmacological Basis for Antispasmodic, Bronchodilator, and Antidiarrheal Potential of *Dryopteris ramosa* (Hope) C. via In Vitro, In Vivo, and In Silico Studies, Iqbal, Iram, Saqib, Fatima, Latif, Muhammad Farhaj, Shahzad, Hamna, Dima, Lorena, Sajer, Bayan, Manea, Rosana, Pojala, Ciprian, Necula, Radu, ACS OMEGA, 06.08.2023

DOI: [10.1021/acsomega.3c01907](https://doi.org/10.1021/acsomega.3c01907)

<https://pubs.acs.org/doi/10.1021/acsomega.3c01907>

8. The imaging evaluation of typical and atypical calcifications in different anatomical regions study in Brasov, Romania , G Sechel, A Repanovici, R Manea, V Burtea, The Medical-Surgical Journal vol 124 (2), pg 290-297, 30.06.2020,

<https://revmedchir.ro/index.php/revmedchir/article/view/2121>

9. The Many Hidden Faces of Gallbladder Carcinoma on CT and MRI Imaging-From A to Z, Autors: Neculoiu, Damaris, Neculoiu, Lavinia Claudia, Popa, Ramona Mihaela, Manea, Rosana Mihaela, Diagnostics, 19.03.2024

<https://doi.org/10.3390/diagnostics14050475>

10. Gender Differences for His Bundle Pacing Long-Term Performance in the Elderly Population; autors: Catalin Pestrea , Ecaterina Cicala, Dragos Lovin, Adrian Gheorghe, Florin Ortan, Rosana Manea, Journal of Cardiovascular Development and Disease, 28.02.2025

<http://doi.org/10.3390/jcdd12030088>

07.03.2025



A Rare Case of Single Coronary Artery: Getting to the Heart of the Matter

IMAGES IN CLINICAL
RADIOLOGY

RAMONA MIHAELA POPA 

REBECCA PÂNTEA 

PETRIȘOR MACAȘOI

ROSANA MIHAELA MANEA 

*Author affiliations can be found in the back matter of this article

]u[ubiquity press

ABSTRACT

Single coronary artery anomaly represents a particularly rare entity, which may present with variable clinical scenarios, but in most cases remains asymptomatic. It is considered to be one of the pathological states to cause sudden death, especially in young adults [1].

We hereby report a rare case of a R-III type of single coronary artery as classified by Lipton et al., which is only about 15% of all the cases of coronary anomalies. Coronary CT angiography as well as invasive coronarography provide accurate details regarding the origin, course and termination of coronary anomalies, as well as evaluation of associated coronary lesions, further guiding the optimal treatment strategy in each case.

Teaching Point: The main teaching point of this case report is to clearly underline the importance of coronary CT angiography in obtaining a comprehensive evaluation of coronary artery anatomy and associated coronary lesions, representing important aspects, which further guide accurate treatment and management.

CORRESPONDING AUTHOR:

Ramona Mihaela Popa

Clinical Emergency County
Hospital of Brașov, RO

ramonapopa@gmail.com

KEYWORDS:

coronary artery; coronary
CTA; coronary angiography;
coronary anatomy; coronary
anomaly; single coronary
artery; right coronary artery

TO CITE THIS ARTICLE:

Popa RM, Pântea R, Macașoi
P, Manea RM. A Rare Case of
Single Coronary Artery: Getting
to the Heart of the Matter.
*Journal of the Belgian Society
of Radiology*. 2023; 107(1):
50, 1–3. DOI: [https://doi.
org/10.5334/jbsr.3122](https://doi.org/10.5334/jbsr.3122)

CASE HISTORY

A 60-year-old female was admitted to the Emergency Department with fatigability, palpitations and low blood pressure. She was known with hypertension grade 3 and a medical history of myocardial infarction treated with balloon angioplasty of the left circumflex artery (LCX) a month ago.

Cardiac computed tomography (CT) was performed and 3D volume rendering images illustrated a rare coronary anomaly type RIII according to Lipton's Classification of Single Coronary Artery, characterized by a single coronary artery arising from the right sinus of Valsava, representing the right coronary artery (RCA; Figure 1, purple arrow). The posterolateral branch (PLB; Figure 1, pink arrow) presented a long vascular path, with a normal calibre. The posterior descending artery (PDA; Figure 1, blue arrow) presented a normal calibre and a normal vascular path coursing in the posterior interventricular groove.

Moreover, from the proximal segment of the RCA arose (at the same level):

- the LCX (yellow arrow), which coursed on the posterior contour of the aortic root to the left atrioventricular groove and
- the left anterior descending artery (LAD; Figure 1, green arrow), which coursed on the anterior surface of the pulmonary trunk, reaching the anterior interventricular sulcus; the LAD presented a small calibre distally as it descended to the notch of cardiac apex.

Calcium score was 0. However, due to non-calcified atherosclerotic plaques, the following stenosis were noted:

- 30–40% stenosis involving the mid segment of the RCA and
- 60–70% stenosis at the ostium of the LCX.

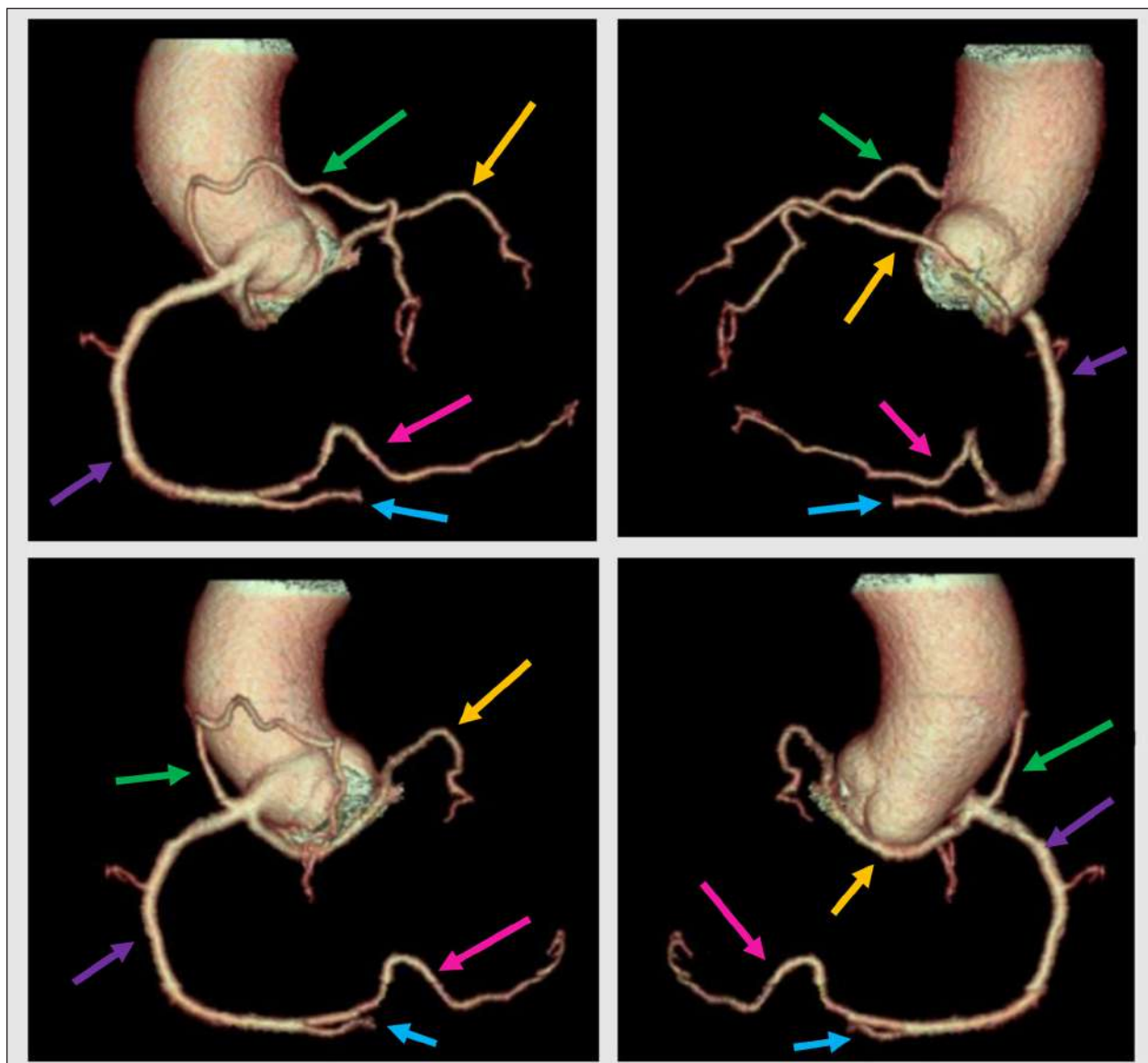


Figure 1.

Therefore, the patient was referred to the catheterization laboratory for coronary angiography through the access of the right femoral artery. The cannulation of the RCA revealed a 40% stenosis of its second segment and a 80% remaining stenosis of the LCX at the ostium. Subsequently, percutaneous coronary intervention was performed painstakingly using a drug-eluting stent (2.25–18mm), which was delivered to the ostial lesion of the LCX, followed by NC balloon post-dilatation (3.0–12mm). The immediate postinterventional coronarography showed a good angiographic result, with a 25% remaining stenosis, but with adequate distal flow –TIMI 3.

Patient remained asymptomatic at 1 month and 6 months follow-up.

COMMENTS

Congenital anomalies involving the origin of the coronary arteries are rare entities, with variable clinical scenarios, representing a significant cause of sudden cardiac death [1].

Some anomalies, such as intramyocardial course, subendocardial course, as well as pre-pulmonic, retro-aortic, transseptal anomalies, are almost always benign based on the course alone [1]. However, if the aberrant coronary artery courses between the outflow tracts, in the case of type R/LIIB or R/III, patients are prone to


major clinical complications, related to the dilatation of the great outflow tracts (aorta, pulmonary trunk) during exercise, with secondary compression of the aberrant coronary artery along their course [1].

COMPETING INTERESTS

The authors have no competing interests to declare.

AUTHOR AFFILIATIONS

Ramona Mihaela Popa  orcid.org/0000-0002-1884-766X
Clinical Emergency County Hospital of Braşov, RO

Rebecca Pântea  orcid.org/0009-0002-1757-0512
Clinical Emergency County Hospital of Braşov, RO

Petrişor Macaşoi
Clinical Emergency County Hospital of Braşov, RO

Rosana Mihaela Manea  orcid.org/0000-0002-4882-512X
Clinical Emergency County Hospital of Braşov, RO

REFERENCE

1. **Desmet W, Vanhaeke J, Vrolix M**, et al. Isolated single coronary artery: A review of 50 000 consecutive coronary angiographies. *European Heart Journal*. December 1992; 13(12): 1637–1640. DOI: <https://doi.org/10.1093/oxfordjournals.eurheartj.a060117>

TO CITE THIS ARTICLE:

Popa RM, Pântea R, Macaşoi P, Manea RM. A Rare Case of Single Coronary Artery: Getting to the Heart of the Matter. *Journal of the Belgian Society of Radiology*. 2023; 107(1): 50, 1–3. DOI: <https://doi.org/10.5334/jbsr.3122>

Submitted: 25 February 2023 **Accepted:** 28 April 2023 **Published:** 07 July 2023

COPYRIGHT:

© 2023 The Author(s). This is an open-access article distributed under the terms of the Creative Commons Attribution 4.0 International License (CC-BY 4.0), which permits unrestricted use, distribution, and reproduction in any medium, provided the original author and source are credited. See <http://creativecommons.org/licenses/by/4.0/>.

Journal of the Belgian Society of Radiology is a peer-reviewed open access journal published by Ubiquity Press.

ORIGINAL PAPER



Analysis of breast cancer subtypes and their correlations with receptors and ultrasound

GABRIELA SECHEL¹⁾, LILIANA MARCELA ROGOZEA¹⁾, NADINNE ALEXANDRA ROMAN¹⁾, DANIEL CIURESCU²⁾, MARIA ELENA COCUZ¹⁾, ROSANA MIHAELA MANEA²⁾

¹⁾Department of Basic, Preventive and Clinical Sciences, Transilvania University of Braşov, Romania

²⁾Department of Medical and Surgical Clinical Sciences, Transilvania University of Braşov, Romania

Abstract

The study aim was to evaluate the ultrasound (US) signs of the mammary lesions classified in the Breast Imaging-Reporting and Data System (BI-RADS) score category 3, 4, and 5, corresponding to US BI-RADS. It also followed the correlation between US changes of lesions suggestive for malignancy with the histopathological results and evaluated the proper management of those lesions. There were correlations of breast cancer (BC) subtypes with the receptors [estrogen receptor (ER), progesterone receptor (PR), human epidermal growth factor receptor 2 (HER2)], and Ki67 index, and the signs of conventional ultrasonography and US elastography. We selected 108 female patients examined with US, mammography and fine-needle biopsy who presented suspicions for malignancy lesions. Following the immunohistochemical analysis, they were classified in one of the BC subtypes. According to *chi*-squared analysis of molecular cancer subtypes correlation to receptors and Ki67 index, we found significant associations between both luminal A and luminal B HER2-negative subtypes and hormone receptors (ER, PR). These have an inverse relationship with Ki67 index elevated values; luminal B HER2-positive subtype has a direct association with HER2 presence; HER2-enriched subtype was statistically significant associated to HER2 presence and elevated Ki67 index values but had an inverse relationship to hormone receptors (ER, PR); triple-negative subtype was strongly associated to Ki67 index values and inversely correlated to ER and PR. We found luminal A subtype as being the most common and luminal B HER2-positive subtype as having the fewer cases.

Keywords: breast cancer, ER, PR, HER2, Ki67, ultrasound.

Introduction

One of the most frequent diseases in women is breast cancer (BC), with a significant contribution to all-cause mortality [1, 2].

Several ultrasound (US) characteristics of malignant breast lesions, such as hypoechogenicity, irregular shape, vertical orientation, presence of spicules, posterior acoustic shadowing, absence of calcifications, and increased vascular signal can be associated with BC subtypes, improving both the diagnosis and case management [3].

Breast elastography is a complementary imaging technique, utilized only in association with B-mode US, which improves BC diagnosis. The Tsukuba score is used to differentiate between benign and malignant breast lesions.

Breast elastography is a rapid and simple method that can improve the sensitivity and specificity of US, especially when we have focal lesions categorized as Breast Imaging-Reporting and Data System (BI-RADS) 3 and 4. This technique improves patient management and reduces unnecessary biopsies but requires follow-up [4–7].

The need for a more accurate understanding of BC, including the need for appropriate treatment, led to research concluded in the introduction of new information regarding the molecular characterization of breast tumors. This data is meant to complete the existing histopathology and imaging information defining a breast tumor.

Their definition is based on the presence of four different tumor cells compounds: estrogen receptor (ER), progesterone receptor (PR), human epidermal growth factor receptor 2 (HER2), and Ki67.

The therapeutic decision must be based on understanding the disease and also on the use of different types of investigation and treatment, which need to respect the ethical rules, to obtain a right informed consent [8] and analyze the different types of cancer not only in a public health context [9] but also like an individual major health problem in any stage of detection and treatment, including palliative care period [10].

Immunohistochemistry plays an important role in detecting biomarker expression concerning breast pathology and it has demonstrated a strong correlation between receptor expression and patient's response to therapy. Gene profile analysis is important but expensive and difficult to perform routinely. ER, PR, HER2, and Ki67 are the most common immunomarkers used in determining the prognostic of BC and for deciding the therapeutic strategy [11].

According to *St. Gallen Consensus* 2013 Classification, there are five molecular subtypes of BC (Table 1) [12, 13].

The grouped calcifications evident on the US exam at the level of a lesion and confirmed mammography and histopathological (HP) examination, more than five per 1 cm, raise suspicion of malignancy [14].

Table 1 – Characterization of BC molecular subtypes

Molecular BC subtype	Receptor			Ki67 index	Prognosis	Responds to therapy
	ER	PR	HER2			
Luminal A	+	+	–	Low (<14%)	Good	Hormonal therapy
Luminal B HER2-negative	+	+	–	Low (≥14%)	Worse	Hormonal therapy
Luminal B HER2-positive	+	+	+	–	Worse	HER2-targeted therapy (Trastuzumab) + hormonal therapy
HER2-enriched	–	–	+	–	Worse	HER2-targeted therapy (Trastuzumab)
Triple-negative (basal-like)	–	–	–	Possible high	Bad	Chemotherapy

BC: Breast cancer; ER: Estrogen receptor; HER2: Human epidermal growth factor receptor 2; PR: Progesterone receptor.

Aim

The study analyzed the correlation of US changes of lesions suggestive of malignancy with the HP results. There were correlations of BC subtypes with the ER, PR, and HER2 receptors, and Ki67 index, and the US aspect of the mammary tumor formations.

Patients, Materials and Methods

The study was prospective for a period of six months, in 2019, as part of a screening conducted in a private Hospital in Braşov, Romania, within the Department of Radiology and Medical Imaging. Out of 2502 patients, 108 were selected who were US-framed in one of the lesions categorized as BI-RADS 3, 4, and 5 scores, and on whom biopsy was performed [immunohistochemical (IHC) detection] at the level of the suspected US lesion.

The distribution of patients by age groups was as follows: five patients in the 21–30 years group, nine patients in the 31–40 years group, 20 in the 41–50 years group, 27 patients in the 51–60 years group, 31 in the 61–70 years group, 10 patients in the 71–80 age group and six patients over 81 years (Figure 1).

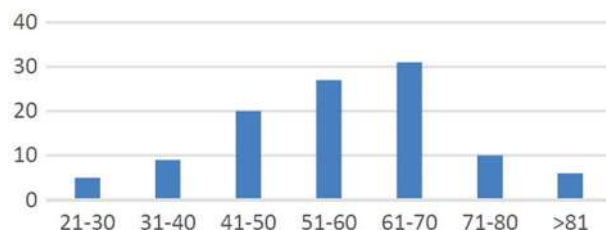


Figure 1 – Distribution of cases by age categories.

The devices used in the study were:

- for mammograms: Senographe Crystal Nova (General Electric), Mammomat 3000 Nova (Siemens);
- for ultrasonography: Logiq S7 (General Electric) US machine, RS80 with Prestige (Samsung) US machine.

Statistical Package for the Social Sciences (SPSS) 20.0 software was used to analyze all the patients selected. Count data were expressed and compared using χ^2 (chi-squared) test, $p < 0.05$ (considered statistically significant), and Cramér's V test interpretation (>0.25 – very strong; >0.15 – strong; >0.10 – moderate; >0.05 – weak; >0 – no or very weak). Cramér's V statistic is frequent used as measure of association between two categorical variables. Cramér's V test is the most widely used of the nominal-based measures of chi-squared test, offering a good standardization from 0 to 1, regardless of the size of the table [15].

Results

Out of 2502 patients evaluated in the screening, we selected 108 patients examined by US, mammography, and fine-needle biopsy, who presented suspicions for malignancy lesions, having BI-RADS score of 4 or 5. Following the IHC analysis, they were classified in one of the BC subtypes.

The highest incidence of US lesions was more frequent between 51 and 70 years old, with an average of 27.9%, and the lowest incidence was observed under the age of 30, 4.9% respectively.

Lesions to the right breast were more common, with a difference of 4% as compared to the left breast. Unique breast lesions were observed in 57.8% of cases; multiple lesions either in one breast or bilaterally were noted in 42.2% of cases. In 60.78% of the cases, the lesion was present in the external upper quadrant, followed by 18.62% in the internal upper quadrant, and with a lower percentage in the lower quadrants (11.76% inferior external and 8.82% in the lower medial quadrant).

Over half (51%) of the mammary tumors suspected of malignancy found on US examination had dimensions over 2 cm and have been easily emphasized; in 29% of the cases, dimensions situated between 1–2 cm and 20% lesions measure less than 1 cm and were more present in younger patients.

We considered the following characteristics as being malignant lesions on the US examination: hypoechoic, inhomogeneous structure, microlobulations, including microcalcifications vascular signal, and hypervascularization inside the tumor. Eighty-three (76.85%) cases were confirmed for BC, 23 (21.3%) cases were classified as benign lesions and two (1.85%) cases were inconclusive and were due to repeat the examination.

Analyzing the distribution of BC patients by subtype (immunohistopathologically), we found the highest incidence of the luminal A subtype – 53.57% of the cases, most frequently evidenced in the 51–60 years age group. The luminal B subtype was present in 22.61% of the cases, most frequently evidenced in the 41–50 years age group. The triple-negative subtype was present in 10.71% of the cases, most frequently evidenced in the 61–70 years age group. Less than 10% were HER2-positive enriched-subtype – 7.14%, and luminal B HER2-positive subtype – 5.95%. We found luminal A subtype to be the most common and luminal B HER2-positive subtype as having fewer cases (Figure 2).

The US characteristics of the mammary lesions were analyzed and correlated to all molecular receptors (ER, PR, HER2) significant for this type of cancer, and Ki67

index, and with HP subtypes according to *St. Gallen Consensus 2013 Classification* (Table 2).

The following aspects were noted:

- ER and PR were positively correlated with luminal A ($p<0.001$) and luminal B HER2-negative subtypes ($p<0.001$ for ER and $p=0.007$ for PR), and inversely correlated with HER2-enriched ($p=0.001$ for ER and $p=0.004$ for PR) and triple-negative subtypes ($p<0.001$);
- HER2 was correlated with luminal B HER2-positive ($p=0.04$) and HER2-enriched (score 3) ($p<0.001$) subtypes;
- 14% of Ki67 was positively correlated with HER2-enriched ($p=0.003$) and triple-negative ($p<0.001$) subtypes, and inversely correlated with luminal A ($p<0.001$) and luminal B HER2-negative ($p<0.001$) subtypes.

Table 2 – Correlation between breast cancer molecular subtypes and ER, PR, HER2 molecular receptors, and Ki67 index

Molecular receptors	<i>p</i> / OR	Subtype				
		Luminal A	Luminal B HER2-negative	Luminal B HER2-positive	HER2-enriched	Triple-negative
ER-positive	<i>p</i>	<0.0001	0.0002	0.0790	0.0010	<0.0001
	OR	>1	>1	>1	<1	<1
PR-positive	<i>p</i>	<0.0001	0.0072	0.2774	0.0040	0.0003
	OR	>1	>1	>1	<1	<1
HER2-positive	<i>p</i>	0.0910	0.3463	0.0481	<0.0001	0.5388
	OR	<1	<1	>1	>1	>1
Ki67 index >14%	<i>p</i>	<0.0001	<0.0001	0.0938	0.0033	<0.0001
	OR	>1	>1	>1	>1	>1

ER: Estrogen receptor; HER2: Human epidermal growth factor receptor 2; OR: Odds ratio; PR: Progesterone receptor.

Multiple US findings were correlated with ER presence ($p=0.045$) and HER2-positive ($p=0.012$) immunoeexpression.

According to the data analysis using Cramér's V test, the following HP subtypes were correlated with the presence of vascularization at the level of US-examined lesions: the luminal B HER2-negative and triple-negative subtypes were moderately correlated (values >0.10), and the luminal B HER2-positive and luminal B HER2-positive subtypes were poorly correlated (values >0.05) (Table 3). The increased vascularization present in US was correlated with the absence of PR ($p=0.014$).

Table 3 – Correlations between breast cancer subtypes and ultrasound signs – lesion vascularization and the presence of adenopathy (Phi / Cramér's V test)

Subtype	Phi / Cramér's V test values	
	Vascularization	Adenopathy
Luminal A	0.004359	0.116868
Luminal B HER2-negative	0.108289	0.123667
Luminal B HER2-positive	0.073902	0.038259
HER2-enriched	0.098183	0.150414
Triple-negative	0.127273	0.112194

HER2: Human epidermal growth factor receptor 2.

In our study, 70.58% of the evaluated patients have adenopathy; the majority being axillary and less parasternal in the case of lesions in the internal quadrants, adenopathy was anatomopathologically confirmed, but sometimes without describing their HP characteristics by the examining doctor, respectively partially or totally increase of the thickness of the cortex, reduction, or disappearance of the sinus. 29.41% of the patients did not have axillary pathological adenopathy at the first evaluation; the observed cases had lesions with dimensions less than 1 cm compared to

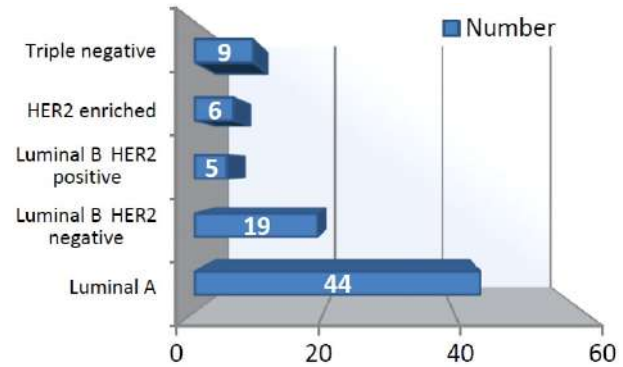


Figure 2 – Distribution of breast cancer patients by immunohistopathological subtype.

those who had adenopathy, in which the tumor formation was frequently over 2 cm.

According to the data analysis performed using Cramér's V test, the following HP subtypes were correlated with the presence of adenopathy in the US-examined lesions: the luminal A subtype, the luminal B HER2-negative subtype, the non-luminal HER2-positive subtype, and the triple-negative subtype correlated moderately (values >0.10) with US appearance of adenopathy (Table 4).

Table 4 – Correlations between breast cancer subtypes and ultrasound signs – contour (Phi / Cramér's V test)

Subtype	Phi / Cramér's V test values	
	Well-defined contour	Inaccurate contour delimited / speculated
Luminal A	0.203144	0.201165
Luminal B HER2-negative	0.066156	0.121548
Luminal B HER2-positive	0.095229	0.114610
HER2-enriched	0.117161	0.071309
Triple-negative	0.130319	0.075011

HER2: Human epidermal growth factor receptor 2.

The US presence of adenopathy was associated with the absence of PR ($p=0.007$), with equivocal score (score 2) of HER2 ($p=0.038$), and with increased score (>14%) of Ki67 index ($p=0.005$). In addition, adenopathy correlated with the onset of invasive ductal carcinoma ($p=0.018$) of mucinous carcinoma ($p=0.013$) and with grade 3 malignancy of BC ($p=0.007$).

Regarding the correlations between BC subtype and US signs (contour, lobulation), we found the following: (i) US-examined malignant lesions showed an irregular contour in 83.33% of cases, compared to the lesions

highlighted mammographically in the same cases; (ii) US was able to correctly describe the contour, especially if the breast tissue was dense, compared to mammography, where the inaccurate contour was described in 53.16% of the lesions.

A percentage of 16.67% of the US-detected tumors presented well-defined contour; these patients were mostly less than 50 years of age.

Concerning lobulation, the most frequent US characteristic was microlobulation in 44% cases, followed by macrolobulation in 19% cases, and absence of lobulation in 37% of cases. This statement demonstrates the necessity of lesions reevaluation, especially when first they were considered benign and if the age of the patient is young. The US reevaluation of these lesions after six months showed their evolution towards a suspected US malignant lesion, which leads to biopsy and determination of the BC subtype.

According to the data analysis using Cramér's V test, the following HP subtypes correlated with well-defined margins of the US-examined lesions: luminal A subtype was strongly correlated (values >0.15), luminal B HER2-negative and luminal B HER2-positive subtypes were weakly correlated (values >0.05), and non-luminal HER2-positive and triple-negative subtypes were moderately correlated (values >0.10).

The following HP subtypes were correlated with indefinitely delimited margins of the US-examined lesions: luminal A subtype strongly correlated (values >0.15), luminal B HER2-negative and luminal B HER2-positive subtypes moderately correlated (values >0.10), and HER2-enriched and triple-negative subtypes poorly correlated (values >0.05) (Table 5). The malignant characters of the breast tumor formation are highlighted in Figure 3.

Table 5 – Correlations between breast cancer subtypes and ultrasound signs – lobulation (Phi / Cramér's V test)

Subtype	Phi / Cramér's V test values		
	No lobulation	Macro-lobulation	Micro-lobulation
Luminal A	0.097921	0.062323	0.063706
Luminal B HER2-negative	0.187659	0.021881	0.250740
Luminal B HER2-positive	0.114488	0.101800	0.007448
HER2-enriched	0.075241	0.005898	0.040996
Triple-negative	0.011692	0.036661	0.050965

HER2: Human epidermal growth factor receptor 2.

Inaccurate or spiked margins were correlated with the presence of ER ($p<0.001$), the presence of PR ($p=0.001$), HER2-negative ($p<0.001$), and low values ($<14\%$) of Ki67 index ($p=0.018$). In addition, luminal A, invasive ductal carcinoma, grade 2 malignancy HP subtype was correlated with the US character of imprecise or spiculate margins.

The data analyzed by means of the Cramér's V test revealed that the following HP subtypes were correlated with the presence of microlobulations in the US-examined lesions: the luminal A subtype and the triple-negative subtype were weakly correlated (values >0.05), and the luminal B HER2-negative subtype was strongly correlated (values >0.15).

Microlobulations were correlated with the presence of ER ($p=0.007$), the presence of PR ($p=0.003$), the absence of HER2 ($p=0.008$), and the luminal B HER2-negative subtype ($p=0.009$).

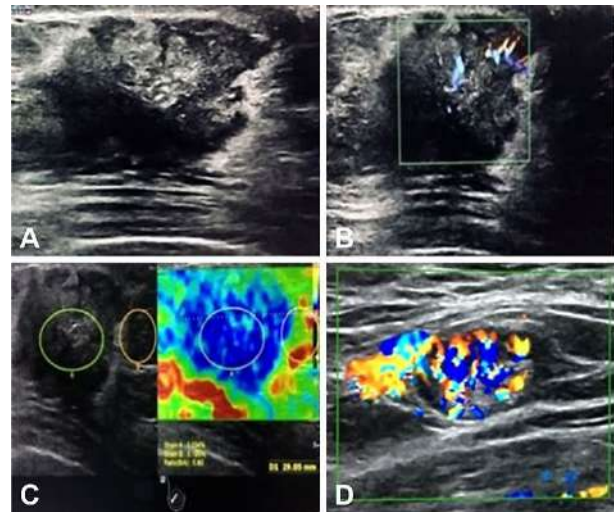


Figure 3 – Ultrasound examination of a 78-year-old patient, right breast, upper and external quadrant: hypoechoic lesion, irregular, with microlobulations (A), and increased vascular signal (B), increased elastographic value – strain ratio 5.8 (C), axillary pathological adenopathy (D). Anatomopathological characteristics: invasive breast carcinoma; ER-positive 80%; PR-positive 60–70%; HER2-negative (score 0); Ki67 index 10%; luminal A subtype. ER: Estrogen receptor; HER2: Human epidermal growth factor receptor 2; PR: Progesterone receptor.

The following HP subtypes were correlated with the presence of macrolobulation in the US-examined lesions: the luminal A subtype weakly correlated (values >0.05) and the luminal B HER2 subtype was moderately positively correlated (values >0.10) (Table 6).

Table 6 – Correlations between breast cancer subtypes and ultrasound signs – structure (Phi / Cramér's V test)

Subtype	Phi / Cramér's V test values	
	Homogeneous	Non-homogeneous \pm halo
Luminal A	0.134840	0.133598
Luminal B HER2-negative	0.020197	0.055777
Luminal B HER2-positive	0.070381	0.091882
HER2-enriched	0.061980	0.012643
Triple-negative	0.019263	0.062869

HER2: Human epidermal growth factor receptor 2.

According to the data analysis using Cramér's V test, the following HP subtypes were correlated with the homogeneous structure of the US-examined lesions: the luminal A subtype was moderately correlated (values >0.10), and the luminal B HER2-positive and HER2-enriched subtypes were weakly correlated (values >0.05).

The following HP subtypes were correlated with the non-homogeneous structure of the US-examined lesions: the luminal A subtype was moderately correlated (values >0.10), and the luminal B HER2-negative, luminal B HER2-positive, and triple-negative subtypes were weakly correlated (values >0.05).

The non-homogeneous structure or presence of the peripheral wall was correlated with the presence of ER ($p=0.022$) and the presence of PR ($p=0.006$). In addition, invasive ductal breast carcinoma was correlated with the presence of the non-homogeneous character of the tumor ($p=0.045$) (Table 7).

Table 7 – Correlations between breast cancer subtypes and ultrasound signs – calcifications (Phi / Cramér's V test)

Subtype	Phi / Cramér's V test values			
	Without calcifications	Macrocalcification	Isolated microcalcifications	Focal microcalcifications
Luminal A	0.057085	0.025885	0.039479	0.053300
Luminal B HER2-negative	0.078145	0.116912	0.038880	0.037830
Luminal B HER2-positive	0.139798	0.030264	0.085029	0.062318
HER2-enriched	0.024821	0.033315	0.026743	0.085749
Triple-negative	0.030857	0.041416	0.016623	0.042640

HER2: Human epidermal growth factor receptor 2.

It is important to differentiate benign (with increase with age) from suspected malignant microcalcifications, as more than half of non-palpable cancers are ductal carcinoma *in situ*.

According to the data analysis based on the Cramér's V test, the following HP subtypes were correlated with the absence of calcifications in the US-examined lesions: the luminal A and luminal B HER2-negative subtypes weakly correlated (values >0.05), and luminal B HER2-positive subtype moderately correlated (values >0.10).

The luminal B HER2 subtype was positively correlated

(values >0.05) with the presence of isolated microcalcifications in the US-examined lesions.

The analysis of the data performed by means of the Cramér's V test revealed that the HP subtypes were correlated with the presence of focal microcalcifications in the US-examined lesions: luminal A, luminal B HER2-positive, and HER2-enriched subtypes poorly correlated (values >0.05).

The luminal B HER2-negative subtype was moderately correlated (values >0.10) with the presence of macrocalcifications in the US-examined lesions (Table 8).

Table 8 – Correlations between breast cancer subtypes and ultrasound signs – posterior acoustic changes (Phi / Cramér's V test)

Subtype	Phi / Cramér's V test values				
	Posterior amplification	Without attenuation	Total attenuation	Total bilateral symmetrical marginal shadow	Bilateral asymmetric marginal shadow
Luminal A	0.080158	0.222727	0.075011	0.159091	0.093275
Luminal B HER2-negative	0.044667	0.010265	0.056649	0.051325	0.034391
Luminal B HER2-positive	0.021300	0.050487	0.100657	0.066431	0.031159
HER2-enriched	0.023447	0.190131	0.027427	0.073127	0.085749
Triple-negative	0.029148	0.018182	0.075011	0.030303	0.000000

HER2: Human epidermal growth factor receptor 2.

US analysis of the attenuation created by the suspicious mammary lesion revealed that most lesions presented asymmetric bilateral shadow (35.29% of cases); in 32.35% of cases, no posterior acoustic changes were noted. The total attenuation was found in 22.54% of cases and the bilateral symmetrical marginal shadow in 8.82% of cases. In less than 1% of cases, the lesions were described as presenting acoustic amplification. The malignant characters of the breast tumor formation, especially details of the contour and structure, were highlighted in Figure 4.

The Cramér's V test-based data analysis showed that the following HP subtypes were correlated with the presence of US-examined lesions without posterior acoustic changes: the non-luminal positive, luminal A and HER2 subtypes strongly correlated (values >0.15), and the luminal B HER2-positive subtype poorly correlated (values >0.05). The luminal A subtype was weakly correlated (values >0.05) with the US character of the posterior acoustic amplification of the examined lesions.

The following HP subtypes were correlated with the total posterior acoustic attenuation of the US-examined lesions: luminal A, luminal B HER2-negative and triple-negative subtypes were poorly correlated (values >0.05), and luminal B HER2-positive subtype was moderately correlated (values >0.10).

Regarding the correlation of the BC subtypes with the bilateral symmetric marginal shadow character of the US-examined lesions, it was found that luminal A subtype was strongly correlated (values >0.15), and luminal B HER2-negative, luminal B HER2-positive and HER2-enriched subtypes were weakly correlated (values >0.05).

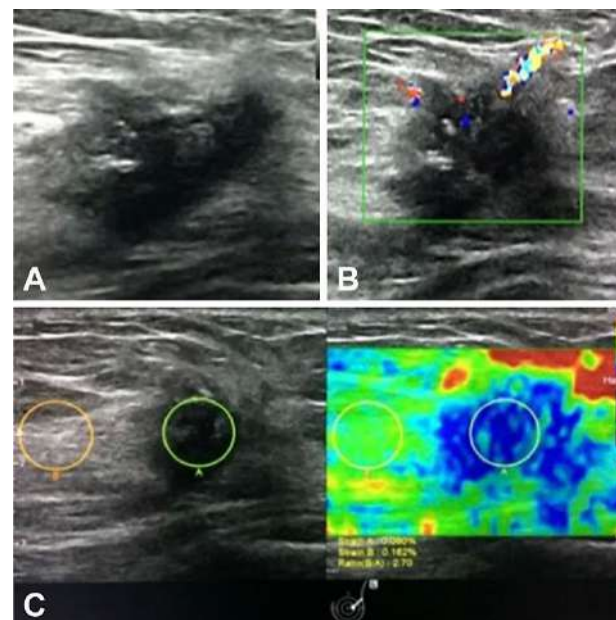


Figure 4 – Ultrasound examination of a 65-year-old patient, left breast, upper and outer quadrant: hypoechoic lesion, irregular mass, echogenic rim (A), increased vascular signal, focal microcalcifications (B), increased elastography value – strain ratio 2.70 (C). Anatomopathological characteristics: ER-negative; PR-negative; HER2-positive (score 2+); Ki67 index 60–70%; HER2-enriched subtype. ER: Estrogen receptor; HER2: Human epidermal growth factor receptor 2; PR: Progesterone receptor.

The luminal A and HER2-enriched subtypes were weakly correlated (values >0.05) with the bilateral asymmetric marginal shadow character of the US-examined lesions.

Asymmetrical bilateral acoustic attenuation on US examination was correlated with the presence of PR ($p=0.02$) and grade 2 malignant BC ($p=0.04$).

The statistics obtained by means of the Cramér's V test showed the following results:

- Tumors' vascularization has a direct relationship with luminal B HER2-negative and triple-negative subtypes with moderate correlation (values >0.10), and with the absence of PR ($p=0.014$);

- Pathological lymph nodes were positively correlated with luminal A, luminal B HER2-negative, HER2-enriched, and triple-negative subtypes, and with the absence of PR ($p=0.007$), with HER2 equivocal score (score 2) ($p=0.038$), with increased score ($>14\%$) of Ki67 index ($p=0.005$), with the onset of invasive ductal carcinoma ($p=0.018$), mucinous carcinoma ($p=0.013$), and with grade 3 malignancy of BC ($p=0.007$);

- Ill-defined margins had a positive relationship with luminal A, luminal B HER2-negative, luminal B HER2-positive subtypes, and with the presence of ER ($p<0.001$), the presence of PR ($p=0.001$), HER2-negative (score 1) ($p<0.001$), low values ($<14\%$) of Ki67 index ($p=0.018$), invasive ductal carcinoma, and grade 2 malignancy;

- The luminal B HER2-negative subtype was correlated with the presence of microlobulations in the US-examined lesions; microlobulations were correlated with ER-positive ($p=0.007$), PR-positive ($p=0.003$), the absence (score 1) of HER2 ($p=0.008$), and the luminal B HER2-negative subtype ($p=0.009$), as well;

- The luminal B HER2-positive subtype was positively correlated with the presence of macrolobulation in the US-examined lesions;

- The luminal A subtype was positively correlated with the inhomogeneous internal structure of the US-examined lesions; this ultrasonography characteristic was correlated with ER-positive ($p=0.022$), PR-positive ($p=0.006$), and invasive ductal breast carcinoma ($p=0.045$), as well;

- The luminal B HER2-negative subtype was moderately correlated (values >0.10) with the presence of macrocalcifications in the US-examined lesions;

- The luminal B HER2-positive subtype was correlated with the total posterior acoustic attenuation of the US-examined lesions;

- The luminal A subtype was correlated with the bilateral symmetrical marginal shadowing character of the US-examined lesions; asymmetrical bilateral acoustic attenuation on US was correlated with the presence of PR ($p=0.02$) and grade 2 malignant BC ($p=0.04$).

✉ Discussions

According to *St. Gallen Consensus* 2013, breast tumors were classified into five categories based on their molecular characteristics [12]: three non-basal subtypes (luminal A, luminal B HER2-negative and luminal B HER2-positive) and two basal-like subtypes (HER2-enriched and triple-negative) [16]. Luminal A and luminal B subtypes were

considered those which were positive for ER and PR, and which form the luminal-like group [17–19].

By analyzing the distribution of BC patients depending on IHC subtype, we found the highest incidence of the luminal A subtype in 53.57% of the cases, which aligns with Naeem *et al.* findings, most frequently evidenced in the 51–60 years old age group [20]. Patients diagnosed with BC luminal A subtype were among the youngest ones, while patients presenting HER2 immunoexpression were found to be older of age ($p=0.01$), as Wen *et al.* postulate in their study [3].

The luminal B HER2-negative subtype was present in 22.61% of the cases, which is different from the study conducted by Su *et al.*, most frequently evidenced in the 41–50 years age groups [21].

The triple-negative subtype was present in 10.71% of the cases, as resulted in other studies, most frequently evidenced in the 61–70 years age groups [22].

Less than 10% of BCs were HER2-enhanced (7.14%) and luminal B HER2-positive (5.95%) subtypes.

Kondov *et al.* determined the incidence of different BC subtypes, as follows: luminal A was the most frequent one, followed by luminal B HER2-negative, luminal B HER2-positive, HER2-enriched, and the least frequent one was triple-negative; in the present study, we found HER2-enriched patients to be more numerous than the luminal B HER2-positive ones [23].

Determining BC subtype has a major impact on therapeutic decisions, as well as on disease prognosis [23]. The necessity for BC molecular subtyping is emphasized by the need for individualized, more targeted therapy, as several studies have shown [24–27].

The luminal A subtype was associated in our study with posterior acoustic attenuation, as mentioned by Irshad *et al.* [28], with inhomogeneous internal structure and presence of pathological lymph nodes. Wen *et al.* study suggested that the basal-like subtype had no posterior features ($p=0.041$), compared to the present study where HER2 and basal-like subtypes presented acoustic shadowing ($p=0.03$) [3].

The luminal B HER2-negative subtype was especially correlated with microlobulations, macrocalcifications, pathological lymph nodes, and increased vascular signal. Zhang *et al.* found that luminal B subtypes could be associated with increased vascularity [29].

According to Wen *et al.*, US characteristics, such as microlobulated margins, are more frequently found in BC HER2 subtypes ($p=0.002$), while the spiculated contour seems to be characteristic of the luminal (A and B) subtypes [3].

The luminal B HER2-positive subtype had a positive correlation with ill-defined margins, macrolobulation, and posterior acoustic attenuation [30, 31].

Çelebi *et al.* mentioned the association of ill-defined margins and posterior acoustic shadowing with luminal A and luminal B subtypes [32].

The HER2-enriched subtype had a strong correlation with the presence of pathological lymph nodes and well-defined margins, while the triple-negative subtype was associated with pathological lymph nodes, enhanced

vascularization, and well-defined margins [30, 33, 34]. Imagistic investigations, such as computed tomography (CT), magnetic resonance imaging (MRI), positron emission tomography (PET) or US, represent important tools for detecting lymph node metastases.

Imaging investigation is a mandatory step in determining the staging of tumor, node, and metastasis (TNM) and focuses on the management of the patient's disease. Furthermore, the prognosis is influenced by the presence or absence of metastases [35].

US and mammography were the two imagistic methods used in our study to assess breast tumors. US is considered a tool that can be used regardless of age, especially on women less than 40, both as a screening method and as a complementary investigation when a woman presents a palpable tumor [36, 37]. It is recommended to be performed as a routine for breast control, as it helps to evaluate false positive results [38–40].

In our study, we used US-guided biopsy, as referred in studies underlying its utility [37].

An attempt in identifying US features correlated to the risk of malignancy was conducted by Nam *et al.* They did not manage to draw a consistent conclusion regarding this topic because of the insignificant number of patients diagnosed by US investigation with a BI-RADS 3 formation; these patients developed histopathologically confirmed BC during the follow-up. Both Nam *et al.* study and ours revealed a high incidence of bilateral implication on patients receiving a BI-RADS 3 score, while BC detected on these patients was infrequent. Based on these remarks, we recommend routine breast US evaluation for patients on average risk for malignancy diagnosed with a BI-RADS 3 lesion [41].

Ultrasonography brought important information and adjusted the diagnosis when the dense breast was examined on mammography, as in other studies of Houssami *et al.* [42] and Tagliafico *et al.* [43].

An additional useful US imaging method for breast examination is elastography, a non-invasive technique based on determining tissue stiffness. Small dimension tumors, cystic formations, or tumors possessing a corpuscular core represents the lesions most frequently evaluated using this tool. It has been concluded that breast elastography can both reduce the number of unnecessary biopsies and postpone reappraisal for BI-RADS 3 US lesions [44].

It is recommended that breast elastography only be used as a complementary method to the traditional US technique, when assessing suspected malignancy breast lesions. It would adjust the US BI-RADS score according to tissue stiffness [45].

Mammography was used both for asymptomatic and symptomatic patients, as it has a higher sensitivity than US for non-invasive BCs, correlated with breast calcifications presence detected only by mammography [46]. The dense breast tissue examined on women under 50 represented a difficulty in detecting mammographic lesions but the US examination completed the diagnosis due to the hypoechogenic appearance of the tumors, which brought a significant contribution [47]. In women over 50 years, the occurrence of a predominantly adipose tissue allowed

the correct highlighting of the mammary lesion [48]. Multiple suspicious mammographic lesions required complementary US examination for an appropriate characterization. Therefore, we must mention that both mammography and US brought an important contribution in detecting and characterizing breast lesions.

Pathological lymph nodes were present in 70.58% of the examined patients, a finding similar to that in a study conducted by Zhang *et al.* [49]. Most of them had an axillary localization and fewer parasternal (in case of internal quadrants lesions). Pathological lymph nodes were also histopathologically confirmed but on US examination, some of them were not characterized as presenting increased thickness of the cortex (partially or totally) and reduction or disappearance of the sinus. These false-negative results on an US could be a consequence of small dimensions of the lymph nodes [50]. 29.41% of the patients did not have axillary pathological lymph nodes on the first evaluation. Those without pathological lymph nodes most frequently had tumors less than 1 cm in diameter; in comparison, those who had pathological lymph nodes had tumors over 2 cm.

On US evaluation, suspicious mammary tumors were described as presenting an ill-defined contour or spiculate margins on 83.33% of cases, compared to only 53.16% on mammography examination of the same patients, emphasizing the fact that ultrasonography has a higher sensitivity, especially when describing fibro-glandular tissue [51]. The rest of them (16.67%) presented well-defined margins and this characteristic was most often present in patients under 50.

Regarding lobulation of mammary tumors, microlobulations were present in 44% of cases, macrolobulations in 19% cases, and 37% of cases were without lobulations; this highlights the necessity for follow-up when describing benign lesions on the first examination, especially if the patient is very young [52]. The six months US reevaluation of these lesions demonstrated their evolution towards a suspicion for malignant tumor, which implied biopsy and histopathological and IHC analysis.

US examination of the posterior acoustic attenuation character related to suspicious mammary lesion emphasized the fact that most lesions presented asymmetric bilateral shadowing (35.29% of the cases); in 32.35% of the cases, no posterior acoustic changes were noticed. The total attenuation was highlighted in 22.54% of cases and the bilateral symmetrical marginal shadowing in 8.82% of cases. In less than 1% of the cases, the lesions were described as presenting posterior acoustic amplification. The posterior acoustic attenuation was rather associated with two subtypes (luminal A and B), a finding similar to other studies [31, 34, 28].

According to *chi*-squared analysis of molecular cancer subtypes correlation to receptors and Ki67, we found a significant association between both luminal A and luminal B HER2-negative subtypes and hormone receptors (ER, PR); these have an inverse relationship with Ki67 index elevated values; the luminal B HER2-positive subtype has a direct association with HER2 presence; the HER2-enriched subtype was statistically significant associated with HER2

presence and elevated Ki67 values but had an inverse relationship to hormone receptors (ER, PR); the triple-negative subtype was strongly associated to Ki67 values and inversely correlated to ER and PR. Stolnicu *et al.* stated that the ER-/PR+ BC phenotype can be associated with small-size tumors, the HER2 presence, the absence of lymph node metastases, and younger patients; although it was found to be the most infrequent cancer subtype in their study, it had the best long-term prognosis probably correlated to PR targeted therapy [53].

✉ Conclusions

In our study, luminal A subtype has the highest incidence, and luminal B HER2-positive subtype was the least common. Posterior acoustic shading, inhomogeneous internal structure, and poorly defined edges appear to be associated with both luminal A and luminal B subtypes, while the well-defined contour was characteristic of triple-negative BCs. On the other hand, the presence of pathological lymph nodes was accentuated on all subtypes: luminal A, luminal B, HER2-enriched and triple-negative subtypes. Improved vascularization was rather associated with luminal B and triple-negative subtypes, according to our findings. The study showed that the expression of the value of IHC receptors influences the therapeutic decision, and immunological therapy has an essential role in the patient's evolution and in the prognosis of the disease. Moreover, different associations between the IHC subtypes of BC and molecular receptors could predict a certain genetic predisposition to develop specific BC and can be used in medical practice.

Conflict of interests

The authors declare that they have no conflict of interests.

References

- Formenti SC, Arslan AA, Love SM. Global breast cancer: the lessons to bring home. *Int J Breast Cancer*, 2012, 2012: 249501. <https://doi.org/10.1155/2012/249501> PMID: 22295243 PMCID: PMC3262607
- Bangal VB, Shinde KK, Gavhane SP, Singh RK. Breast carcinoma in women – a rising threat. *Int J Biomed Adv Res*, 2013, 4(2):73–76. <https://doi.org/10.7439/ijbar.v4i2.902>
- Wen X, Yu Y, Yu X, Cheng W, Wang Z, Liu L, Zhang L, Qin L, Tian J. Correlations between ultrasonographic findings of invasive lobular carcinoma of the breast and intrinsic subtypes. *Ultraschall Med*, 2019, 40(6):764–770. <https://doi.org/10.1055/a-0715-1668> PMID: 30253431
- Sigrist RMS, Liau J, El Kaffas A, Chammas MC, Willmann JK. Ultrasound elastography: review of techniques and clinical applications. *Theranostics*, 2017, 7(5):1303–1329. <https://doi.org/10.7150/thno.18650> PMID: 28435467 PMCID: PMC5399595
- Gheonea IA, Donoiu L, Camen D, Popescu FC, Bondari S. Sonoelastography of breast lesions: a prospective study of 215 cases with histopathological correlation. *Rom J Morphol Embryol*, 2011, 52(4):1209–1214. PMID: 22203924
- Rizzatto G. Real-time elastography of the breast in clinical practice – the Italian experience. *Medix Hitachi Suppl*, 2007, 1:12–15.
- Chiorean A, Duma MM, Dudea SM, Iancu A, Dumitriu D, Roman R, Sfrânguș S. Real-time ultrasound elastography of the breast: state of the art. *Med Ultrason*, 2008, 10(2):73–82. <http://medultrason.ro/real-time-ultrasound-elastography-of-the-breast-state-of-the-art/index.htm>
- Olimid AP, Rogozea LM, Olimid DA. Ethical approach to the genetic, biometric and health data protection and processing in the new EU General Data Protection Regulation (2018). *Rom J Morphol Embryol*, 2018, 59(2):631–636. PMID: 30173275
- Rogozea L, Purcaru D, Leășu F, Nemet C. Biomedical research – opportunities and ethical challenges. *Rom J Morphol Embryol*, 2014, 55(2 Suppl):719–722. PMID: 25178352
- Constantin DA, Cloriceanu IH, Tănășu MM, Popa D, Bădău D, Burtea V, Nemet GC, Rogozea LM. Ethical dilemmas in communicating bad news following histopathology examination. *Rom J Morphol Embryol*, 2017, 58(3):1121–1125. PMID: 29250700
- Zaha DC. Significance of immunohistochemistry in breast cancer. *World J Clin Oncol*, 2014, 5(3):382–392. <https://doi.org/10.5306/wjco.v5.i3.382> PMID: 25114853 PMCID: PMC4127609
- Goldhirsch A, Winer EP, Coates AS, Gelber RD, Piccart-Gebhart M, Thürlimann B, Senn HJ; Panel members. Personalizing the treatment of women with early breast cancer: highlights of the St Gallen International Expert Consensus on the Primary Therapy of Early Breast Cancer 2013. *Ann Oncol*, 2013, 24(9):2206–2223. <https://doi.org/10.1093/annonc/mdt303> PMID: 23917950 PMCID: PMC3755334
- Eniu A, Morar-Bolba G, Lisencu C, Martin D, Galatâr M, Fetica B, Rancea A. Protocolul Comisiei Multidisciplinare pentru Decizie Terapeutică (CDT) în Cancerul de Sân. *Institutul Oncologic „Prof. Dr. Ion Chiricuță”*. *J Radiother Med Oncol*, 2013, 19(2):5–27. <https://srrom.ro/revista/volum-19-numarul-2-2013/> https://srrom.ro/wp-content/uploads/2018/04/V19_N02_2013_pp005.pdf
- Sechel G, Repanovici A, Manea R, Burtea V. The imaging evaluation of typical and atypical calcifications in different anatomical regions study in Brasov, Romania. *Med Surg J Rev Med Chir Soc Med Nat Iași*, 2020, 124(2):290–297. <https://www.revmedchir.ro/index.php/revmedchir/article/view/2121> <https://www.revmedchir.ro/index.php/revmedchir/article/download/2121/1622/>
- Akoglu H. User's guide to correlation coefficients. *Turk J Emerg Med*, 2018, 18(3):91–93. <https://doi.org/10.1016/j.tjem.2018.08.001> PMID: 30191186 PMCID: PMC6107969
- Gulzar R, Shahid R, Saleem O. Molecular subtypes of breast cancer by immunohistochemical profiling. *Int J Pathol*, 2018, 16(2):129–134. https://www.researchgate.net/profile/Ruqaiya-Shahid/publication/328744478_Molecular_Subtypes_of_Breast_Cancer_by_Immunohistochemical_Profiling/links/5be0697da6fdcc3a8dc115c1/Molecular-Subtypes-of-Breast-Cancer-by-Immunohistochemical-Profiles.pdf
- Hu Z, Fan C, Oh DS, Marron JS, He X, Qaqish BF, Livasy C, Carey LA, Reynolds E, Dressler L, Nobel A, Parker J, Ewend MG, Sawyer LR, Wu J, Liu Y, Nanda R, Tretiakova M, Ruiz Orrico A, Dreher D, Palazzo JP, Perreard L, Nelson E, Mone M, Hansen H, Mullins M, Quackenbush JF, Ellis MJ, Olapade OI, Bernard PS, Perou CM. The molecular portraits of breast tumors are conserved across microarray platforms. *BMC Genomics*, 2006, 7:96. <https://doi.org/10.1186/1471-2164-7-96> PMID: 16643655 PMCID: PMC1468408
- Sotiriou C, Neo SY, McShane LM, Korn EL, Long PM, Jazaeri A, Martiat P, Fox SB, Harris AL, Liu ET. Breast cancer classification and prognosis based on gene expression profiles from a population-based study. *Proc Natl Acad Sci U S A*, 2003, 100(18):10393–10398. <https://doi.org/10.1073/pnas.1732912100> PMID: 12917485 PMCID: PMC193572
- Habashy HO, Powe DG, Abdel-Fatah TM, Gee JMW, Nicholson RI, Green AR, Rakha EA, Ellis IO. A review of the biological and clinical characteristics of luminal-like oestrogen receptor-positive breast cancer. *Histopathology*, 2012, 60(6): 854–863. <https://doi.org/10.1111/j.1365-2559.2011.03912.x> PMID: 21906125
- Naeem S, Naz S, Riyaz A, Jehangir F, Afzal N. Immunohistochemical analysis of breast cancer subtypes and their correlation with Ki 67 index. *J Ayub Med Coll Abbottabad*, 2018, 30(1):94–96. PMID: 29504340
- Su Y, Zheng Y, Zheng W, Gu K, Chen Z, Li G, Cai Q, Lu W, Shu XO. Distinct distribution and prognostic significance of molecular subtypes of breast cancer in Chinese women: a population-based cohort study. *BMC Cancer*, 2011, 11:292. <https://doi.org/10.1186/1471-2407-11-292> PMID: 21749714 PMCID: PMC3157458

- [22] Badowska-Kozakiewicz AM, Budzik MP. Immunohistochemical characteristics of basal-like breast cancer. *Contemp Oncol (Pozn)*, 2016, 20(6):436–443. <https://doi.org/10.5114/wo.2016.56938> PMID: 28239279 PMCID: PMC5320452
- [23] Kondov B, Milenković Z, Kondov G, Petrushevska G, Bashenska N, Bogdanovska-Todorovska M, Tolevska N, Ivkovski L. Presentation of molecular subtypes of breast cancer detected by immunohistochemistry in surgically treated patients. *Open Access Maced J Med Sci*, 2018, 6(6):961–967. <https://doi.org/10.3889/oamjms.2018.231> PMID: 29983785 PMCID: PMC6026408
- [24] Goldhirsch A, Coates AS, Gelber RD, Glick JH, Thürlimann B, Senn HJ; St Gallen Expert Panel Members. First – select the target: better choice of adjuvant treatments for breast cancer patients. *Ann Oncol*, 2006, 17(12):1772–1776. <https://doi.org/10.1093/annonc/mdl398> PMID: 17071934
- [25] Goldhirsch A, Glick JH, Gelber RD, Coates AS, Thürlimann B, Senn HJ; Panel members. Meeting highlights: International Expert Consensus on the primary therapy of early breast cancer 2005. *Ann Oncol*, 2005, 16(10):1569–83. <https://doi.org/10.1093/annonc/mdl326> PMID: 16148022
- [26] Yeh IT, Mies C. Application of immunohistochemistry to breast lesions. *Arch Pathol Lab Med*, 2008, 132(3):349–358. <https://doi.org/10.5858/2008-132-349-AOITBL> PMID: 18318578
- [27] Yersal O, Barutca S. Biological subtypes of breast cancer: Prognostic and therapeutic implications. *World J Clin Oncol*, 2014, 5(3):412–424. <https://doi.org/10.5306/wjco.v5.i3.412> PMID: 25114856 PMCID: PMC4127612
- [28] Irshad A, Leddy R, Pisano E, Baker N, Lewis M, Ackerman S, Campbell A. Assessing the role of ultrasound in predicting the biological behavior of breast cancer. *AJR Am J Roentgenol*, 2013, 200(2):284–290. <https://doi.org/10.2214/AJR.12.8781> PMID: 23345347
- [29] Zhang L, Li J, Xiao Y, Cui H, Du G, Wang Y, Li Z, Wu T, Li X, Tian J. Identifying ultrasound and clinical features of breast cancer molecular subtypes by ensemble decision. *Sci Rep*, 2015, 5:11085. <https://doi.org/10.1038/srep11085> PMID: 26046791 PMCID: PMC4457139
- [30] Rashmi S, Kamala S, Murthy SS, Kotha S, Rao YS, Chaudhary KV. Predicting the molecular subtype of breast cancer based on mammography and ultrasound findings. *Indian J Radiol Imaging*, 2018, 28(3):354–361. https://doi.org/10.4103/ijri.IJRI_78_18 PMID: 30319215 PMCID: PMC6176670
- [31] Tandon A, Srivastava P, Manchada S, Wadhwa N, Gupta N, Kaur N, Pant CS, Pal R, Bhatt S. Role of sonography in predicting the hormone receptor status of breast cancer: a prospective study. *J Diagn Med Sonogr*, 2017, 34(1):3–14. <https://doi.org/10.1177/8756479317721663>
- [32] Çelebi F, Pilancı KN, Ordu Ç, Ağacayak F, Alço G, İlğün S, Sarsenov D, Erdoğan Z, Özmen V. The role of ultrasonographic findings to predict molecular subtype, histologic grade, and hormone receptor status of breast cancer. *Diagn Interv Radiol*, 2015, 21(6):448–453. <https://doi.org/10.5152/dir.2015.14515> PMID: 26359880 PMCID: PMC4622390
- [33] Cen D, Xu L, Li N, Chen Z, Wang L, Zhou S, Xu B, Liu CL, Liu Z, Luo T. BI-RADS 3–5 microcalcifications can preoperatively predict breast cancer HER2 and Luminal A molecular subtype. *Oncotarget*, 2017, 8(8):13855–13862. <https://doi.org/10.18632/oncotarget.14655> PMID: 28099938 PMCID: PMC5355144
- [34] Boissierie-Lacroix M, Mac Grogan G, Debled M, Ferron S, Asad-Syed M, Brouste V, Mathoulin-Pelissier S, Hurtevent-Labrot G. Radiological features of triple negative breast cancers (73 cases). *Diagn Interv Imaging*, 2012, 93(3):183–190. <https://doi.org/10.1016/j.diii.2012.01.006> PMID: 22421282
- [35] Urano M, Denewar FA, Murai T, Mizutani M, Kitase M, Ohashi K, Shiraki N, Shibamoto Y. Internal mammary lymph node metastases in breast cancer: what should radiologists know? *Jpn J Radiol*, 2018, 36(11):629–640. <https://doi.org/10.1007/s11604-018-0773-9> PMID: 30194586
- [36] Britton P, Warwick J, Wallis MG, O'Keeffe S, Taylor K, Sinnatambay R, Barter S, Gaskarth M, Duffy SW, Wishart GC. Measuring the accuracy of diagnostic imaging in symptomatic breast patients: team and individual performance. *Br J Radiol*, 2012, 85(1012):415–422. <https://doi.org/10.1259/bjr/32906819> PMID: 21224304 PMCID: PMC3486650
- [37] Evans A, Trimboli RM, Athanasios A, Baileyguyer C, Baltzer PA, Bick U, Camps Herrero J, Clauser P, Colin C, Cornford E, Fallenberg EM, Fuchsjaeger MH, Gilbert FJ, Helbich TH, Kinkel K, Heywang-Köbrunner SH, Kuhl CK, Mann RM, Martincich L, Panizza P, Pediconi F, Pijnappel RM, Pinker K, Zackrisson S, Forrai G, Sardanelli F; European Society of Breast Imaging (EUSOBI), with language review by Europa Donna–The European Breast Cancer Coalition. Breast ultrasound: recommendations for information to women and referring physicians by the European Society of Breast Imaging. *Insights Imaging*, 2018, 9(4):449–461. <https://doi.org/10.1007/s13244-018-0636-z> PMID: 30094592 PMCID: PMC6108964
- [38] Lee SH, Yi A, Jang MJ, Chang JM, Cho N, Moon WK. Supplemental screening breast US in women with negative mammographic findings: effect of routine axillary scanning. *Radiology*, 2018, 286(3):830–837. <https://doi.org/10.1148/radiol.2017171218> PMID: 29083988
- [39] Berg WA, Blume JD, Cormack JB, Mendelson EB, Lehrer D, Böhm-Vélez M, Pisano ED, Jong RA, Evans WP, Morton MJ, Mahoney MC, Larsen LH, Barr RG, Farria DM, Marques HS, Boparai K; ACRIN 6666 Investigators. Combined screening with ultrasound and mammography vs mammography alone in women at elevated risk of breast cancer. *JAMA*, 2008, 299(18):2151–2163. <https://doi.org/10.1001/jama.299.18.2151> PMID: 18477782 PMCID: PMC2718688
- [40] Sardanelli F, Boetes C, Borisch B, Decker T, Federico M, Gilbert FJ, Helbich T, Heywang-Köbrunner SH, Kaiser WA, Kerin MJ, Mansel RE, Marotti L, Martincich L, Mauriac L, Meijers-Heijboer H, Orecchia R, Panizza P, Ponti A, Purushotham AD, Regitnig P, Del Turco MR, Thibault F, Wilson R. Magnetic resonance imaging of the breast: recommendations from the EUSOMA working group. *Eur J Cancer*, 2010, 46(8):1296–1316. <https://doi.org/10.1016/j.ejca.2010.02.015> PMID: 20304629
- [41] Nam SY, Ko EY, Han BK, Shin JH, Ko ES, Hahn SY. Breast imaging reporting and data system category 3 lesions detected on whole-breast screening ultrasound. *J Breast Cancer*, 2016, 19(3):301–307. <https://doi.org/10.4048/jbc.2016.19.3.301> PMID: 27721880 PMCID: PMC5053315
- [42] Houssami N, Lord SJ, Ciatto S. Breast cancer screening: emerging role of new imaging techniques as adjuncts to mammography. *Med J Aust*, 2009, 190(9):493–497. <https://doi.org/10.5694/j.1326-5377.2009.tb02526.x> PMID: 19413520
- [43] Tagliafico AS, Calabrese M, Mariscotti G, Durando M, Tosto S, Monetti F, Airdi S, Bignotti B, Nori J, Bagni A, Signori A, Sormani MP, Houssami N. Adjunct screening with tomosynthesis or ultrasound in women with mammography-negative dense breast: interim report of a prospective comparative trial. *J Clin Oncol*, 2016, 34(16):1882–1888. <https://doi.org/10.1200/JCO.2015.63.4147> PMID: 26962097
- [44] Goddi A, Bonardi M, Alessi S. Breast elastography: a literature review. *J Ultrasound*, 2012, 15(3):192–198. <https://doi.org/10.1016/j.jus.2012.06.009> PMID: 23449849 PMCID: PMC3558110
- [45] Zahran MH, El-Shafei M, Emara DM, Eshiba SM. The role of ultrasound elastography in evaluation of breast masses. *Acta Sci Med Sci*, 2019, 3(9):140–151. <https://www.actascientific.com/ASMS-3-9.php> <https://www.actascientific.com/ASMS/pdf/ASMS-03-0394.pdf>
- [46] Kim MY, Kim HS, Choi N, Yang JH, Yoo YB, Park KS. Screening mammography-detected ductal carcinoma *in situ*: mammographic features based on breast cancer subtypes. *Clin Imaging*, 2015, 39(6):983–986. <https://doi.org/10.1016/j.clinimag.2015.06.006> PMID: 26259866
- [47] Melnikow J, Fenton JJ, Whitlock EP, Miglioretti DL, Weyrich MS, Thompson JH, Shah K. Supplemental screening for breast cancer in women with dense breasts: a systematic review for the U.S. Preventive Services Task Force. *Ann Intern Med*, 2016, 164(4):268–278. <https://doi.org/10.7326/M15-1789> PMID: 26757021 PMCID: PMC5100826
- [48] Ali MA, Czene K, Eriksson L, Hall P, Humphreys K. Breast tissue organisation and its association with breast cancer risk. *Breast Cancer Res*, 2017, 19(1):103. <https://doi.org/10.1186/s13058-017-0894-6> PMID: 28877713 PMCID: PMC5586066
- [49] Zhang YN, Wang CJ, Xu Y, Zhu QL, Zhou YD, Zhang J, Mao F, Jiang YX, Sun Q. Sensitivity, specificity and accuracy of ultrasound in diagnosis of breast cancer metastasis to the axillary lymph nodes in Chinese patients. *Ultrasound Med Biol*, 2015, 41(7):1835–1841. <https://doi.org/10.1016/j.ultrasmedbio.2015.03.024> PMID: 25933712
- [50] Ewing DE, Layfield LJ, Joshi CL, Travis MD. Determinants of false-negative fine-needle aspirates of axillary lymph nodes in

- women with breast cancer: lymph node size, cortical thickness and hilar fat retention. *Acta Cytol*, 2015, 59(4):311–314. <https://doi.org/10.1159/000440797> PMID: 26422248
- [51] Burkett BJ, Hanemann CW. A review of supplemental screening ultrasound for breast cancer: certain populations of women with dense breast tissue may benefit. *Acad Radiol*, 2016, 23(12):1604–1609. <https://doi.org/10.1016/j.acra.2016.05.017> PMID: 27374700
- [52] McDonald ES, McCarthy AM, Weinstein SP, Schnall MD, Conant EF. BI-RADS category 3 comparison: probably benign category after recall from screening before and after implementation of digital breast tomosynthesis. *Radiology*, 2017, 285(3):778–787. <https://doi.org/10.1148/radiol.2017162837> PMID: 28715278 PMCID: PMC5708302
- [53] Stolnicu S, Bauer O, Naznean A, Podoleanu C, Georgescu R. ER-/PR+ subset of invasive breast carcinoma (IBC): a distinct phenotype with good prognosis. *Pol J Pathol*, 2018, 69(3):311–313. <https://doi.org/10.5114/pjp.2018.79551> PMID: 30509058
- [52] McDonald ES, McCarthy AM, Weinstein SP, Schnall MD, Conant EF. BI-RADS category 3 comparison: probably benign

Corresponding author

Maria Elena Cocuz, Lecturer, MD, PhD, Department of Basic, Preventive and Clinical Sciences, Faculty of Medicine, Transilvania University of Braşov, 56 Nicolae Bălcescu Street, 500019 Braşov, Romania; Phone +40268–412185, e-mail: maria_elenacocuz@yahoo.com

Received: April 8, 2021

Accepted: October 1, 2021

Application of the Measurement of Carotid Intima-Media Thickness for Prediction of the Essential Hypertension in Children

ROSANA MANEA¹, BIANCA ELENA POPOVICI^{1*}, CARMEN DANIELA NECULOIU², DAN MINEA¹, ALINA CALIN³

¹ Transilvania University of Brasov, Faculty of Medicine, Medical and Surgical Specialties Department, 29 Eroilor Blvd. 500036, Brasov, Romania

² Transilvania University of Brasov, Faculty of Medicine, Fundamental, Prophylactic and Clinical Department, 29 Eroilor Blvd. 500036, Brasov, Romania

³ Dunarea de Jos University of Medicine and Pharmacy, 47 Domneasca Str., 800008, Galati, Romania

Hypertension is a major risk factor for progression of the atherosclerotic process and for developing of degenerative cardiovascular diseases in adulthood. The aim of this study is to evaluate how the measurement of carotid intima - media thickness for prediction of essential hypertension in children can be used. The study group included 81 children and the control group 61 children, all aged between 5 - 17 years and 11 months old, and admitted in Children Hospital Brasov in the period of 2009 - 2014. The study protocol included: BMI, blood pressure and Doppler echography of the common carotid artery for each group. Mean age of the patients from the study group was 13.67 years, 43.20 % girls and 56.80 % boys, while in the control group, the mean age was 14.07 years, 54.10% girls and 45.90 % boys. 70.37% of the children from the study group presented obesity, while in the control group 40.98% were obese. The IMTC study group ranged from 0.52 - 0.69 mm and the limits of the normotensive subjects were 0.32 - 0.54 mm. In both groups the obese patients were found to have increased carotid artery intima-media, which means that IMTC was positively correlated with BMI ($p=0.000001$). It is necessary to identify diagnostic methods easily applicable for children, allowing involvement of the characteristics of the arterial wall in the degenerative pathological processes. Increased intima-media ratio is positively correlated with high values of blood pressure.

Keywords: carotid intima - media thickness, hypertension, children

The incidence of essential hypertension in children is in continuous progress despite efforts of the medical staff to prevent the disease and to educate people regarding long term effects. Hypertension is a major risk factor for progression of the atherosclerotic process, and also for degenerative cardiovascular diseases developing in adulthood [1]. Today is obvious that this unfavorable outcome is common at blood pressure values of 115/75 mmHg in children and the risk doubles with each rise of the blood pressure (with 20/10 mmHg) [2].

There is a strong interaction between high blood pressure values, dysfunction of the vascular endothelium and atherosclerosis. This determines transformation of the vessels in a rigid system impairing the blood flow and maintaining hypertension. Constant high blood pressure values lead firstly to endothelial dysfunction and then to structural alterations of the arterial vessels [3]. The presence of the endothelial dysfunction maintains the hypertension progression [4]. One of the earliest change is the apparition of the atherosclerotic plaque and this was observed in young subjects as early as aged two [5]. These structural changes of the arterial vessels can be proved using Doppler echography of the common carotid artery, respectively measurement of the intima-media thickness (IMTc). Our study aims to investigate the existence of a correlation between hypertension and IMTc.

Experimental part

Methods

The study group included 81 children, boys and girls, aged between 5 and 17 years and 11 months, admitted in Children Hospital Brasov between 2009-2014. In these batches, repeated measurements of blood pressure show

high levels for age, gender and height. The patients with secondary hypertension were excluded (1 case). (Secondary hypertension). The control group included 61 children, boys and girls, also with age between 5 and 17 years and 11 months, with normal values of blood pressure.

The study protocol included:

Measurement of weight and height; the body mass index (BMI) was calculated according to the formula: $BMI = W/H^2$, where W = weight (kilos), H = height (meters).

Blood pressure was determined according to *The Fourth Report on the Diagnosis, Evaluation and Treatment of High Blood Pressure in Children and Adolescents. National High Blood Pressure Education Program Working Group on High Blood Pressure in Children and Adolescents* [6].

Doppler echography of the common carotid artery for each group. We used ultrasound machine Fukuda. The examinations were performed with linear transducer with 12.5-13 MHz. The principle of the examination was to expose the common carotid artery (which can be assimilated with a pipe) and to evaluate the anterior and posterior walls and the blood flow. In a normal system the flow should be laminar without turbulence because the walls are smooth without asperities like atherosclerotic plaque. The dimensions of the walls should be less than 0.40 mm.

Subjects were examined in a quiet ambient, thermal comfort, noise free, after 15 min break from physical effort. Examination position was supine, face up and head turned to the opposite side of the examined artery (45°). We performed manually 5 measurements for each wall (anterior and posterior); a distance of 1 cm for the left and the right carotid artery was used to study the arithmetic

* email: biancadr@yahoo.com; Phone: +40745010095

average of the values obtained. The data were compared with the values considered normal for the age group[8].

Statistical analysis: We used ANOVA statistical calculation method applied for continuous variables and chi-square test to compare groups. We considered statistically significant a p value < 0.05.

Methodology of measurement of IMTc

We had measured the carotid intima-media thickness (IMTc) by analyzing B-mode ultrasound imaging which was obtained manually in real time. Ultrasound examination was performed by a single person with a linear transducer with 12.5-13 MHz frequency, with an ultrasound imaging system Fukuda. The examinations were performed in a quiet room, after 15 minutes of resting, with patient lied on bed in dorsal decubitus position with head rotated at 45° on the opposite side of the carotid artery which was examined. With this technique it can be visualized 2 parallel echogenic lines separated by an anechoic space, at the common carotid artery. The 2 lines means the blood-intima and media-adventitia interfaces. The distance between the 2 lines has the significance of the thickness of the intima-media complex. The measurements were made at 1 cm from carotid bulbous, for the both anterior and posterior wall. We made 5 determinations for each wall, for right and left common carotid artery and we used the mean value in our study. We compared the values obtained with the normative values.

Results and discussions

The study group involved 81 patients who, at admission were detected with blood pressure values (fig. 1) greater

than the 95th percentile for age, sex and class. 46 were boys (56.79%) and 35 girls (43.20%). The ages of the subjects ranged from 5.9 years to 17.11 years (mean age 13.67 years). The control group included 61 subjects, 28 boys (45.90%) and 33 girls (54.09%), aged 5.7 to 17.10 years (mean age 14.07 years). In the study group, 57 children (70.37%) presented obesity (BMI > 95th percentile), 10 children (12.34%) were overweight (BMI between 85 and 95 percentile) and 14 (17.28%) were normal weight (BMI < 85). In the control group 29 (47.54%) children had normal weight (BMI < 85), 7 subjects (11.47%) were overweight (BMI between 85 and 95 percentiles) and 25 subjects (40.98%) were obese (BMI > 95th percentile). Demographic and clinical data are presented in table 1.

In the study group in which most children were obese or overweight systolic blood pressure was higher as expected for the age and gender. In the control group the systolic blood pressure was normal for age and gender. There is a significant difference between the two groups; 44 subjects (56.41 %) of the study group registered BP values > 99th percentile for age, gender and class, which shows occurrence of severe HTAE early.

Following IMTC, we noticed a positive correlation to hypertension (fig. 2), this correlation was significantly higher in hypertensive subjects compared to normotensive. All subjects who were later confirmed as having elevated blood pressure had increased IMTC and even registered as having characteristic complications such as hypertension and left ventricular hypertrophy modification of retinal vessels in eye fundus examination. In addition, the subjects

	CONTROL GROUP			STUDY GROUP			P
	cases	media	std.dev	cases	media	std.dev	
Age	53	14.06	2.79	78	13.83	3.16	0.673102
WB	32	3139.34	562.60	49	3301.02	632.74	0.244134
W	53	54.31	17.56	78	64.64	20.14	0.478138
H	53	1.528	0.1386	78	1.547	0.1684	0.002925
BMI	53	23.01	6.65	78	26.37	4.79	0.001016
SBP	53	107.04	6.14	78	133.47	15.41	0.000000
DBP	53	63.75	7.33	78	77.86	11.60	0.000000
IMTc	50	0.37	0.06	75	0.43	0.06	0.000000

Table 1
DEMOGRAPHIC
CHARACTERISTICS, CLINICAL
FEATURES OF THE STUDY
GROUP AND CONTROL
GROUP

WB = weight of birth; W = weight; H = height; BMI = body mass index; SBP = systolic blood pressure; DBP = diastolic blood pressure; IMTc = intima-media thickness at carotid artery.

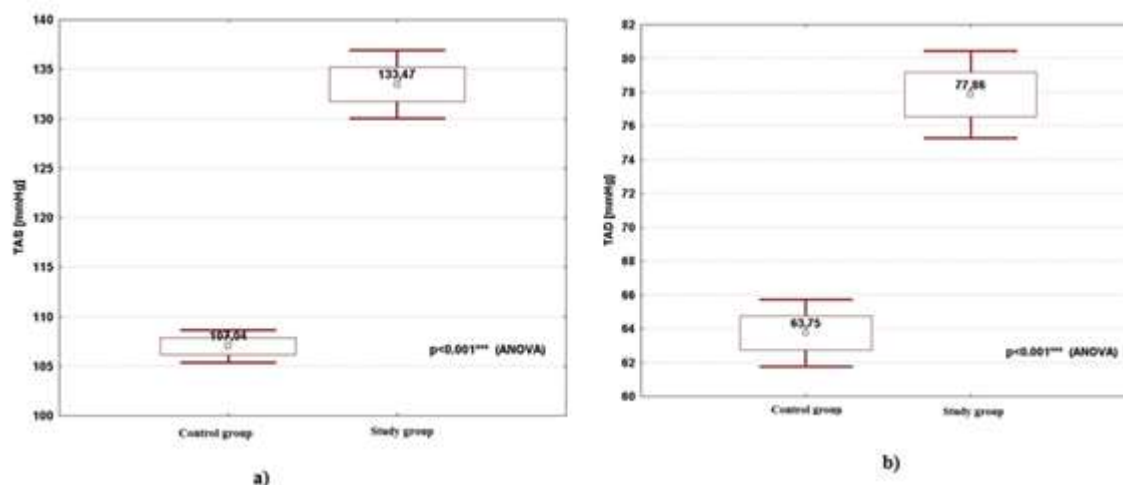


Fig. 1. The variations of blood pressure in both groups;
A) SBP. B) DBP

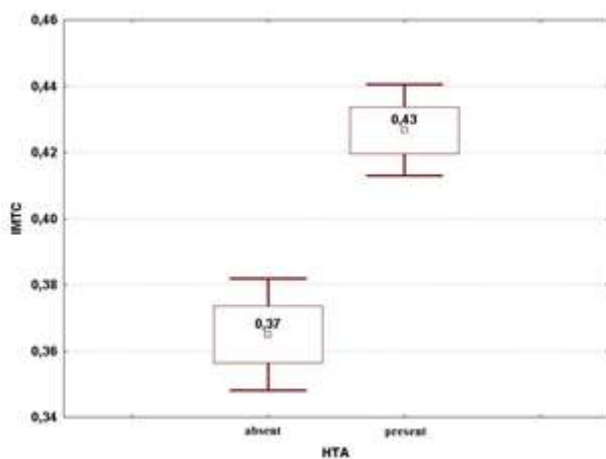


Fig. 2. Correlation between high values of BP and IMTC

associated high blood pressure values and obesity (BMI > 95th). The IMTC in the study group ranged from 0.52 to 0.69 mm and for normotensive subject's limits were 0.32 to 0.54 mm.

For all patients from the study, obesity was found increased when compared to carotid artery intima-media policy.

In the study group we noticed a positive correlation between IMTC, TAS values ($p = 0.0001$) (fig. 3) and DBP ($p = 0.0001$) (fig. 3). Patients with SBP and DBP values greater than the 99th percentile were those who experienced the most severe changes in intima-media ratio (values greater than 0.5 mm). One possible explanation could be that the condition of increased pressure exerted on artery walls correlated with the time factor (how long these mechanical forces act on the arterial wall), causes changes in the tissue structure (live, with intense metabolism), making it a rigid structure like a tube. Clearly, the time factor plays an important role in modifying IMTC because in these subjects there is evidence that hypertension was installed for at least 6 months before the examination.

In the control group, 17 subjects (27.86%) had increased IMTC but they were normotensive obese (BMI > 95th) suggesting that this could be also the consequence of atherosclerotic changes.

In our study, age of onset of HTAE was between 10 to 17 years in 72 subjects (88.88%) and 6 to 10 years old in 9 subjects (11.12%). Although the percentage is small and statistically insignificant, we must highlight the young age of onset. Scientific literature offers references for lowering the age of onset at 10-12 years. A significant number of subjects had elevated BP and arterial vascular damage

revealed by increased IMTC. This may be an argument to support apparition of the condition for at least 6 months prior. Pathological processes occurring in the arterial wall, consequences of the high pressure can be emphasized using Doppler ultrasound by measuring intima-media thickness pressure. Increased intima-media ratio is an evidence for structural changes in the arterial wall.

We applied this method in the present study outlining bilateral common carotid artery measurements as being the hallmark of a well-defined tube wall thickness that can be monitored using the Doppler technique and so we managed to emphasize the presence of structural changes in case of high pressure. This thickness variations are complex pathophysiological process arguments for atherosclerosis and plaque formation, which both deform the interface with the bloodstream and determine turbulent blood flow in the arteries. The study found that the value of IMTC is higher in children with high blood pressure compared to children who had normal blood pressure (positive correlated to systolic blood pressure and diastolic blood pressure).

In the study group IMTC values were increased for both obese and normal weight patients, thus showing that high blood pressure regime itself may determine, over time, not only endothelial dysfunction but permanent structural changes in the arterial wall. On the other hand, we cannot ignore the fact that in our study, the proportion of obese subjects was significant for both groups of children (high blood pressure and normal blood pressure).

Moreover, we noticed that increased IMTC positively correlated with BMI. Thus, we observed a slight association between obesity and increased IMTC [9, 10] and therefore it is difficult to specify the exact contribution of each of the two variables (blood pressure and obesity) in the process of reconfiguration of the arterial wall and blood flow alteration. It is certain that endothelial dysfunction and vascular endothelial structural changes are common in both obesity and hypertension and that between the two disorders a close interdependence occurs. It would be interesting to study the functional parameters such as vascular distensibility, vascular arterial geometry and flow-mediated vasodilation.

Carotid intima media thickness is one of the most studied parameters regarding evaluation of the atherosclerosis and hypertension not only in adults but also in children and adolescents [11]. In the present study we had demonstrate that IMTC has a strong correlation with high levels of blood pressure (BP) in childhood. In these subjects we found structural modifications of the common carotid artery characterized by augmented wall thickness as a prove of

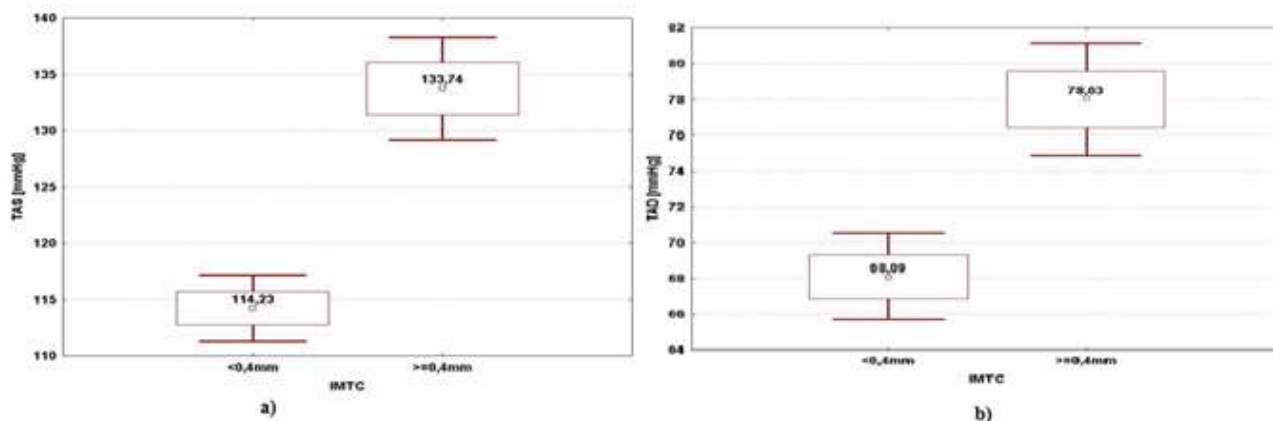


Fig. 3. The variation of IMTC with blood pressure
A) SBP B) DBP

the early atherosclerotic modification that had already taken place despite of early age. Glagov et al.[12] had described for the first time arterial remodeling and the correlation of this with atherosclerosis process.

It is very difficult to evaluate cardiovascular risk in children and to find proper and valuable methods to define this [13] although it is widely accepted that degenerative cardiovascular diseases begins in childhood [14]. In our study group the youngest was five years old and it was a surprise to find that even so young structural impairment in carotid artery was already present confirming the hypothesis of early onset of the atherosclerosis [15]. The study had revealed that one of the most important factor that is affecting carotid IMT is blood pressure, both systolic and diastolic values. Many trials had been studied the impact of blood pressure (systolic, diastolic, mean value, 24-hours continuous monitoring) on the carotid IMT and had demonstrated that high levels of these factors determine the increasing of the intima-media thickness and the antihypertensive treatment determine the regression of IMT [16]. Date of the present study showed that carotid IMT is correlated not only with high levels of systolic blood pressure and diastolic blood pressure but with the body mass index (BMI); children with normal values of blood pressure but with BMI above 95 percentiles had demonstrated enlargement of the carotid IMT. Now we know that metabolic syndrome is including features as hypertension and obesity and our study showed the primary importance of BP and BMI in determining early abnormalities of the arterial wall.

Our findings are similar with other studies that had demonstrated this correlation [13, 17,18]. Carotid intima-media thickening is reflecting the presence of subclinical atherosclerotic changes even in childhood and predict the future cardiovascular events in adulthood.

Conclusions

Elevated blood pressure values in pediatric patients is a fact and moreover, essential hypertension is a disease common in children aged 10. It is necessary to identify the diagnostic methods easily applicable to children: noninvasive, reproducible, allowing involvement of the characteristics of the arterial wall in understanding and handling of the degenerative pathological processes.

Measures of the intima-media vessel wall ratio of the common carotid artery using Doppler echocardiography appears to meet these requirements. Increased intima-media ratio is positively correlated with high blood pressure values, both systolic and diastolic hypertension and represents an indicator for structural changes occurring after high pressure works on the endothelium.

Because there is a positive correlation between BMI values and IMTC we can conclude that the determination of this ratio provides useful information regarding the onset and progression of atherogenesis long before clinical signs of organ involvement appear.

References

- 1 LUMA G.B., ROSEANN T. SPIOTTA (2006) Hypertension in Children and Adolescents. *Am Fam Physician* ;73 (9): 1558-68.
- 2 JUONALA M., VIHKARI J. S., RÖNNEMAA T., HELENIUS, H., TAITTONEN, L et al (2006) Elevated Blood Pressure in Adolescent

- Boys Predicts Endothelial Dysfunction. *The Cardiovascular Risk in Young Finns Study. Hypertension*; 48:424-430.
- 3.MARC B. LANDE, NANCY L. CARSON, JASON ROY, CECILIA C. et al (2006). Effects of Childhood Primary Hypertension on Carotid Intima Media Thickness. A Matched Controlled Study. *Hypertension*; 48:40-44.
4. JOSEPH T. FLYNN (2006) What Is the Significance of Increased intima Media thickness in Hypertensive Adolescents? *Hypertension*; 48:23-24.
5. IANNUZZI A, LICENZIATI MR, ACAMPORA C, DE MICHELE M, IANNUZZO G (2007) Carotid artery wall hypertrophy in children with metabolic syndrome. *Journal of Human Hypertension* 1-6.
- 6.*** The Fourth Report on the Diagnosis, Evaluation and Treatment of High Blood Pressure in Children and Adolescents (2004) National High Blood Pressure Education Program Working Group on High Blood Pressure in Children and Adolescents. *Pediatrics*; 114(2): 555-57.
7. DANIELS SR. (1999) Hypertension-induced cardiac damage in children and adolescents *Blood Press Monit.* 1999;4: 165-170.
8. JOURDAN, C., WÜHL, E., LITWIN, M., FAHR, K., TRELEWICZ, J. et al. (2005) Normative values for intima-media thickness and distensibility of large arteries in healthy adolescents. *J Hypertens* ; 23:1707-1715.
9. LI, S., CHEN, W., SRINIVASAN, S. R., BOND, M. G., TANG, R., URBINA, E. M., et al. S.(2003) Childhood Cardiovascular Risk Factors and Carotid Vascular Changes in Adulthood: The Bogalusa Heart Study. *JAMA*; 290(17): 2271-2276.
10. WUNSCH R. DESOUSA G, REINHER T. (2005) Intima-media thickness in obesity: relations to hypertension and dyslipidemia. *Arch Dis Child.* 90: 1097.
11. JUONALA M, JARVISALO M J, MAKI-TORKKO N, KAHONEN M, VIHKARI JSA, et al. (2005) Risk Factors Identified in Childhood and Decreased Carotid Artery Elasticity in Adulthood: The Cardiovascular Riskin Younf Finns Study. *Circulation*; 112:1486-1493.
12. GLAGOV S, WEISENBERG E, ZARINS CK, STANKUNAVICIUS R, KOLETTIS GJ. (1987) Compensatory enlargement of human atherosclerotic coronary arteries. *N Engl J Med*;316: 1371-1375.
13. IANNUZZI A, LICENZIATI MR, ACAMPORA C, DE MICHELE M, IANNUZZO G, et al. (2007) Carotid artery wall hypertrophy in children with metabolic syndrome. *Journal of Human Hypertension*; 1-6.
14. INGELFINGER JR, (2004) Pediatric antecedents of adult cardiovascular disease - Awareness and intervention. *N Engl J Med* ; 350: 2123-2126.
15. MCGILL HC JR, MCMAHAN CA, HERDERICK EE, MALCOM GT, TRACY RE et al. (2000) Origin of atherosclerosis in childhood and adolescence. *Am J Clin Nutr* ; 72(supp): 1307S - 15S.
16. WANG JG, STAESSEN JA, LI Y, VAN BORTEL LM, NAWROT T et al. (2006) Cartotid intima-media thickness and antihypertensive treatment: a meta-analyses of randomized controlled trials. *Stroke*; 37: 1933-1940.
17. RAITAKARI OT, JUONALA M, KAHONEN M, TAITTONEN L, LAITINEN T, et al. (2003) Cardiovascular Risk Factors in Childhood and Carotid Artery Intima-Media Thickness in Adulthood. *JAMA*,Vol 290, No 17: 2277-2282.
18. de FERRANTI SD, GAUVREAU K, LUDWIG DS, NEWBURGER JW, RIFAI N. (2006) Inflammation and changes in metabolic syndrome abnormalities in US adolescents: findings from the 1988-1994 and 1999-2000 National health and Nutrition Examination Surveys. *Clin Chem*; 52: 1325-1330.

Manuscript received: 18.12.2017

Article

Biomolecular Screening of *Pimpinella anisum* L. for Antioxidant and Anticholinesterase Activity in Mice Brain

Aamir Mushtaq ^{1,*} , Fatima Habib ², Rosana Manea ³ , Rukhsana Anwar ⁴, Umar Farooq Gohar ⁵ , Muhammad Zia-Ul-Haq ⁶, Mobasher Ahmad ², Claudia Mihaela Gavris ^{3,*}  and Liana Chicea ^{7,*}

¹ Department of Pharmaceutical Sciences, Government College University, Lahore 54000, Pakistan

² Gulab Devi Institute of Pharmacy, Gulab Devi Educational Complex, Lahore 54000, Pakistan

³ Faculty of Medicine, Transilvania University of Brasov, 500036 Brasov, Romania

⁴ Department of Pharmacology, Punjab University College of Pharmacy, University of the Punjab, Lahore 54000, Pakistan

⁵ Institute of Industrial Biotechnology, Government College University, Lahore 54000, Pakistan

⁶ Office of Research, Innovation and Commercialization, Lahore College for Women University, Lahore 54000, Pakistan

⁷ Faculty of Medicine, University “Lucian Blaga” Sibiu, 550169 Sibiu, Romania

* Correspondence: aamir_mushtaq@hotmail.com or aamir.mushtaq@gcu.edu.pk (A.M.); mclaudia.gavris@gmail.com (C.M.G.); liana.chicea@gmail.com (L.C.); Tel.: +92-3336295580 (A.M.)

Abstract: Hundreds of the plants have been explored and evaluated for antioxidant and anti-amnesic activities, so far. This study was designed to report the biomolecules of *Pimpinella anisum* L. for the said activities. The aqueous extract of dried *P. anisum* seeds was fractionated via column chromatography and the fractions so obtained were assessed for the inhibition of acetylcholinesterase (AChE) via in vitro analysis. The fraction which best inhibited AChE was so named as the *P. anisum* active fraction (PaAF). The PaAF was then chemically analyzed via GCMS, which indicated that oxadiazole compounds were present in it. The PaAF was then administered to albino mice to conduct the in vivo (behavioral and biochemical) studies. The results of the behavioral studies indicated the significant ($p < 0.001$) increase in inflexion ratio, by the number of hole-pokings through holes and time spent in a dark area by PaAF treated mice. Biochemical studies demonstrated that the oxadiazole present in PaAF on one hand presented a noteworthy reduction in MDA and the AChE level and on the other hand promoted the levels of CAT, SOD and GSH in mice brain. The LD₅₀ for PaAF was calculated as 95 mg/Kg/p.o. The findings thus supported that the antioxidant and anticholinesterase activities of *P. anisum* are due to its oxadiazole compounds.

Keywords: dementia; brain; apiol; cholinergic; natural products; memory



Citation: Mushtaq, A.; Habib, F.; Manea, R.; Anwar, R.; Gohar, U.F.; Zia-Ul-Haq, M.; Ahmad, M.; Gavris, C.M.; Chicea, L. Biomolecular Screening of *Pimpinella anisum* L. for Antioxidant and Anticholinesterase Activity in Mice Brain. *Molecules* **2023**, *28*, 2217. <https://doi.org/10.3390/molecules28052217>

Academic Editors: Raffaele Capasso and Lorenzo Di Cesare Mannelli

Received: 30 January 2023

Revised: 17 February 2023

Accepted: 22 February 2023

Published: 27 February 2023



Copyright: © 2023 by the authors. Licensee MDPI, Basel, Switzerland. This article is an open access article distributed under the terms and conditions of the Creative Commons Attribution (CC BY) license (<https://creativecommons.org/licenses/by/4.0/>).

1. Introduction

Alzheimer’s disease (AD) is one of the major and distinct forms of dementia in the geriatric population. The incidence of this disease is 1/8 in American people above the age of 60 years. Its prevalence rate may double in next 20 years [1]. The deficiency of cholinergic neurons in specific region of brain (hippocampus) is the principal hallmark of this disease. The pathophysiologic factor of AD is acetylcholine (ACh) [2]. Oxidative stress such as that caused by reactive oxygen species also contributes to progression of disease [3]. The unavailability of antioxidants in the routine diet is the major cause of a high level of oxidative stress which may lead to dementia. Similarly, acetylcholinesterase (AChE) is a very important enzyme which contributes to pathogenesis in AD by reducing ACh levels in the brain [4]. The excessive breakdown of ACh at synapsis can be prevented by the inhibition of AChE [5]. Tacrine and rivastigmine (inhibitors of acetylcholinesterase) are widely practiced all over the world to overcome this cholinergic dysfunction. However, their less significant effects on memory performance as well as adverse effects have recommended

the need for some alternate therapies for AD [6]. Natural products have been progressively investigated for the isolation of therapeutic substances for the last few decades. The safe and toxicity-free profile of natural herbs always encourage the use of crude natural products for neurodegenerative brain disorders [7]. Herbs are the richest source of anti-inflammatory and anti-oxidant substances which may be used for the prevention of dementia along with rejuvenation of brain and other body parts [8]. Many essential oils, volatile oils, aromatic extracts and herbal products have been scientifically investigated for anti-inflammatory and antioxidant properties and they have been proven very beneficial for brain health [9]. Most of the relevant scientific work has reported that progressive memory loss is due to cholinergic crisis and plant extracts have been of great interest to scientists to overcome this problem. In a study conducted by Torre et al. (2022), 90 extracts from 30 native plants of Spain were scientifically tested, out of which 21 extracts showed very high anticholinesterase activity. The phenolic contents of the extracts were reported to possess anti AChE and antioxidant potential [10]. Similarly, ginseng and licorice are famous at treating cerebral inflammation in patients with AD or other cognitive disorders [11].

P. anisum (Umbelliferae) is an annual herb and widely cultivated in Asia Minor and India [12]. Most commonly, it is used for the treatment of abdominal cramps, constipation, colic, duodenal ulcers, dysmenorrhea, nausea, inflammation [13] and epilepsy [14]. Eugenol, α -terpineol, 1,8-cineol, α -pinene [15], limonene, trans anethole [16], palmitic acid, linoleic acid and oleic acid have been reported in dried *P. anisum* seeds, which possess strong anti-cholinesterase activity.

It has already been reported in previous studies that *P. anisum* possesses strong anti-epileptic, cerebroprotective [14] and enzyme-inhibition potential [17], which is why we selected this plant and found its anti-amnesic potential [18]. This study was designed to report the biomolecules present in the aqueous extract of dried *P. anisum* seeds which are responsible for the memory-enhancing potential. We also made attempts to report the acute toxicity of the plant.

2. Results

2.1. Fractionation by Column Chromatography

Aqueous extract of dried *P. anisum* seeds was fractionated using column chromatography and various solvents in different ratios. We obtained forty fractions which were identified using the thin-layer chromatographic (TLC) technique. We mixed all the fractions and purified them by repassing them through the column, and finally thirteen fractions were obtained (Figure 1), upon which in vitro testing was conducted.

2.2. In Vitro Testing of Purified Fractions

It was observed that only fraction number F-8 exhibited in vitro anticholinesterase activity and all other remaining fractions fail to do so (Table 1). Fraction F-8 was selected for in vivo studies and was named as the *P. anisum* active fraction (PaAF). The chemical constituents present in PaAF were analyzed via GC-MS analysis.

2.3. Results of GC-MS Analysis

The GC-MS analysis of the *P. anisum* active fraction (PaAF) indicated the presence of oxadiazole compounds, i.e., 1,2,5 oxadiazole, 1-benzylbenzimidazole 3-oxide, apiol and cyclohexanone (Table 2). The chromatogram obtained through GC-MS analysis is shown in Figure 2.

2.4. Findings of Behavioral Studies

The findings of behavioral studies through different paradigms indicated that animals treated with the *P. anisum* active fraction (PaAF) exhibited a significantly ($p < 0.001$) higher inflexion ratio in comparison to the scopolamine-treated hyper-amnesic mice. The light/dark test paradigm indicated that active-fraction-treated animals explored the dark compartment and remained most of the time in dark area in comparison to amnesic control mice. Similarly, it was observed via the hole board test that active-fraction-treated mice

presented a significantly ($p < 0.001$) higher number of pokings through the holes of the apparatus as compared to scopolamine-induced hyper-amnesic mice. The detailed numerical values of behavioral studies are recorded in Table 3.

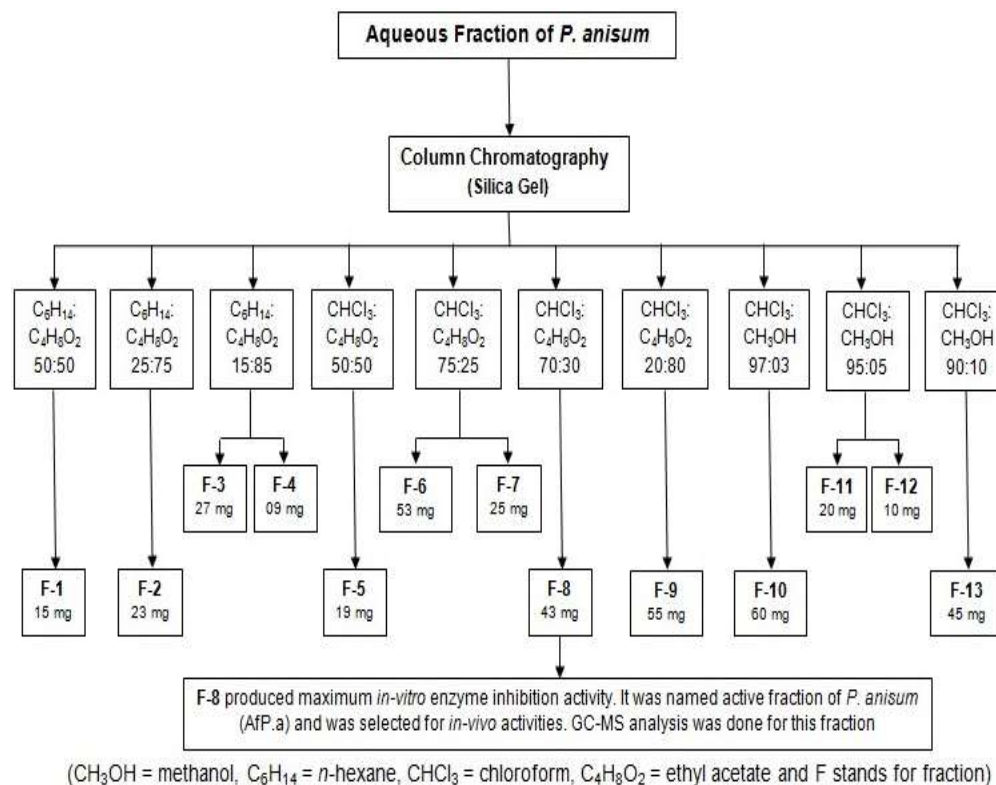


Figure 1. Fractionation of aqueous extract of *P. anisum* into sub fractions via column chromatography.

Table 1. In vitro analysis of the purified fraction of *P. anisum* for anti-cholinesterase activity.

Fractions	Color of Solution	AChE Inhibition
F-1	Purple	No
F-2	Purple	No
F-3	Purple	No
F-4	Purple	No
F-5	Purple	No
F-6	Purple	No
F-7	Purple	No
F-8	Colorless	Yes
F-9	Purple	No
F-10	Purple	No
F-11	Purple	No
F-12	Purple	No
F-13	Purple	No

Table 2. GC-MS analysis of PaAF and identification of compounds.

Compound Name	Molecular Formula	Molecular Weight (g/mol)	Mass Peak	Retention Time (min)
1-Benzylbenzimidazole 3-oxide	$C_{14}H_{12}N_2O$	224	43	2.683
Apiol	$C_{12}H_{14}O_4$	222	146	20.158
Cyclohexanone	$C_6H_{10}O$	98	34	4.567
1,2,5 oxadiazole	$C_2H_2N_2O$	70	26	2.992

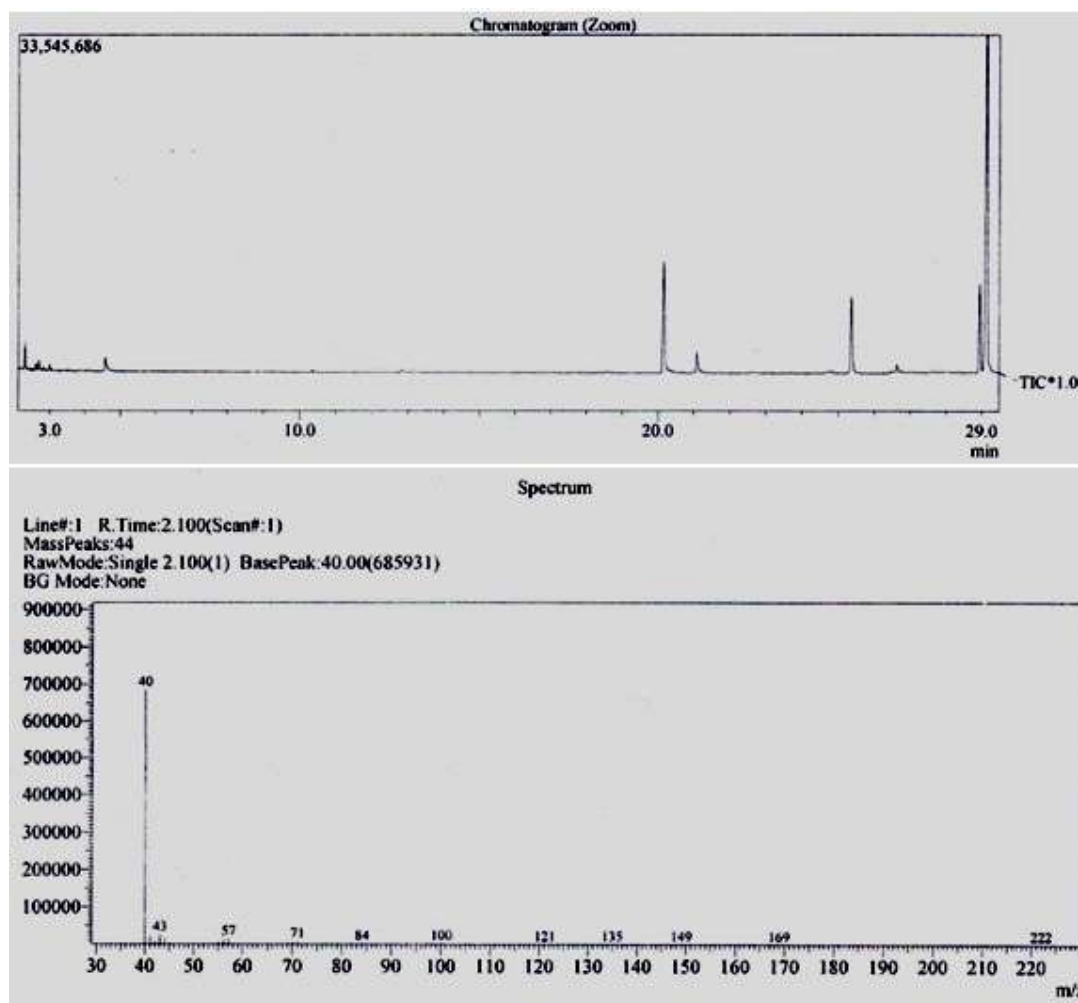


Figure 2. GC-MS analysis of *P. anisum* active fraction (PaAF).

Table 3. Effect of PaAF on enhancement of memory and learning tasks.

Group	Elevated Plus Maze			Light/Dark Paradigm				Hole-Board	
	Day-1	Day-2	I.R	Time Spent on Day-1		Time Spent on Day-2		Day-1	Day-2
	I ¹ (s)	I ² (s)		L.Cmpt (s)	D.Cmpt (s)	L.Cmpt (s)	D.Cmpt (s)	n.Pok/5 min	n.Pok/5 min
G-1	23.16 ± 1.17	16.66 ± 0.98	0.26 ± 0.07	50.83 ± 2.42	249.17 ± 2.42	41.50 ± 1.76	258.50 ± 1.76	48.33 ± 1.33	43.33 ± 1.74
G-2	68.11 ± 2.39 ^a	81.02 ± 2.78 ^a	−0.18 ± 0.05 ^a	173.22 ± 6.99 ^a	126.78 ± 7.20 ^a	179.00 ± 5.89 ^a	121.00 ± 5.88 ^a	21.00 ± 1.13 ^a	29.01 ± 1.81 ^a
G-3	20.83 ± 0.87 ^{b,σ}	17.16 ± 1.07 ^{b,σ}	0.17 ± 0.04 ^{b,σ}	41.66 ± 4.41 ^{b,σ}	258.34 ± 4.41 ^{b,σ}	31.67 ± 2.47 ^{b,σ}	268.33 ± 2.47 ^{b,σ}	55.50 ± 2.21 ^{b,σ}	45.50 ± 1.80 ^{b,σ}
G-4	35.50 ± 0.92 ^{b,α}	25.66 ± 1.30 ^{b,β}	0.29 ± 0.02 ^{b,σ}	62.50 ± 2.14 ^{b,σ}	237.50 ± 2.14 ^{b,σ}	49.17 ± 2.38 ^{b,σ}	250.83 ± 2.38 ^{b,σ}	44.00 ± 1.82 ^{b,σ}	42.66 ± 1.60 ^{b,σ}
G-5	46.16 ± 1.68 ^{b,α}	41.16 ± 1.85 ^{b,α}	0.10 ± 0.03 ^{b,σ}	66.00 ± 5.63 ^{b,σ}	234.00 ± 5.63 ^{b,σ}	64.00 ± 4.47 ^{b,σ}	236.00 ± 4.47 ^{b,α}	37.84 ± 2.70 ^{b,β}	39.50 ± 1.47 ^{b,σ}
G-6	41.00 ± 1.59 ^{b,α}	36.16 ± 1.85 ^{b,α}	0.11 ± 0.03 ^{b,σ}	55.83 ± 6.63 ^{b,σ}	244.17 ± 6.63 ^{b,σ}	53.33 ± 6.28 ^{b,σ}	246.67 ± 6.28 ^{b,σ}	39.66 ± 1.76 ^{b,γ}	43.33 ± 1.70 ^{b,σ}
G-7	36.00 ± 1.59 ^{b,α}	31.50 ± 1.92 ^{b,α}	0.12 ± 0.04 ^{b,σ}	52.50 ± 5.73 ^{b,σ}	247.5 ± 5.73 ^{b,σ}	51.66 ± 3.80 ^{b,σ}	248.34 ± 3.80 ^{b,σ}	41.00 ± 1.52 ^{b,σ}	44.16 ± 1.24 ^{b,σ}

Note: G-1 = Normal Control, G-2 = Amnesic Control, G-3 = Standard Control-A, G-4 = Standard Control-B, G-5 = Experimental Control-I, G-6 = Experimental Control-II, G-7 = Experimental Control-III, I¹ = Initial Transfer Latency, I² = Retention Transfer Latency, I.R = Inflexion Ratio, L.Cmpt = Light Compartment, D.Cmpt = Dark Compartment and n.Pok = No. of hole-pokings. Data were presented as mean ± SEM ($n = 6$) and statistically analyzed using one-way ANOVA and we used Dunnett's test for the comparison of the groups. All the groups (G-I and G-3 to G-7) were compared to G-2. The value of $p \leq 0.001$ was expressed as ^a for comparison of G-1 to G-2. The level of significance for comparison of G-3 to G-7 with G-2 was expressed as ^b, indicating p value of ≤ 0.001 , ≤ 0.01 , ≤ 0.05 and ≥ 0.05 , respectively, and for comparison of G-3 to G-7 with G-1, it was denoted with signs; ^α, ^β, ^γ, or ^σ, indicating p value of ≤ 0.001 , ≤ 0.01 , ≤ 0.05 and ≥ 0.05 , respectively.

2.5. Findings of Biochemical Studies

The biochemical investigations indicated that the brain homogenates of active-fraction-treated mice presented a significant ($p < 0.001$) reduction in MDA and AChE content in comparison to scopolamine-treated mice. Similarly, a significant ($p < 0.001$) improvement

in the level of SOD, CAT and GSH was observed in active-fraction-treated mice (Table 4). However, the level of ChAT remained unchanged in active-fraction-treated mice (Table 5).

Table 4. Estimation of levels of AChE, MDA, SOD, CAT and GSH in mice brain.

Groups	AChE μmol/min/mg	MDA nmol/h/g	SOD U/mg of Homogenate	Catalase U/mg of Homogenate	GSH μmol/mg
Group-1	3.79 ± 0.21	1.52 ± 0.11	25.91 ± 0.61	1.91 ± 0.17	40.21 ± 1.10
Group-2	8.01 ± 0.31 ^a	6.91 ± 0.40 ^a	7.61 ± 0.24 ^a	0.56 ± 0.04 ^a	17.92 ± 0.33 ^a
Group-3	3.52 ± 0.30 ^{b,σ}	1.40 ± 0.08 ^{b,σ}	25.11 ± 0.89 ^{b,σ}	2.01 ± 0.06 ^{b,σ}	46.99 ± 0.89 ^{b,γ}
Group-4	4.61 ± 0.23 ^{b,σ}	2.60 ± 0.11 ^{b,β}	22.02 ± 0.61 ^{b,α}	1.40 ± 0.07 ^{b,β}	39.99 ± 1.23 ^{b,σ}
Group-5	6.31 ± 0.31 ^{b,α}	2.29 ± 0.19 ^{b,σ}	20.03 ± 0.61 ^{b,α}	1.10 ± 0.07 ^{c,α}	37.02 ± 1.89 ^{b,σ}
Group-6	5.91 ± 0.19 ^{b,α}	1.99 ± 0.13 ^{b,σ}	20.21 ± 0.71 ^{b,α}	1.30 ± 0.07 ^{b,β}	36.99 ± 1.69 ^{b,σ}
Group-7	4.40 ± 0.31 ^{b,σ}	1.88 ± 0.17 ^{b,σ}	21.14 ± 0.49 ^{b,α}	1.71 ± 0.06 ^{b,σ}	40.07 ± 1.39 ^{b,σ}

G-1 = Normal Control, G-2 = Amnesic Control, G-3 = Standard Control-A, G-4 = Standard Control-B, G-5 = Experimental Control-I, G-6 = Experimental Control-II and G-7 = Experimental Control-III. One way-ANOVA followed by Dunnett's test was applied as a statistical tool to analyze the data and data were expressed as mean ± SEM. After comparison of Group-I to II (denoted by ^a for $p \leq 0.001$), the remaining groups were compared with Group-II (denoted by ^a for $p \leq 0.001$). The level of significance was expressed either by ^b, ^c, indicating a p value of ≤ 0.001 , ≤ 0.01 , ≤ 0.05 and ≥ 0.05 , respectively. Similarly, Groups III-VII were also compared with Group-I and significance level was expressed either by ^α, ^β, ^γ, or ^σ, indicating a p value of ≤ 0.001 , ≤ 0.01 , ≤ 0.05 and ≥ 0.05 , respectively.

Table 5. Estimation of choline acetyltransferase levels in mice brain.

Groups	Treatment	ChAT (μmol/min/mg)
G-A	Normal Control	12.10 ± 0.89
G-B	Amnesic Control	6.99 ± 0.81 *
G-C	Test Control-A	10.92 ± 0.71 ^{ns}
G-D	Test Control-B	10.44 ± 1.31 ^{ns}
G-E	Test Control-C	8.81 ± 0.94 ^{ns}

Note: All the groups (B, C, D and E) were compared with Group-A. "*" represents $p < 0.001$ while ^{ns} indicates $p > 0.05$.

2.6. Acute Toxicity

The findings of the acute toxicity study indicated that no deaths were recorded up to a dose of 100 mg/Kg/p.o. However, the animals started dying at a dose of 150 mg/Kg/p.o. (3 out of 5 animals died in this group). All animals died in Group-4 by administration of a single acute toxic dose of 200 mg/Kg/p.o. From this data the LD₅₀ for the *P. anisum* active fraction (P.aAF) was calculated as 95 mg/Kg/p.o.

3. Discussion

The current study was performed to report the active ingredients of *P. anisum* for the prevention of dementia. Initially, methanolic and aqueous extracts of *P. anisum* were tested for behavioral and biochemical studies. This manuscript is a continuation of this series which involved the identification of the active moieties responsible for anti-cholinesterase and anti-oxidant activities in mice brains. The GC-MS analysis indicated that the *P. anisum* active fraction (P.aAF) contained apiol, 1-benzylbenzimidazole 3-oxid, cyclohexanone and a heterocyclic aromatic compound, 1,2,5 oxadiazole (Table 2). 1,2,5 oxadiazole belongs to the azole family and possesses antioxidant, anti-epileptic, anti-diabetic, anti-microbial, anti-Alzheimer's and enzyme-inhibition activities [19].

The findings of biochemical studies indicated that the *P. anisum* active fraction (P.aAF) at a dose of 7 mg/Kg/p.o. produced a significant ($p < 0.001$) increase in the level of SOD, CAT and GSH in mice brains, while the MDA contents were reduced significantly. This indicates the strong antioxidant potential of the P.aAF 7 mg/Kg/p.o. dose. Previous studies have explained that oxadiazole compounds prevent the oxidative load of the body by scavenging free radicals. Hence, they can be used as potent antioxidant substances [20]. Studies have also proved that oxadiazole compounds prevent the cellular damage of the body by reducing lipid peroxidation reactions. Oxygen free radicals produced in the body

participate in lipid peroxidation reactions and, as a result, the MDA contents are increased in the brain and cerebrospinal fluid. Thus, MDA can be used as a valuable marker to investigate the oxidizing load of the body [21]. It was observed that the MDA contents were significantly high in scopolamine-treated mice. Scopolamine was used to induce amnesia in mice and is actually responsible for the increase in the oxidizing load in mice brains. The overproduction of hydroxyl free radicals results in the propagation of lipid peroxidation reactions and, as a consequence, the MDA contents are raised in brain homogenates [22]. It is clear from the biochemical investigation that P.aAF significantly ($p < 0.001$) lowered the MDA contents of mice brains by the inhibition of lipid peroxidation reactions. The significant reduction in the level of MDA contents (Table 4) by administration of P.aAF might be due the presence of the oxadiazole present in it. Similarly, the reference drug piracetam also protected neurons from oxidative stress. It involves the improvement in mitochondrial function along with enhancement of ATP production. It also enhances the membrane fluidity of the hippocampus and prevents the neuron from oxidative stress [23].

Similarly, it was also observed that the animals treated only with scopolamine presented a marked reduction in the levels of SOD, GSH and CAT. These are important endogenous anti-oxidants which prevent the body from free radicals and reactive substances. A reduction in the level of natural antioxidants promoted free-radical-induced apoptosis in mice brains. Similarly, the administration of scopolamine in mice resulted in the over-expression of cytokines such as interleukin-1 β and other inflammatory proteins, which induced amnesia via the cholinergic dysfunction of the mice brain [24]. The findings of biochemical studies suggested that the pretreatment of animals with P.aAF prevented the oxidizing load of the mice brain by increasing GSH, CAT and SOD level. The reduced GSH is responsible for the donation of its electrons to the reactive oxygen species, thus neutralizing them so they do not produce damage. Similarly, it also prevents lipid peroxidation reactions and minimizes the damage produced by heavy metals. On the other hand, SOD is responsible for neutralizations of the superoxide species, providing a first-line defense against oxidizing species. Increased levels of CAT in mice brains reduces hydrogen peroxide into molecular oxygen and simple water and, hence, protects the brain from damage [25,26].

Our findings also suggested that P.aAF possesses a strong anticholinesterase activity in brain homogenates of the mice (Table 4). This enzymatic inhibition might be attributed to the oxadiazole compounds of *P. anisum*. Acetylcholinesterase inhibition by oxadiazole compounds is responsible for providing the plant with its memory-enhancing potential. Previous studies indicated that 1,2,4 oxadiazole is much more famous for its broad range of pharmacological potentials [19], and various derivatives of oxadiazole compounds have been synthesized by substitution at certain positions of the oxadiazole ring [27]. Substitution at the R¹ and R² side chains on 1,2,4 oxadiazoles have imparted them with a strong anticholinesterase activity and 1,3,4 oxadiazoles have been proven to be parent compounds which offer both acetylcholinesterase- and butyrylcholinesterase-inhibition activities [28].

The behavioral studies supported the biochemical mechanism of memory enhancement of the test substance. The results of elevated plus maze (EPM) paradigm indicated that the inflexion ratio was significantly ($p < 0.001$) improved in the P.aAF-treated group compared to the amnesic control group. The increase in inflexion ratio is the hallmark of improvement in memory. The EPM paradigm is one of the widely employed paradigms to assess the memory-enhancement effect of natural products [29]. Similarly, the reduction in contact time in a light compartment and increased hole-poking by the P.aAF-treated mice indicated the improvement in retention power, as given in Table 3.

Acute toxicity studies were performed via the administration of a single acute toxic dose of the *P. anisum* active fraction (P.aAF) to different groups of mice, and the LD₅₀ was calculated as 95 mg/Kg/p.o. for P.aAF. The therapeutic index was calculated as 13.57 and it was observed that the administration of P.aAF in a toxic dose (150 mg/Kg/p.o.) produced marked behavioral changes in animals. Spasticity of muscles and hypersecretions

of saliva (Table 6) were observed in these animals. This might be due to the presence of apiol in the *P. anisum* active fraction. It has been reported in previous studies that apiol is a very potent appetite stimulant and also promotes the enzymatic secretions of the digestive tract [30]. From all the above discussions, it is quite clear that the GC-MS analysis reported the presence of oxadiazole compounds in the *P. anisum* active fraction (P.aAF). These oxadiazole compounds not only possess a strong anti-oxidant potential but are also responsible for the anticholinesterase activity of the plant. Thus, the memory-enhancing effect of the *P. anisum* plant is attributed to the presence of its oxadiazole compounds, which inhibit acetyl cholinesterase on one hand, and promote the level of natural anti-oxidants in the mice brain on the other hand.

Table 6. Acute toxicity study showing effect of P.aAf (150 mg/Kg/p.o.) on behavioral and physiological characteristics of mice.

Behavioral Changes	Number of Days													
	I	II	III	IV	V	VI	VII	VIII	IX	X	XI	XII	XIII	XIV
Ataxia	✓	✓	✓	✓	✓	✓	✓	✓	✓	✓	✓	✓	✓	✓
Strabo Tail	✓	✓	✓	✓	✓	✓	✓	✓	✓	✓	✓	✓	✓	✓
Blanching	✓	✓	✓	✓	✓	✓	✓	✓	✓	✓	✓	✓	✓	✓
Secretions	✓	✓	✓	✓	✓	✓	✓	✓	✓	✓	✓	✓	✓	✓
Convulsions	✓	✓	✓	✓	✓	✓	✓	✓	✓	✓	✓	✓	✓	✓
Salivation	✓	✓	✓	✓	✓	✓	✓	✓	✓	✓	✓	✓	✓	✓
Hyperactivity	✓	✓	✓	✓	✓	✓	✓	✓	✓	✓	✓	✓	✓	✓
Rigidity	✓	✓	✓	✓	✓	✓	✓	✓	✓	✓	✓	✓	✓	✓
Hypnosis	✓	✓	✓	✓	✓	✓	✓	✓	✓	✓	✓	✓	✓	✓
Ptosis	✓	✓	✓	✓	✓	✓	✓	✓	✓	✓	✓	✓	✓	✓
Irritability	✓	✓	✓	✓	✓	✓	✓	✓	✓	✓	✓	✓	✓	✓
Pilo erection	✓	✓	✓	✓	✓	✓	✓	✓	✓	✓	✓	✓	✓	✓
Muscle Spasm	✓	✓	✓	✓	✓	✓	✓	✓	✓	✓	✓	✓	✓	✓
Loss of Traction	✓	✓	✓	✓	✓	✓	✓	✓	✓	✓	✓	✓	✓	✓

Note: "✓" = Effect is present, "✗" = Effect is absent.

4. Materials and Methods

4.1. Extraction and Fractionation via Column Chromatography

4.1.1. Botanical Material

The dried seeds of *P. anisum* were purchased from a grocery shop and they were identified by a botanist at GC-University Lahore. The specimen was assigned an identification code (Herb.Bot.3385) and was preserved in the herbarium of GC-University Lahore.

4.1.2. Extraction and Fractionation

The dried seeds were ground into a coarse-sized powder and the methanolic extract was prepared using the maceration technique [31]. The methanolic extract was used as a mother fraction of the plant extract, from which we extracted *n*-hexane, chloroform, ethyl acetate, *n*-butanol and aqueous fractions of the extract. All other fractions were left behind and only the aqueous fraction of *P. anisum* was purified using column chromatography, because our previous study reported that among all fractions, only the aqueous fraction was capable of producing memory-enhancing effects [18].

4.1.3. Column Chromatography

For column chromatography, a medium-sized glass column was used, which was packed with almost 10 g of silica gel-60 after making its slurry in the same solvent as was used for the mobile phase. The column was packed properly and solvent was run through the column following the standard procedures [32]. Then, the known quantity of aqueous extract of *P. anisum* was dissolved in the solvent and its uniform mixture was prepared. It was then loaded into the glass column quite carefully, with the help of pipette, in such a way that a uniform thick layer of the sample mixture was formed above the slurry. Finally, the solvent was added above the sample layer in a sufficient quantity and the stopper of the column was opened to obtain the separated fractions in the flask. Different solvents

were used in different ratios to obtain the separation of the contents of the aqueous extract of *P. anisum*. Using this technique, we got 16 fractions that were collected in small glass vials and were labelled properly. They were then used for further studies.

4.2. In Vitro Anti-Cholinesterase Activity

The purified fractions obtained through column chromatography were then analyzed for in vitro anticholinesterase activity. We used the NAFB micro-well plate assay technique by making a solution mixture by dissolving 0.25 mg of β -naphthyl acetate in 1 mL of methanol. We took 10 μ L of purified plant fraction and mixed it with 50 μ L of the above-prepared β -naphthyl acetate solution. The temperature of the reaction mixture was reduced and maintained at 4 °C, and then we added 200 μ L of acetylcholine esterase (3.33 U/mL) solution to it and it was incubated for 40 to 50 min in the same conditions. Then, a solution of Fast Blue B salt solution was prepared by dissolving 2.5 mg of it in 1 mL of distilled water. Finally, 10 μ L of the Fast Blue B salt was added to the reaction mixture dropwise, and a change in color was observed. If the color of the reaction mixture turned purple, it indicated that there was no inhibition of the cholinesterase enzyme by the test substance, while no change in color specified a strong anticholinesterase action of the test substance [33].

4.3. GC-MS Analysis

The purified fraction which produced a strong in vitro anticholinesterase activity was named as the *P. anisum* active fraction (P.aAF), which was selected and analyzed using the GC-MS technique. We used GC-MS equipment (Agilent 6890N) with the following specifications: capillary column (TR-5-MS), 30 Mts dimensions, 0.25 μ m film thickness, and 0.25 mm internal diameter. The carrier gas used in the GC-MS was 99.99% helium and the flow speed of the mobile was adjusted to 1 mL/min. The temperature of the oven was raised from 40 to 250 °C at a rate of 10 °C/min and the temperature of the ion source was fixed at 200 °C, the injector at 250 °C and the detector at 280 °C at the time of the sample injection. The test sample (purified fraction in concentration of 1 mg/mL) was dissolved in methanol and was injected in an aliquot of 2 μ L at the already adjusted temperature. The compounds present in the sample were then identified by their molecular masses via interpretation of the GC-MS library, and the structures of compounds were also expressed [31].

4.4. Animals

The in vivo studies were performed on Swiss, male albino mice having a weight of 25 ± 5 g. They were housed in polycarbonate cages in the animal house of Punjab University College of Pharmacy (PUCP), Lahore, and in standard living conditions, i.e., a humidity of 50%, a temperature of 25 ± 2 °C and an equal 12 h light and dark span [34]. The ethical approval for the use of animals was granted by the Animal Ethics Committee of PUCP, vide letter no AEC/PUCP/1072 after reviewing the research protocols and study design. The animals were given treatment according to the study design mentioned in Table 7.

4.5. In Vivo Behavioral and Biochemical Studies

The purified fraction of *P. anisum* which produced the maximum in vitro anticholinesterase activity (P.aAF) was administered in the animals as per the study design (Table 7) and then behavioral and biochemical studies were conducted. We used an elevated-plus-maze hole-board paradigm and light/dark test apparatuses to perform the behavioral studies. The biochemical analysis was conducted via an estimation of acetylcholinesterase (AChE), malondialdehyde (MDA), catalase (CAT), superoxide dismutase (SOD) and glutathione (GSH) levels in mice brains with all the detailed procedures as mentioned in our previously published manuscripts [31,34].

Table 7. Study design for behavioral and biochemical studies.

Groups	Treatment from Day 1–7
G-1 (Normal Control)	Normal saline 10 mL/Kg/p.o.
G-2 (Amnesic Control)	5% CMC 10 mL/Kg/p.o.
G-3 (Standard Control-A)	Piracetam 200 mg/Kg/p.o.
G-4 (Standard Control-B)	Piracetam 200 mg/Kg/p.o.
G-5 (Experimental Control-I)	P.aAF 3.5 mg/Kg/p.o.
G-6 (Experimental Control-II)	P.aAF 7 mg/Kg/p.o.
G-7 (Experimental Control-III)	P.aAF 7 mg/Kg/p.o.

Note: For preparation of oral doses, piracetam and scopolamine were dissolved in normal saline. However, P.aAF was suspended in 5% CMC. As per study design, P.aAF was administered daily for seven days to respective groups while scopolamine was only administered to G-2, G-4, G-5 and G-6 in a single oral dose on the 7th day of study. On the same day after 2 h of treatment, and on the next day, we performed the behavioral studies on mice, and finally the animals were dissected to perform biochemical evaluation on the 8th day.

4.6. Choline Acetyltransferase Activity (ChAT)

This part of study was performed on a 2nd set of experimental animals which were treated according to the study design mentioned in Table 8. To perform this test, we prepared the reagent by dissolving 10 μ L of 0.5 M sodium phosphate buffer having a pH of 7.2, 7.6×10^{-4} M neostigmine sulfate solution, 3 M NaCl solution, 1.1×10^{-3} Molar EDTA, acetyl coenzyme-A (6.2×10^{-3} M prepared in 0.01N HCl) and 1 molar choline chloride. It was then incubated at 37 °C for twenty-five minutes. Then, 100 μ L of brain homogenate was mixed thoroughly with 0.2 mL of the reagent and incubated at 37 °C for twenty-five minutes. It was then boiled for two minutes in a water bath and then added up with oxygen less distilled water. The reaction took place and proteins were denatured, which were then separated out via high-speed centrifugation. Finally, 0.5 mL of supernatant was mixed up with 10 μ L of 10^{-3} molar 4,4-dithiodipyridine and the absorbance of the mixture was taken at 324 nm using a double-beam UV-visible spectrophotometer [35].

Table 8. Study design for estimation of choline acetyltransferase (ChAT) levels in mice brains.

Groups	Treatment
G-A (Normal Control)	Normal saline 10 mL/Kg/p.o. for 7 days
G-B (Amnesic Control)	5% CMC 10 mL/Kg/p.o. for 6 days then Scopolamine 10 mg/Kg/p.o. on 7th day.
G-C (Experimental Control-I)	P.aAF 7 mg/Kg/p.o. for 7 days consecutively
G-D (Experimental Control-II)	Scopolamine 10 mg/Kg/p.o. on 1st day then P.aAF 7 mg/Kg/p.o. from day 2 to 7.
G-E (Experimental Control-III)	P.aAF 7 mg/Kg/p.o. for 6 days then Scopolamine 10 mg/Kg/p.o. on 7th day.

Note: On 8th day, we finally dissected the animals and performed biochemical evaluation of ChAT levels on brain homogenates of the mice.

4.7. Acute Toxicity Study

We followed OECD guidelines 423, 2001 as mentioned in our previous study [31] for the assessment of the acute toxic effects of the active fraction of *P. anisum* (P.aAF) on female albino mice (25 ± 5 g). Initial pilot studies were performed on mice and we determined the dose range at which death in animals was observed. No death was recorded when the extract was used up to 100 mg/Kg/p.o; however, all the animals died when treated with an acute single dose of 200 mg/Kg/p.o. To find the LD₅₀, 20 animals were equally divided into four groups with $n = 5$. Group-I was kept as normal control while group-II to Group-IV were orally treated with P.aAF in respective doses of 100, 150 and 200 mg/Kg. Animals were kept under observation to record the behavioral and physical changes along with the number of mortalities [36] and, finally, LD₅₀ was calculated as [37]: LD₅₀ = Least Lethal Dose – $\Sigma (a \times b)/n$.

4.8. Statistics

The numerical data were presented as mean \pm SEM. One-way ANOVA followed by Dunnett's test was applied for the multiple comparison and student's t-test analysis was applied on the data set using Graph Pad Prism software version 7 and a value of p of <0.05 was marked as significant.

5. Conclusions

Understanding the medicinal importance of dried *P. anisum* seeds, its different extracts were prepared and aqueous extract was purified using column chromatography. The purified fraction of the aqueous extract exhibited marked anticholinesterase and antioxidant activities in albino mice. The chemical analysis indicated the presence of oxadiazole compounds in it. Thus, the aqueous extract of *P. anisum* contains oxadiazole compounds which build up memory by reducing both AChE and oxidizing stress in mice brains. Its LD₅₀ was calculated as 95 mg/Kg/p.o and clinical data were limited to ensure its therapeutic safety. Hence, there is a strong need to perform clinical trials to explore the therapeutic potential and safety profile. Studies are further required to investigate the effectiveness of the tested substance for the treatment of other neurological disorders such as Alzheimer's, along with testing of the toxicity profile in more detail.

Author Contributions: A.M.: Conceptualization; Methodology; Investigation; Writing—original draft preparation. F.H.: Formal analysis; Methodology; Investigation; Writing—original draft preparation. R.M.: Software; Validation; Visualization; Writing—review and editing. R.A.: Conceptualization; Project administration; Supervision. Visualization; U.F.G.: Data curation; Validation; Resources; Investigations. M.Z.-U.-H.: Data curation; Validation; Resources; Investigations. M.A.: Conceptualization; Project administration; Supervision. Visualization; C.M.G.: Software; Validation; Visualization; Writing—review and editing. L.C.: Software; Validation; Visualization; Writing—review and editing. All authors have read and agreed to the published version of the manuscript.

Funding: This research received no external funding.

Institutional Review Board Statement: The study was conducted according to the guidelines of the Declaration of Helsinki, and approved by the Institutional Review Board of Punjab University College of Pharmacy, Lahore (Animal Ethics Committee of PUCP vide letter no AEC/PUCP/1072).

Informed Consent Statement: Not applicable.

Data Availability Statement: All the data are shown in manuscript.

Acknowledgments: Authors are thankful to the Punjab University College of Pharmacy, and Gulab Devi Educational Complex, Lahore, to facilitate the research.

Conflicts of Interest: The authors declare no conflict of interest.

References

1. Prasad, K.N.; Hovland, A.R.; Cole, W.C.; Prasad, K.C.; Nahreini, P.; Edwards-Prasad, J.; Andreatta, C.P. Multiple antioxidants in the prevention and treatment of Alzheimer disease: Analysis of biologic rationale. *Clin. Neuropharmacol.* **2000**, *23*, 2–13. [[CrossRef](#)] [[PubMed](#)]
2. Akhondzadeh, S.; Noroozian, M.; Mohammadi, M.; Ohadinia, S.; Jamshidi, A.; Khani, M. *Melissa officinalis* extract in the treatment of patients with mild to moderate Alzheimer's disease: A double blind, randomised, placebo controlled trial. *J. Neurol. Neurosurg. Psychiatry* **2003**, *74*, 863–866. [[CrossRef](#)]
3. Umare, M.; Wankhede, N.; Bajaj, K.; Trivedi, R.; Taksande, B.; Umekar, M.; Mahore, J.; Kale, M. Interweaving of reactive oxygen species and major neurological and psychiatric disorders. *Ann. Pharm. Fr.* **2022**, *80*, 409–425. [[CrossRef](#)]
4. Amina, B.; Soumeia, B.; Salim, B.; Mahieddine, B.; Sakina, B.; Chawki, B.; Francesca, N.; Marzia, V.; Carmine, N. Chemical profiling, antioxidant, enzyme inhibitory and in silico modeling of *Rosmarinus officinalis* L. and *Artemisia herba alba* Asso. essential oils from Algeria. *S. Afr. J. Bot.* **2022**, *147*, 501–510. [[CrossRef](#)]
5. Hung, N.H.; Quan, P.M.; Satyal, P.; Dai, D.N.; Hoa, V.V.; Huy, N.G.; Giang, L.D.; Ha, N.T.; Huong, L.T.; Hien, V.T. Acetylcholinesterase inhibitory activities of essential oils from Vietnamese traditional medicinal plants. *Molecules* **2022**, *27*, 7092. [[CrossRef](#)] [[PubMed](#)]
6. Li, N.; Liu, J.-H.; Zhang, J.; Yu, B.-Y. Comparative evaluation of cytotoxicity and antioxidative activity of 20 flavonoids. *J. Agr. Food Chem.* **2008**, *56*, 3876–3883. [[CrossRef](#)]

7. Kandiah, N.; Ong, P.A.; Yuda, T.; Ng, L.L.; Mamun, K.; Merchant, R.A.; Chen, C.; Dominguez, J.; Marasigan, S.; Ampil, E. Treatment of dementia and mild cognitive impairment with or without cerebrovascular disease: Expert consensus on the use of *Ginkgo biloba* extract, EGB 761[®]. *CNS Neurosci. Ther.* **2019**, *25*, 288–298. [\[CrossRef\]](#)
8. Govindarajan, R.; Vijayakumar, M.; Pushpangadan, P. Antioxidant approach to disease management and the role of ‘Rasayana’ herbs of Ayurveda. *J. Ethnopharmacol.* **2005**, *99*, 165–178. [\[CrossRef\]](#)
9. Rout, S.; Tambe, S.; Deshmukh, R.K.; Mali, S.; Cruz, J.; Srivastav, P.P.; Amin, P.D.; Gaikwad, K.K.; de Aguiar Andrade, E.H.; de Oliveira, M.S. Recent trends in the application of essential oils: The next generation of food preservation and food packaging. *Trends Food Sci. Technol.* **2022**, *129*, 421–439. [\[CrossRef\]](#)
10. de Torre, M.P.; Caverio, R.Y.; Calvo, M.I. Anticholinesterase activity of selected medicinal plants from Navarra region of Spain and a detailed phytochemical investigation of *Origanum vulgare* L. ssp. *vulgare*. *Molecules* **2022**, *27*, 7100. [\[CrossRef\]](#)
11. Noori, T.; Dehpour, A.R.; Sureda, A.; Sobarzo-Sanchez, E.; Shirooie, S. Role of natural products for the treatment of Alzheimer’s disease. *Eur. J. Pharmacol.* **2021**, *898*, 173974. [\[CrossRef\]](#)
12. Bakhshi, M.; Kamalinejad, M.; Shokri, M.; Forouzani, G.; Heidari, F.; Tofangchiha, M. In vitro antibacterial effect of *Pimpinella anisum* essential oil on *Enterococcus faecalis*, *Lactobacillus casei*, *Actinomyces naeslundii*, and *Aggregatibacter actinomycetemcomitans*. *Folia Med.* **2022**, *64*, 799–806. [\[CrossRef\]](#)
13. Shojaii, A.; Abdollahi Fard, M. Review of pharmacological properties and chemical constituents of *Pimpinella anisum*. *ISRN Pharm.* **2012**, *2012*, 510795. [\[CrossRef\]](#)
14. Karimzadeh, F.; Hosseini, M.; Mangeng, D.; Alavi, H.; Hassanzadeh, G.R.; Bayat, M.; Jafarian, M.; Kazemi, H.; Gorji, A. Anticonvulsant and neuroprotective effects of *Pimpinella anisum* in rat brain. *BMC Complement. Altern. Med.* **2012**, *12*, 76. [\[CrossRef\]](#)
15. Dohi, S.; Terasaki, M.; Makino, M. Acetylcholinesterase inhibitory activity and chemical composition of commercial essential oils. *J. Agr. Food Chem.* **2009**, *57*, 4313–4318. [\[CrossRef\]](#)
16. Ahmed, F.; Ghalib, R.M.; Sasikala, P.; Ahmed, K.M. Cholinesterase inhibitors from botanicals. *Pharmacogn. Rev.* **2013**, *7*, 121. [\[CrossRef\]](#) [\[PubMed\]](#)
17. Das, S.; Singh, V.K.; Dwivedy, A.K.; Chaudhari, A.K.; Dubey, N.K. Nanostructured *Pimpinella anisum* essential oil as novel green food preservative against fungal infestation, aflatoxin B1 contamination and deterioration of nutritional qualities. *Food Chem.* **2021**, *344*, 128574. [\[CrossRef\]](#) [\[PubMed\]](#)
18. Mushtaq, A.; Anwar, R.; Ahmad, M. Memory enhancing effect of anise (*Pimpinella anisum*) with respect to its antioxidant activity in albino mice. *J. Anim. Plant Sci.* **2019**, *29*, 602–610.
19. Wang, M.; Liu, T.; Chen, S.; Wu, M.; Han, J.; Li, Z. Design and synthesis of 3-(4-pyridyl)-5-(4-sulfamido-phenyl)-1, 2, 4-oxadiazole derivatives as novel GSK-3 β inhibitors and evaluation of their potential as multifunctional anti-Alzheimer agents. *Eur. J. Med. Chem.* **2021**, *209*, 112874. [\[CrossRef\]](#) [\[PubMed\]](#)
20. Gobec, M.; Tomasic, T.; Markovic, T.; Mlinaric-Rascan, I.; Dolenc, M.S.; Jakopin, Z. Antioxidant and anti-inflammatory properties of 1, 2, 4-oxadiazole analogs of resveratrol. *Chem. Biol. Interact.* **2015**, *240*, 200–207. [\[CrossRef\]](#) [\[PubMed\]](#)
21. Chawla, G.; Kumar, U.; Bawa, S.; Kumar, J. Syntheses and evaluation of anti-inflammatory, analgesic and ulcerogenic activities of 1, 3, 4-oxadiazole and 1, 2, 4-triazolo [3, 4-b]-1, 3, 4-thiadiazole derivatives. *J. Enzyme Inhib. Med. Chem.* **2012**, *27*, 658–665. [\[CrossRef\]](#)
22. Tsikas, D. Assessment of lipid peroxidation by measuring malondialdehyde (MDA) and relatives in biological samples: Analytical and biological challenges. *Anal. Biochem.* **2017**, *524*, 13–30. [\[CrossRef\]](#) [\[PubMed\]](#)
23. Eraky, S.M.; Ramadan, N.M.; El-Magd, N.F.A. Ameliorative effects of bromelain on aluminum-induced Alzheimer’s disease in rats through modulation of TXNIP pathway. *Int. J. Biol. Macromol.* **2022**, *227*, 1119–1131. [\[CrossRef\]](#) [\[PubMed\]](#)
24. Yoon, W.B.; Choi, H.J.; Kim, J.E.; Park, J.W.; Kang, M.J.; Bae, S.J.; Lee, Y.J.; Choi, Y.S.; Kim, K.S.; Jung, Y.-S. Comparison of scopolamine-induced cognitive impairment responses in three different ICR stocks. *Lab. Anim. Res.* **2018**, *34*, 317–328. [\[CrossRef\]](#) [\[PubMed\]](#)
25. Papas, M.; Catalan, J.; Barranco, I.; Arroyo, L.; Bassols, A.; Yeste, M.; Miró, J. Total and specific activities of superoxide dismutase (SOD) in seminal plasma are related with the cryotolerance of jackass spermatozoa. *Cryobiology* **2020**, *92*, 109–116. [\[CrossRef\]](#) [\[PubMed\]](#)
26. Tsosura, T.V.S.; Dos Santos, R.M.; Neto, A.H.C.; Chiba, F.Y.; Carnevali, A.C.N.; Mattera, M.S.d.L.C.; Belardi, B.E.; Cintra, L.T.Â.; da Silva Machado, N.E.; Matsushita, D.H. Maternal apical periodontitis increases insulin resistance and modulates the antioxidant defense system in the gastrocnemius muscle of adult offspring. *J. Endod.* **2021**, *47*, 1126–1131. [\[CrossRef\]](#)
27. Mohammadi-Khanaposhtani, M.; Mahdavi, M.; Saeedi, M.; Sabourian, R.; Safavi, M.; Khanavi, M.; Foroumadi, A.; Shafiee, A.; Akbarzadeh, T. Design, synthesis, biological evaluation, and docking study of acetylcholinesterase inhibitors: New acridone-1, 2, 4-oxadiazole-1, 2, 3-triazole Hybrids. *Chem. Biol. Drug Des.* **2015**, *86*, 1425–1432. [\[CrossRef\]](#)
28. Elghazawy, N.H.; Zaafar, D.; Hassan, R.R.; Mahmoud, M.Y.; Bedda, L.; Bakr, A.F.; Arafa, R.K. Discovery of New 1, 3, 4-Oxadiazoles with dual activity targeting the cholinergic pathway as effective anti-Alzheimer agents. *ACS Chem. Neurosci.* **2022**, *13*, 1187–1205. [\[CrossRef\]](#)
29. Báñez-Lopez, S.; Montero-Pedrazuela, A.; Bosch-García, D.; Venero, C.; Guadano-Ferraz, A. Increased anxiety and fear memory in adult mice lacking type 2 deiodinase. *Psychoneuroendocrinology* **2017**, *84*, 51–60. [\[CrossRef\]](#)

30. Alegiry, M.H.; Hajrah, N.H.; Alzahrani, N.A.Y.; Shawki, H.H.; Khan, M.; Zrelli, H.; Atef, A.; Kim, Y.; Alsafari, I.A.; Arfaoui, L. Attitudes toward psychological disorders and alternative medicine in Saudi participants. *Front. Psychiatry* **2021**, *12*, 577103. [CrossRef]
31. Mushtaq, A.; Anwar, R.; Gohar, U.F.; Ahmad, M.; Marc, R.A.; Mureşan, C.C.; Irimie, M.; Bobescu, E. Biomolecular evaluation of *Lavandula stoechas* L. for nootropic activity. *Plants* **2021**, *10*, 1259. [CrossRef] [PubMed]
32. Jaffuel, G.; Chappuis, L.; Guillard, D.; Turlings, T.C.; Glauser, G. Improved separation by at-column dilution in preparative hydrophilic interaction chromatography. *J. Chromatogr. A* **2018**, *1532*, 136–143. [CrossRef]
33. Monadi, T.; Azadbakht, M.; Ahmadi, A.; Chabra, A. A Comprehensive Review on the Ethnopharmacology, Phytochemistry, Pharmacology, and Toxicology of the Mandragora Genus; from Folk Medicine to Modern Medicine. *Curr. Pharm. Des.* **2021**, *27*, 3609–3637. [CrossRef]
34. Mushtaq, A.; Anwar, R.; Ahmad, M. *Lavandula stoechas* (L) a Very Potent Antioxidant Attenuates Dementia in Scopolamine Induced Memory Deficit Mice. *Front. Pharmacol.* **2018**, *9*, 1375. [CrossRef]
35. Chao, L.-P.; Wolfgram, F. Spectrophotometric assay for choline acetyltransferase. *Anal. Biochem.* **1972**, *46*, 114–118. [CrossRef] [PubMed]
36. El Hilaly, J.; Israili, Z.H.; Lyoussi, B. Acute and chronic toxicological studies of *Ajuga iva* in experimental animals. *J. Ethnopharmacol.* **2004**, *91*, 43–50. [CrossRef] [PubMed]
37. Akhila, J.S.; Shyamjith, D.; Alwar, M. Acute toxicity studies and determination of median lethal dose. *Curr. Sci.* **2007**, *97*, 917–920. Available online: <http://www.jstor.org/stable/24099255> (accessed on 21 January 2023).

Disclaimer/Publisher's Note: The statements, opinions and data contained in all publications are solely those of the individual author(s) and contributor(s) and not of MDPI and/or the editor(s). MDPI and/or the editor(s) disclaim responsibility for any injury to people or property resulting from any ideas, methods, instructions or products referred to in the content.



Clear Cell Renal Cell Carcinoma: Local Recurrence and Bilateral Adrenal Metastases - A Case Report

CASE REPORT

ELIZA-MARIA POPA

ROSANA MANEA

ROXANA-ELENA BIRLA-COROIU

**Author affiliations can be found in the back matter of this article*

]u[ubiquity press

ABSTRACT

Introduction: Clear cell renal cell carcinoma is the most frequent type of renal cell carcinoma, which is often diagnosed incidentally in an advanced stage.

Case History: We present the case of a 49-year-old man who presented to the emergency department with no specific symptoms. After computed tomography (CT) evaluation, the suspicion was raised of a left renal tumour. The aim of this case study is to underline the importance of rapid diagnosis and further investigation of clear cell renal cell carcinoma and the severity of this type of cancer.

Conclusions: Clear cell renal cell carcinoma has no specific symptoms. For the complete diagnosis and further monitoring, the use of CT is necessary.

Teaching Point: Clear cell renal cell carcinoma treated with partial nephrectomy can relapse near the surgical scar and progress with metachronous bilateral adrenal metastases, especially when close follow-up is not performed due to the pandemic situation.

CORRESPONDING AUTHOR:

Roxana-Elena Birla-Coroiu

Clinical and Emergency
Hospital of Brasov, RO

coroiu.roxana@gmail.com

KEYWORDS:

clear cell renal cell carcinoma;
local recurrence; adrenal
metastases; renal tumor;
computed tomography

TO CITE THIS ARTICLE:

Popa E-M, Manea R, Birla-Coroiu R-E. Clear Cell Renal Cell Carcinoma: Local Recurrence and Bilateral Adrenal Metastases - A Case Report. *Journal of the Belgian Society of Radiology*. 2022; 106(1): 42, 1-4. DOI: <https://doi.org/10.5334/jbsr.2772>

INTRODUCTION

Clear cell renal cell carcinoma is the most frequent type of renal cell carcinoma, which, in the great majority of cases has an asymptomatic clinical behavior [1]. For this reason, often, renal masses are diagnosed in an advanced stage during investigations for other purposes [1]. The most frequent sign that may occur at the laboratory evaluation is microscopic haematuria. A CT scan is performed to determine the cause because this can appear from other reasons like nephrocalcinosis [2].

The purpose of this case study is to determine the value of CT scan in the diagnosis and post-treatment monitoring clear cell renal cell carcinoma.

CASE HISTORY

A 49-year-old man, with no personal history and without treatment, was admitted to the hospital with nausea and persistent epigastric abdominal pain for two days

for which he self-administered an antispastic drug. The clinical examination and the blood tests from the first evaluation were normal.

An abdominal CT scan with contrast administration was performed (*Figure 1*), and the appearance raised the suspicion of a left renal tumour.

After one-month, partial nephrectomy is performed, and the left renal lesion is totally removed. The clinical evolution after the surgery was favourable. The histopathological exam revealed clear cell renal carcinoma, and the patient went home with the recommendation to have another CT-scan investigation after six months.

Because of the pandemic situation, the patient did not follow any treatment and have postponed the scheduled investigation.

Another control CT scan with contrast administration was performed after one year and four months which revealed the appearance of a new left sinus renal nodular lesion (*Figure 2*) and bilateral adrenal nodular lesions, suggestive for adrenal metastases (*Figure 3*).

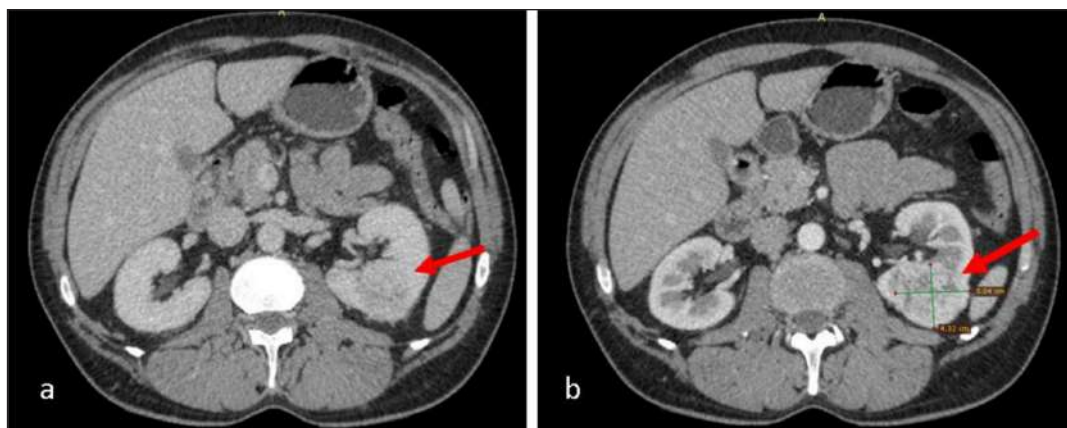


Figure 1 CT scan with contrast administration (CA): **a.** heterogeneous exophytic nodular lesion in the lower pole of the left kidney with small bulging into sinus, measuring 4.3/5/6 cm (AP/T/CC); **b.** the lesion enhances at periphery and has an irregular necrotic centre.

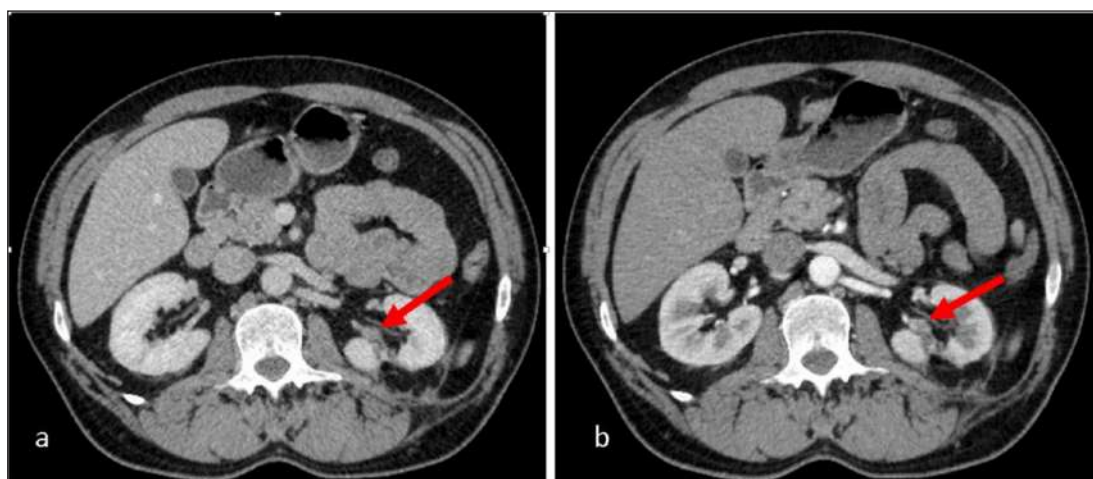


Figure 2 CT scan with CA: **a.** heterogeneous nodular lesion in the sinus of left remnant kidney; **b.** the lesion enhances at periphery and has necrotic centre.



Figure 3 Arterial phase CT scan: **a, b**, two, nodular, enhancing solid lesions in the right adrenal gland; **c**, a solitary, nodular, enhancing solid lesion in the left adrenal gland.

For the recently discovered lesions, the patient was recommended for chemotherapy for three months. After six months, a control CT scan revealed an evolutive aspect of the left sinusal renal lesion, with increased size with 25% and increased size of the bilateral adrenal lesions with 20%.

Considering the progressive imaging aspect and the poor prognosis, the medical team decide that left nephrectomy followed by adjuvant immunotherapy and chemotherapy is the best decision for the patient treatment.

COMMENT

Over 90% of renal cancers are represented by renal cell carcinoma. Seventy percent of these are represented by clear cell renal cell carcinoma [3]. We presented the case of a patient with left-sided clear cell renal cell carcinoma who was incidentally diagnosed and for whom it was performed partial nephrectomy. After one year and four months, another abdominal CT investigation found a local recurrence of the kidney tumour and simultaneous bilateral adrenal metastases.

According to the literature, in most cases the patients have no symptoms that suggest this disease. Approximately 30% of patients come to the hospital with symptoms related to local advanced or metastatic disease [1, 4].

Among the most frequent metastatic sites of kidney cancer is ipsilateral adrenal gland [4], and it can appear synchronous between 2–10% of cases or metachronous, which is a rare event [5].

Simultaneous bilateral adrenal metastases were found only in less than 1% of patients; there are approximately 20 cases described in literature [6].

CONCLUSIONS

We presented the case of a 49-year-old man who was diagnosed incidentally with left renal mass after an abdominal CT scan. The histopathological result was clear


cell renal cell carcinoma. The evolution of the patient was unfavourable and after a period local recurrence and simultaneous bilateral adrenal metastases were found.


The prognosis of clear cell renal cell carcinoma is poor, with high mortality; therefore a rapid diagnosis and treatment are required.

COMPETING INTERESTS

The authors have no competing interests to declare.

AUTHOR AFFILIATIONS

Eliza-Maria Popa  orcid.org/0000-0001-8468-0012
Clinical and Emergency Hospital of Brasov, RO

Rosana Manea  orcid.org/0000-0002-4882-512X
Transilvania University of Brasov, RO

Roxana-Elena Birla-Coroiu  orcid.org/0000-0003-2831-9251
Clinical and Emergency Hospital of Brasov, RO

REFERENCES

1. **Gray RE, Harris GT.** Renal cell carcinoma: Diagnosis and management. *Am Fam Physician*. 2019; 99(3): 179–184. Available at: <https://www.aafp.org/afp/2019/0201/p179.html>
2. **Sechel G, Repanovici A, Manea R, Burtea V.** The imaging evaluation of typical and atypical calcifications in different anatomical regions study in Brasov, Romania. *Med. Surg. J.* 2020; 124(2): 290–297. Available at: <https://www.revmedchir.ro/index.php/revmedchir/article/view/2121>
3. **Jonasch E, Walker CL, Rathmell WK.** Clear cell renal cell carcinoma ontogeny and mechanisms of lethality. *Nat Rev Nephrol*. 2021; 17: 245–261. DOI: <https://doi.org/10.1038/s41581-020-00359-2>
4. **Koutalellis GE, Felekouras E, Evangelou C, Koritsiadis G.** Renal cell carcinoma with bilateral synchronous adrenal gland metastases: A case report. *Cases Journal*. 2009; 2: 7298. DOI: <https://doi.org/10.4076/1757-1626-2-7298>
5. **Peters I, Hora M, Herrmann TR, et al.** Incidence of synchronous and metachronous adrenal metastases

following tumour nephrectomy in renal cell cancer patients: A retrospective bi-centre analysis. *SpringerPlus*. 2013; 2: 293. DOI: <https://doi.org/10.1186/2193-1801-2-293>

6. **Pandey T, Pandey S, Singh V, Sharma A.** Bilateral renal cell carcinoma with bilateral adrenal metastasis: A therapeutic challenge. *BMJ Case Reports*. 2018; 11: e227176. DOI: <https://doi.org/10.1136/bcr-2018-227176>

TO CITE THIS ARTICLE:

Popa E-M, Manea R, Birla-Coroiu R-E. Clear Cell Renal Cell Carcinoma: Local Recurrence and Bilateral Adrenal Metastases - A Case Report. *Journal of the Belgian Society of Radiology*. 2022; 106(1): 42, 1–4. DOI: <https://doi.org/10.5334/jbsr.2772>

Submitted: 31 January 2022 Accepted: 10 March 2022 Published: 06 May 2022

COPYRIGHT:

© 2022 The Author(s). This is an open-access article distributed under the terms of the Creative Commons Attribution 4.0 International License (CC-BY 4.0), which permits unrestricted use, distribution, and reproduction in any medium, provided the original author and source are credited. See <http://creativecommons.org/licenses/by/4.0/>.

Journal of the Belgian Society of Radiology is a peer-reviewed open access journal published by Ubiquity Press.



Giant Thoracic Aortic Aneurysm Rupture in a Patient with Extensive Atherosclerotic Disease

RAMONA MIHAELA POPA

CHIRIȚĂ ANDREI-CONSTANTIN

ROSANA MIHAELA MANEA

*Author affiliations can be found in the back matter of this article

**IMAGES IN CLINICAL
RADIOLOGY**

ubiquity press

ABSTRACT

Aneurysmal dilatations can affect any aortic segment and represent the result of various causes, atherosclerotic disease being the most common and frequently involved.

We hereby illustrate a case of a patient with thoracic aortic aneurysm rupture due to extensive atherosclerotic disease, with multiple complex penetrating ulcerated atherosclerotic plaques located in the descending aorta.

CT angiography evaluation included a comprehensive description of imaging features and extent of the thoracic aortic aneurysm, the presence of thrombus, relationship to adjacent structures and branches, associated complications.

Teaching Point: Thoracic aortic aneurysm rupture due to extensive atherosclerotic disease with multiple penetrating ulcers.

CORRESPONDING AUTHOR:

Ramona Mihaela Popa

Department of Radiology
and Medical Imaging, Clinical
Emergency County Hospital
of Braşov, 500326 Braşov,
Romania

rammonapopa@gmail.com

KEYWORDS:

aorta, thoracic aortic
aneurysm, thoracic
aortic aneurysm rupture,
atherosclerotic disease,
CT angiography

TO CITE THIS ARTICLE:

Popa RM, Andrei-Constantin C, Manea RM. Giant Thoracic Aortic Aneurysm Rupture in a Patient with Extensive Atherosclerotic Disease. *Journal of the Belgian Society of Radiology*. 2024; 108(1): 10, 1–4. DOI: <https://doi.org/10.5334/jbsr.3314>

CASE HISTORY

A 69-year-old male was admitted to the Emergency Department with persistent cough, haemoptysis, haematemesis, dyspnoea and low blood pressure. The patient's history includes grade 3 hypertension and chronic kidney disease stage V.

A frontal chest X-ray (Figure 1) illustrated a left perihilar well-defined macronodular opacity of medium intensity

(yellow arrow). Bilateral interstitial densification with a reticular pattern and diffuse distribution can be noted.

Native CT acquisitions (Figure 2) depicted a large descending aortic calibre with a discrete hyperattenuating crescentic sign on the left lateral aspect of the descending aorta (pink arrow). Left pleural effusion, with hyperdense areas, suggestive of haemothorax, can be noted.

Multiple pulmonary consolidations in the left inferior lobe and micronodular interstitial densification

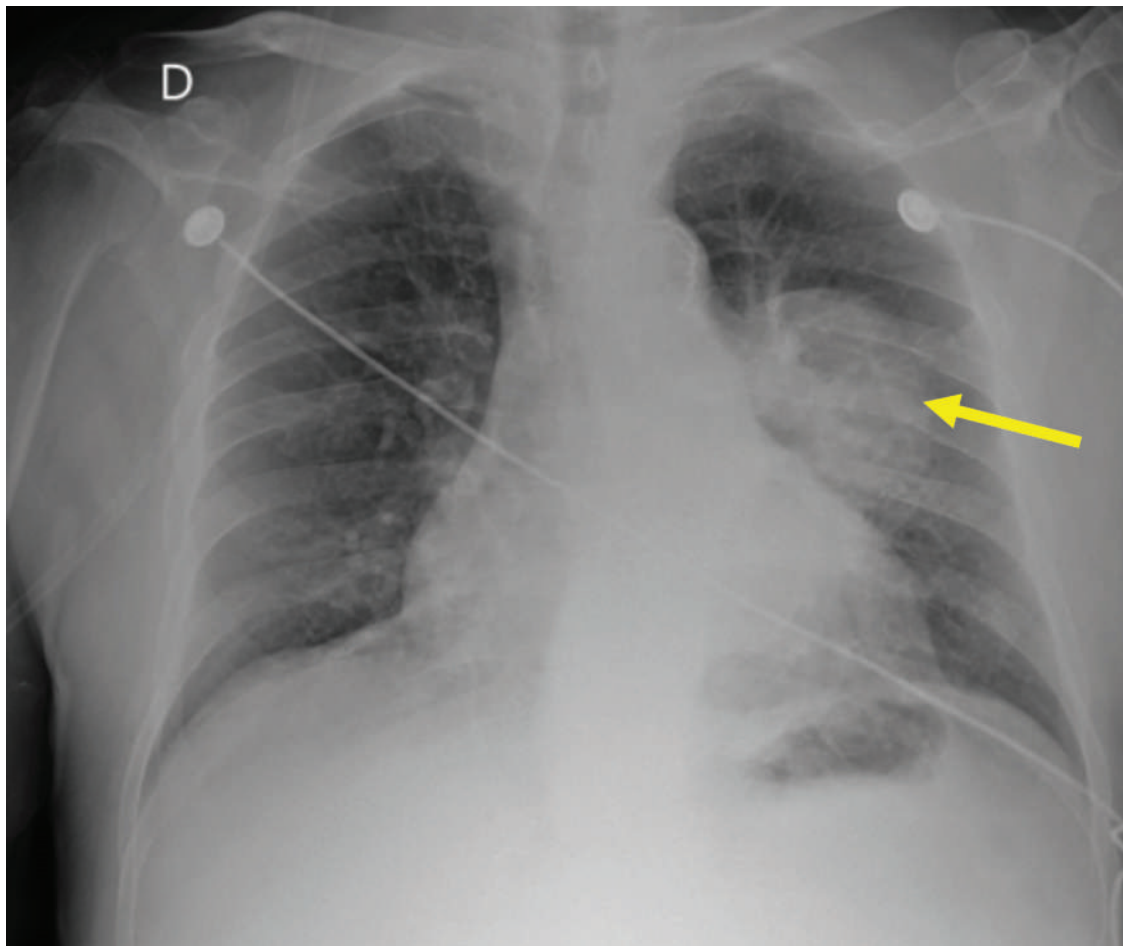


Figure 1 Frontal chest X-ray.

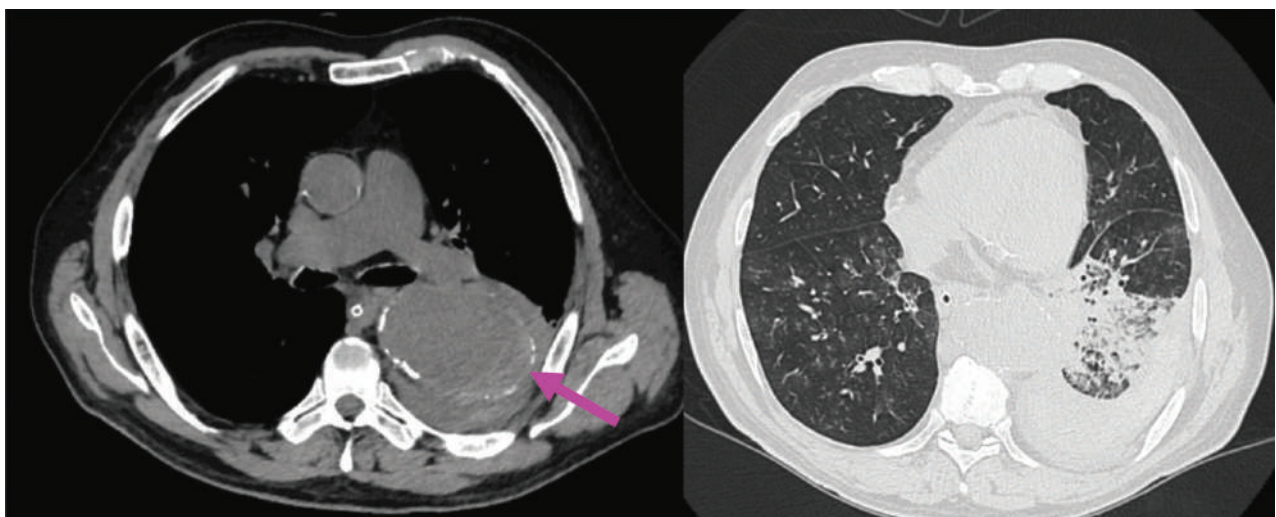


Figure 2 Native CT acquisitions - axial sections.

patterns in the right lower lobe can be noted—suggestive of intrapulmonary haemorrhage, cannot exclude the coexistence of an infectious component.

Contrast-enhanced CT acquisitions (Figures 3 and 4) revealed rupture of a giant saccular aneurysm of the descending thoracic aorta (green arrows) with active

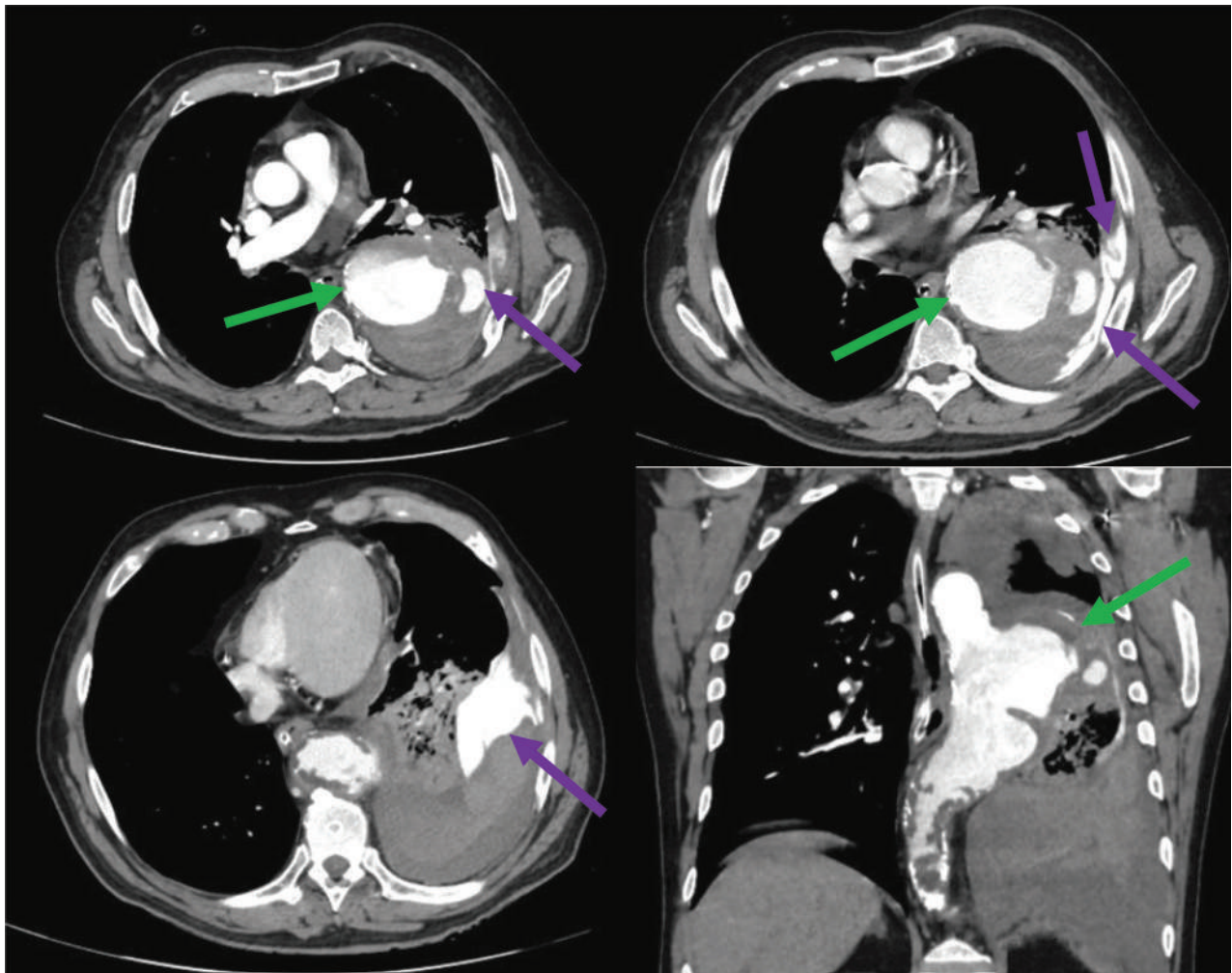


Figure 3 Contrast-enhanced CT acquisitions - arterial phase - axial and coronal sections.

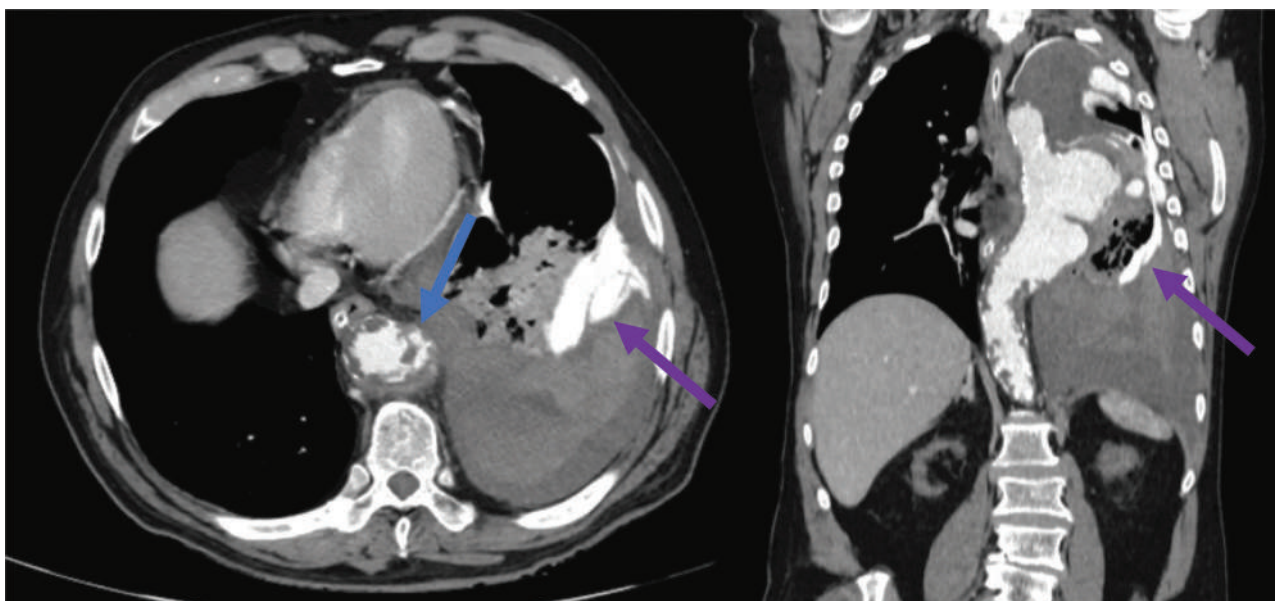


Figure 4 Contrast-enhanced CT acquisitions - arterial phase - axial and coronal sections.

contrast substance extravasation into the left inferior pulmonary lobe and into the left pleural cavity with associated haemothorax (purple arrows).

The aortic aneurysm measured 55/67 mm in the axial plane and 104 mm in the cranio-caudal length. The proximal aspect was projected near the aortic arch (vertebral level T4–T5) at 90 mm caudal to the left subclavian artery emergence, and the distal extent was projected at T9 vertebral level. An associated circumferential irregular mural thrombus can be noted.

The entire aorta and all its branches demonstrate remarkably widespread atherosclerosis, including multiple complex plaques. Multiple atherosclerotic non-calcified plaques with irregular margins pointing to the aortic lumen, most of them ulcerated, can be seen in the descending aortic segment (Figure 4—blue arrow).

COMMENT

An aneurysm represents an abnormal focal dilatation of a blood vessel [1]. Thoracic aortic aneurysms are divided into true aneurysms and false aneurysms (pseudoaneurysms) [1]. True aneurysms contain all three layers of the aortic wall, whereas false aneurysms never involve all three layers and are contained by the adventitia or periaortic tissues [1].

Thoracic aorta aneurysmal dilatations are mostly the result of atherosclerotic disease, as illustrated in our case [1]. Other causes include degeneration of the medial layer of the aortic wall (idiopathically or due to genetic disorders, including Marfan syndrome and Ehlers–Danlos syndrome), aortic dissection, trauma, syphilis, noninfective aortitis, rheumatic fever, rheumatoid arthritis, ankylosing spondylitis, giant cell arteritis, relapsing polychondritis, Takayasu arteritis, Reiter

syndrome, systemic lupus erythematosus, scleroderma, psoriasis, ulcerative colitis, radiation, Behçet disease and congenital anomaly [1].

Initial evaluation includes a CT angiography of the entire thoraco-abdominal aorta, because an abdominal aortic aneurysm occurs in 28% of patients with a thoracic aortic aneurysm [1].


In our case, the aortic aneurysm rupture was the result of an extensive atherosclerotic disease with multiple penetrating ulcers in the descending aorta.

The most important differential diagnosis should always include aortitis, which presents concentric regular wall thickening and hypoattenuating wall, which enhances postcontrast!

AUTHOR AFFILIATIONS

Ramona Mihaela Popa  orcid.org/0000-0002-4294-9949
Department of Radiology and Medical Imaging, Clinical
Emergency County Hospital of Braşov, 500326 Braşov, Romania

Chiriţă Andrei-Constantin Department of Radiology and
Medical Imaging, Clinical Emergency County Hospital of Braşov,
500326 Braşov, Romania

Rosana Mihaela Manea  orcid.org/0000-0003-1032-0449
Faculty of Medicine, “Transilvania” University of Braşov, Romania,
500036 Braşov, Romania, Department of Radiology and Medical
Imaging, Clinical Emergency County Hospital of Braşov, 500326
Braşov, Romania

REFERENCE

1. **Agarwal PP, Chughtai A, Matzinger FR, Kazerooni EA.** Multidetector CT of thoracic aortic aneurysms. *Radiographics*. 2009;29(2):537–552. DOI: <https://doi.org/10.1148/rg.292075080>.

TO CITE THIS ARTICLE:

Popa RM, Andrei-Constantin C, Manea RM. Giant Thoracic Aortic Aneurysm Rupture in a Patient with Extensive Atherosclerotic Disease. *Journal of the Belgian Society of Radiology*. 2024; 108(1): 10, 1–4. DOI: <https://doi.org/10.5334/jbsr.3314>

Submitted: 13 August 2023 **Accepted:** 5 January 2024 **Published:** 2 February 2024

COPYRIGHT:

© 2024 The Author(s). This is an open-access article distributed under the terms of the Creative Commons Attribution 4.0 International License (CC-BY 4.0), which permits unrestricted use, distribution, and reproduction in any medium, provided the original author and source are credited. See <http://creativecommons.org/licenses/by/4.0/>.
Journal of the Belgian Society of Radiology is a peer-reviewed open access journal published by Ubiquity Press.

Pharmacological Basis for Antispasmodic, Bronchodilator, and Antidiarrheal Potential of *Dryopteris ramosa* (Hope) C. via In Vitro, In Vivo, and In Silico Studies

Iram Iqbal, Fatima Saqib,* Muhammad Farhaj Latif, Hamna Shahzad, Lorena Dima,* Bayan Sajer, Rosana Manea, Ciprian Pojala, and Radu Necula



Cite This: *ACS Omega* 2023, 8, 26982–27001



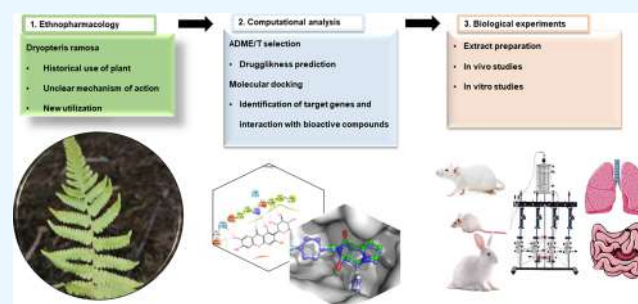
Read Online

ACCESS |

Metrics & More

Article Recommendations

ABSTRACT: *Background:* *Dryopteris ramosa* is used as an old treatment for several diseases. *D. ramosa* fronds are eaten to treat gastrointestinal (GIT) issues and as an antibiotic. However, there is a dearth of literature justifying its traditional use. *Aims and objectives:* the current work used biological and molecular docking studies to support traditional usage and elucidate *D. ramosa*'s multitarget mechanism. *Materials and methods:* Bioactive compounds were docked in silico. Force displacement transducers coupled with a power lab data gathering system examined the effects of compounds on rabbit jejunum, trachea, and aorta tissues. Albino mice and rats were used for in vivo studies. *Results:* Bioactive compounds interacted with inflammation, asthma, and diarrhea genes, according to in silico studies. *D. ramosa* crude extract (Dr.Cr) calmed impulsive contractions and K⁺ (80 mM)-provoked contractions in the jejunum and tracheal tissue dose-dependently, showing the presence of the Ca⁺⁺ channel-blocking (CCB) effect, further verified by the rightward parallel shift of CRCs equivalent to verapamil. Polarity-based fractionation showed spasmolytic activity in Dr.DCM and muscarinic receptors mediated spasmogenic activity in the Dr.Aq fraction. Dr.Cr vasoconstricted the aortic preparation, which was totally blocked by an angiotensin II receptor antagonist. This suggests that Dr. Cr's contractile effect is mediated through angiotensin receptors. In rats and mice, it showed anti-inflammatory and antidiarrheal action. *Conclusion:* This study supports the traditional medicinal uses of *D. ramosa* against GIT disorders and may be an important therapeutic agent in the future.



1. INTRODUCTION

Since the beginning of their evolutionary history, humans have had discrete pharmacological knowledge of the medicinal effects of plants, leaving traces in prehistoric and subsequent cultural heritage.¹ Ethnopharmacology is the scientific study of conventional medical procedures and how many cultures use plants, animals, and minerals for therapeutic purposes. But there have also been a number of disputes around this topic including cultural appropriation and violation of intellectual property rights of native people, as there are instances where pharmaceutical companies have patented traditional practices without the consent of indigenous communities. These debates show how important it is for ethnopharmacology to take ethical concerns and cultural sensitivity seriously in order to uphold and value indigenous knowledge and practices.² Besides this, recently, the transition from conventional ethnopharmacology to drug discovery has been facilitated by the introduction of specialized extraction techniques including sophisticated new methodologies such as high-performance liquid chromatography (HPLC), liquid chromatography-mass spectrometry (LC-MS), gas chromatography-mass spectrometry (GC-MS), chemoinformatic techniques, the advancement

of isolation and characterization techniques, and the rise in computing power including molecular docking and gene target prediction of compounds.¹ A lot has been accomplished recently in the rapidly developing discipline of ethnopharmacology. Using cutting-edge methods like metabolomics and high-throughput screening, scientists are discovering new molecules in traditional medicinal plants. These substances have the potential to be turned into novel treatments and medications.³ The validity of the effectiveness and safety of conventional medicines has been greatly aided by ethnopharmacology. Clinical trials are being carried out by researchers to examine the efficacy of conventional treatments

Received: March 21, 2023

Accepted: June 21, 2023

Published: July 20, 2023



for a variety of illnesses, such as cancer, diabetes, and infectious disorders, as we already know a number of drugs including taxol, vinca alkaloids (vinblastine, vincristine), quinine, and artemisinin, which are isolated from plants.¹ People are more interested in using medicinal plants as a result of their conviction that plant extracts are more effective, readily accessible, inexpensive, and have few adverse effects than other options.³ Ayurvedic medicines and Chinese ancient medicine have grown in fame as complementary therapies for serious ailments in recent years.⁴ Ma huang, ginseng, ginkgo, P. zizyphi, magnolia, bupleurum, and Huang qin are typical Chinese herbs employed to treat asthma,^{5,6} while in the Unani medical system commonly used formulation is Qurs Sartan Kafoori (for the treatment of chronic bronchitis, cough, and tuberculosis).⁷

Due to its rich biodiversity and diverse climate zones, Pakistan is home to a diverse array of medicinal plants. In the North, it has the Himalayan range, the Hindu Kush range, and the Karakoram range.^{8,9} The Himalayas is regarded as a botanical treasure trove.⁸ The Himalayan people are well-versed in the use of medicinal herbs for traditional reasons. These herbs are employed not only as healing agents for fever, chest, and intestinal disorders but also as a key raw material in the production of traditional and modern medications.¹⁰ Since ancient times, ferns have been employed as a remedy for a variety of human ailments, including bruises, burns, bleeding, colds, diarrhea, constipation, gastric ulcers, and many more.¹¹

Dryopteris ramosa, also known as kunji or pakha, is a medicinally important plant native to the Himalayan region that grows in wet and shaded areas at high altitudes.^{10,12} It is used as a vegetable against ulceration in the gastrointestinal tract, for constipation,^{13–15} and as an aphrodisiac,¹³ provides strength to the body,¹⁴ and acts as a vulnerable diuretic and stomachic, having antibacterial potential and febrifuge.¹⁶ The juice from the plant is used to relieve stomach aches.¹⁷ As it acts as an astringent, so in addition to its therapeutic purposes, it also has some cosmetic benefits.¹⁶

Ferns have survived since the Paleozoic era; it is hypothesized that they have some distinctively useful secondary metabolites in comparison to other plant species. Studies have discovered many useful phytochemicals from the ferns, those counting different alkaloids, flavonoids, phenols, steroids, triterpenoids, amino acids, and fatty acids, thus providing an indication for the medicinal significance of the plant.¹⁸ *D. ramosa* has presented marked antibacterial, antifungal, enzyme inhibition,¹² and antioxidant activities.^{12,19}

2. METHODOLOGY

2.1. Extract Preparation. *D. ramosa* Linn. (<http://www.theplantlist.org>, accessed 04-07-2021) was collected from Haripur, KPK during July–Aug 2021 and identified by the assistance of expert taxonomist Prof Dr. Muhammad Zafar, Quaid-e-Azam University, Islamabad, and voucher specimen # 131415 was deposited in the herbarium of Pakistan, Quaid-e-Azam University, Islamabad. The plant was washed and air-dried at ambient temperature for about 2 weeks and ground into a coarse powder. 1 kg of the powder was then added to a solution of 70:30 ethanol/water in an amber glass flask for maceration with periodic shaking for 7 days. To remove herbal pieces, this soaked substance was first filtered using a muslin cloth, and the liquid thus obtained was later filtered by filter paper, and a similar method was used for the second and third time maceration. Later on, all collected filtrates were combined

and concentrated on a Rota evaporator (BUCHI) at 37 ± 2 °C. A layer of the semisolid substance (Dr.Cr) with a dark brown color and honey-like consistency is produced with a % yield of 15% approx. The resulting extract was kept in an amber-colored airtight bottle in a cool, dry location (a refrigerator set to -4 °C) for further studies. Fractionation was accomplished by combining 20 g of Dr.Cr with 100 mL of distilled water (DW) and 100 mL of dichloromethane (DCM), resulting in one DCM layer and another aqueous layer. Both layers were separated out and dried, giving fractions of Dr.Dcm and Dr.Aq, respectively.^{20,21}

2.2. Chemicals. Experiments were conducted using compounds of approx. 99.9% purity. Calcium chloride (CaCl_2), sodium chloride (NaCl), glucose ($\text{C}_6\text{H}_{12}\text{O}_6$), potassium chloride (KCl), sodium bicarbonate (NaHCO_3), potassium dihydrogen phosphate (KH_2PO_4), magnesium sulfate (MgSO_4), magnesium chloride (MgCl_2), sodium dihydrogen phosphate (NaH_2PO_4), and ethyl alcohol ($\text{C}_2\text{H}_5\text{OH}$) were provided by Merck, Deemastadt, (Germany). Acetylene chloride, ethylenediaminetetraacetic acid (EDTA), atropine sulfate, aspirin, carbachol (CCh), phenylephrine (PE), acetylcholine (Ach), cyproheptadine, pyrilamine, verapamil HCl were bought from Sigma Chemical Co., St. Louis, MO. Ammonium hydroxide and sodium hydroxide were provided by BDH Laboratory Supplies, England.

2.3. Animal Housing. For the experimental purpose, albino rabbits (♀/♂, weight: 1.5–2.0 kg), Sprague Dawley rats (♀/♂, weight: 150–250 g), and mice (♀/♂, weight: 20–30 g) were obtained from Animal House, Faculty of Pharmacy, Bahauddin Zakariya University, Multan. Animals were retained under controlled environmental conditions at a temperature of 23 ± 3 °C and 30–70% relative humidity, followed by a light and dark cycle with standard food and ad libitum water. Animals were given unrestrained water access but were denied meals the night before the trial. Rabbits were killed after a blow to the neck, whereas mice and rats were sacrificed via cervical dislocation. All permitted ethical rules specified by “The Institute of Laboratory Animal Resources, Commission on Life Sciences” (NRC,1996) were trailed in the whole research.²²

2.4. Qualitative Phytochemical Detection. Exploratory phytochemical screening of *D. ramosa* crude ethanolic extract (Dr.Cr) was performed to identify secondary metabolites of the plant like cardiac glycosides, flavonoids, saponins, tannins, alkaloids, phenols, and steroids.

2.5. In Silico Approaches. **2.5.1. ADMET Profile and Drug-Likeness.** The previously identified bioactive compounds of *D. ramosa* (gallic acid, quercetin, caffeic acid, vanillic acid, cinnamic acid,²³ iriflophenon glycoside,²⁴ mangiferin, isomangiferin,¹⁹ and verapamil) were evaluated for absorption, distribution, metabolism, excretion, and toxicity (ADMET) in the Quickprop module of Maestro (Schrodinger Suite 2015), SWISS ADME (<http://www.swissadme.ch/>, accessed on: May 28, 2022)²⁵ and PkCSM (<http://biosig.unimelb.edu.au/pkcsm/prediction>, accessed on 28 May 2022)²⁶ to evaluate ADMET and drug-likeness parameters. Several rules, such as (1) Lipinski’s rule of 5, (2) Ghose rule, (3) Veber’s rule, (4) Egan’s rule, and (5) Muegge’s rule, were applied to the target compounds via SWISS ADME to confirm their drug-like properties and to recognize the count of debased parameters. The ADMET properties like water solubility, topological polar surface area, molar refractivity, CaCO_2 cell permeability, volume of distribution, intestinal absorption, unbound fraction,

hepatotoxicity, total renal clearance, and ability to inhibit the P-glycoprotein were also calculated using pkCSM.

2.5.2. Molecular Docking. The previously reported method of Sirous et al.²⁷ was used to perform molecular docking studies for protein and bioactive compounds.

2.5.2.1. Ligand Preparation. The PubChem database (<https://pubchem.ncbi.nlm.nih.gov>, accessed on May 28, 2022) was employed to retrieve two-dimensional (2D) structures of already reported bioactive compounds from *D. ramosa*, and these ligands were modified in the LigPrep module of Maestro (Schrodinger Suite 2018, Schrödinger, Inc. NY) for the ionization, minimization, and optimization of ligands. The Epik tool of this module was used to produce the ionization state of ligands at cellular pH (7.4 ± 0.5), and the OPLS3e force field was applied using the module for minimization as well as optimization of these ligand structures that produce the minimal energy conformers of ligands.

2.5.2.2. Protein Preparation. Maximum-resolution protein X-ray structures for molecular docking were retrieved using the Protein Databank (RCSB PDB) (<https://www.rcsb.org>, accessed on May 28, 2022). These structures were put through the Maestro (Schrodinger Suite 2018, Schrödinger, Inc., New York) Protein Preparation Wizard to add H-atoms to the structure of the protein, remove extra water molecules from the solvents, assign bond orders, create disulfide bridges, fill in the absent side chains, and generate the protonation condition using the Epik tool for protein assemblies for ligands at the cellular level pH (7.4 ± 0.5). Following refining, PROPKA was used at pH 7.0 to improve the protein structures. Using the OPLS3e force field, we carried out restrained minimization for energy and geometry optimization of the protein structure.

2.5.2.3. Receptor Grid Generation. The Receptor Grid Generation module of Maestro defined the active regions of protein structures for molecular docking (Schrodinger Suite 2018). With the use of some already bound protein ligands and existing literature, a cubic grid block for each protein was created. The grid box's dimensions were changed to be 16 Å long. The potential of the receptor's nonpolar components was reduced to 1.0 Å on the van der Waals radius of nonpolar protein atoms with a partial atomic charge cutoff of 0.25 Å.

2.5.2.4. Molecular Docking. The premade ligand structures and protein structures were put via Maestro's Ligand Docking (Glide) module's extra precision (XP) mode (Schrodinger Suite 2018), utilizing a grid file for the receptor that had already been created. A 0.80 Å van der Waals radii scaling factor was changed with a partial charge cutoff of 0.15 Å. Using the VSGB solvation model and the OPLS3e force field, the Prime MM-GBSA module was utilized to analyze the docking results and identify the binding dynamics of ligand molecules with the target protein structure.

2.5.2.5. Inhibition Constant (K_i). The following equation was used for the calculation of the inhibition constant by using the binding free energy of a ligand previously produced by Prime MM-GBSA.

$$dG = -RT(\ln K_i)$$

or

$$K_i = \exp(-dG/RT)$$

where dG = binding free energy of the ligand, R = gas constant ($\text{cal mol}^{-1} \text{K}^{-1}$), R = gas constant ($\text{cal mol}^{-1} \text{K}^{-1}$), and T = normal ambient temperature (298 K).

2.6. In Vitro Assays. Isolated tissue responses in physiological conditions were noted by Bio science isometric and isotonic force displacement transducers attached to the Power lab data acquisition system (AD Instruments, Bella Vista, NSW, Australia), displaying results on a computer having lab chart software (version 6) installed. The effect of the test substance was measured as the percentage change in the response of tissue recorded after the administration of test doses.^{28,29}

2.6.1. Preparation of Isolated Jejunum. Rabbits were sacrificed to obtain the jejunum. Mesenteries were removed from the tissue, and jejunal segments of 2–3 cm lengths were prepared and suspended in priorly filled 15 mL of tissue organ baths having carbogen (5% CO_2 and 95% O_2) bubbling through Tyrode's solution having NaCl (136.9 mM), NaHCO_3 (11.90 mM), MgCl_2 (1.05 mM), KCl (2.68 mM), glucose (5.55 mM), CaCl_2 (1.8 mM), and NaH_2PO_4 (0.42 mM) and maintained at 37 °C. All tissues were permitted to equilibrate for around 30 min, before being stabilized with a 3 min interval of Ach (1 μM) to get a persistent tissue response prior to the inclusion of any drug solution or plant extract. Before starting the experiment, the isolated tissue organ bath fluid was replaced with fresh Tyrode solution, and spontaneous rhythmical contractions were noted prior to testing the drug. The possible spasmolytic or spasmogenic response of Dr.Cr was studied on equilibrated jejunal preparation by cumulative addition of different doses of Dr.Cr. A dose–response curve was created, and the response was reported as a percentage of the control contractions. For determination of CCB activity, 80 mM KCl was used to precontract the jejunum.^{30,31}

To further illustrate the Ca^{++} channel antagonistic action, isolated rabbit jejunum tissues were stabilized in regular Tyrode solutions, that solution was subsequently replaced with calcium-free Tyrode solution containing 0.1 mM EDTA (chelating agent), for around 30 min. This solution was then replaced with Ca^{++} -free and K^{+} -rich Tyrode solution having NaCl (91.0 mM), NaHCO_3 (11.89 mM), $\text{C}_6\text{H}_{12}\text{O}_6$ (5.6 mM), KCl (50.1 mM), Na_2HPO_4 (0.43 mM), EDTA (0.12 mM), and MgCl_2 (2.0 mM) for about 30 min to get stability. The control of concentration–response curves (CRCs) of Ca^{++} was created by applying Ca^{++} concentration in a cumulative way. A gradual increase in the contraction of jejunal tissue indicates the dependency of the contractile response of smooth muscles on extracellular calcium.^{28,31}

After two cycles, superimposable curves were attained, and tissues were then washed and given time to stabilize in the presence of various dose concentrations of Dr.Cr, and CRCs were recreated after incubation times of 50 ± 10 min and compared with control curves.³¹

2.6.2. Preparation of Isolated Trachea. The trachea was divided into 2–3 mm rings (2–3 cartilaginous rings) after being dissected. The tracheal rings were cut longitudinally on the side opposing smooth muscle, creating a strip having smooth muscles sandwiched between cartilaginous sides of the strip. Following that, the tissues were fixed in an isolated tissue organ bath having carbogen (5% CO_2 and 95% O_2) bubbling through Krebs solution having NaCl (118.2 mM), NaHCO_3 (25.0 mM), CaCl_2 (2.5 mM), KCl (4.7 mM), MgSO_4 (1.2 mM), and glucose (11.7 mM) and maintained at 37 °C. A preload stress of 1 g was given to tissues, and the tissues were permitted to equilibrate for 50 ± 10 min prior to any experiment.

Table 1. ADMET Profiling of Bioactive Compounds of *Dryopteris ramosa*^a

parameters	quercetin	verapamil	caffeic acid	vanillic acid	cinnamic acid	iriflophenon glycoside	gallic acid	mangiferin	isomangiferin
mol_MW	302.24	454.608	180.16	168.149	148.161	408.361	170.121	422.345	422.345
QPlogPoct	18.568	19.073	12.439	10.056	8.672	27.834	13.33	30.016	29.413
QPlogPw	14.428	6.393	9.878	8.113	5.688	22.572	12.015	25.851	25.62
QPlogPo/w	0.367	3.856	0.545	1.042	1.897	−0.841	−0.579	−1.702	−1.811
QPlogS	−2.909	−5.766	−1.293	−1.393	−1.616	−2.491	−0.68	−2.505	−2.252
QPlogHERG	−5.109	−6.792	−2.169	−1.601	−2.348	−5.16	−1.401	−5.006	−4.429
QPPCaco	18.199	848.556	22.354	77.585	206.809	5.182	10.235	3.618	3.058
QPlogBB	−2.419	−0.444	−1.546	−0.883	−0.548	−3.439	−1.652	−3.467	−3.329
QPPMDCK	6.511	458.292	10.343	39.698	114.551	1.675	4.446	1.136	0.947
QPlogKp	−5.544	−2.642	−4.499	−3.787	−2.54	−6.18	−5.468	−6.774	−7.032
QPlogKhsa	−0.343	0.847	−0.804	−0.747	−0.518	−0.789	−0.987	−0.899	−0.851
CNS permeability	−2	1	−2	−1	−1	−2	−2	−2	−2
percent human oral absorption	51.649	100	54.287	66.869	79.497	21.85	41.634	1.055	0
GIT absorption	high	high	high	high	high	low	high	low	low
intestinal absorption (human)	77.207	92.836	69.407	78.152	94.833	46.248	43.374	46.135	48.512
bioavailability score	0.55	0.55	0.56	0.85	0.85	0.55	0.56	0.17	0.17
BBB permeant	no	yes	no	no	yes	no	no	no	no
CYP1A2 antagonist	yes	no	no	no	no	no	no	no	no
CYP2C19 antagonist	no	no	no	no	no	no	no	no	no
CYP2C9 antagonist	no	no	no	no	no	no	no	no	no
CYP2D6 antagonist	yes	yes	no	no	no	no	no	no	no
CYP3A4 antagonist	yes	yes	no	no	no	no	yes	no	no
P-glycoprotein substrate	yes	yes	no	no	no	yes	no	yes	yes
P-glycoprotein I blocker	no	yes	no	no	no	no	no	no	no
P-glycoprotein II blocker	no	yes	no	no	no	no	no	no	no
Lipinski violations	0	0	0	0	0	1	0	2	2
Ghose violations	0	2	0	0	2	1	2	1	1
Weber violations	0	1	0	0	0	1	0	1	1
Egan violations	0	0	0	0	0	1	0	1	1
Muegge violations	0	0	1	1	1	2	1	3	3

^aMW: molecular weights of the molecules in Dalton, i.e., 130.0–500.0; QPlogPo/w: the forecast lipophilicity partition coefficient of octanol/water, ranging from 2 to 6.5; QPlogS: aqueous solubility predicted: −6.5 to 0.5; QPlogHERG: IC₅₀ for HERG K⁺ channel blockade predicted > 5; QPPCaco: foreseeable apparent Caco-2 cell, a model for the gut–blood barrier, with weak permeability if < 25 and large permeability if > 500; QPlogBB: brain/blood partition coefficient predicted, −3 to 1.2; QPPMDCK: blood–brain barrier nonactive transport predicted by apparent MDCK cell permeability in nm/sec with < 25 bad and > 500 fantastic predictions; QPlogKp: skin permeability predicted, −8.0 to −1.0 cm/s; QPlogKhsa: anticipated serum albumin binding of human, −1.5 to 1.5; and CNS permeability: greater than −2 able to penetrate.

High K (KCl, 80 mM) and carbachol (1 μ M) were utilized in order to achieve a persistent agonistic response for the purpose of determining the broncho-relaxant action of Dr.Cr. A sustained reaction is attained after 45 min, at which point the extract was applied cumulatively to attain a concentration-dependent inhibitory response of the extract. Isometric tissue responses were captured using Bio science transducers.³¹

2.6.3. Preparation of Isolated Aorta. To examine the impact of the plant extract on vascular resistance, the descending thoracic portion of the aorta was cut into 2–3 mm broad rings, placed in isolated tissue organ baths individually, and given 50 \pm 10 min to equilibrate. At the beginning of the experiment and throughout, a preload stress of 2 g was applied. Each tissue organ bath had carbogen (5% CO₂ and 95% O₂) bubbling through Krebs solution having NaCl (118.2 mM), NaHCO₃ (25.0 mM), CaCl₂ (2.5 mM), KCl (4.7 mM), MgSO₄ (1.2 mM), and glucose (11.7 mM) and was kept at a temperature of 37 $^{\circ}$ C. To clarify any potential vasorelaxant or vasoconstrictor effects, Dr.Cr was added cumulatively to a baseline resting state.³² Prazocin, losartan, and cyproheptadine were used as pretreatments on isolated aortic rings in order to clarify the mechanism of contraction.³³

2.7. In Vivo Activity. 2.7.1. Anti-Inflammatory Activity.

The previously described carrageenan-induced rat paw edema assay was used to test Dr.Cr for its possible anti-inflammatory effect, after minor adjustments.³⁴ 20 Wistar albino rats (\varnothing , δ) weighing between 180 and 220 g were divided into four groups, i.e., Group I: control group (0.9% saline), Group II: drug group (aspirin 0.01 g/kg), and Groups III and IV: test groups of Dr.Cr doses (0.1 and 0.2 g/kg, respectively). Edema was induced by inoculating 1% carrageenan into the sub-planter area of the right hind paw after 55 \pm 5 min of dose administration (IP) of Dr.Cr, and the extent of the edema was measured up to 4 h later using a plethysmometer (UGO Basile, Italy). Results were expressed as the percentage inhibition of edema.

2.7.2. Castor Oil-Induced Diarrhea. Twenty mice of either gender (\varnothing , δ) were randomly divided into four groups having five animals in each group to test the antidiarrheal effects of the Dr.Cr extract. Before the experiment, all of the groups were kept in separate cages with free access to water; however, food was withheld for the night prior to testing. Group I labeled as the negative control group was orally given 0.9% saline (NS) at a dose of 10 mL/kg. Loperamide (10 mg/kg) was given orally to Group II, which was designated as the positive control

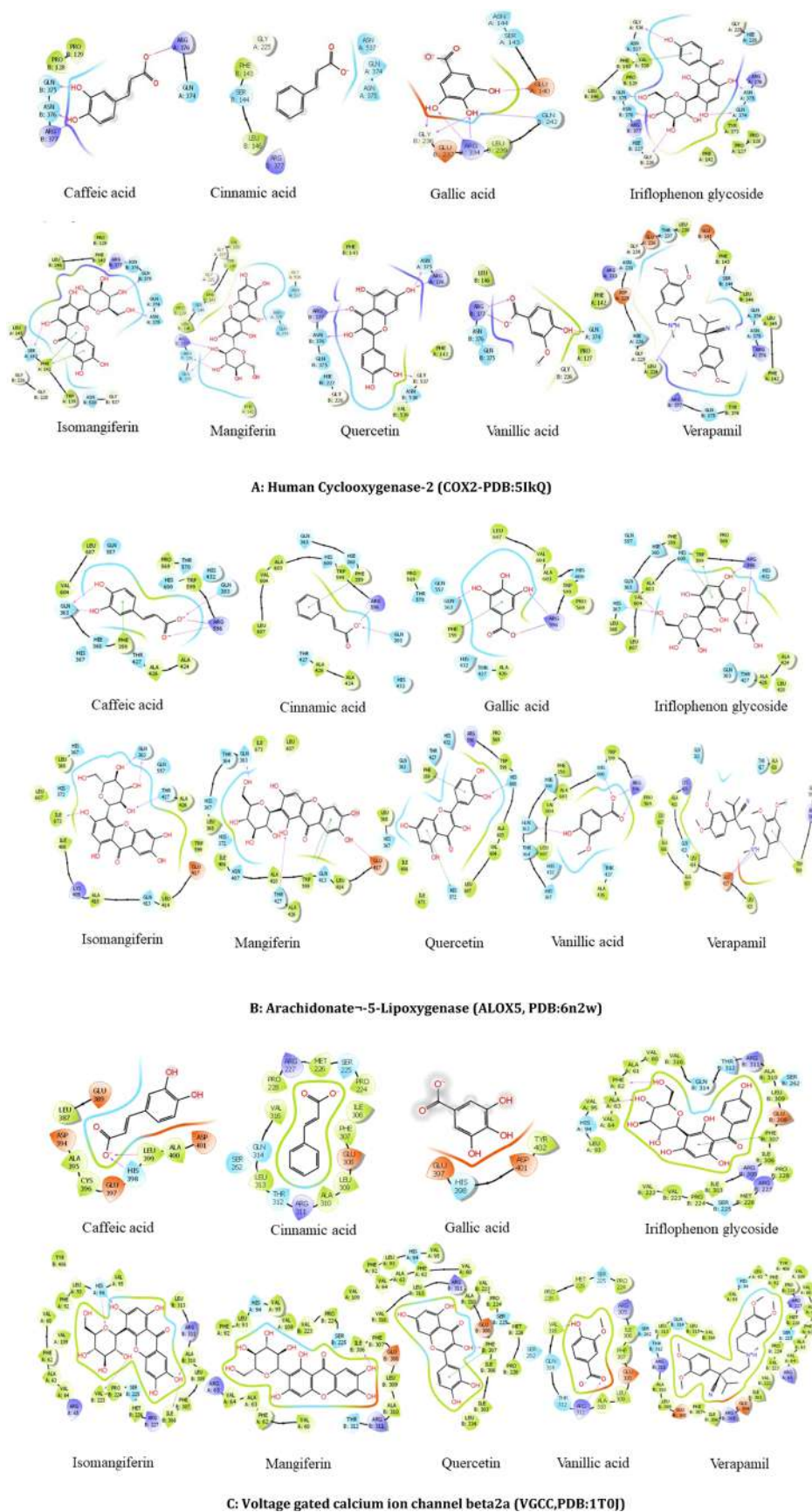


Figure 1. continued

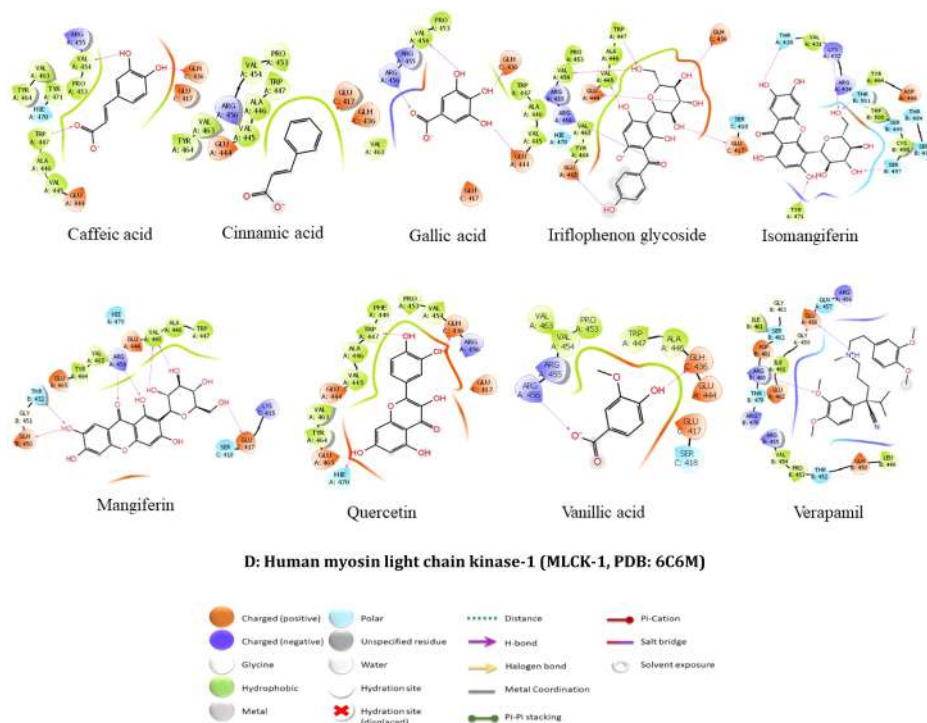


Figure 1. Two-dimensional protein/ligand interaction between bioactive compounds (caffeic acid, cinnamic acid, gallic acid, mangiferin, quercetin, vanillic acid, and verapamil) and proteins: (A) human cyclooxygenase-2 (COX2-PDB:5IkQ), (B) arachidonate-5-lipoxygenase (ALOX5, PDB:6n2w), (C) voltage-gated calcium ion channel β 2a (VGCC, PDB:1T0J), and (D) human myosin light chain kinase-1 (MLCK-1, PDB: 6C6M).

group. Groups III and IV were given Dr.Cr doses of 0.2 and 0.4 g/kg, respectively. 30 min after the administration of treatment, all groups were orally administered 10 mL/kg castor oil to induce diarrhea and monitored for wet diarrheal spots for up to 4 h.²⁸ The mean amount of feces for each group was determined and the outcomes were presented as %age inhibition.

$$[(D_{cn} - D_t)/D_{cn}] \times 100$$

where D_{cn} is the mean defecation of the control group and D_t is the mean defecation of the test group.

2.8. Statistical Analysis. All of the results are expressed as mean \pm (S.E.M). "GraphPad Prism (GraphPad, San Diego, California: <http://www.graphpad.com>)" was utilized to obtain the median effective concentrations (EC_{50} value) with a 95% (CI). In the instance of the in vivo study, statistical analysis was one-way ANOVA and two-way ANOVA, and it was further trailed by Dunnett's test, where a probability of ($p < 0.05$)* was deemed significant statistically.³⁵

3. RESULTS AND DISCUSSION

Natural medicine has seen a significant rise in popularity over the last two decades.³⁶ Ethnopharmacological methods offer hints in the search for bioactive substances.²⁴ *Dryopteris ramosa* has many traditional uses including its use in GIT disorders and also as a febrifuge. Therefore, this study was designed to validate the potential mechanisms of *D. ramosa* in digestive and respiratory systems by an integrated strategy of molecular docking of *D. ramosa* bioactive compounds and its validation through different in vitro and in vivo experimental models.

3.1. Pilot Phytochemical Screening. Preliminary phytochemical analysis of ethanolic extract (Dr.Cr) showed flavonoids, glycosides, saponins, phenols, tannins, and steroids

amid secondary bioactive metabolites of the plant. Flavonoids have been shown to have antispasmodic and calcium channel-blocking properties.^{37,38}

3.2. In Silico Studies. **3.2.1. ADMET Analysis.** A literature review shows that several bioactive compounds have been extracted from *D. ramosa* including gallic acid, quercetin, caffeic acid, vanillic acid, cinnamic acid, iriflophenon glycoside, mangiferin, and isomangiferin.^{19,23,24} These compounds were subjected to an ADMET analysis utilizing the Schrödinger QikProp module,³⁹ SWISS ADME, and PkCSM (Table 1). The aqueous solubility, octanol/water partition coefficient, and a number of other physical characteristics may all be predicted. Cell permeability, the brain/blood partition coefficient, QPlogKhsa to forecast binding affinity to serum albumin of humans, and QPlogHERG to measure HERG K⁺ channel blockade and human oral absorption percentage were determined.

3.2.2. Molecular Docking. Docking seeks to appropriately assess the strength of binding by accurately predicting a ligand's shape inside the confines of a binding pocket.⁴⁰ The bioactive compounds iriflophenon glycoside, isomangiferin, mangiferin, quercetin, gallic acid, caffeic acid, vanillic acid, cinnamic acid, and verapamil were docked with selected proteins, human cyclooxygenase-2 (COX2-PDB: 5IkQ), arachidonate-5-lipoxygenase (ALOX5, PDB: 6n2w), voltage-gated calcium ion channel β 2a (VGCC, PDB: 1T0J), and human myosin light chain kinase-1 (MLCK-1, PDB: 6C6M), to check their affinity with binding sites of these proteins for the possible mechanism of action. According to earlier research, quercetin and caffeic acid may have antispasmodic effects,^{41,42} and quercetin is reported to be a regulator of the tone of GIT,⁴³ thus leading to the presence of antispasmodic as well as antidiarrheal effects of the plant. Our results showed

Table 2. Docking Score and Binding Energies of Bioactive Compounds with Human Cyclooxygenase-2, Arachidonate-5-Lipoxygenase, Voltage-Gated Calcium Ion Channel β 2a, and Human Myosin Light Chain Kinase-1^a

compounds	docking score	glide energy	dG bind	log pK _i	dG Coulomb	dG covalent	dG H-bond	dG lipo	dG solv GB	dG vdW	H-bond	other bonds
Human Cyclooxygenase-2 (COX2-PDB: 5LQO)												
inflophenon glycoside	-9.77	-47.43	-37.8	-13.19	-33.69	15.91	-4.35	-12.54	44.69	-44.92	conventional H-bond: Val538 (2.77 Å), Arg377 (2.15 Å), Gly226 (2.24 Å), Asn376 (1.69 Å), Gln375 (1.72 Å), Gln374 (1.97 Å), Asn375 (1.83 Å), Gly536 (1.92 Å), carbon H-bond: Pro129 (2.75 Å), Arg377 (2.61 Å), Asn376 (2.67 Å), Asn376 (3.04 Å), π -donor hydrogen bond: Asn375 (2.90 Å)	π -cation; π -donor hydrogen bond: Arg376 (4.18 Å)
isomangiferin	-8.85	-50.25	-38.57	-13.52	-34.55	4.97	-3.05	-12.18	53.78	-44.74	conventional H-bond: Arg377 (2.87 Å), Arg377 (2.08 Å), Gln375 (2.81 Å), Gln375 (1.82 Å), Asn375 (1.98 Å), Ser143 (2.08 Å), carbon H-bond: Gly226 (2.63 Å), (2.88 Å), Gln375 (2.59 Å)	π -cation: Arg376 (4.97 Å), π - π T-shaped: Phe142 (4.63 Å), π -alkyl: Leu145 (5.25 Å)
mangiferin	-8.03	-48.09	-26.53	-8.29	-23.06	3.41	-3.29	-13.24	55.81	-43.45	conventional H-bond: Val228 (2.66 Å), Asn375 (1.76 Å), Arg377 (2.05 Å), Arg377 (3.00 Å), Gln375 (2.46 Å), Asn376 (1.82 Å), (1.93 Å), carbon H-bond: Gln374 (2.46 Å), Gln375 (2.79 Å)	
quercetin	-8	-45.98	-44.83	-16.24	-25.9	2.58	-3.39	-7.5	31.3	-36.8	conventional H-bond: Arg376 (2.46 Å), Arg376 (2.93 Å), Arg377 (2.26 Å), Val539 (2.81 Å), Asn376 (1.99 Å), (1.82 Å), Asn375 (2.08 Å), Gly537 (1.82 Å), π -donor hydrogen bond: Asn376 (2.80 Å)	
gallic acid	-6.88	-31.09	-9.38	-0.84	-53.63	5.2	-4.3	-5.38	64.83	-15.34	conventional H-bond: Gln242 (2.04 Å), Gln242 (2.57 Å), Arg334 (2.02 Å), Arg334 (1.86 Å), Gly236 (1.85 Å), Gly236 (1.75 Å), Glu140 (1.95 Å), carbon H-bond: Ser143 (2.71 Å), Asn144 (2.91 Å), Leu239 (2.68 Å), π -lone pair: Glu237 (2.90 Å)	
caffeic acid	-6.05	-26.07	-14.17	-2.92	-49.11	7.63	-3.97	-6.03	58.65	-19.9	conventional H-bond: Arg376 (2.13 Å), Arg377 (2.03 Å), Gln375 (1.73 Å), Asn376 (1.70 Å)	electrostatic attractive charge: Arg376 (3.38 Å)
vanillic acid	-5.46	-24.62	-14.42	-3.03	-49.45	2.98	-3.01	-5.97	64.34	-21.31	conventional H-bond: Arg377 (2.11 Å), Arg377 (2.11 Å), Gln374 (1.91 Å), carbon H-bond: Gly226 (2.97 Å)	electrostatic attractive charge: Arg377 (3.47 Å)
verapamil	-4.31	-49.04	-27.11	-8.54	53.87	6.01	-1.45	-22.1	-2.17	-58.64	conventional H-bond: Arg376 (2.78 Å), Leu224 (2.08 Å), carbon H-bond: Ser144 (2.32 Å), Gln375 (2.76 Å), Tyr374 (2.75 Å), Gln374 (2.48 Å), Tyr374 (2.56 Å), Gly235 (2.57 Å), Gln236 (2.79 Å), Asp229 (2.68 Å), Glu141 (2.73 Å), Glu141 (2.70 Å)	alkyl: Pro129 (5.04 Å), Pro127 (4.94 Å), Leu238 (4.61 Å), π -alkyl: Phe142 (4.87 Å), Phe143 (5.18 Å)
cinnamic acid	-2.15	-16.3	0.79	3.57	-24.01	0.29	-0.24	-9.29	59.7	-24.34	conventional H-bond: Asn375 (2.64 Å), carbon H-bond: Gln374 (2.88 Å)	π - π T-shaped: Phe143 (4.50 Å)

Table 2. continued

compounds	docking score	glide energy	dG bind	log pK _i	dG Coulomb	dG covalent	dG H-bond	dG lipo	dG solv GB	dG vdW	H-bond	other bonds
isomangiferin	-8.55	-49.99	-47.84	-17.55	-35.88	3.77	Arachidonate-5-lipoxygenase (ALOX5, PDB: 6n2w) -2.92	-13.67	41.82	-39.95	conventional H-bond: Thr427 (2.27 Å), Gln363 (1.79 Å), Gln363 (1.65 Å), Ile673 (2.20 Å), (1.87 Å), carbon H-bond: Leu368 (2.61 Å), His372 (2.79 Å)	π - σ : Trp599 (2.50 Å), π - π T-shaped: Trp599 (5.89 Å), Trp599 (4.96 Å)
mangiferin	-8.03	-41.78	-30.3	-9.93	-19.03	5.51	-3.04	-11.85	36.28	-34.25	conventional H-bond: His367 (2.19 Å), Thr427 (1.80 Å), Thr427 (2.99 Å), Gln363 (1.88 Å), (1.56 Å), (1.84 Å), Glu417 (2.05 Å), carbon H-bond: (2.57 Å), carbon H-bond: Gln363 (3.07 Å)	
iriflophenon glycoside	-7.03	-37.37	-32.17	-10.74	-29.05	6.29	-2.64	-13.17	43.47	-33.02	conventional H-bond: His367 (2.09 Å), Arg596 (2.77 Å), Gln363 (1.76 Å), (1.63 Å), (1.79 Å), carbon H-bond: Thr427 (3.06 Å), His432 (2.45 Å), Gln363 (2.77 Å), Gln363 (2.99 Å)	π -cation: Arg596 (2.79 Å), π - π T-shaped: Phe359 (5.33 Å), Trp599 (5.41 Å), π -alkyl: Ala603 (5.43 Å), Ala426 (3.67 Å)
caffeic acid	-5.19	-25.45	-16.09	-3.76	48.9	4.99	-2.7	-10.6	-27.91	-26.83	conventional H-bond: Gln303 (2.19 Å), His360 (2.76 Å), Arg596 (2.49 Å), Gln363 (1.77 Å), Gln363 (1.99 Å)	electrostatic attractive charge: Arg596 (4.33 Å), π - π T-shaped: Phe359 (5.19 Å), Trp599 (5.89 Å)
verapamil	-5.1	-38.67	-49.39	-18.22	-28.27	6.15	-1.21	-25.17	43.96	-40.74	conventional H-bond: Thr427 (2.15 Å), carbon H-bond: Thr427 (3.04 Å), Arg596 (2.73 Å), Ala603 (2.41 Å), Glu417 (2.67 Å), Ala603 (2.65 Å), Gly595 (2.88 Å)	salt bridge; electrostatic attractive charge: Glu417 (2.12 Å), π -anion: Glu417 (3.86 Å), π - π stacked: Trp599 (4.68 Å), Trp599 (3.63 Å), alkyl: Ala426 (3.87 Å), Ala603 (4.48 Å), Ala603 (4.30 Å), Ala606 (3.92 Å), Leu607 (4.81 Å), Leu607 (3.93 Å), Leu420 (5.30 Å), Arg596 (4.46 Å), π -alkyl: Trp599 (3.95 Å), Trp599 (4.79 Å), Ala603 (4.64 Å)
gallic acid	-4.97	-24.08	-23.4	-6.93	53.56	4.12	-2.18	-9.65	-42.83	-24.11	conventional H-bond: Arg596 (2.15 Å), Gln363 (1.88 Å), carbon H-bond: His432 (2.66 Å), π - π T-shaped: Phe359 (4.88 Å)	electrostatic attractive charge: Arg596 (4.30 Å), π - π T-shaped: Phe359 (4.88 Å)
vanillic acid	-4.97	-24.2	-11.11	-1.60	32.67	4.12	-3.44	-9.41	-16.03	-16.78	conventional H-bond: Arg596 (2.65 Å), Arg596 (2.10 Å), His600 (1.98 Å), Gln363 (2.09 Å), carbon H-bond: His600 (2.68 Å), π -alkyl: His432 (4.44 Å)	electrostatic attractive charge: Arg596 (3.94 Å), π -alkyl: His432 (4.44 Å)
quercetin	-4.41	-43.93	-32.62	-10.94	-25.6	3.3	-2.08	-9.68	44.25	-38.28	conventional H-bond: His600 (2.20 Å), Ile673 (2.95 Å), carbon H-bond: Leu368 (2.68 Å)	π -donor hydrogen bond: His372 (2.88 Å), π - π stacked: His367 (4.57 Å), π - π T-shaped: His372 (5.32 Å), π -alkyl: Leu607 (4.80 Å), Leu607 (5.16 Å)
cinnamic acid	-2.96	-19.93	-7.72	-0.12	65.92	3.66	-1.49	-10.86	-37.42	-25.35	conventional H-bond: Gln303 (2.34 Å), His360 (2.83 Å)	electrostatic attractive charge: Arg596 (4.23 Å), π - π T-shaped: Phe359 (5.17 Å), Trp599 (5.66 Å)
isomangiferin	-8.63	-51.7	-47.04	-17.20	-36.23	5.44	-4.03	-8.15	32.25	-35.3	Voltage-Gated Calcium Ion Channel β 2a (VGCC β 2a, PDB: 1IT0)	
											conventional H-bond: Val60 (3.03 Å), His94 (2.61 Å), His94 (1.58 Å), Ala310 (2.93 Å), carbon H-bond: Ala63 (3.00 Å), Pro224 (1.52 Å), Val223 (2.65 Å), Leu93 (1.31 Å)	π -alkyl: Val60 (5.40 Å), Ala63 (4.95 Å), Pro224 (5.23 Å), Met226 (5.30 Å), Ala63 (3.84 Å), Met226 (5.45 Å), Ala310 (5.46 Å)
iriflophenon glycoside	-6.28	-46.15	-29.63	-9.64	-19.9	10.16	-2.84	-9.19	32.99	-39.62	conventional H-bond: Val95 (2.47 Å), Ala63 (2.49 Å), Phe62 (2.01 Å), Val95 (1.96 Å), (1.90 Å), carbon H-bond: Phe62 (2.80 Å), Pro228 (2.27 Å), (2.40 Å)	π -alkyl: Ala310 (3.88 Å), Leu309 (5.03 Å)
quercetin	-5.44	-37.71	-34.94	-11.95	-14.04	3.66	-2.4	-6.87	14.04	-28.08	conventional H-bond: Phe307 (2.31 Å), Ile303 (2.94 Å), carbon H-bond: Arg311 (2.31 Å)	π -alkyl: Val60 (4.63 Å), Ala63 (3.67 Å), Ala310 (4.43 Å)

Table 2. continued

compounds	docking score	glide energy	dG bind	log pK _i	dG Coulomb	dG covalent	dG H-bond	dG lipo	dG solv GB	dG vdW	H-bond	other bonds
Voltage-Gated Calcium Ion Channel $\beta 2a$ (VGCC, PDB: 1T0J)												
mangiferin	-5.23	-39.26	-33.19	-11.19	-36.87	2.26	-3.44	-9.58	47.29	-30.39	conventional H-bond: Phe63 (2.82 Å), Leu93 (2.21 Å), (1.60 Å), (1.75 Å), carbon H-bond: Arg311 (2.34 Å), Leu93 (2.89 Å)	π - π stacked: Phe307 (5.69 Å), amide- π stacked: Ala61c; O; Phe62 (4.05 Å), π -alkyl: Pro224 (5.12 Å), Arg311 (4.34 Å), Val60 (4.59 Å), Ala63 (4.22 Å), Ala310 (4.75 Å), Arg311 (5.30 Å), Arg311 (4.46 Å) π -alkyl: leu309(4.09 Å)
vanillic acid	-4.14	-18.19	-14.38	-3.02	34.15	3.36	-1.25	-8.89	-19.44	-21.75	conventional H-bond: B-Arg311; H-vanillic acid: O4arg311 (2.71 Å), B-Val316: H-vanillic acid: O2val316 (2.77 Å), vanillic acid: H19-B:Met226: Omet226 (2.84 Å), carbon H-bond: vanillic acid: H16-B:Met226; Omet226 (2.69 Å), vanillic acid: H17-B:lle306; Oile306 (1.84 Å)	
verapamil	-3.94	-47.44	-46.37	-16.91	-18.55	1.36	-0.62	-15.85	34.96	-46.63	conventional H-bond: Leu93 (2.46 Å), Val223 (2.29 Å), carbon H-bond: Phe92 (2.84 Å), Ala61 (2.86 Å), Ala61 (2.80 Å), Ser225 (2.17 Å), Ser225 (2.58 Å), Gln314 (1.77 Å), Ser225 (2.12 Å)	π -lone pair: Leu93 (2.97 Å), Phe307 (2.86 Å), amide- π stacked: Val64c; O; Arg65 (3.97 Å), Pro224c; O; Ser225 (4.29 Å), alkyl: Ala63 (3.08 Å), Ala63 (4.23 Å), Ala310 (3.66 Å), Met226 (5.04 Å), Val60 (4.19 Å), Val109 (5.29 Å), Val109 (4.45 Å), Val223 (5.40 Å), Arg227 (4.80 Å), π -alkyl: Phe92 (3.63 Å), Phe307 (4.64 Å), Pro224 (5.13 Å), Leu309 (5.44 Å), Val316 (4.44 Å), Val64 (5.08 Å)
gallic acid	-3.85	-20.92	-10.52	-1.34	-4.84	0.32	-2.98	-2.96	11.89	-11.92	conventional H-bond: His398 (3.08)	
caffeic acid	-2.74	-20.38	-19.27	-5.14	-11.43	0.42	-2.21	-7.54	19.21	-16.63	conventional H-bond: His398 (2.12 Å), Leu399 (2.40 Å), carbon H-bond: Ala395 (1.84 Å)	
cinnamic acid	-2.45	-14.99	-10.23	-1.21	25.29	3.8	-0.96	-9.22	-7.44	-20.32	carbon H-bond: Pro228 (2.01 Å), Phe307 (1.93 Å)	π -anion: Phe307 (4.15 Å), π -alkyl: Leu309 (4.62 Å)
Human Myosin Light Chain Kinase-1 (MLCK-1, PDB: 6C6M)												
isomangiferin	-8.41	-43.547	-35.77	-12.31	-32.43	5.3	-4.63	-7.34	29.91	-26.2	conventional H-bond: Lys432 (2.30 Å), Tyr464 (1.85 Å), Tyr471 (2.59 Å), Tyr471 (2.02 Å), Ser486 (2.99 Å), Ser497 (2.02 Å), Ser499 (3.09 Å), Ser497 (2.84 Å), (1.88 Å), Thr430 (2.80 Å), carbon H-bond: Thr430 (3.03 Å), Ser497 (2.68 Å), (2.56 Å), Asp466 (2.61 Å)	π -alkyl: Lys432 (4.02 Å), Lys432 (3.96 Å)
inflophenon glycoside	-7.549	-50.881	-0.91	2.83	-110.98	12.84	-5.87	-8.07	137.09	-25.3	conventional H-bond: Trp447 (1.92 Å), Arg456 (2.23 Å), Glu417 (1.99 Å), Glu444 (1.82 Å), Glu436 (2.17 Å), Trp447 (2.87 Å), Val454 (2.25 Å), (1.79 Å), Val445 (1.71 Å), Glu465 (2.32 Å), carbon H-bond: Trp447 (2.91 Å), Trp447 (2.64 Å), Tyr464 (2.81 Å), Glu444 (2.63 Å), Glu417 (2.46 Å), Val454 (2.39 Å)	electrostatic attractive charge: Arg456 (5.58 Å), π -cation: Arg456 (4.31 Å), π -Alkyl: Val463 (4.81 Å)
mangiferin	-6.916	-47.548	-40.48	-14.35	-49.13	7.44	-4.62	-7.75	38.49	-24.58	conventional H-bond: Arg456 (2.04 Å), Arg456 (2.61 Å), Arg456 (2.29 Å), Thr452 (2.09 Å), Val445 (1.60 Å), Val445 (1.70 Å), Glu417 (1.96 Å), (1.53 Å), (1.73 Å), Glu450 (1.67 Å), carbon H-bond: Glu444 (2.70 Å), Glu417 (2.65 Å), Glu417 (2.95 Å), π -donor hydrogen bond: Glu465 (3.02 Å)	
gallic acid	-6.684	-24.759	-10.71	-1.42	-26.28	5.23	-3.19	-6.94	38.98	-18.51	electrostatic attractive charge: Arg456 (3.32 Å), conventional H-bond: Arg456 (2.25 Å)	π -alkyl: Ala446 (5.07 Å), Val463 (5.30 Å)

Table 2. continued

compounds	docking score	glide energy	dG bind	log pK _i	dG Coulomb	dG covalent	dG H-bond	dG lipo	dG solv GB	dG vdW	H-bond	other bonds
Voltage-Gated Calcium Ion Channel β 2a (VGCC, PDB: 1T0J)												
quercetin	-6.39	-37.974	-40.43	-14.33	-42.57	5.48	-2.44	-9.45	34.41	-24.56	Glu436 (2.40 Å), Val454 (1.80 Å), Glu444 (1.91 Å), carbon H-bond: Arg456 (3.08 Å), Arg456 (2.56 Å) conventional H-bond: His470 (1.87 Å), Glu436 (1.61 Å), Trp447 (1.57 Å), π -donor hydrogen bond: Trp447 (2.98 Å)	π -anion: Glu444 (4.99 Å), π -alkyl: Val463 (4.81 Å), Val463 (5.22 Å), Ala446 (4.24 Å), Val463 (5.37 Å)
vanillic acid	-5.176	-22.344	-13.52	-2.64	-20.73	2.8	-1.86	-8.14	31.5	-17.08	conventional H-bond: Glu436 (1.66 Å), carbon H-bond: Arg456 (2.79 Å), Trp447 (2.48 Å), Trp447 (2.62 Å), (2.36 Å), Val454 (2.55 Å)	salt bridge; electrostatic attractive charge: Arg456 (2.10 Å), electrostatic attractive charge: Lys415 (4.90 Å), alkyl: Pro453 (5.43 Å), π -alkyl: Ala446 (5.14 Å)
caffeic acid	-5.16	-29.551	-17.44	-4.34	-6.08	2.14	-1.8	-10.31	28.3	-29.66	conventional H-bond: Trp447 (2.43 Å), Val454 (1.86 Å), Glu436 (1.85 Å), π -donor hydrogen bond: Trp447 (3.14 Å)	electrostatic attractive charge: Arg456 (4.91 Å), π -alkyl: Ala446 (4.10 Å), Val463 (5.35 Å)
cinnamic acid	-2.407	-22.11	-17.26	-4.27	-0.96	0.64	-0.13	-11.11	19.57	-25.25	π -donor hydrogen bond: Trp447 (2.82 Å)	salt bridge; electrostatic attractive charge arg: 456 (3.25 Å), π -alkyl: Ala446 (4.12 Å), Val463 (5.46 Å)
verapamil	-2.313	-44.76	-36.37	-12.57	4.36	2.44	-1.48	-14.93	14.51	-40.84	conventional H-bond: Arg480 (2.48 Å), Arg480 (2.44 Å), Glu458 (2.78 Å), carbon H-bond: Arg480 (2.68 Å), Glu457 (2.67 Å), Glu458 (2.62 Å), Ser482 (2.46 Å), Glu457 (2.51 Å), Glu458 (2.74 Å), Asp481 (2.70 Å), Asp481 (2.73 Å), (2.51 Å), Pro453 (2.77 Å), Glu458 (2.65 Å)	alkyl: Val454 (4.29 Å), Arg480 (4.49 Å), π -alkyl: Leu449 (4.37 Å)

^adG binding: binding free energy, Log pK_i: logarithmic of inhibition constant (K_i), dG Coulomb: Coulomb binding energy, dG H-bond: hydrogen binding energy, dG lipophilic: lipophilic binding energy, dG solv GB: generalized born electrostatic solvation energy, dG vdW: van der Waals forces energy; all these energies contribute to binding free energy (dG binding).

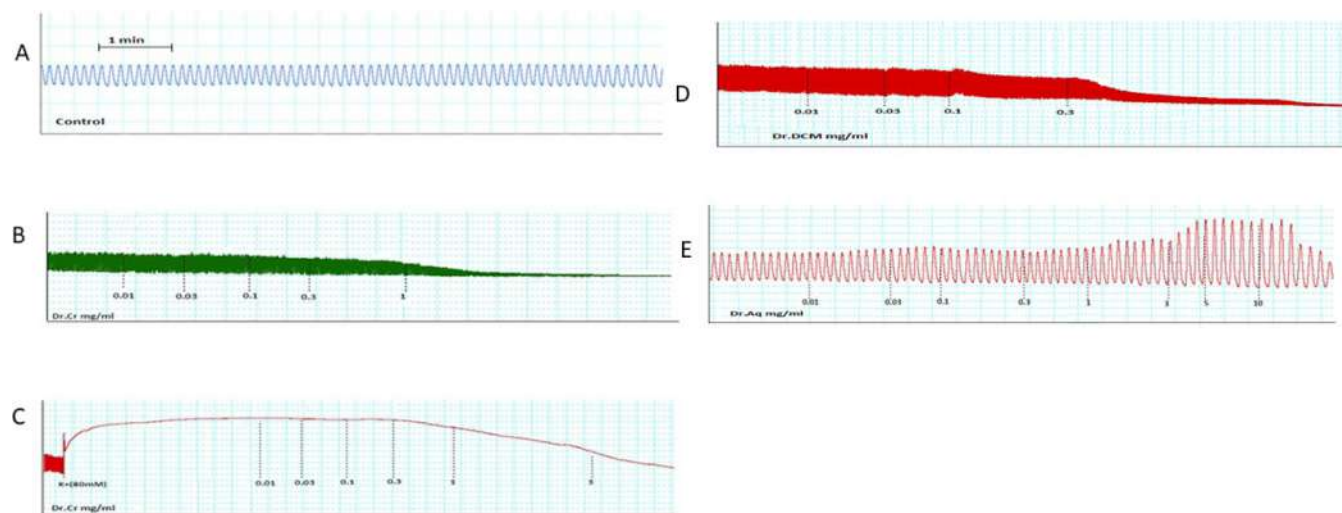


Figure 2. (A) Spontaneously contracting isolated jejunum tissue preparation. Concentration-dependent response of Dr.Cr on (B) spontaneous (C) high-K⁺ (80 mM)-induced contractions on isolated jejunum tissue. (D) Concentration-dependent response of Dr.DCM on spontaneous contractions on isolated jejunum tissue. (E) Concentration-dependent response of Dr.Aq on spontaneous contractions on isolated jejunum tissue.

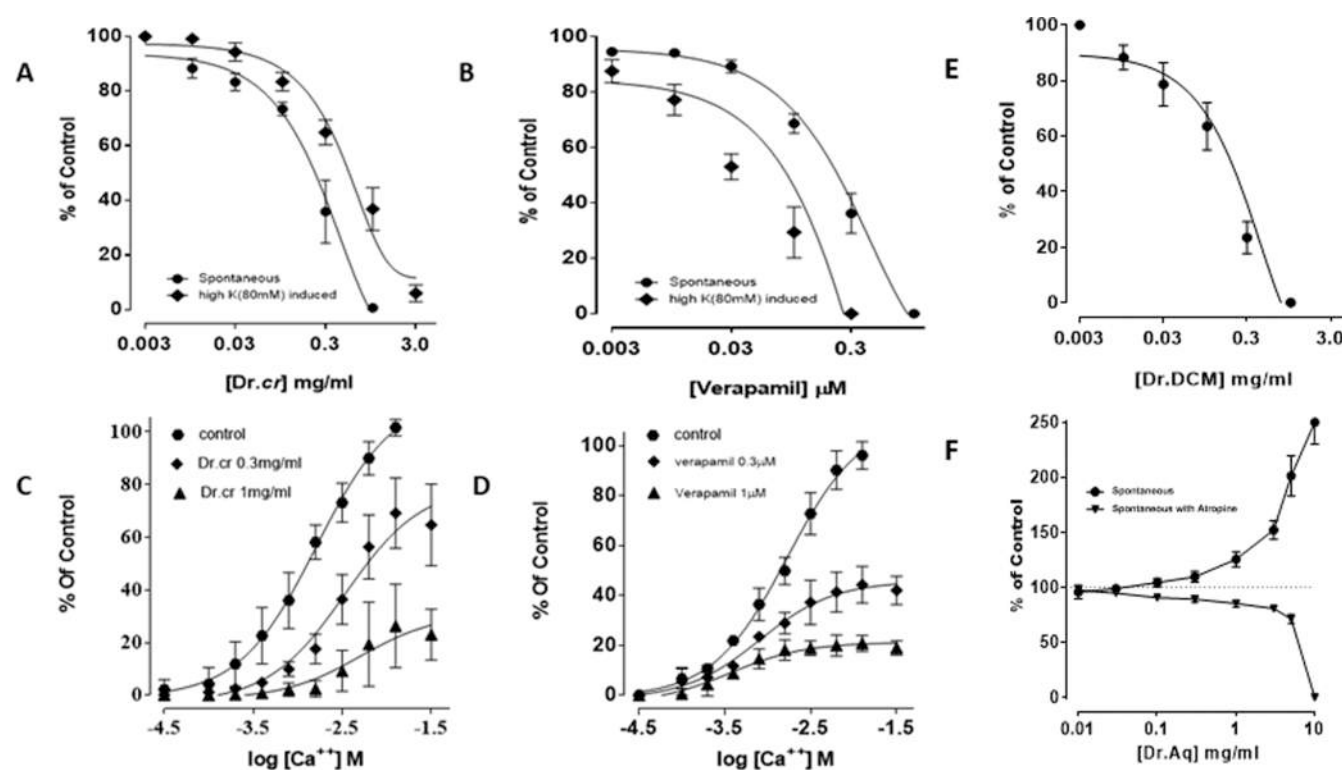


Figure 3. (A) Concentration-dependent response of Dr.Cr on spontaneous and high-K⁺ (80 mM)-induced contractions in jejunum tissue preparations (*N* = 5). (B) Concentration-dependent response of verapamil on spontaneous and high-K⁺ (80 mM)-induced contractions in isolated jejunum tissue preparations (*N* = 5). (C) Concentration-dependent response of Dr.Cr on the concentration–response curve of calcium (Ca⁺⁺) in isolated rabbit jejunum tissue preparations (*N* = 5). (D) Concentration-dependent response of verapamil on the concentration–response curve of calcium (Ca⁺⁺) in isolated rabbit jejunum tissue preparations (*N* = 5). (E) Concentration-dependent response of Dr.DCM on spontaneous contractions on isolated jejunum tissue (*N* = 5). (F) Concentration-dependent response of Dr.Aq on spontaneous contractions and atropine-treated contractions on isolated jejunum tissue (*N* = 5).

that iriflophenon glycoside, quercetin, and isomangiferin were projected with the least binding energies and referred to as leading bioactive compounds having comparable binding affinities with verapamil (Figure 1 and Table 2).

3.2.2.1. Voltage-Gated Calcium Ion Channel $\beta_2\alpha$ (VGCC, PDB:1T0J). According to what we discovered, isomangiferin (docking score: -8.63 kcal/mol, ΔG binding: -47.04 kcal/

mol, pK_i : -17.20 μ M) scored 1st for voltage-gated calcium channels and formed conventional H-bonds with Val60 (3.03 Å), His94 (2.61 Å), His94 (1.58 Å), and Ala310 (2.93 Å); carbon H-bonds with Ala63 (3.00 Å), Pro224 (1.52 Å), Val223 (2.65 Å), and Leu93 (1.31 Å); and π -alkyl bonds with Val60 (5.40 Å), Ala63 (4.95 Å), Pro224 (5.23 Å), Met226 (5.30 Å), Ala63 (3.84 Å), Met226 (5.45 Å), and Ala310 (5.46 Å).

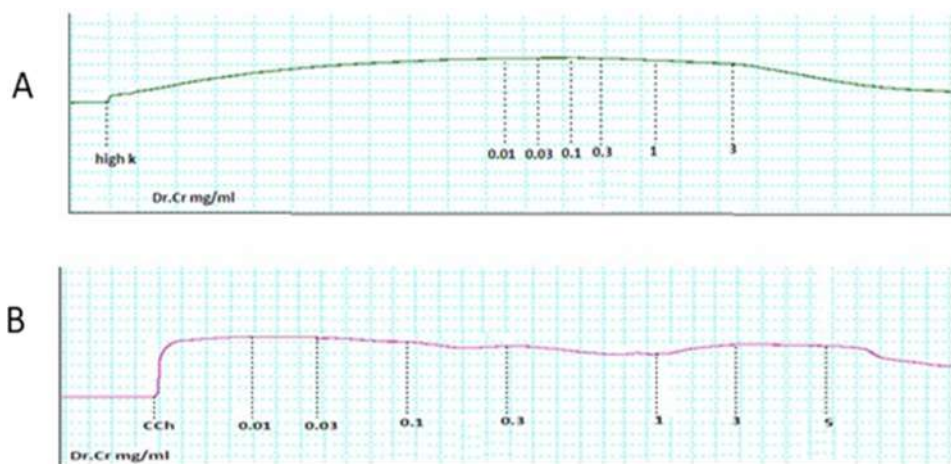


Figure 4. Concentration-dependent response of Dr.Cr on (A) high-K⁺ (80 mM)-induced and (B) carbachol (1 μ M) made contractions in tracheal tissues.

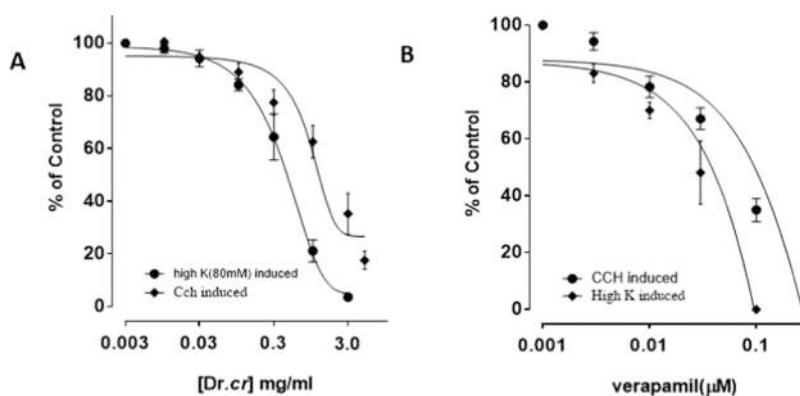


Figure 5. (A) Concentration-dependent response of ethanolic extract Dr.Cr on high-K⁺ (80 mM)-induced and 1 μ M carbachol-induced contractions in isolated tracheal tissues ($N = 5$). (B) Concentration-dependent response of standard drug verapamil on high-K⁺ (80 mM)- and 1 μ M carbachol-induced contractions in tracheal tissues ($N = 5$).

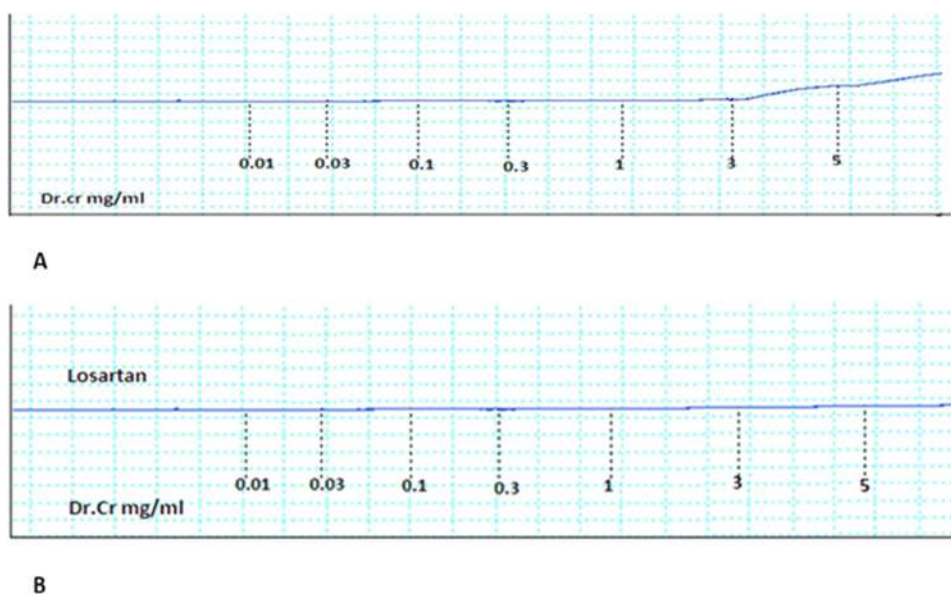


Figure 6. Concentration-dependent response of ethanolic extract Dr.Cr on steadied isolated aortic tissue (a) without losartan and (b) tissue pretreated with losartan.

Iriflophenon glycoside (docking score: -6.28 kcal/mol, ΔG binding: -29.63 kcal/mol, pK_i : -9.46 μ M) stood second in its

docking score, making conventional H-bonds with Val95 (2.47 Å), Ala63 (2.49 Å), Phe62 (2.01 Å), and Val95 (1.96 Å) and

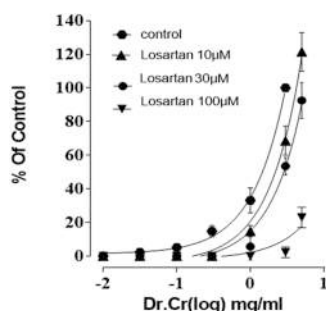


Figure 7. Dose-dependent response of Dr.Cr in isolated aortic rings pretreated with different concentrations of losartan ($N = 5$).

(1.90 Å); carbon H-bonds with Phe62 (2.80 Å), and Pro228 (2.27 Å), (2.40 Å); and π -alkyl bonds with Ala310 (3.88 Å) and Leu309 (5.03 Å). Quercetin (docking score: -5.44 kcal/mol, ΔG binding: -34.94 kcal/mol, pK_i : -11.95 μ M) forms conventional H-bonds with Phe307 (2.31 Å) and Ile303 (2.94 Å); a carbon H-bond with Arg311 (2.31 Å); and π -alkyl bonds with Val60 (4.63 Å), Ala63 (3.67 Å), and Ala310 (4.43 Å). Mangiferin (docking score: -5.23 kcal/mol, ΔG binding: -33.19 kcal/mol, pK_i : -11.19 μ M) makes conventional H-bonds with Phe62 (2.82 Å) and Leu93 (2.21 Å), (1.60 Å), and (1.75 Å); carbon H-bonds with Arg311 (2.34 Å) and Leu93 (2.89 Å), π - π stacked with Phe307 (5.69 Å); amide- π stacked with Ala61c,O;Phe62 (4.05 Å); and π -alkyl bonds with Pro224 (5.12 Å), Arg311 (4.34 Å), Val60 (4.59 Å), Ala63 (4.22 Å), Ala310 (4.75 Å), Arg311 (5.30 Å), and Arg311 (4.46 Å). Vanillic acid (docking score: -4.14 kcal/mol, ΔG binding: -14.38 kcal/mol, pK_i : -3.02 μ M) forms conventional H-bonds with B:Arg311:H-vanillic acid:O4arg311 (2.71 Å), B:Val316:H-vanillic acid:O2val316 (2.77 Å), and vanillic acid:H19-B:Met226:Omet226 (2.84 Å); carbon H-bonds with vanillic acid:H16-B:Met226:Omet226 (2.69 Å) and vanillic acid:H17-B:Ile306:Oile306 (1.84 Å); and a π -alkyl bond with vanillic acid-B: Leu309leu309 (4.09 Å). Verapamil (docking score: -3.94 kcal/mol, ΔG binding: -46.37 kcal/mol, pK_i : -16.91 μ M) forms conventional H-bonds with Leu93 (2.46 Å) and Val223 (2.29 Å); carbon H-bonds with Phe92 (2.84 Å), Ala61 (2.86 Å), Ala61 (2.80 Å), Ser225 (2.17 Å), Ser225 (2.58 Å), Gln314 (1.77 Å), and Ser225 (2.12 Å); π -lone pair with Leu93 (2.97 Å) and Phe307 (2.86 Å); amide- π stacked with Val64c,O;Arg65 (3.97 Å) and Pro224c,O;Ser225 (4.29 Å); alkyl with Ala63 (3.08 Å), Ala63 (4.23 Å), Ala310 (3.66 Å), Met226 (5.04 Å), Val60 (4.19 Å), Val109 (5.29 Å), Val109 (4.45 Å), Val223 (5.40 Å), and Arg227 (4.80 Å); and π -alkyl with Phe92 (3.63 Å), Phe307 (4.64 Å), Pro224 (5.13 Å), Leu309 (5.44 Å), Val316 (4.44 Å), and Val64 (5.08 Å). Gallic acid (docking score: -3.85 kcal/mol, ΔG binding: -10.52 kcal/mol, pK_i : -1.34 μ M) makes a conventional H-

bond with His398 (3.08). Caffeic acid (docking score: -2.74 kcal/mol, ΔG binding: -19.27 kcal/mol, pK_i : -5.14 μ M) forms conventional H-bonds with His398 (2.12 Å) and Leu399 (2.40 Å) and a carbon H-bond with Ala395 (1.84 Å). Cinnamic acid (docking score: -2.45 kcal/mol, ΔG binding: -10.23 kcal/mol, pK_i : -1.21 μ M) makes carbon H-bonds with Pro228 (2.01 Å) and Phe307 (1.93 Å); π -anion with Phe307 (4.15 Å); and π -alkyl with Leu309 (4.62 Å).

3.2.2.2. Human Myosin Light Chain Kinase-1 (MLCK-1, PDB: 6C6M). Isomangiferin (docking score: -8.41 kcal/mol, ΔG binding: -35.77 kcal/mol, pK_i : -12.31 μ M) makes conventional H-bonds with Lys432 (2.30 Å), Tyr464 (1.85 Å), Tyr471 (2.59 Å), Tyr471 (2.02 Å), Ser486 (2.99 Å), Ser497 (2.02 Å), Ser499 (3.09 Å), Ser497 (2.84 Å), (1.88 Å), and Thr430 (2.80 Å); carbon H-bonds with Thr430 (3.03 Å), Ser497 (2.68 Å), (2.56 Å), and Asp466 (2.61 Å); and π -alkyl with Lys432 (4.02 Å), Lys432 (4.91 Å), and Lys432 (3.96 Å). Iriflophenon glycoside (docking score: -7.549 kcal/mol, ΔG binding: -0.91 kcal/mol, pK_i : -2.83 μ M) makes different conventional H-bonds with Trp447 (1.92 Å), Arg456 (2.23 Å), Glu417 (1.99 Å), Glu444 (1.82 Å), Glu436 (2.17 Å), Trp447 (2.87 Å), Val454 (2.25 Å) and (1.79 Å), Val445 (1.71 Å), and Glu465 (2.32 Å); carbon H-bonds with Trp447 (2.91 Å), Trp447 (2.64 Å), Tyr464 (2.81 Å), Glu444 (2.63 Å), Glu417 (2.46 Å), and Val454 (2.39 Å); electrostatic attractive charge with Arg456 (5.58 Å); π -cation with Arg456 (4.31 Å); and π -alkyl with Val463 (4.81 Å). Mangiferin (docking score: -6.916 kcal/mol, ΔG binding: -40.48 kcal/mol, pK_i : -14.35 μ M) makes conventional H-bonds with Arg456 (2.04 Å), Arg456 (2.61 Å), Arg456 (2.29 Å), Thr452 (2.09 Å), Val445 (1.60 Å), Val445 (1.70 Å), Glu417 (1.96 Å), (1.53 Å), and (1.73 Å), and Glu450 (1.67 Å); carbon H-bonds with Glu444 (2.70 Å), Glu417 (2.65 Å), and Glu417 (2.95 Å); a π -donor hydrogen bond with Glu465 (3.02 Å). Gallic acid (docking score: -6.684 kcal/mol, ΔG binding: -10.71 kcal/mol, pK_i : -1.42 μ M) has electrostatic attractive charge with Arg456 (3.32 Å); conventional H-bonds with Arg456 (2.25 Å), Glu436 (2.40 Å), Val454 (1.80 Å), and Glu444 (1.91 Å); carbon H-bonds with Arg456 (3.08 Å) and Arg456 (2.56 Å); and π -alkyl with Ala446 (5.07 Å) and Val463 (5.30 Å). Quercetin (docking score: -6.39 kcal/mol, ΔG binding: -40.43 kcal/mol, pK_i : -14.33 μ M) makes conventional H-bonds with His470 (1.87 Å), Glu436 (1.61 Å), and Trp447 (1.57 Å); π -anion with Glu444 (4.99 Å); π -donor hydrogen bond with Trp447 (2.98 Å); and π -alkyl with Val463 (4.81 Å), Val463 (5.22 Å), Ala446 (4.24 Å), and Val463 (5.37 Å). Vanillic acid (docking score: -5.176 kcal/mol, ΔG binding: -13.52 kcal/mol, pK_i : -2.64 μ M) makes a conventional H-bond with Glu436 (1.66 Å); carbon H-bonds with Arg456 (2.79 Å), Trp447 (2.48 Å), Trp447 (2.62 Å), (2.36 Å), and Val454 (2.55 Å); salt bridge and electrostatic attractive charge with Arg456 (2.10 Å);

Table 3. Outcome of Crude Ethanolic Extract *D. ramosa* in Terms of the Percentage of Inflammation Reduced ($N = 5$; Data Shown as Mean \pm SEM)^a

groups	dose	% inhibition of paw volume			
		0–1 h	0–2 h	0–3 h	0–4 h
group I	NS 0.5 mL				
group II	Aspirin 0.01 g/kg	17.072 \pm 0.20	21.968 \pm 0.27	54.864 \pm 0.29	69.978 \pm 0.7
group II	Dr.Cr 0.1 g/kg	17.218 \pm 0.09	19.934 \pm 0.170	28.6 \pm 0.27***	36.226 \pm 0.23***
group IV	Dr.Cr 0.2 g/kg	38.65 \pm 0.22***	43.648 \pm 0.377***	50.826 \pm 0.24*	59.554 \pm 0.54***

^a*** $p < 0.001$, ** $p < 0.01$, * $p < 0.05$ compared with positive control.

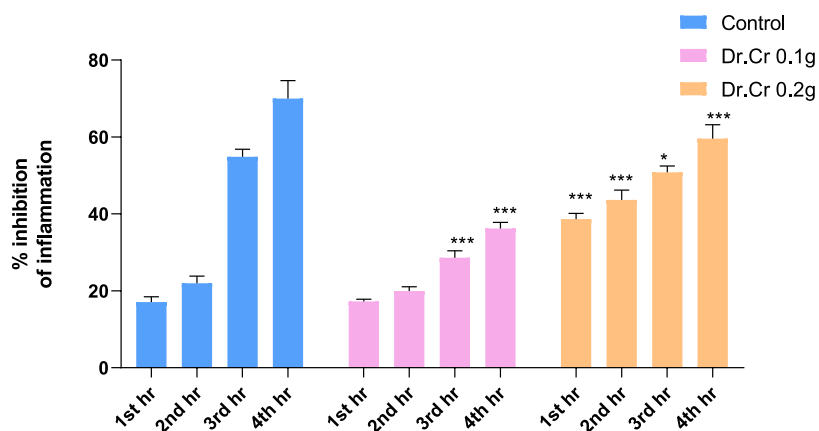


Figure 8. Dr.Cr and aspirin's impact on rat paw edema brought on by carrageenan is measured in terms of the proportion of inhibition of inflammation. Values expressed as mean \pm SEM ($N = 5$). For data analysis, two-way ANOVA with RM testing was used. *** $p < 0.001$, ** $p < 0.01$, * $p < 0.05$ compared with positive control.

Table 4. Effect of Ethanolic Plant Extract (Dr.Cr) in Castor Oil-Provoked Diarrhea in Mice ($N = 5$)

groups	dose	no. of wet feces			
		0–1 h	0–2 h	0–3 h	0–4 h
group I	10 mL/kg	5	8	12	7
group II	5 mg/kg	0	1	1	0
group III	200 mg/kg	2	1	4	0
group IV	400 mg/kg	0	2	3	0

Table 5. Percentage Protection against Castor Oil-Induced Diarrhea by Ethanolic Plant Extract (Dr.Cr)^{a,b}

groups	dose	total number of feces	%age protection
group I	10 mL/kg	8 \pm 0.50	
group II	5 mg/kg	0.5 \pm 0.1***	93.75
group III	200 mg/kg	1.75 \pm 0.29**	78.125
group IV	400 mg/kg	1.25 \pm 0.26***	84.375

^a $N = 5$; data shown as mean \pm SEM. ^b*** $p < 0.001$, ** $p < 0.01$, * $p < 0.05$.

electrostatic attractive charge with Lys415 (4.90 Å); alkyl with Pro453 (5.43 Å); and π -alkyl with Ala446 (5.14 Å). Caffeic acid (docking score: -5.16 kcal/mol, ΔG binding: -17.44 kcal/mol, pK_i : -4.34 μ M) forms conventional H-bonds with Trp447 (2.43 Å), Val454 (1.86 Å), and Glu436 (1.85 Å); a π -donor hydrogen bond with Trp447 (3.14 Å); electrostatic attractive charge with Arg456 (4.91 Å); π -alkyl with Ala446 (4.10 Å) and Val463 (5.35 Å). Cinnamic acid (docking score: -2.407 kcal/mol, ΔG binding: -17.26 kcal/mol, pK_i : -4.27 μ M) makes a π -donor hydrogen bond with trp447 (2.82 Å); salt bridge and electrostatic attractive charges with 456 (3.25 Å); and π -alkyl with Ala446 (4.12 Å) and Val463 (5.46 Å). Verapamil (docking score: -2.313 kcal/mol, ΔG binding: -36.37 kcal/mol, pK_i : -12.57 μ M) makes conventional H-bonds with Arg480 (2.48 Å), Arg480 (2.44 Å), and Glu458 (2.78 Å); carbon H-bonds with Arg480 (2.68 Å), Gln457 (2.67 Å), Glu458 (2.62 Å), Ser482 (2.46 Å), Gln457 (2.51 Å), Glu458 (2.74 Å), Asp481 (2.70 Å), Asp481 (2.73 Å) and (2.51 Å), Pro453 (2.77 Å), and Glu458 (2.65 Å); alkyl with Val454 (4.29 Å) and Arg480 (4.49 Å); and π -alkyl with Leu449 (4.37 Å).

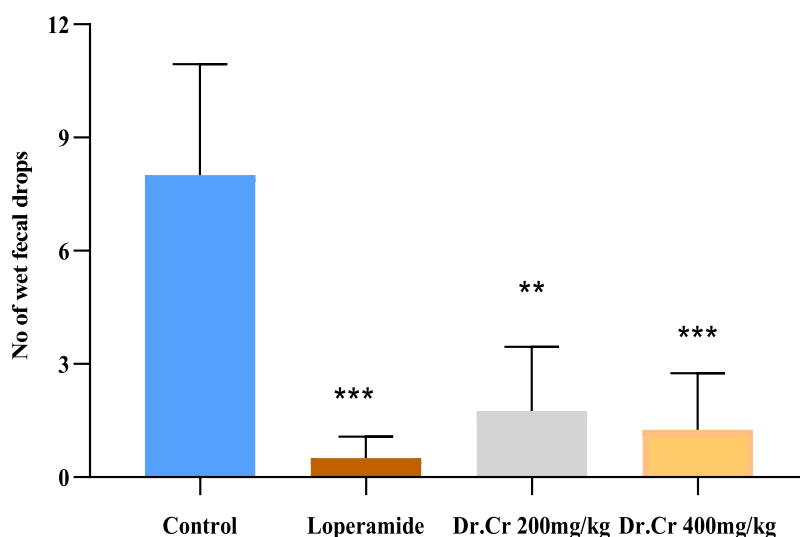


Figure 9. Effect of Dr.Cr on castor oil-induced diarrhea. Values expressed as mean \pm SEM ($N = 5$). For data analysis, the multiple comparison test and standard one-way ANOVA testing were used. *** $p < 0.001$, ** $p < 0.01$, * $p < 0.05$ compared with negative control.

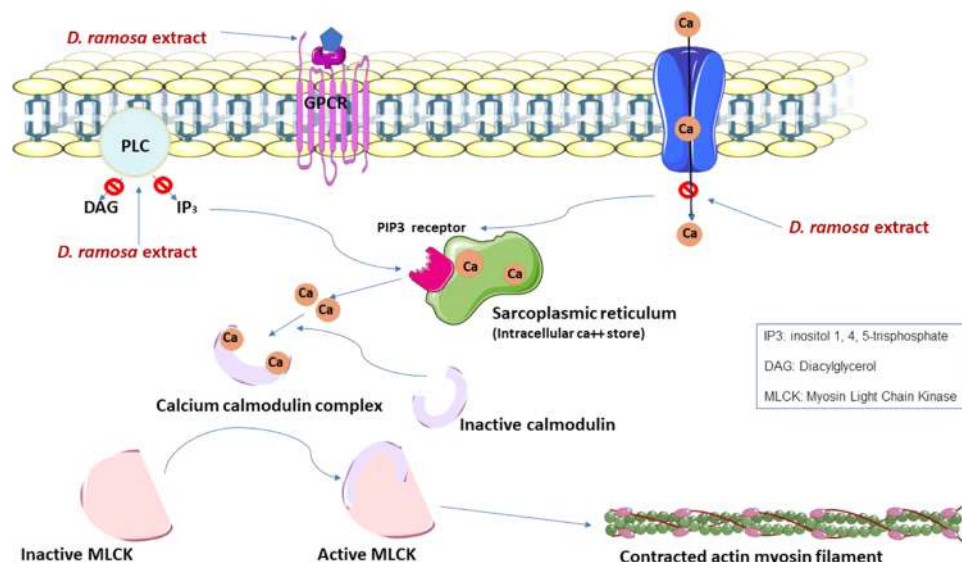


Figure 10. Schematic diagram of the proposed mechanism of *D. ramosa* extracts on the L-type voltage-gated Ca²⁺ channel, M₃ muscarinic receptor, and phosphoinositide phospholipase C (PLC).

3.2.2.3. Human Cyclooxygenase-2 (COX2-PDB:5lkQ). Iriflophenon glycoside (docking score: -9.77 kcal/mol, ΔG binding: -37.8 kcal/mol, pK_i : -13.19 μ M) forms conventional H-bonds with Val538 (2.77 Å), Arg377 (2.15 Å), Gly226 (2.24 Å), Asn376 (1.69 Å), Gln375 (1.72 Å), Gln374 (1.97 Å), Asn375 (1.83 Å), and Gly336 (1.92 Å); carbon H-bonds with Pro129 (2.75 Å), Arg377 (2.61 Å), Asn376 (2.67 Å), and Asn376 (3.04 Å); a π -donor hydrogen bond with Asn375 (2.90 Å); and π -cation and π -donor hydrogen bond with Arg376 (4.18 Å). Isomangiferin (docking score: -8.85 kcal/mol, ΔG binding: -38.57 kcal/mol, pK_i : -13.52 μ M) makes conventional H-bonds with Arg377 (2.87 Å), Arg377 (2.08 Å), Gln375 (2.81 Å), Gln375 (1.82 Å), Asn375 (1.98 Å), and Ser143 (2.08 Å); carbon H-bonds with Gly226 (2.63 Å), (2.88 Å), and Gln375 (2.59 Å), π -cation with Arg376 (4.97 Å); π - π T-shaped with Phe142 (4.63 Å); and π -alkyl with Leu145 (5.25 Å). Mangiferin (docking score: -8.03 kcal/mol, ΔG binding: -26.53 kcal/mol, pK_i : -8.29 μ M) makes conventional H-bonds with Val228 (2.66 Å), Asn375 (1.76 Å), Arg377 (2.05 Å), Arg377 (3.00 Å), Gln375 (2.46 Å), and Asn376 (1.82 Å) and (1.93 Å); and carbon H-bonds with Gln374 (2.46 Å) and Gln375 (2.79 Å). Quercetin (docking score: -8 kcal/mol, ΔG binding: -44.83 kcal/mol, pK_i : -16.24 μ M) makes conventional H-bonds with Arg376 (2.46 Å), Arg376 (2.93 Å), Arg377 (2.26 Å), Val539 (2.81 Å), Asn376 (1.99 Å) and (1.82 Å), Asn375 (2.08 Å), and Gly537 (1.82 Å); and a π -donor hydrogen bond with Asn376 (2.80 Å). Gallic acid (docking score: -6.88 kcal/mol, ΔG binding: -9.38 kcal/mol, pK_i : -0.84 μ M) makes conventional H-bonds with Gln242 (2.04 Å), Gln242 (2.57 Å), Arg334 (2.02 Å), Arg334 (1.86 Å), Gly236 (1.85 Å), Gly236 (1.75 Å), and Glu140 (1.95 Å); carbon H-bonds with Ser143 (2.71 Å), Asn144 (2.91 Å), and Leu239 (2.68 Å); and π -lone pair with Glu237 (2.90 Å). Caffeic acid (docking score: -6.05 kcal/mol, ΔG binding: -14.17 kcal/mol, pK_i : -2.92 μ M) makes conventional H-bonds with Arg376 (2.13 Å), Arg377 (2.03 Å), Gln375 (1.73 Å), and Asn376 (1.70 Å); and electrostatic attractive charge with Arg376 (3.38 Å). Vanillic acid (docking score: -5.46 kcal/mol, ΔG binding: -14.42 kcal/mol, pK_i : -3.03 μ M) makes conventional H-bonds with Arg377 (2.11

Å), Arg377 (2.11 Å), and Gln374 (1.91 Å); a carbon H-bond with Gly226 (2.97 Å); and electrostatic attractive charge with Arg377 (3.47 Å). Verapamil (docking score: -4.31 kcal/mol, ΔG binding: -27.11 kcal/mol, pK_i : -8.54 μ M) makes conventional H-bonds with Arg376 (2.78 Å) and Leu224 (2.08 Å); carbon H-bonds with Ser144 (2.32 Å), Gln375 (2.76 Å), Tyr374 (2.75 Å), Gln374 (2.48 Å), Tyr374 (2.56 Å), Gly235 (2.57 Å), Glu236 (2.79 Å), Asp229 (2.68 Å), Glu141 (2.73 Å), and Glu141 (2.70 Å); alkyl with Pro129 (5.04 Å) and Pro127 (4.94 Å), alkyl with Leu238 (4.61 Å); and π -alkyl with Phe142 (4.87 Å) and Phe143 (5.18 Å). Cinnamic acid (docking score: -2.15 kcal/mol, ΔG binding: 0.79 kcal/mol, pK_i : 3.57 μ M) makes a conventional H-bond with Asn375- (2.64 Å); a carbon H-bond with Gln374 (2.88 Å); and π - π T-shaped with Phe143 (4.50 Å).

3.2.2.4. Arachidonate-5-lipoxygenase (ALOX5, PDB: 6n2w). Isomangiferin (docking score: -8.55 kcal/mol, ΔG binding: -47.84 kcal/mol, pK_i : -17.55 μ M) makes conventional H-bonds with Thr427 (2.27 Å), Gln363 (1.79 Å), Gln363 (1.65 Å), and Ile673 (2.20 Å) and (1.87 Å) and carbon H-bonds with Leu368 (2.61 Å) and His372 (2.79 Å). Mangiferin (docking score: -8.03 kcal/mol, ΔG binding: -30.3 kcal/mol, pK_i : -9.93 μ M) makes conventional H-bonds with His367 (2.19 Å), Thr427 (1.80 Å), Thr427 (2.99 Å), Gln363 (1.88 Å), (1.56 Å), and (1.84 Å), and Glu417 (2.05 Å); a carbon H-bond with (2.57 Å); a carbon H-bond with Gln363 (3.07 Å); π - σ with Trp599 (2.50 Å); and π - π T-shaped with Trp599 (5.89 Å) and Trp599 (4.96 Å). Iriflophenon glycoside (docking score: -7.03 kcal/mol, ΔG binding: -32.17 kcal/mol, pK_i : -10.74 μ M) makes conventional H-bonds with His367 (2.09 Å), Arg596 (2.77 Å), and Gln363 (1.76 Å), (1.63 Å), and (1.79 Å); carbon H-bonds with Thr427 (3.06 Å), His432 (2.45 Å), Gln363 (2.77 Å), and Gln363 (2.99 Å); a π -cation bond with Arg596 (2.79 Å); π - π T-shaped with Phe359 (5.33 Å) and Trp599 (5.41 Å); and π -alkyl with Ala603 (5.43 Å) and Ala426 (3.67 Å). Caffeic acid (docking score: -5.19 kcal/mol, ΔG binding: -16.09 kcal/mol, pK_i : -3.76 μ M) makes conventional H-bonds with Gln303 (2.19 Å), His360 (2.76 Å), Arg596 (2.49 Å), Gln363 (1.77 Å), and Gln363 (1.99 Å); electrostatic attractive charge

with Arg596 (4.33 Å); and π - π T-shaped with Phe359 (5.19 Å) and Trp599 (5.89 Å). Verapamil (docking score: -5.1 kcal/mol, ΔG binding: -49.39 kcal/mol, pK_i : -18.22 μM) makes a conventional H-bond with Thr427 (2.15 Å); carbon H-bonds with Thr427 (3.04 Å), Arg596 (2.73 Å), Ala603 (2.41 Å), Glu417 (2.67 Å), Ala603 (2.65 Å), and Gly595 (2.88 Å); salt bridge and electrostatic attractive charge with Glu417 (2.12 Å); π -anion with Glu417 (3.86 Å); π - π stacked with Trp599 (4.68 Å) and Trp599 (3.63 Å); alkyl with Ala426 (3.87 Å), Ala603 (4.48 Å), Ala603 (4.30 Å), Ala606 (3.92 Å), Leu607 (4.81 Å), Leu607 (3.93 Å), Leu420 (5.30 Å), and Arg596 (4.46 Å); and π -alkyl with Trp599 (3.95 Å), Trp599 (4.79 Å), and Ala603 (4.64 Å). Gallic acid (docking score: -4.97 kcal/mol, ΔG binding: -23.4 kcal/mol, pK_i : -6.93 μM) makes conventional H-bonds with Arg596 (2.15 Å) and Gln363 (1.88 Å); a carbon H-bond with His432 (2.66 Å); π - π T-shaped with Phe359 (4.88 Å); electrostatic attractive charge with Arg596 (4.30 Å); and π - π T-shaped with Phe359 (4.88 Å). Vanillic acid (docking score: -4.97 kcal/mol, ΔG binding: -11.11 kcal/mol, pK_i : -1.60 μM) makes conventional H-bonds with Arg596 (2.65 Å), Arg596 (2.10 Å), His600 (1.98 Å), and Gln363 (2.09 Å); a carbon H-bond with His600 (2.68 Å); π -alkyl with His432 (4.44 Å); electrostatic attractive charge with Arg596 (3.94 Å); and π -alkyl with His432 (4.44 Å). Quercetin (docking score: -4.41 kcal/mol, ΔG binding: -32.62 kcal/mol, pK_i : -10.94 μM) forms conventional H-bonds with His600 (2.20 Å) and Ile673 (2.95 Å); a carbon H-bond with Leu368 (2.68 Å); a π -donor hydrogen bond with His372 (2.88 Å); π - π stacked with His367 (4.57 Å); π - π T-shaped with His372 (5.32 Å); and π -alkyl with Leu607 (4.80 Å) and Leu607 (5.16 Å).

Isomangiferin, iriflophenon glycoside, quercetin, mangiferin, and vanillic acid displayed a strong binding affinity for L-type voltage-gated calcium ion channels during molecular docking analysis, and in addition to these, gallic acid, caffeic acid, and cinnamic acid showed an affinity for myosin light chain kinase. All these binding affinities and predicted properties of these bioactive compounds are similar to those of verapamil, a known calcium channel blocker. Therefore, it can be presumed that *D. ramosa* has a powerful antispasmodic effect, which is caused by the significant binding affinity of compounds for their intended protein targets, inhibiting the signal transduction process of smooth muscle contraction. But there is a discrepancy. These predictions invalidate the traditional use and reported in vivo activity of the methanolic extract of *D. ramosa* as a laxative.⁴⁴ To address this discrepancy, we have parted the active constituents of the crude ethanolic extract of *D. ramosa* (Dr.Cr) through further polarity-based fractionation into Dr.Aq and Dr.DCM.

3.3. In Vitro Activities. 3.3.1. Response on Rabbit Jejunum Preparations. For validation of this proposed mechanism of action of *D. ramosa*, all three extracts Dr.Cr, Dr.DCM, and Dr.Aq were evaluated on isolated jejunum tissue preparations. Jejunum is used because of its high reactivity among smooth muscles.²⁸ An isolated tissue is unaffected by any neurological or hormonal influences and only responds intrinsically, so it is employed for the study of underlying mechanisms.⁴⁵ When extracts were added to spontaneously contracting jejunum, diversity in results was found. Dr.Cr resulted in the inhibition of spontaneous contractions and demonstrated spasmodic action (Figure 2B) in a cumulative dose range of 0.003–1 mg/mL with an EC_{50} value 0.41 mg/mL (95% CI: 0.20–0.85, $n = 5$) in a manner comparable to

verapamil.⁴⁶ Dr.DCM also caused suppression of contractions, while Dr.Aq enhanced the contractile response (Figure 2D,E). The spasmogenic effect of Dr.Aq was blocked by atropine (1 μM), thus indicating the presence of some cholinomimetic constituents and supporting its use as a laxative.⁴⁷

There are a number of physiological mediators that regulate the motor tone of the gastrointestinal tract by controlling the movement of Ca^{++} inside and out of cells.⁴⁸ These physiological agents raise cytosolic calcium ion concentrations either by increasing the influx of calcium from the extracellular fluid or by stimulating its release from cytosolic calcium stores.⁴¹ The PLC is stimulated by the M3 muscarinic receptor's activation, and this in turn causes the secondary messenger inositol 1,4,5-trisphosphate (IP3) and diacylglycerol (DAG) to be hydrolyzed from phosphatidylinositol 4,5-bisphosphate. Inositol 1,4,5-trisphosphate receptors (IP3R) on the sarcoplasmic reticulum are stimulated by IP3 to release calcium ions, which raises the level of calcium in the cytosol. The formation of a calcium/calmodulin complex is brought about by the activation of a regulatory protein kinase C (PKC) by DAG and calcium. Myosin light chains (MLCs) are phosphorylated as a result of this calcium/calmodulin combination, activating another myosin light chain kinase (MLCK). Phosphorylated MLCs and actin then form an interaction network to produce a contractile response.⁴⁷ The primary cause of smooth muscle spontaneous contraction is a transient rise or drop in free Ca^{++} in the cytosol. This readily available cytosolic Ca^{++} interacts with the contractile components of the muscle to generate a transient activation or deactivation of the contractile components, resulting in the elicit of resting membrane potential and the contractile response of smooth muscles (Figure 10).

In order to more thoroughly assess the antispasmodic mode of action of Dr.Cr, rabbit jejunum tissue was exposed to prolonged constriction by addition of high- K^+ (80 mM). Studies show that at high concentrations, K^+ activates the Ca^{++} channels (voltage-dependent), causing an invasion of free Ca^{++} into the cytosol and a significant depolarization of the membrane action potential, which causes a persistent contraction that lasts for a long time.⁴⁷ Repolarization results in a relaxation of the smooth muscle.²⁹ Dr.Cr, when added cumulatively, completely relaxed the high- K^+ (80 mM) evoked contractions (Figure 2C) in a tissue organ bath having a concentration of 0.003–3 mg/mL with EC_{50} of 0.76 μM (95% confidence interval: 0.48–1.19, $n = 5$; Figure 3A), thus preventing the stimulated depolarization. The membrane action potential is repolarized and substances that inhibit smooth muscle contractions caused by high- K^+ levels appear to impede Ca^{++} influx into the cytosol.⁴⁷ Verapamil, a common calcium channel blocker that was used as a positive control, demonstrated a comparable response and relaxed both spontaneous and high potassium-induced contractions, with EC_{50} values of 0.34 μM (95% CI: 0.22–0.51, $n = 5$) and 0.04 μM (95% CI: 0.02–0.10, $n = 5$), respectively (Figure 3B). For confirmation of the calcium channel-blocking response of Dr.Cr, CRCs of calcium were constructed in the absence and presence of extract. All Ca^{++} channel blockers have the trait of blocking calcium's sluggish entry, and this effect can be reversed by adding Ca^{++} .⁴⁹ Pretreating with the extract Dr.Cr caused calcium CRCs to be suppressed at doses of 0.3 and 1 mg/mL with a rightward parallel shift on jejunum tissue preparation, comparable to that of verapamil at doses of 0.1 and 0.3 μM .⁵⁰ These results were compared with the common

calcium channel blocker verapamil, which caused complete suppression of CRCs at doses of 0.3 and 1 μM compared to Dr.Cr (Figure 3C,D). This outcome suggests the existence of Ca^{++} channel blockers in Dr.Cr, since they are helpful in cases when the gut is overactive.⁴⁹ Wahid et al. reported the strong affinity of quercetin with PLC.⁴⁷ Antispasmodic agents disrupt this pathway, and they are used to treat overactive gastrointestinal ailments.^{29,51} Numerous investigations have revealed that the Ca^{++} antagonistic effect of medicinal herbs is the primary cause of their mode of action.⁵⁰ Multiple diseases can be cured through the interactions between bioactive substances and their target proteins.⁵²

3.3.2. Response on the Trachea. The potential bronchodilator properties of *D. ramosa* were investigated, as it has the presence of flavonoids, and besides their antispasmodic properties, flavonoids are also known to play a role as bronchodilators.^{53–55} Capasso et al.³⁷ studied the bronchodilator effect of quercetin on rat tracheal tissues. Djelili et al.⁵⁸ reported that quercetin and rutin had a bronchodilator effect on isolated human bronchus tissues. Chang et al.⁵⁶ reported the antiasthmatic activity of quercetin and rutin. Ko et al.⁵⁷ studied the broncho-relaxant effect of quercetin on KCl (30 mM), and carbachol (0.2 μM)-induced spastic contraction on isolated guinea pig tracheal tissue preparations. To explore the mechanism of relaxation, investigations of Dr.Cr were conducted in isolated rabbit tracheal preparations that had already been precontracted with CCh (1 μM) and high- K^{+} (80 mM).⁵⁸ Dr.Cr inhibited high- K^{+} (80 mM)-induced contraction in rabbit tracheal preparation (Figure 4) in a dose-dependent manner with a corresponding EC_{50} of 0.6194 mg/mL (95% CI: 0.388 to 0.988, $n = 5$). The response of Dr.Cr on CCh-induced contraction was insignificant, since it did not totally relax the contraction caused by 1 μM CCh until 10 mg/mL (Figure 5A). So, it confirmed the speculations that the extract contained some cholinomimetic and calcium channel blocker constituents,⁴⁷ and CCB was a prominent mechanism for the bronchodilator effect.⁵⁹ Partial relaxation of CCh-induced contractions showed that Dr.Cr had some muscarinic M3 receptor activity, which is masked at higher doses by some other bioactive agonist compounds, as depicted by the spasmogenic effect of Dr.Aq at the jejunum (Figure 2E). Comparatively, verapamil, a common Ca^{++} channel antagonist, reduced high- K^{+} (80 mM), and CCh (1 μM) provoked contractions with corresponding EC_{50} values of 0.063 μM /mL (95% CI: 0.02–0.17, $n = 5$) and 0.09 μM /mL (95% CI: 0.063–0.14, $n = 5$; Figure 5B). Given that they are intended to be tracheal relaxants, CCBs are also known to be useful as a cough remedy.⁶⁰

3.3.3. Effect on the Aorta. Moreover, the smooth muscle relaxant effect of Dr.Cr was confirmed on isolated aortic rings where it caused a contractile reaction on stable aortic tissue preparation (Figure 6A), potentially as a result of activation of one or more types of receptors on the aorta. This contractile response of Dr.Cr decreases when tissue is pretreated with losartan (Figure 6B). Dose–response curves of Dr.Cr after pretreatment with increasing concentrations of losartan are made, and it is shown in Figure 7 that by increasing the concentration of losartan, dose–response curves are shifted toward the right by suppression of contractions at initial doses of Dr.Cr, which are concluded to be mediated through activation of angiotensin II receptors.³¹

3.4. In Vivo Activities. **3.4.1. Effect on Carrageenan-Induced Rat Paw Edema.** The presence of flavonoids in *D.*

ramosa suggests the anti-inflammatory effect of plants, as studies have shown the relation of the anti-inflammatory effect of plants with the presence of flavonoids.¹⁸ Dr.Cr significantly reduced the inflammation by inhibiting edema in the paws of rats at dosages of 0.1 and 0.2 g/kg in treatment groups compared to the control group. Carrageenan causes edema to develop in two stages. During the first hour following carrageenan exposure, histamines, serotonin, prostaglandins, and cytoplasmic enzymes are released from neighboring cells of wounded tissue. After the first hour, the second phase begins, and it is characterized by a rise in prostaglandin secretion and the release of leukotrienes and kinins from the inflammatory area.^{61,62} The suppression of edema following pretreatment with Dr.Cr (0.1 g/kg; I/P), at time intervals of the 1st, 2nd, 3rd, and 4th hours, was measured to be 17.218, 19.934, 28.6, and 36.226%, respectively. In contrast, pretreatment with Dr.Cr (0.2 g/kg; I/P) led to percentages of 38.65, 43.648, 50.826, and 59.554% at respective intervals of the 1st, 2nd, 3rd, and 4th hours, respectively, while standard aspirin therapy (0.01 g/kg; I/P) resulted in 17.072, 21.968, 54.864, and 69.978% suppression of inflammation, respectively (Table 3 and Figure 8). Dr.Cr substantially reduced the edema in the second phase and proposed that it works by inhibiting the formation of cyclooxygenase. This result is equivalent to that of nonsteroidal anti-inflammatory medications. These results are also validated by the results of our docking studies, which showed strong interaction of bioactive compounds from ethanolic extract of *D. ramosa* like iriflophenon glycoside, isomangiferin, mangiferin, and different polyphenolic compounds quercetin, gallic acid, caffeic acid, vanillic acid, and cinnamic acid with the human cyclooxygenase-2 enzyme, suggesting the role of these compounds in anti-inflammatory activity.

3.4.2. Effect on Diarrhea Brought on by Castor Oil. Diarrhea is described as the abnormal passing of soft stools as a result of problems with the colon's ability to carry water and electrolytes. Castor oil alters colonic water and electrolyte transport, which results in diarrhea and increases peristaltic motions.⁶³ Dr.Cr caused a significant decline in the number of wet drops of feces in mice (Table 4). Group I (positive control group) receiving normal saline (NS) at 10 mL/kg dose showed 8 ± 0.50 wet drops of feces. Group II (negative control) receiving loperamide at 5 mg/kg dose showed 0.5 ± 0.1 fecal drops. Groups III and IV receiving extract at 200 and 400 mg/kg doses showed 1.75 ± 0.29 and 1.25 ± 0.26 fecal drops, respectively (Table 5 and Figure 9). As shown in (Table 5) both 200 and 400 mg/kg doses of ethanolic crude extract were found to produce a decrease in the frequency of defecation and diarrheal stools in castor oil-treated mice groups in 4 h observations in comparison to the negative control (normal saline) group. There was significant postponement in the commencement of diarrhea at a dose of 400 mg/kg comparable to loperamide. This dose-dependent increase in protection from diarrhea plus delay in onset of diarrhea at a high dose (84.38% at dose 400 mg/kg) is comparable to loperamide (93.75% at 10 mg/kg dose; Table 5). Loperamide has a propensity to interfere with the calcium-mediated signaling system, hence regulating intestinal tone.⁶⁴ Thus, in vivo results showed that extract reduces intestinal tone experiments by blocking the calcium channel. These results are supported by in vitro and in silico studies (Figure 10).

4. CONCLUSIONS

The prospective compounds like quercetin, mangiferin, and isomangiferin are promising bioactive compounds of *Dryopteris ramosa*, which showed a strong binding affinity to L-type voltage-gated Ca⁺⁺ channels, human myosin light chain kinase, Cox2, and arachidonate-5-lipoxygenase during computational studies and during validation of these proposed effects through biological experiments. The hydroethanolic extract (Dr.Cr) of *D. ramosa* (Linn.) exhibited spasmolytic, spasmogenic, bronchodilator, and vasoconstrictive activities through different mechanisms. The spasmolytic and bronchodilator activities are mediated through blockage of Ca⁺⁺ channels, spasmogenic activity through activation of muscarinic receptors, and vasoconstrictive activity may be due to the presence of angiotensin II agonistic compounds. Also, it has anti-inflammatory activity, so it may be helpful in treating asthma as well as diarrhea by controlling the contractile effect via calcium-mediated signaling.

AUTHOR INFORMATION

Corresponding Authors

Fatima Saqib – Department of Pharmacology, Bahauddin Zakariya University, Multan 60000, Pakistan; orcid.org/0000-0001-6242-7147; Email: fatima.saqib@bzu.edu.pk

Lorena Dima – Faculty of Medicine, Transilvania University of Brasov, Brasov 500036, Romania; Email: lorenadima@yahoo.com

Authors

Iram Iqbal – Department of Pharmacology, Bahauddin Zakariya University, Multan 60000, Pakistan

Muhammad Farhaj Latif – Department of Pharmacology, Bahauddin Zakariya University, Multan 60000, Pakistan

Hamna Shahzad – Department of Biochemistry, Bahauddin Zakariya University, Multan 60000, Pakistan

Bayan Sajer – Department of Biological Sciences, College of Science, King Abdulaziz University, Jeddah 80200, Saudi Arabia

Rosana Manea – Faculty of Medicine, Transilvania University of Brasov, Brasov 500036, Romania

Ciprian Pojala – Faculty of Medicine, Transilvania University of Brasov, Brasov 500036, Romania

Radu Necula – Faculty of Medicine, Transilvania University of Brasov, Brasov 500036, Romania

Complete contact information is available at:

<https://pubs.acs.org/10.1021/acsomega.3c01907>

Author Contributions

F.S. and I.I.: conceptualization; M.F.L. and H.S.: methodology; L.D., R.M., C.P., and R.N.: validation; I.I.: formal analysis; I.I., B.S., and L.D.: data curation; F.S., B.S., I.I., M.F.L., and H.S.: writing—original draft preparation; and L.D., R.M., C.P., and R.N.: writing—review and editing. All authors have read and agreed to the published version of the manuscript.

Funding

This research received no external funding.

Notes

The authors declare no competing financial interest.

REFERENCES

- (1) Pirintsos, S.; Panagiotopoulos, A.; Bariotakis, M.; Daskalakis, V.; Lionis, C.; Sourvinos, G.; Karakasioti, I.; Kampa, M.; Castanas, E.

From Traditional Ethnopharmacology to Modern Natural Drug Discovery: A Methodology Discussion and Specific Examples. *Molecules* **2022**, *27*, No. 4060.

- (2) Heinrich, M. New medicines based on traditional knowledge: Indigenous and intellectual property rights from an ethnopharmacological perspective. *Ethnopharmacology* **2015**, *75*–86.

- (3) Heinrich, M.; Gibbons, S. Ethnopharmacology in drug discovery: an analysis of its role and potential contribution. *J. Pharm. Pharmacol.* **2010**, *53*, 425–432. From NLM.

- (4) Wahid, M.; Ali, A.; Saqib, F.; Aleem, A.; Bibi, S.; Afzal, K.; Ali, A.; Baig, A.; Khan, S. A.; Bin Asad, M. H. H. Pharmacological exploration of traditional plants for the treatment of neurodegenerative disorders. *Phytother. Res.* **2020**, *34*, 3089–3112.

- (5) Hon, K.-L.; Ki Fung, C.; KC Leung, A.; Ngan-Ho Leung, T.; KK Ng, D. Complementary and alternative medicine for childhood asthma: an overview of evidence and patents. *Recent Pat. Inflammation Allergy Drug Discovery* **2015**, *9*, 66–79.

- (6) Wen, M.-C.; Wei, C.-H.; Hu, Z.-Q.; Srivastava, K.; Ko, J.; Xi, S.-T.; Mu, D.-Z.; Du, J.-B.; Li, G.-H.; Wallenstein, S. Efficacy and tolerability of antiasthma herbal medicine intervention in adult patients with moderate-severe allergic asthma. *J. Allergy Clin. Immunol.* **2005**, *116*, S17–S24.

- (7) Hameed, S.; Hans, S.; Nandan, S.; Fatima, Z. Mechanistic insights into the antimicrobial action of unani formulation, Qurs Sartan Kafoori. *J. Tradit. Complement. Med.* **2022**, *12*, 162–171.

- (8) Hamayun, M. Ethnobotanical profile of Utror and Gabral valleys, district Swat, Pakistan. *Ethnobotanical leaflets* **2005**, *2005*, 9.

- (9) Shinwari, Z. K.; Qaiser, M. Efforts on conservation and sustainable use of medicinal plants of Pakistan. *Pak. J. Bot.* **2011**, *43*, 5–10.

- (10) Tariq, A.; Adnan, M.; AbdElsalam, N. M.; Fouad, H.; Hussain, K.; Ullah, R.; Ullah, A. Richness and cover of nontimber economic plants along altitude in temperate Himalayan forest-use types. *Sci. World J.* **2014**, *2014*, No. 748490. From NLM.

- (11) Benjamin, A.; Manickam, V. *Medicinal pteridophytes from the Western Ghats*, 2007.

- (12) Alam, F.; Khan, S. H. A.; Asad, M. Phytochemical, antimicrobial, antioxidant and enzyme inhibitory potential of medicinal plant *Dryopteris ramosa* (Hope) C. Chr. *BMC Complement. Med. Ther.* **2021**, *21*, No. 197. From NLM.

- (13) Arshad, M.; Ahmad, M. Medico-botanical investigation of medicinally important plants from Galliat areas, NWFP (Pakistan). *Ethnobotanical Leaflets* **2004**, *2004*, 6.

- (14) (a) Sabeen, M.; Ahmad, S. S. Exploring the folk medicinal flora of Abbottabad city, Pakistan. *Ethnobotanical Leaflets* **2009**, *2009*, 1. (b) Adnan, M.; Begum, S.; Latif, A.; Tareen, A. M.; Lee, L. Medicinal plants and their uses in selected temperate zones of Pakistani Hindukush-Himalaya. *J. Med. Plants Res.* **2012**, *6*, 4113–4127.

- (15) Abbasi, A. M.; Khan, M. A.; Shah, M. H.; Shah, M. M.; Pervez, A.; Ahmad, M. Ethnobotanical appraisal and cultural values of medicinally important wild edible vegetables of Lesser Himalayas-Pakistan. *J. Ethnobiol. Ethnomed.* **2013**, *9*, 66. From NLM.

- (16) Ahmad, K. S.; Qureshi, R.; Hameed, M.; Ahmad, F.; Nawaz, T. Conservation assessment and medicinal importance of some plants resources from Sharda, Neelum Valley, Azad Jammu and Kashmir, Pakistan. *Int. J. Agric. Biol.* **2012**, *14*, 997–1000.

- (17) Ahmad, K. S.; Habib, S. Indigenous knowledge of some medicinal plants of Himalaya region, Dawarian village, Neelum valley, Azad Jammu and Kashmir, Pakistan. *Univers. J. Plant Sci.* **2014**, *2*, 40–47.

- (18) Mir, S. A.; Mishra, A. K.; Reshi, Z. A.; Sharma, M. P. Preliminary phytochemical screening of some pteridophytes from district Shopian (J & K). *Int. J. Pharm. Pharm. Sci.* **2013**, *5*, 632–637.

- (19) Ishaque, M.; Bibi, Y.; Qayyum, A.; Iriti, M. Isolation and Structural Confirmation of Xanthone Isomers from *Dryopteris ramosa* (Hope) C. Chr. and Their In Vitro Antioxidant Mechanism. *Arabian J. Sci. Eng.* **2021**, *46*, S327–S337.

- (20) Bashir, S.; Janbaz, K. H.; Jabeen, Q.; Gilani, A. H. Studies on spasmogenic and spasmolytic activities of *Calendula officinalis* flowers. *Phytother. Res.* **2006**, *20*, 906–910. From NLM.
- (21) Abdur Rahman, H. M.; Bashir, S.; Gilani, A. H. Calcium channel blocking activity in *Desmostachya bipinnata* (L.) explains its use in gut and airways disorders. *Phytother. Res.* **2013**, *27*, 678–684. From NLM.
- (22) Council, N. *National Institutes of Health Guide for the Care and Use of Laboratory Animals*; The National Academies Press: Washington, DC, 2011.
- (23) Baloch, R.; Uzair, M.; Chauhdary, B. Phytochemical analysis, antioxidant and cytotoxic activities of *Dryopteris ramosa*. *Biomed. Res.* **2019**, *30*, 764–769.
- (24) Ishaque, M.; Bibi, Y.; Ayoubi, S. A.; Masood, S.; Nisa, S.; Qayyum, A. Iriflophenone-3-C- β -D Glucopyranoside from *Dryopteris ramosa* (Hope) C. Chr. with Promising Future as Natural Antibiotic for Gastrointestinal Tract Infections. *Antibiotics* **2021**, *10*, 1128.
- (25) Daina, A.; Michielin, O.; Zoete, V. SwissADME: a free web tool to evaluate pharmacokinetics, drug-likeness and medicinal chemistry friendliness of small molecules. *Sci. Rep.* **2017**, *7*, No. 42717.
- (26) Pires, D. E. V.; Blundell, T. L.; Ascher, D. B. pkCSM: predicting small-molecule pharmacokinetic and toxicity properties using graph-based signatures. *J. Med. Chem.* **2015**, *58*, 4066–4072.
- (27) Sirous, H.; Chemi, G.; Campiani, G.; Brogi, S. An integrated in silico screening strategy for identifying promising disruptors of p53-MDM2 interaction. *Comput. Biol. Chem.* **2019**, *83*, No. 107105.
- (28) Saqib, F.; Usman, F.; Malik, S.; Bano, N.; Ur-Rahman, N.; Riaz, M.; Vlaic, R. A. M.; Mureşan, C. C. Antidiarrheal and Cardio-Depressant Effects of *Himalaiella heteromalla* (D. Don) Raab-Straube: In Vitro, In Vivo, and In Silico Studies. *Plants* **2022**, *11*, No. 78.
- (29) Saqib, F.; Janbaz, K. H. Rationalizing ethnopharmacological uses of *Alternanthera sessilis*: A folk medicinal plant of Pakistan to manage diarrhea, asthma and hypertension. *J. Ethnopharmacol.* **2016**, *182*, 110–121.
- (30) Rehman, S.; Imran, M. An ethno-botanical review of seeds of *Cucumis sativa* (Maghz-e-tukhme khiyarain) from Unani Medicine and its Pharmacological Updates. *Int. J. Adv. Pharm. Med. Bioallied Sci.* **2021**, *9*, 31–36.
- (31) Janbaz, K. H.; Zaeem, A. M.; Saqib, F.; Imran, I.; Zia-Ul-Haq, M.; Abid, R. M.; Jaar, H.Z.E.; Moga, M. Scientific Basis for Use of *Pyrus pashia* Buch.-Ham. ex D. Don. Fruit in Gastrointestinal, Respiratory and Cardiovascular Ailments. *PLoS One* **2015**, *10*, No. e0118605.
- (32) Gilani, A. H.; Bashir, S.; Janbaz, K. H.; Khan, A. Pharmacological basis for the use of *Fumaria indica* in constipation and diarrhea. *J. Ethnopharmacol.* **2005**, *96*, 585–589. From NLM.
- (33) García, X.; Cartas-Heredia, L.; Lorenzana-Jimenez, M.; Gijón, E. Vasoconstrictor effect of *Cissus sicyoides* on guinea-pig aortic rings. *Gen. Pharmacol.* **1997**, *29*, 457–462.
- (34) Ratheesh, M.; Helen, A. Anti-inflammatory activity of *Ruta graveolens* Linn on carrageenan induced paw edema in wistar male rats. *Afr. J. Biotechnol.* **2007**, *6*, 1209–12011.
- (35) Zarei, M.; Mohammadi, S.; Komaki, A. Antinociceptive activity of *Inula britannica* L. and patuletin: in vivo and possible mechanisms studies. *J. Ethnopharmacol.* **2018**, *219*, 351–358.
- (36) Balarastaghi, S.; Delirrad, M.; Jafari, A.; Majidi, M.; Sadeghi, M.; Zare-Zardini, H.; Karimi, G.; Ghorani-Azam, A. Potential benefits versus hazards of herbal therapy during pregnancy; a systematic review of available literature. *Phytother. Res.* **2022**, *36*, 824–841.
- (37) Capasso, R.; Aviello, G.; Romano, B.; Atorino, G.; Pagano, E.; Borrelli, F. Inhibitory effect of quercetin on rat trachea contractility in vitro. *J. Pharm. Pharmacol.* **2009**, *61*, 115–119.
- (38) Djelili, H.; Arrar, L.; Naline, E.; Devillier, P. Relaxant Effects of Quercetin and Rutin on Human Isolated Bronchus. *Chin. Med.* **2012**, *03*, 94–100.
- (39) *Release, S. 1: QikProp*; Schrödinger, LLC: New York, NY, 2020.
- (40) Waszkowycz, B.; Clark, D. E.; Gancia, E. Outstanding challenges in protein–ligand docking and structure-based virtual screening. *Wiley Interdiscip. Rev.: Comput. Mol. Sci.* **2011**, *1*, 229–259.
- (41) Wahid, M.; Saqib, F.; Qamar, M.; Ziora, Z. M. Antispasmodic activity of the ethanol extract of *Citrullus lanatus* seeds: Justifying ethnomedicinal use in Pakistan to treat asthma and diarrhea. *J. Ethnopharmacol.* **2022**, *295*, No. 115314.
- (42) Ventura-Martinez, R.; Angeles-Lopez, G. E.; Gonzalez-Trujano, M. E.; Carrasco, O. F.; Deciga-Campos, M. Study of Antispasmodic and Antidiarrheal Activities of *Tagetes lucida* (Mexican Tarragon) in Experimental Models and Its Mechanism of Action. *J. Evidence-Based Complementary Altern. Med.* **2020**, *2020*, No. 7140642. From NLM.
- (43) Amira, S.; Rotonondo, A.; Mulè, F. Relaxant effects of flavonoids on the mouse isolated stomach: structure-activity relationships. *Eur. J. Pharmacol.* **2008**, *599*, 126–130. From NLM.
- (44) Nazir, S.; Khan, H.; Khan, S. A.; Alam, W.; Ghaffar, R.; Khan, S. H. A.; Daglia, M. In vivo acute toxicity, laxative and antiulcer effect of the extract of *Dryopteris Ramose*. *Cell. Mol. Biol.* **2021**, *67*, 9–16.
- (45) Ajay, M.; Chai, H. J.; Mustafa, A. M.; Gilani, A. H.; Mustafa, M. R. Mechanisms of the anti-hypertensive effect of *Hibiscus sabdariffa* L. calyces. *J. Ethnopharmacol.* **2007**, *109*, 388–393. From NLM.
- (46) Yasin, M.; Hussain Janbaz, K.; Imran, I.; Gilani, A. U.; Bashir, S. Pharmacological studies on the antispasmodic, bronchodilator and anti-platelet activities of *Abies webbiana*. *Phytother. Res.* **2014**, *28*, 1182–1187. From NLM.
- (47) Wahid, M.; Saqib, F.; Ahmedah, H. T.; Gavis, C. M.; De Feo, V.; Hoge, M.; Moga, M.; Chicea, R. *Cucumis sativus* L. seeds ameliorate muscular spasm-induced gastrointestinal and respiratory disorders by simultaneously inhibiting calcium mediated signaling pathway. *Pharmaceuticals* **2021**, *14*, 1197.
- (48) Sharkey, K.; MacNaughton, W. Pharmacotherapy of Gastric Acidity, Peptic Ulcers, and Gastroesophageal Reflux Disease. In *Goodman and Gilman's: The Pharmacological Basis of Therapeutics*; McGraw Hill, 2018; Vol. 13.
- (49) Wahid, M.; Saqib, F. Scientific basis for medicinal use of *Citrullus lanatus* (Thunb.) in diarrhea and asthma: In vitro, in vivo and in silico studies. *Phytomedicine* **2022**, *98*, No. 153978.
- (50) Saqib, F.; Janbaz, K. H. Ethnopharmacological basis for folkloric claims of *Anagallis arvensis* Linn. (Scarlet Pimpernel) as prokinetic, spasmolytic and hypotensive in province of Punjab, Pakistan. *J. Ethnopharmacol.* **2021**, *267*, No. 113634.
- (51) Bin-Jumah, M.; Alwakeel, S. S.; Moga, M.; Buvnariu, L.; Bigiu, N.; Zia-Ul-Haq, M. Application of Carotenoids in Cosmetics. In *Carotenoids: Structure and Function in the Human Body*; Springer, 2021; pp 747–756.
- (52) Zia-Ul-Haq, M. Past, Present and Future of Carotenoids Research. In *Carotenoids: Structure and Function in the Human Body*; Springer, 2021; pp 827–854.
- (53) Saqib, F.; Janbaz, K. H.; Latif, M. F.; Gilani, A. H.; Bashir, S. Ethnopharmacological studies on antispasmodic, bronchodilator and antiplatelet aggregation activities of *Blepharis edulis* Pers. *Asian J. Nat. Appl. Sci.* **2012**, *1*, 33–45.
- (54) Khalid, A.; Zaheer ul, H.; Ghayur, M. N.; Feroz, F.; Atta ur, R.; Gilani, A. H.; Choudhary, M. I. Cholinesterase inhibitory and spasmolytic potential of steroidal alkaloids. *J. Steroid Biochem. Mol. Biol.* **2004**, *92*, 477–484. From NLM.
- (55) Ghayur, M. N.; Khan, H.; Gilani, A. H. Antispasmodic, bronchodilator and vasodilator activities of (+)-catechin, a naturally occurring flavonoid. *Arch. Pharmacol. Res.* **2007**, *30*, 970–975. From NLM.
- (56) Jung, C. H.; Ji, Y. L.; Chul, H. C.; Chang, J. K. Anti-asthmatic action of quercetin and rutin in conscious guinea-pigs challenged with aerosolized ovalbumin. *Arch. Pharmacol. Res.* **2007**, *30*, 1599–1607.
- (57) Ko, W.-C.; Liu, P.-Y.; Chen, J.-L.; Leu, I.-J.; Shih, C.-M. Relaxant Effects of Flavonoids in Isolated Guinea Pig Trachea and Their Structure-Activity Relationships. *Planta Med.* **2003**, *69*, 1086–1090.
- (58) Janbaz, K. H.; Jan, A.; Qadir, M. I.; Gilani, A. H. Spasmolytic, bronchodilator and vasorelaxant activity of methanolic extract of

Tephrosia purpurea. *Acta Pol. Pharm.* **2013**, *70*, 261–269. From NLM.

(59) Ahmed, T. Calcium antagonists: potential for asthma therapy. *Choices Respir Manage* **1992**, *22*, 41–43.

(60) Kamei, J.; Kasuya, Y. Antitussive effects of Ca²⁺ channel antagonists. *Eur. J. Pharmacol.* **1992**, *212*, 61–66. From NLM.

(61) Kumar, V.; Kaithwas, G.; Anwar, F.; Rahman, M.; Patel, D. K.; Singh, Y.; Verma, A. Effect of variable doses of *Paederia foetida* L. combat against experimentally-induced systemic and topical inflammation in Wistar rats. *Curr. Bioact. Compd.* **2018**, *14*, 70–79.

(62) Muller, J. A. I.; Moslaves, I. S. B.; Oliveira, E. J. T.; Portugal, L. C.; Oliveira, R. J.; Mortari, M. R.; Toffoli-Kadri, M. C. Pro-inflammatory response induced by the venom of *Parachartergus fraternus* wasp. *Toxicon* **2021**, *190*, 11–19.

(63) Agbor, G. A.; Longo, F.; Makong, E. A.; Tarkang, P. A. Evaluation of the antidiarrheal and antioxidant properties of *Justicia hypocrateriformis*. *Pharm. Biol.* **2014**, *52*, 1128–1133. From NLM.

(64) Crowe, A.; Wong, P. Potential roles of P-gp and calcium channels in loperamide and diphenoxylate transport. *Toxicol. Appl. Pharmacol.* **2003**, *193*, 127–137.

THE IMAGING EVALUATION OF TYPICAL AND ATYPICAL CALCIFICATIONS IN DIFFERENT ANATOMICAL REGIONS STUDY IN BRASOV, ROMANIA

Gabriela Sechel, Angela Repanovici*, Rosana Manea, Victoria Burtea

Transilvania University of Brasov

*Corresponding author. E-mail: arepanovici@unitbv.ro

THE IMAGING EVALUATION OF TYPICAL AND ATYPICAL CALCIFICATIONS IN DIFFERENT ANATOMICAL REGIONS STUDY IN BRASOV, ROMANIA (Abstract): Calcifications in different anatomical regions were identified by using ultrasound exam, radiography, mammography, and computer tomography, according to the anatomical region investigated. **The aim** of this research is to highlighting and evaluating typical and atypical calcifications in the organs of different anatomical regions, correlating them with age and pathology, finding the best imaging methods for detecting calcifications according to the anatomical region examined. **Material and methods** This was a prospective study was conducted for 2 months in 2018, in a private hospital, on 1338 patients of different ages, with or without symptomatology, who were randomly assigned to the Department of Radiology and Medical Imaging for the following types of examinations: radiography, computer tomography, ultrasound exam and mammography. **Results:** Calcifications found by imagistic methods were evaluated in the following anatomical regions: head, neck, thorax, abdomen, and pelvis. A database was generated where all data was collected and analyzed with SPSS 20.0 software. Various situations have been highlighted by anatomical regions. **Keywords:** AGE, CALCIFICATION, ANATOMICAL REGIONS, ULTRASOUND EXAM, RADIOLOGICAL EXAM, MAMMOGRAPHY, COMPUTED TOMOGRAPHY.

Calcifications may be physiological or pathological and may occur at different ages.

We will briefly describe a general assessment of these calcifications in some anatomical regions considered in the study to understand the importance of their identification, their benign and malignant characterization, and their association with the age and type of imaging examination. The most common intracranial calcifications were highlighted in the pineal gland (a calcification over 1 cm in diameter under the age of 9 years may be suggestive of a neoplasm),

habenula, choroid plexus (frequently evident in the middle portion of the lateral ventricles), basal ganglia (calcifications are 0.3-1.5% and increase with age), falx, tentorium cerebella (affects 10% of the elderly population), sagittal sinus and petroclinoid ligaments (related to elderly degeneration) (1). The most common neoplastic calcification are: oligodendroglioma (70-90%), craniopharyngioma (50-80%), germ cell neoplasms and pineal neoplasms (60-80%), central neurocytoma and primitive neuroectodermal tumor (50-70%), ependymoma (50%), ganglioglioma (35-50%), dysembri-

The imaging evaluation of typical and atypical calcifications in different anatomical regions study in Brasov, Romania

yonic neuroectodermal tumor (20-25%), meningioma (20-25%), choroid plexus papilloma (25%), medulloblastoma and low grade astrocytoma (20%), and pilocystic astrocytoma (10%) (2).

In the chest region calcifications are highlighted in the pulmonary parenchyma, mediastinum, hilar and mediastinal lymph nodes, pleura chest wall, vascular, or any combination of these structures. Gross calcifications are evident on a conventional chest radiograph, but smaller calcific deposits are better evident on digital radiograph, computer tomography and high-resolutions CT (3). Pulmonary calcifications are the common asymptomatic finding discovered on chest X-ray and Chest CT (4).

In breast calcifications high-quality image and magnification on mammographic views are essential for the detection and evaluation of breast calcifications. It is important to differentiate the microcalcifications of benign origin (which increase their frequency with the age) from those that are suspected to be malignant, since 55% of non-palpable cancers are of ductal carcinoma form in situ. Distributions diffuse/scattered are a characteristic of benign calcifications. Regional distribution can signify a 26% probability of malignancy. Grouped/clustered calcifications more than 5 per 1 cm (this being the lower limit) indicate a suspicion of malignancy. Linear distribution calcifications may indicate a 60% and the segmental distribution a 62% malignancy probability (5). The positron emission mammography investigation is useful for assessing patients with suspected focal calcifications present on mammography. This is absolutely necessary for identifying invasive carcinomas and high-grade ductal carcinoma in situ. It becomes useful

for avoiding false negative results of stereotactic biopsy (2).

For region of abdomen and pelvis calcifications can be visualized in normal and abnormal abdominal structure. They appear on radiographs and CT images as radiopaque or hyper-dense lesions (3).

On ultrasound, calcification appears as hyperechoic, posterior acoustic shadowing depending on the size and characteristics of the surface structure of calcification. The color Doppler twinkling artifact is a helpful sign for identifying small calcifications and thus can improve diagnostic (6). Computer tomography is regarded as gold standard for the identification of calcified lesions. Normal structures that calcify are costal cartilage, mesenteric lymph nodes, pelvic vein clots, and prostate gland. A high content of calcium in abnormal structures may indicate pathology of pancreas, renal parenchymal tissue, blood vessels and vascular aneurysms, gallbladder fibroids (leiomyoma). The same is true for biliary, renal, bladder calculi, appendicolith, and teratoma. Gynecological calcifications, fibroids, can become calcified and appear as rounded structures of varying sizes and locations in the pelvis (1). Frequently encountered abdominal and pelvic tumors often present a typical calcification pattern (7).

Miscellaneous Tumors appear as: calcifications with punctate pattern are unusual in the gastrointestinal stromal tumors (3-10%); solid pseudopapillary neoplasm is a peripheral curvilinear, rim (eggshell), punctate pattern of calcification. Calcification is seen as single or multiple form, it can be located peripheral, central or internal septa of tumor and can be punctate (round), amorphous (irregular), curvilinear or rim (eggshell) (8). Calcifications in the pancreas were found in 10-20% of cases

with a peripheral, curvilinear pattern or septal location, including punctate and coarse (amorphous) pattern. Intratumorally calcification can differentiate pancreatic neuroendocrine tumor (20% show calcifications) from adenocarcinoma (2%).

Calcifications in the liver are a rare form of the biliary neoplasm, such as solitary cyst adenocarcinoma, which is well encapsulated. These are rarely found but have been reported in 47% of the cases.

Calcifications in the appendix can be curvilinear, peripheral, and can occur in <50% of cases in mucinous adenoma, low-grade mucinous neoplasm, and mucinous adenocarcinoma. Mucinous neoplasm appears as a round or tubular cystic mass; wall thickening, and the irregular shape raise suspicions of malignancy (9).

Calcifications can be seen in all types of neurogenic tumors with various patterns. The tumor usually occurs in the retroperitoneum of the adrenal gland (10).

Castleman disease is an uncommon benign lymph proliferative disorder. Hyperplasia of lymphoid follicles is located in thorax in 70% of cases, 10-15% in the neck, 10-15% in the abdomen, retroperitoneum and pelvis. Calcifications patterns include punctate, peripheral, central, arborizing calcifications (8-11,12)

MATERIAL AND METHODS

This was a prospective study, conducted for a period of 2 months in the Department of Radiology and Medical Imaging of a private hospital in Brasov. The batch consisted of 1,338 patients of different ages who underwent various imaging investigations, namely: radiographic examination, computed tomography, ultrasound scan, and mammography. The devices on which the study was conducted are radiography

device - Axiom Iconos R200 - *Siemens*, computed tomography - Somatom Emotion 16 - *Siemens*, ultrasound RS 80 with Prestige - *Samsung*, Logiq S7 - *General Electric*, mammography - Senographe Crystal - *General Electric*. Calcifications found imagistically were evaluated in the following anatomical regions: head, neck, thorax, abdomen, and pelvis.

The age-groups of the patients in the study are not homogeneous; thus, we have calculated percentages distributed according to each anatomical area from the total of persons in each age group.

The distribution of the patient batch by age group is unbalanced; therefore, the percentages distributed to each anatomical area were calculated from the total age group. Independent variables are age categories, while dependent variables are the percentage of people with calcifications in different age groups.

A database was generated where all data was collected and analyzed with *SPSS version 20.0* statistical software. The collected data was processed in Excel, the graphs being generated using Pivot tables. The X^2 homogeneity test was applied to determine whether there are statistically significant differences in the age groups of the patients participating in the study and the occurrence of calcifications in these five anatomical regions.

The purpose of this study was to highlight calcifications in different anatomical regions except limbs, in symptomatic or asymptomatic patients, and correlate them with the pathology and type of examination.

RESULTS

Analyzing the presence of the patients in the batch studied by age groups it was

The imaging evaluation of typical and atypical calcifications in different anatomical regions study in Brasov, Romania

found that the most representative incidence was in the 51-60 years old age group (28.7% of the patients), followed by the age group 41-50 years - 18.8% and then the group 61-70 years - 16.8%, these age-groups representing more than half of the studied total of patients. The low incidence was highlighted under the age of 30 and over 80 years, with an average of 4.5%. If we consider the distribution of patients depending on whether or not a symptomatology is present, symptoms in different

regions were found in 67% of patients. Most of them accused frequent pains in the abdominal and cranial region (for both sexes). In the case of female patient's chest pain was noted, especially in the mammary gland. 33% of patients showed no symptoms; most of these patients came for a routine or regular control sent by an occupational physician.

In terms of gender of patients, a slightly higher (by 1%) incidence in the case of the females was noted (tab. I)

TABLE I
Distribution of patients with and without calcifications by age group

Age group	0-10	11-20	21-30	31-40	41-50	51-60	61-70	71-80	>80
With calcifications	3	6	43	85	185	286	191	105	74
Without calcifications	21	38	55	44	67	98	34	3	0
Percentage with calcifications	12.5	13.63	48.87	65.89	73.41	74.47	84.88	97.2	100

Analyzing the presence of calcifications according to the patients' age, it was found that their age-related linear increase was lower for those under 20, reaching 73% for the age group of 41-50, 97% for the group over 70 years, and 100% for the persons in the group over 80 years.

There is an increasing trend in the number of calcifications in total by age. Different trends have been observed for each anatomical region (fig. 1).

The sample we had was not equally distributed by age category and we took in

consideration the percentage of patients presenting calcifications from each age group.

The regression was performed for each anatomical region to analyze age dependency of the anatomical area in the patients presenting calcifications. There was a 91% influence of calcifications on all anatomical regions studied in relation to age. Straights and regression equations have been drawn.

The determination coefficient, R square, for each anatomical region was obtained (fig. 2).

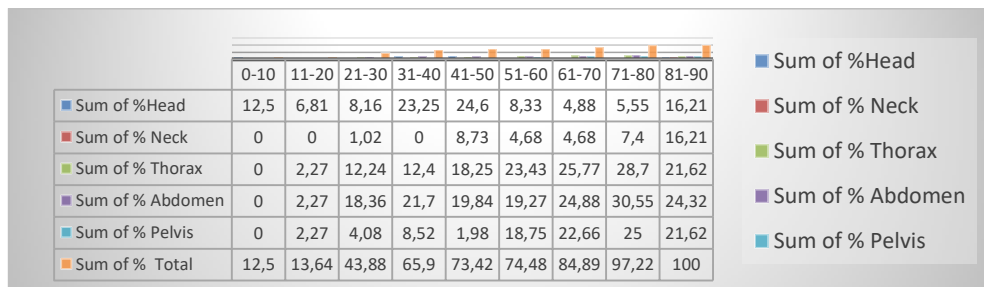


Fig. 1. Percentage distribution of patients according to age group and anatomical region

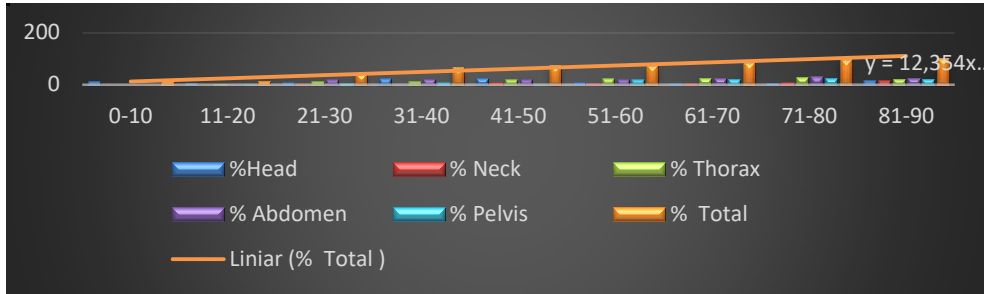


Fig. 2. Linear regression for each anatomical region

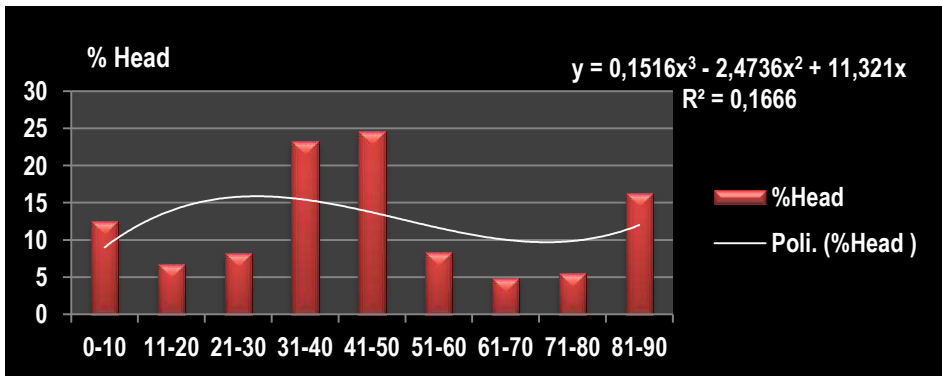


Fig. 3. Polynomial regression between head region and age

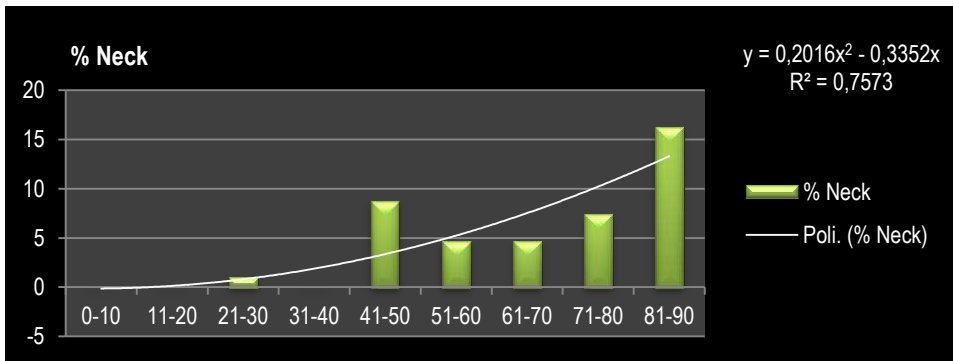


Fig. 4. Polynomial regression between neck region and age

R square shows how much age influences the presence of calcifications in various anatomical regions.

R square in the Head region has an influence of 16% in what calcifications are concerned, but it is inversely proportional with the increase of age. Between 30-50

years there is the highest peak (a mean of approximately 24%). The peak may be influenced by stress factors (fig. 3).

As far as the neck region is concerned, the number of people presenting calcifications increases with age, but a maximum appears around the age of 41-50 of 75% (fig. 4).

The imaging evaluation of typical and atypical calcifications in different anatomical regions study in Brasov, Romania

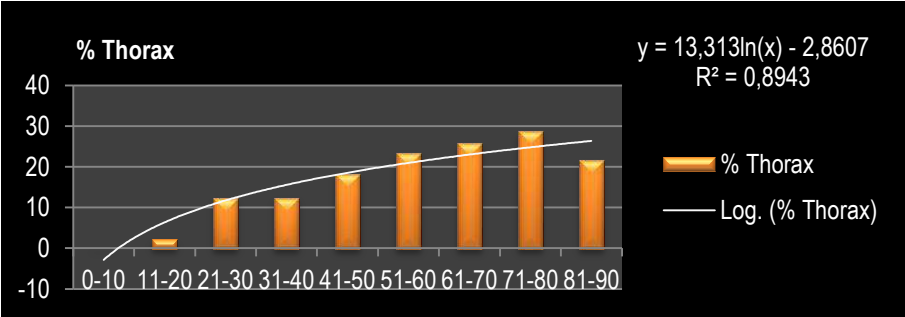


Fig. 5. Logarithmic regression between thorax region and age

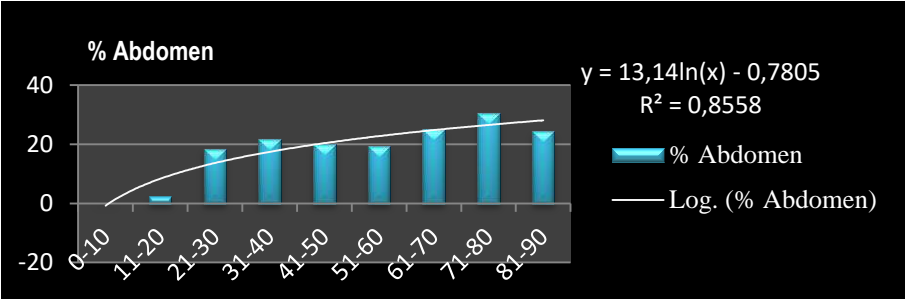


Fig. 6. Logarithmic regression between abdominal region and age

In the case of the thoracic region, we have the strongest correlation of 84% and a proportional increase with age of calcified individuals, but a reduction for the patients over 80 years due to the small number of persons in this age-group who came for an imaging evaluation in the period of the study (fig. 5).

In the abdominal region, we also have a close relationship of 85% and a rise of calcifications with age, but it falls in the case of the patients over 80 years. This may be due to the small number of patients who were present in relation to the other age groups, as was also the case for the results concerning the chest region (fig. 6).

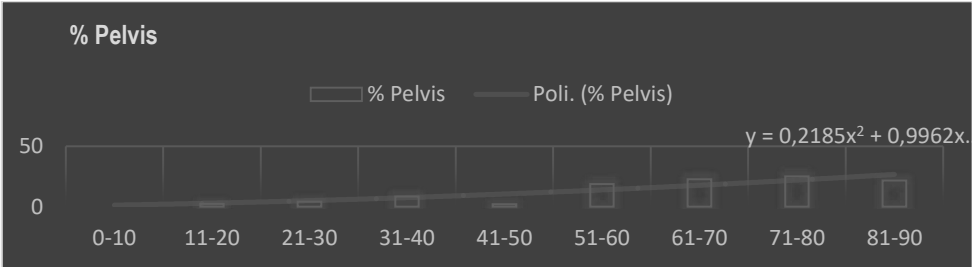


Fig. 7. Logarithmic regression between the pelvic region and age

In the pelvic region we have an 80% correlation, an increase proportional to the

age of people with calcifications, similar to the chest and abdominal region (fig.7.)

TABLE II
Determination coefficient R square for each anatomical region

Anatomic region calcifications / Age	Head	Neck	Thorax	Abdomen	Pelvis
R Square	0.1666	0.7573	0.8943	0.8558	0.8094

By considering the R square determination coefficient for each anatomical region, an influence of age in the occurrence of calcifications in different anatomical regions was found. In the head region, there is a small influence (16%) of age on calcification. Age dependence in the occurrence of calcification in the neck is 75%. The risk of calcification at thorax level is higher, 89%. For the pelvis and the abdomen, the percentage is 85% and 80%, respectively (tab. II). Calcifications were less numerous in the cranial region due to its smaller volume and number of organs located in it than in, for example, the thoracic and abdominal region. Calcifications were more frequent in the elderly patients, but the number of patients who were part of the study, especially those over 80, was smaller. Using SPSS we showed that there are statistically significant differences between the groups analyzed by $X^2 = 25,674$; $p = 0.001$, meaning that age does affect calcifications. Age influences cranial calcifications, as seen in the observed and expected counting table. It is statistically demonstrated that calcifications occur depending on the group of participants and on the age category. DATA-Weight Cases were weighted. By this statistical method, for each anatomical part we have determined the ages in which there is a tendency for the occurrence of more calcifications than is normally expected. In this study, the presence of typical and atypical calcifications in different organs, age groups, case correlations and pathology were analyzed.

DISCUSSION

In the head region, we identified the presence of calcifications in the young age up to 40 years in the pineal gland, habenular commissure, falx, tentorium cerebellum, and a case of congenital calcifications in the *Sturge Weber* syndrome. Between 40-50 years, calcifications occurred in the lenticular nucleus and in one case of cerebral tumor recurrence. After the age of 50, the presence of atheromatous calcium plaques was observed in the intracranial cerebral vessels, associated with the presence of the pathology. Calcifications in the neck region have been noted frequently in nodules in the thyroid gland (with a peak between 40-50 years), increasing also with age at the neck artery. Until the age of 40, calcifications in the thoracic region were revealed in the form of small calcifications at the level of mediastinal adenopathy, wall calcifications in the costal cartilage, while after 40 years at the level of some lung or solitary nodules, solitary or multiples. Calcifications in the abdominal region were surprisingly frequent in the 21-30 age group.

The presence of kidney and gall bladder stones and the environmental influences were more often observed among female patients in this group. After 40 years calcifications have been revealed in the spleen, adrenal gland, pancreas, calcifications associated with the history of pathology, in the male sex these being commonly encountered in the pancreas. At the age of 11-20 years, physiological calcifications in the prostate were present, the pathological calcifications being more frequent after the age of 50. At females, there have been calcifications in the genital

The imaging evaluation of typical and atypical calcifications in different anatomical regions study in Brasov, Romania

sphere, especially calcifications in the uterine fibromatous nodules. In both genders, calcifications of normal structures, namely pelvic vein clots -phlebolith, and at the level of some vessels were noted. Imaging investigations are useful tools for woman after 50, especially in the postmenopausal period.

CONCLUSIONS

In the revised literature, calcifications were highlighted in all anatomical regions, in most organs by different methods, without correlating them with the pathology of other organs, we tracked their incidence and correlated with age and certain pathologies existing only in the analyzed region. Highlighting intracranial calcifications by CT examination requires their description in terms of location of size and shape,

which are necessary for a correct diagnosis and their correlation with age and neurological signs for true diagnosis and therapy. The method is original because the random group determined by collecting imaging investigations for two months, considering five anatomical regions, demonstrates the dependence of the number of patients with calcifications on their age, but also the particularities of each anatomical area. Using imaging investigation and correlating with patient's symptomatology or age is an accessible and noninvasive tool for screening neoplasms and benign tumors, with an impact on group ages people, especially on the elderly. In the future studies we intend to correlate the presence of calcifications in certain organs with their pathology in other anatomical regions.

REFERENCES

1. Yang CZ, Yaniger SI, Jordan VC, Klein DJ, Bittner GD. Most plastic products release estrogenic chemicals: a potential health problem that can be solved. *Environ Health Perspect* 2011; 119(7): 989-996.
2. Yilmaz K, Çalli C, Karabulut N, Öncel C. Intracranial Calcifications on CT. *Diagnostic and Interventional Radiology* 2010; 16 (4): 263-269.
3. Holcombe SA, Ejima S, Wang SC. Calcification of Costal Cartilage in the Adult Rib Cage. *Proceedings of the 2017 International IRCOBI Conference on the Biomechanics of Injury*.
4. Bendayan D, Barziv Y, Kramer MR. Pulmonary Calcifications: A Review. *Respiratory Medicine* 2000; 94 (3): 190-193.
5. Hernández PLA, Estrada TT, Pizarro AL, Cisternas MLD, Tapia CS. Calcificaciones Mamarias: Descripción y Clasificación Según La 5 Aedición BI-RADS. *Revista Chilena de Radiología* 2016; 22(2): 80-91.
6. Yu MH, Kim YJ, Park HS, Jung SI, Jeon HJ. Imaging Patterns of Intratumorally Calcification in the Abdominopelvic Cavity. *Korean Journal of Radiology* 2017; 18(2): 323-335.
7. Belém LC, Zanetti G, Soares Souza A, Hochegger B, Duarte Guimarães M, Nobre LF, Souza Rodrigues R, Marchiori E. Metastatic Pulmonary Calcification: State-of-the-Art Review Focused on Imaging Findings. *Respiratory Medicine* 2014; 108(5): 668-676.
8. Peres LA, Verona Pércio PP. Mineral and Bone Disorder and Vascular Calcification in Patients with Chronic Kidney Disease. *Jornal Brasileiro de Nefrologia* 2014; 36(2): 201-207.
9. Wilson PWF, Kauppila LI, O'Donnell CJ, Kiel DP, Polak JM, Cupples LA. Abdominal Aortic Calcific Deposits are an Important Predictor of Vascular Morbidity and Mortality. *Circulation* 2001; 103(11): 1529-1534.
10. Chen, YG, Kao WY, Tsai SH. Non-specific but Significant. *American Journal of Medicine* 2012; 125(5): 461-464.
11. Omami G. Soft Tissue Calcification in Oral and Maxillofacial Imaging: a pictorial review. *International Journal of Dentistry and Oral Science* 2016; 3(4): 219-224.
12. Yiu AJ, Callaghan D, Sultana R, Bandyopadhyay BC. Vascular Calcification and Stone Disease: A New Look towards the Mechanism. *Journal of Cardiovascular Development and Disease* 2015; 2(3): 141-164.

Interesting Images

The Many Hidden Faces of Gallbladder Carcinoma on CT and MRI Imaging—From A to Z

Damaris Neculoiu ¹, Lavinia Claudia Neculoiu ^{1,*}, Ramona Mihaela Popa ¹ and Rosana Mihaela Manea ^{1,2}¹ Department of Radiology and Medical Imaging, Clinical Emergency County Hospital of Braşov, 500326 Braşov, Romania² Faculty of Medicine, “Transilvania” University of Braşov, Nicolae Bălcescu 56, 500019 Braşov, Romania

* Correspondence: neculoiulavinia@gmail.com

Abstract: Gallbladder carcinoma represents the most aggressive biliary tract cancer and the sixth most common gastrointestinal malignancy. The diagnosis is a challenging clinical task due to its clinical presentation, which is often non-specific, mimicking a heterogeneous group of diseases, as well as benign processes such as complicated cholecystitis, xanthogranulomatous cholecystitis, adenomyomatosis, porcelain gallbladder or metastasis to the gallbladder (most frequently derived from melanoma, renal cell carcinoma). Risk factors include gallstones, carcinogen exposure, porcelain gallbladder, typhoid carrier state, gallbladder polyps and abnormal pancreaticobiliary ductal junction. Typical imaging features on CT or MRI reveal three major patterns: asymmetric focal or diffuse wall-thickening of the gallbladder, a solid mass that replaces the gallbladder and invades the adjacent organs or as an intraluminal enhancement mass arising predominantly from the gallbladder fundus. The tumor can spread to the liver, the adjacent internal organs and lymph nodes. Depending on the disease stage, surgical resection is the curative treatment option in early stages and adjuvant combination chemotherapy at advanced stages. The purpose of this scientific paper is to fully illustrate and evaluate, through multimodality imaging findings (CT and MRI), different presentations and imaging scenarios of gallbladder cancer in six patients and thoroughly analyze the risk factors, patterns of spread and differential diagnosis regarding each particular case.



Citation: Neculoiu, D.; Neculoiu, L.C.; Popa, R.M.; Manea, R.M. The Many Hidden Faces of Gallbladder Carcinoma on CT and MRI Imaging—From A to Z. *Diagnostics* **2024**, *14*, 475. <https://doi.org/10.3390/diagnostics14050475>

Academic Editors: Kazushi Numata, Francescamaria Donati and Piero Boraschi

Received: 2 December 2023

Revised: 11 February 2024

Accepted: 19 February 2024

Published: 22 February 2024



Copyright: © 2024 by the authors. Licensee MDPI, Basel, Switzerland. This article is an open access article distributed under the terms and conditions of the Creative Commons Attribution (CC BY) license (<https://creativecommons.org/licenses/by/4.0/>).

Keywords: gallbladder; gallbladder cancer; biliary tract cancer; CT; MRI; oncology; surgery; metastases

Gallbladder cancer is the most common malignancy of the biliary tract and the sixth most common cancer of the gastrointestinal system [1]. According to GLOBOCAN estimates, gallbladder cancer is relatively rare and stands in 24th place among the most frequent type of cancers worldwide with more than 115,949 new cases in 2020 [2,3]. In the majority of cases, gallbladder carcinoma is asymptomatic or the clinical presentation is often vague, non-specific and discovered at an advanced stage [4,5]. Imaging plays a crucial and decisive role in the diagnosis, staging and subsequent management planning [6]. Occasionally, gallbladder cancer might be discovered following a cholecystectomy. Moreover, gallbladder cancer is thought to be favored by chronic cholelithiasis, cholecystolithiasis, gallbladder polyps and porcelain gallbladder [7]. The prevalence of the disease is primarily among elderly women over 60 years-old. The highest incidence occurs in South American countries, Chile, Ecuador, India, Pakistan, Japan and South Korea. Incidence of gallbladder cancer is 1–2 cases per 100,000 people [3,8,9]. However, gallbladder carcinoma still remains a relatively rare pathology with a poor prognosis and it usually presents at a very advanced stage [1]. Late-stage illness frequently manifests with anorexia, weight loss, abdominal pain and jaundice [3].

Diagnostic imaging modalities for the gallbladder cancer include ultrasound, computerized tomography (CT) and magnetic resonance imaging (MRI). CT and MRI are both effective imaging modalities, but MRI provides superior soft-tissue characterization of the gallbladder and biliary tree. The use of hepatobiliary contrast agents (gadolinium chelates)

with increased hepatobiliary excretion in abdominal MRI imaging may offer valuable information by providing enhanced images of the biliary tree [10].

We hereby fully illustrate the case of a 67-year-old female patient, who was admitted to the Emergency Department with intense pain localized in the right renal fossa, radiating to the right abdominal flank, accompanied by nausea with an onset of approximately two weeks. During the physical examination, a reduced abdominal wall mobility with respiratory movements was observed, along with pain in the right hypochondrium and muscular defense. Her medical history included hypertension grade 3 and congestive heart failure. Laboratory tests showed elevated inflammatory markers (leukocytosis, procalcitonin, CRP) and hypochromic microcytic anemia.

Biphasic (arterial phase followed by venous phase) contrast-enhanced emergency CT was performed (Figure 1), which clearly highlighted a gallbladder hydrops, with asymmetric, irregular gallbladder mural thickening, associated with multiple intraluminal mixed stones (Panel A). The tumoral mass extends directly into the adjacent liver parenchyma in segments IV and V and is in contact with the ascending colon (Panel C). Hepatomegaly can be observed (right hepatic lobe measures = 190 mm), with nodular lesions, disseminated in both hepatic lobes, hypodense, with rim peripheral contrast enhancement, more numerous in the right lobe, presenting various sizes (up to 35 mm in segment V) highly suggestive of liver metastases (Panel B and Panel C). Lymphatic metastases are common in gallbladder cancer. In this particular case, CT showed multiple lymph nodes enlargements in the hilar, mesenteric, celiac and precaval regions, up to 26/25 mm (measured in the hepatic hilum), with associated central necrosis (Panel D).

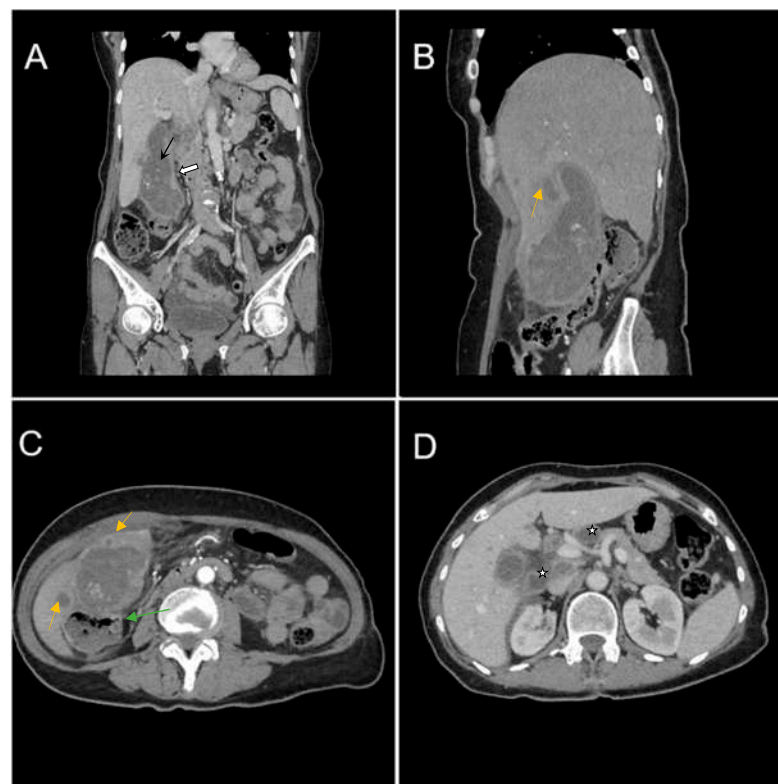


Figure 1. Multiplanar sections of contrast-enhanced CT acquisitions richly illustrating a low differentiated gallbladder adenocarcinoma. (A) Gallbladder hydrops (>40 mm transverse measurement, 142 mm longitudinal measurement) with asymmetric gallbladder mural thickening, 7 mm (white arrow), and multiple intraluminal mixed stones, 5–8 mm (black arrow). (B,C) Liver metastases—hypodense nodular hepatic lesions with rim contrast enhancement (yellow arrow). (C) Tumoral extension into IV, V segments of the right hepatic lobe and contact with the ascending colon (green arrow). (D) Lymphatic metastases (white stars).

The patient was transferred to the General Surgery Department for specialized treatment (intravenous antibiotics, intravenous hydration and correction of electrolyte abnormalities). After laparoscopy and laparotomy, a subhepatic perforated tumor with duodenum and transvers colon invasion was revealed. A partial cholecystectomy was performed with cholecystostomy and intraperitoneal drain. The postoperative evolution progressed without incident.

Formalin-fixed paraffin-embedded tissue sections from gallbladder and liver were examined histologically. The microscopic description was suggestive of poorly differentiated gallbladder adenocarcinoma (G3); pT3NxMx. The liver metastatic site was pathologically confirmed. TNM according to the AJCC (American Joint Committee on Cancer) 8th edition gallbladder cancer staging system was in this case T3N2M1. Oncology follow-up and adjuvant chemotherapy were recommended.

A 55-year-old female patient was admitted to the Emergency Department with right hypochondrium pain and weight loss for 2 weeks, which had worsened over the last two days accompanied by nausea and vomiting. No medical history was noted. Physical examination revealed normal abdominal wall mobility with respiratory movements and a sensitive right hypochondrium. Blood sample demonstrated normal levels of leukocytes and inflammatory markers.

Contrast-enhanced emergency CT (Figure 2) revealed mucosal hyperenhancement of the gallbladder, with irregular, mural thickening (16 mm), a gallstone (15 mm) and pericholecystic fluid and loco-regional inflammatory reactive lymph nodes (Panel A, Panel B and Panel C).

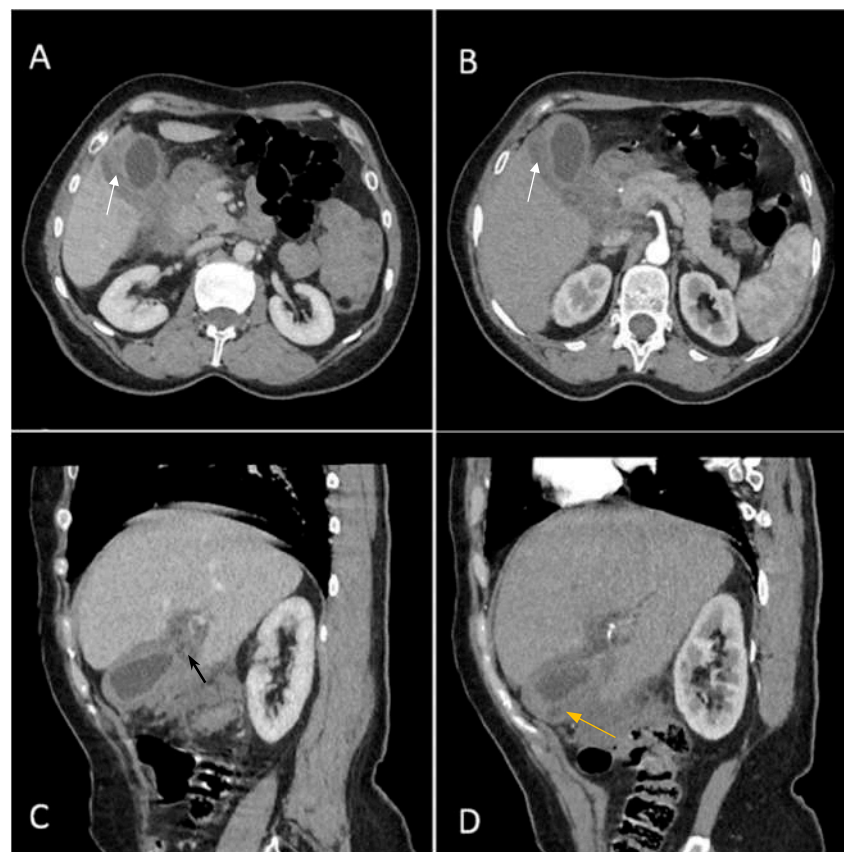


Figure 2. Multiplanar sections of contrast-enhanced CT acquisitions richly illustrating gallbladder carcinoma. (A,B) Gallbladder with irregular mural thickening, 16 mm (white arrow), pericholecystic fluid and loco-regional inflammatory lymph nodes. (C) Gallbladder with an intraluminal gallstone, 15 mm (black arrow). (D) Abscess adjacent to the gallbladder with subtle peripheral contrast enhancement (yellow arrow).

The CT scan depicted an abscess adjacent to the gallbladder with subtle peripheral contrast enhancement, measuring up to 12 mm in size along with inflammatory alterations in the adjacent hepatic parenchyma (Panel D). Inflammatory fat stranding can be observed at the omentum, periduodenum and pericolonic areas, as well as free intraperitoneal fluid.

An acute cholecystitis complicated by pericholecystic abscess was diagnosed. The patient refused hospitalization and specialized treatment. The following day the patient returned to the Emergency Department with severe pain and was admitted directly to the General Surgery Department. Nevertheless, blood sample demonstrated increased levels of CEA (67.83 ng/mL) and CA 19-9 (110.20 U/mL), markers which brought to question the CT imaging diagnosis of an acute cholecystitis complicated by pericholecystic abscess.

Therefore, clinical suspicion of gallbladder carcinoma was raised and an MRI cholangiography was performed (Figure 3). A laparoscopic cholecystectomy was performed and a subhepatic tumoral block with transvers colon invasion was identified. The patient was referred to the Oncology Department for further specialized treatment and follow-up.

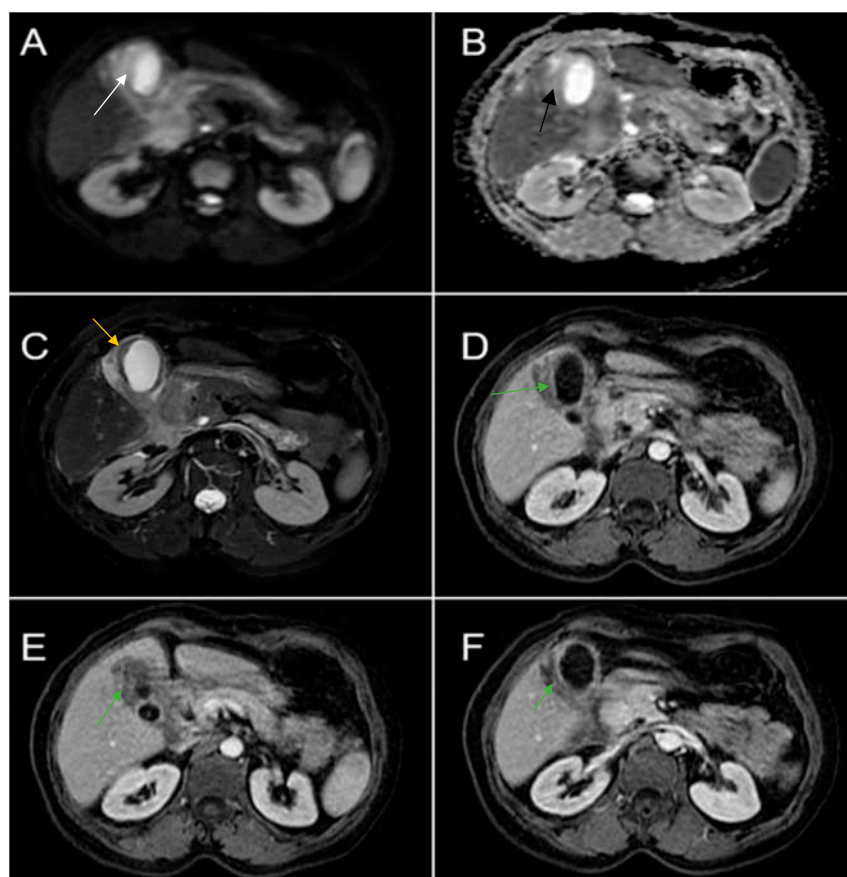


Figure 3. Abdominal MRI sequences highlighting imaging features suggestive of gallbladder carcinoma. (A) Diffusion-weighted imaging (DWI B800) showing bright high signal intensity of the wall thickening of the gallbladder (white arrow). (B) On apparent diffusion coefficient (ADC) map, the wall thickening is dark (black arrow)—illustrating markedly diffusion restriction—which in correlation with increased levels of CEA and CA 19-9 is highly suggestive of gallbladder carcinoma. (C) Axial T2-weighted FIESTA showing asymmetric strongly inhomogeneous wall thickening involving the gallbladder (yellow arrow). (D–F). Axial contrast-enhanced T1-weighted images showing heterogeneous enhancement of the wall thickening (green arrows).

A 49-year-old woman with no relevant medical history presented with a 1-week history of abdominal pain, jaundice, dark-colored urine and clay-colored stool. Physical examinations revealed normal abdominal wall mobility with respiratory movements, pain and abdominal tenderness in the epigastric region. Laboratory results upon admission

revealed elevated transaminases (ASAT 314 U/L, ALAT 484 U/L) and icteric cholestasis (GGT 311 U/L, bilirubin 8.59 mg/dL). The complete blood count was normal.

Contrast-enhanced emergency CT was performed (Figure 4), which richly highlighted a large heterogeneous intraluminal gallbladder mass, localized in the gallbladder fundus, measuring 58/34 mm, irregular, peripheral contrast enhancement on arterial and venous phase and with central hypodensity suggestive of areas of necrosis, extending to the surrounding liver (segment V) (Panel A and Panel C). CT showed a gallstone (17 mm) wedged in the gallbladder neck and intrahepatic biliary dilatation (Panel C and D). The common bile duct was dilated due to the presence of a possible tumoral extension to biliary tract or by the compressive effect of the multiple hilar lymphadenopathies; mesenteric, celiac and retroperitoneal lymphadenopathies with areas of necrosis, measuring up to 25/15 mm were also noted (Panel B). Abdominal contrast-enhanced MRI was performed (Figure 5).

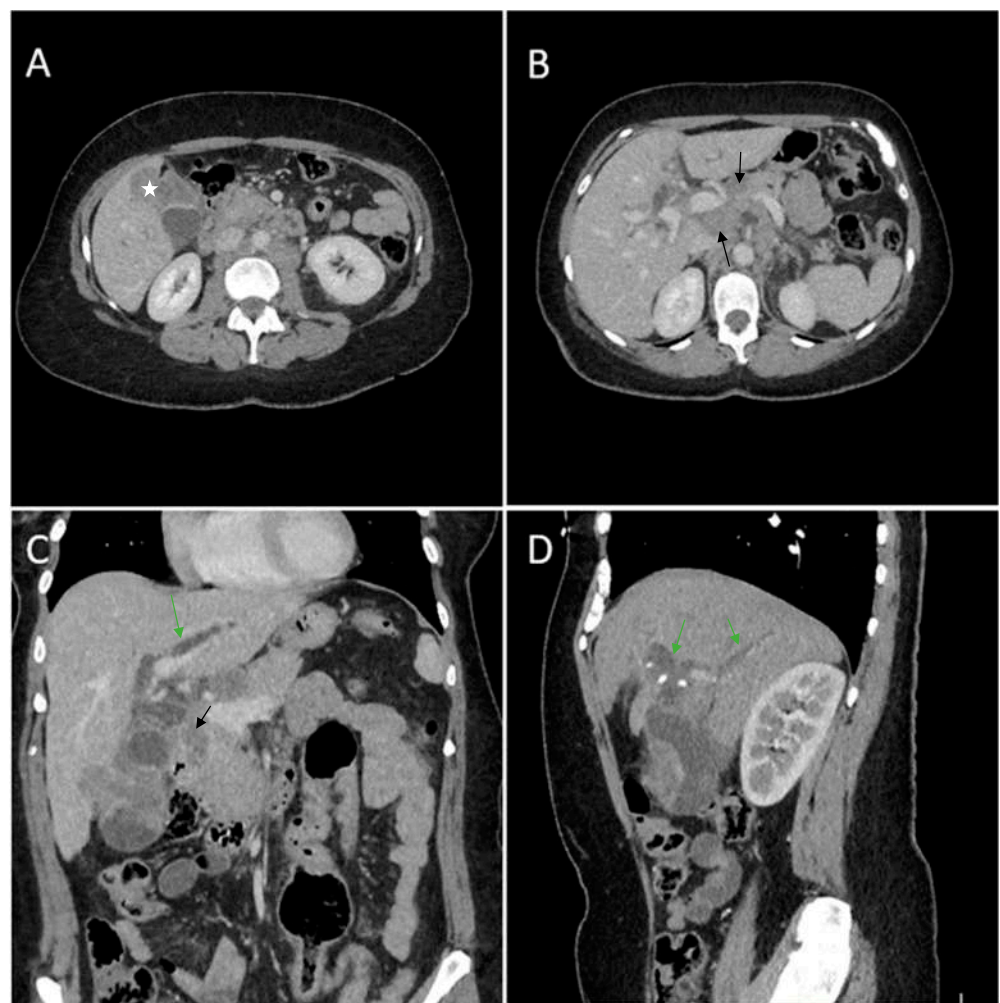


Figure 4. Multiplanar sections of contrast-enhanced CT acquisitions richly illustrating gallbladder carcinoma. (A) Heterogeneous ill-defined intraluminal irregular mass located predominantly in the gallbladder fundus (white star). (B) Multiple lymphadenopathies with areas of necrosis included (black arrows). (C) Gallbladder mass presents extension in the surrounding liver (segment V). (D) Intrahepatic biliary dilatation in both hepatic lobes, predominantly perihilar (green arrows).

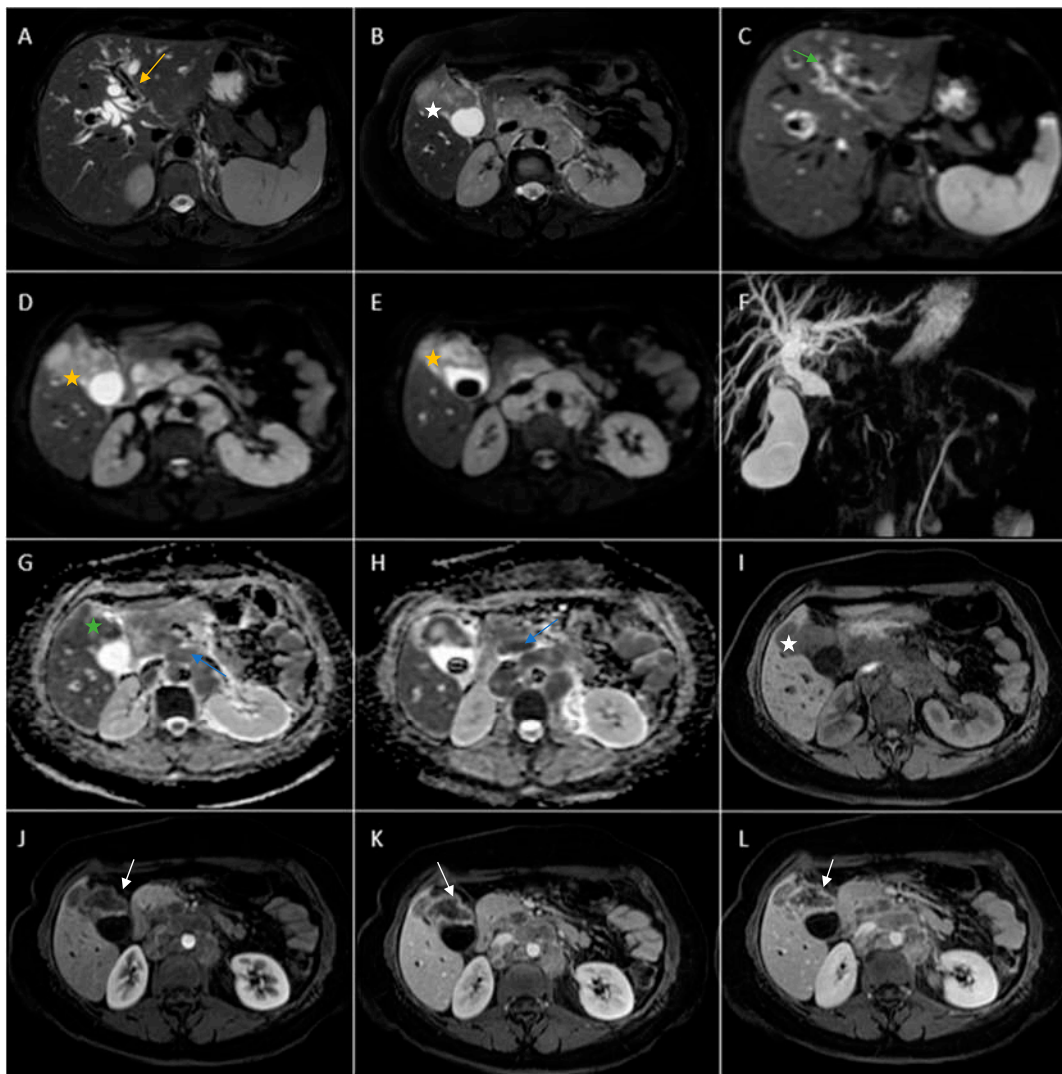


Figure 5. Abdominal MRI vividly illustrating synchronous gallbladder and biliary tract carcinoma with multiple large lymphadenopathies localized in the hepatic hilum, surrounding the cephalic region of the pancreas and in the celiac region. (A) Axial T2-weighted FS showed significant intrahepatic biliary dilatation in both hepatic lobes (yellow arrow). (B) Axial T2-weighted FS showed hypointense intraluminal gallbladder mass (white star) and multiple large lymphadenopathies. (C) Axial diffusion-weighted imaging (DWI B800) showed irregular, asymmetrical thickening of the walls of the intrahepatic bile ducts with high signal intensity suggestive of cholangitis (green arrow). (D,E). DWI B800 highlighted the gallbladder mass; inhomogeneous areas of high signal (yellow stars). (F) Coronal 3D MRCP showed enlarged gallbladder with an intraluminal gallstone and dilated intrahepatic and extrahepatic biliary tree. (G,H). On apparent diffusion coefficient (ADC) map, the gallbladder mass is dark, illustrating markedly diffusion restriction (green star). Multiple large lymphadenopathies are also observed mainly in the lombo-aortic region, in the cephalic pancreatic region and in the hepatic hilum (blue arrow). (I) Axial T1-weighted image showing hypointense irregular tumoral gallbladder mass (white star). (J–L). Axial contrast-enhanced (arterial phase followed by venous phase) T1-weighted image showing rim-enhancing of the tumoral gallbladder mass (white arrow).

Furthermore, endoscopic retrograde cholangiopancreatography showed a stenosis (with the length of 14–15 mm) at the middle third of the major biliary tract, therefore a stent was placed.

In this case, the probable diagnosis was of synchronous gallbladder and biliary tract carcinoma with multiple large lymphadenopathies localized in the hepatic hilum, surrounding the cephalic region of the pancreas and in the celiac region.

Endoscopic ultrasound-guided fine-needle aspiration (EUS-FNA) for gallbladder tissue was performed. Histopathology showed small cell neuroendocrine carcinoma of the gallbladder. Immunohistochemical stains were positive for CK7, synaptophysin (Syn) and chromogranin A (CgA), and the Ki-67 indexes were over 97% cells.

A 69-year-old female patient with a past medical history of diabetes type II presented to the Emergency Department with a 2-day upper abdominal pain, accompanied by hypotension and oligoanuria. Routine laboratory evaluation showed elevated inflammatory markers (leukocytosis, procalcitonin 100 ng/mL, CRP 126 mg/L), elevated transaminases and ferritin. The patient underwent contrast-enhanced computed tomography (Figure 6). CT images depicted a distended gallbladder (99 mm in longitudinal measurement), with asymmetrical thick-walled gallbladder (16 mm), heterogeneous contrast enhancement (Panel A), with a gallbladder neck stone (10 mm), extended to the duodenum (Panel B and Panel C). CT showed multiple low-attenuation hepatic masses with peripheral enhancement, adjacent to the gallbladder fossa (segment V) and intrahepatic biliary tract dilatation. Below the liver and adjacent to the gallbladder fundus, fat standing and free fluid were observed. These imaging findings were suggestive of acute cholecystitis complicated by an intrahepatic abscess or gallbladder carcinoma with wall perforation into the adjacent liver.

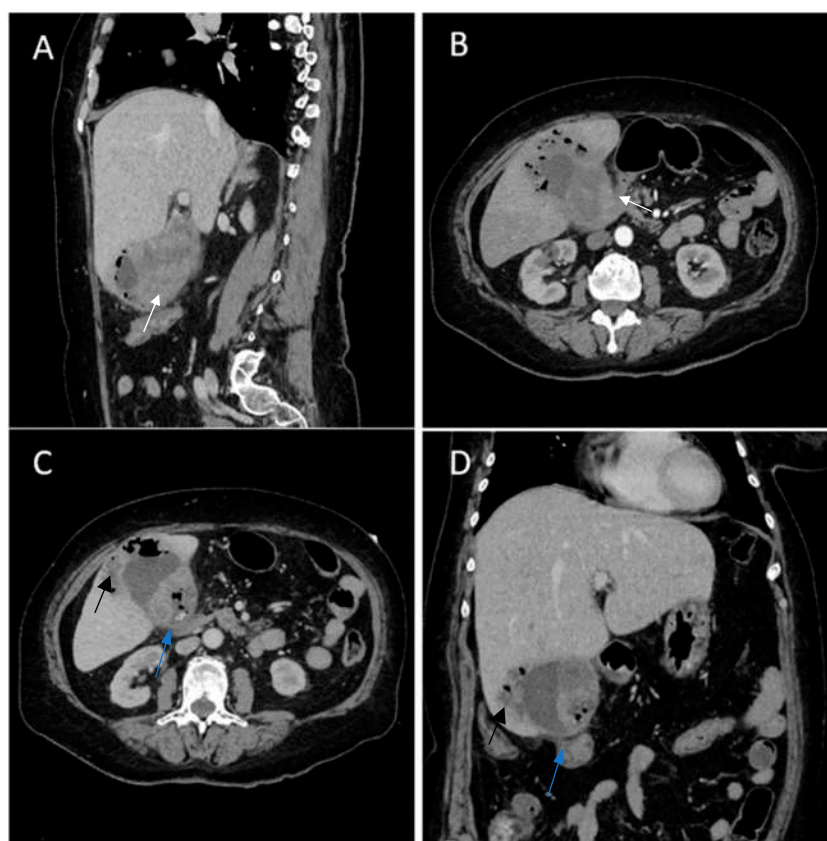


Figure 6. Multiplanar sections of contrast-enhanced CT acquisitions richly illustrating gallbladder carcinoma with an associated necrotizing infectious component. (A,B). Distended gallbladder with asymmetrical thick-walled gallbladder (16 mm) (white arrow). (C,D). Abscess adjacent to the gallbladder (black arrow); extension to the duodenum (blue arrow).

Antibiotic therapy and percutaneous US-guided drainage for liver abscess represented the first-line treatment, without response. After that, surgical drainage and cholecystostomy was performed.

Histopathological analysis revealed gallbladder carcinoma and palliative chemotherapy was proposed.

A 63-year-old man with a history of severe hyponatremia, known prostate adenocarcinoma and gastroduodenal ulcer with Billroth I gastric resection presented with nausea, vomiting, dizziness and weight loss for one month. On physical examination, abdominal tenderness was noted. Routine laboratory evaluation demonstrated normal leukocytes and inflammatory markers, moderate anemia and severe hyponatremia (serum sodium was 108 mmol/L). Contrast-enhanced CT (Figure 7) showed a heterogeneous intraluminal gallbladder mass, measuring 25/24/35 mm, localized in gallbladder fundus (Panel A, Panel B, Panel C and Panel D). The mass had no invasion of the adjacent structures and no associated imaging findings. An abdominal MRI was performed (Figure 8).

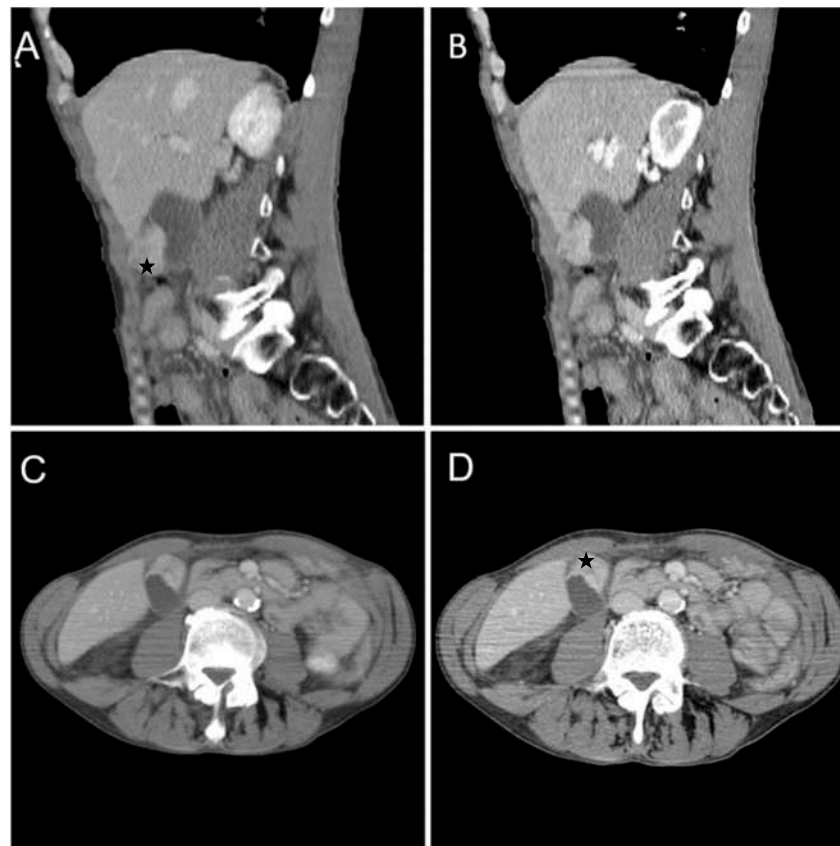


Figure 7. Multiplanar sections of contrast-enhanced CT acquisitions richly illustrating gallbladder carcinoma. (A–D). Heterogeneous, contrast-enhancing intraluminal gallbladder mass located in the gallbladder fundus region (black star).

Furthermore, a laparoscopic cholecystectomy was performed. The histopathological exam revealed gallbladder carcinoma.

The particularity of this case report is amply illustrated by severe hyponatremia presented as paraneoplastic SIADH syndrome (syndrome of inappropriate antidiuretic hormone secretion) in a patient with gallbladder carcinoma.

A 67-year-old female patient with a past medical history of hypertension and autoimmune thyroiditis presented to the Emergency Department with abdominal pain accompanied by nausea and weight loss. Physical examinations revealed abdominal tenderness with a palpable mass in the right hypochondrium. Blood sample demonstrated elevated inflammatory markers, hypochromic microcytic anemia, hepatic cytolysis and increased levels of CEA (12.5 ng/mL) and CA 19-9 (51 U/mL). Contrast-enhanced emergency CT (Figure 9) showed a large mass with heterogeneous enhancement, measuring 94/57 mm, that partially replaced the gallbladder and invaded the liver (segment IVb), pyloric antrum

and duodenum II. Bulky celiac and mesenteric lymphadenopathies with areas of necrosis, measuring up to 27/25 mm were present.

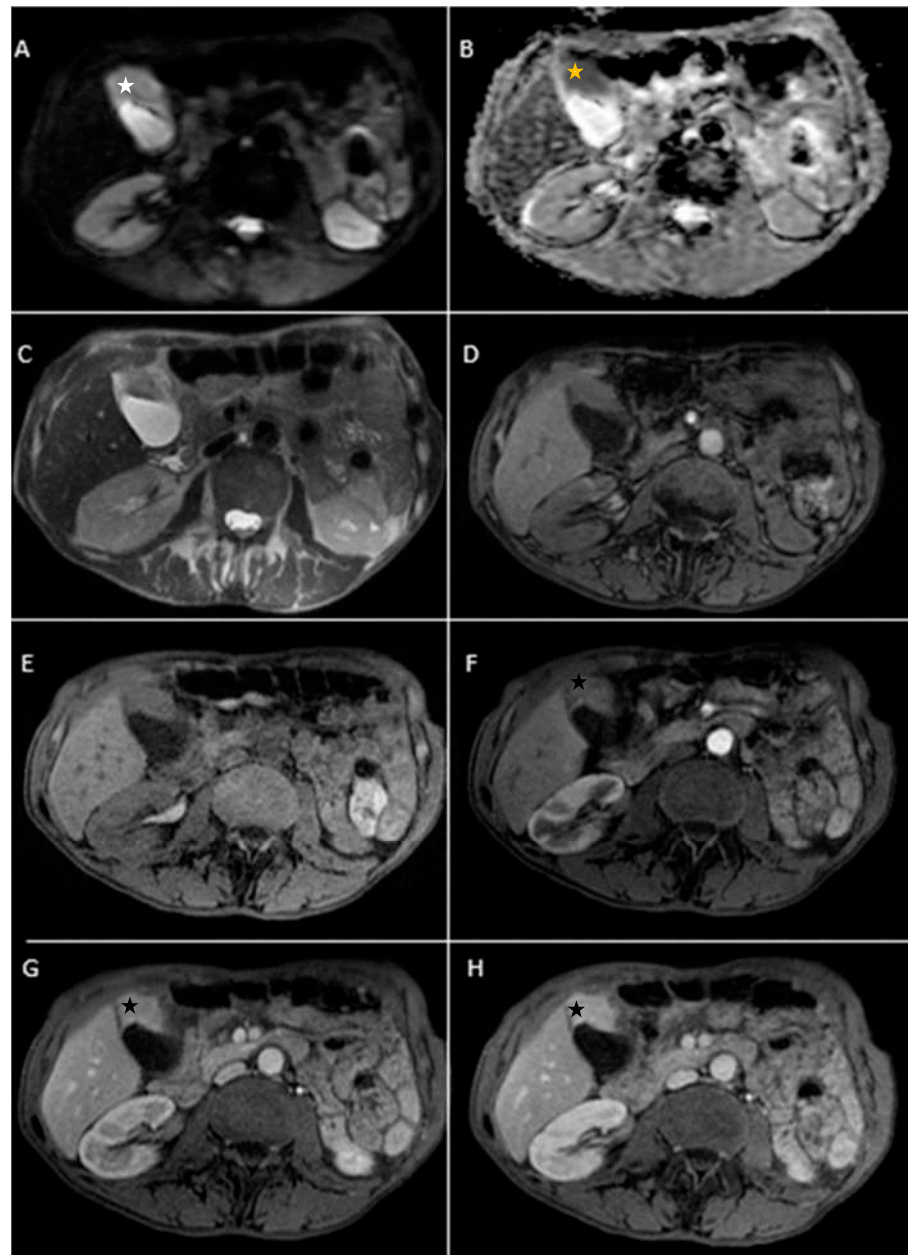


Figure 8. Abdominal MRI sequences highlighting gallbladder carcinoma. (A) Diffusion-weighted imaging (DWI B800) showing areas of moderate-high signal of the intraluminal gallbladder mass located in the fundus area (white star). (B) On ADC map, the intraluminal gallbladder mass is dark—diffusion restriction (yellow star). (C,D). Axial T2-weighted showing distended gallbladder with a heterogeneous hypointense intraluminal mass and axial T1 dual ECHO showing isointense gallbladder mass. (E) Axial T1-weighted image showing isointense gallbladder mass. (F–H). Axial contrast-enhanced T1-weighted image (arterial phase followed by venous phase) showing strong contrast-enhancement of the intraluminal gallbladder mass (black star).

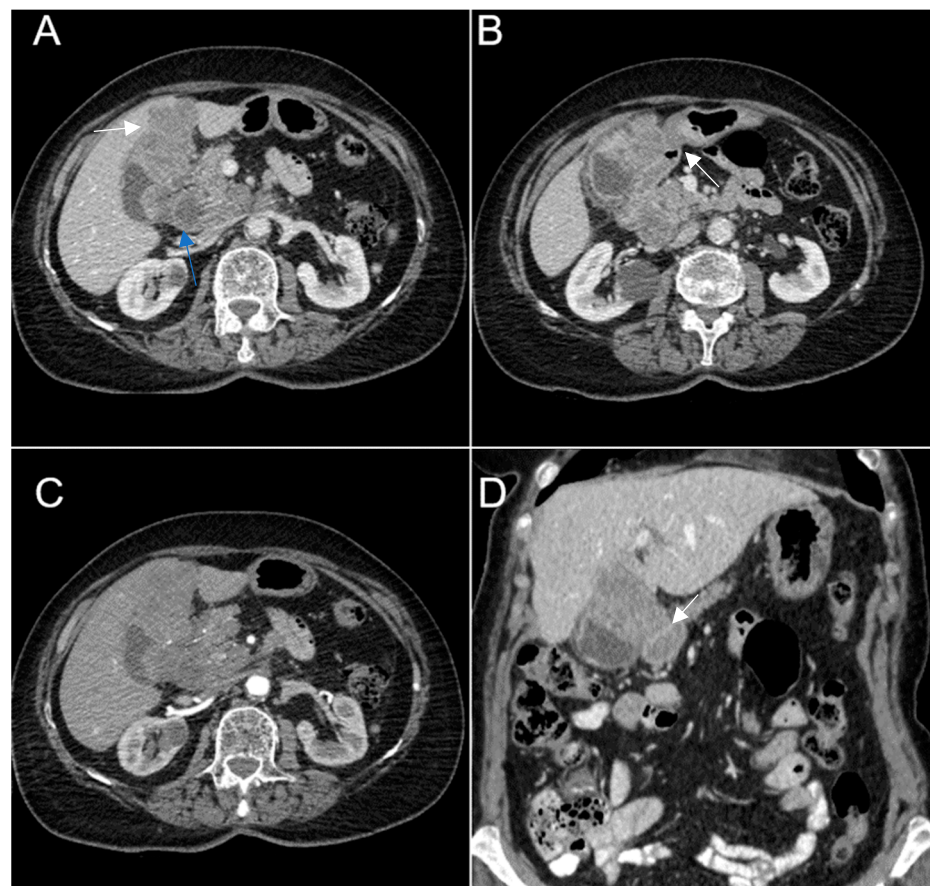


Figure 9. Multiplanar sections of contrast-enhanced CT acquisitions richly illustrating gallbladder carcinoma. (A–D). A large, inhomogeneous pseudonodular mass with heterogeneous contrast enhancement, with invasion in the adjacent liver, pyloric antrum and duodenum II (white arrows). (A) Lymphatic metastases; with compressive effect on the inferior vena cava and right renal artery and vein (blue arrow).

Abdominal MRI was performed (Figure 10).

Endoscopic ultrasound-guided fine-needle aspiration (EUS-FNA) for gallbladder tissue was performed and revealed epithelial gallbladder carcinoma. The biopsy specimens were processed for frozen sectioning. Formalin-fixed paraffin-embedded tissue sections from the gallbladder were examined histologically. The microscopic description revealed proliferation of polygonal cells, abundant clear cytoplasm, large nuclei with irregular membranes and atypical mitotic divisions.

The clinical symptoms of gallbladder cancer are often vague and non-specific and include pain in the right hypochondriac region, nausea and vomiting. In the late stages of the disease weight loss, anorexia and jaundice are often seen [11,12]. In contrast, some patients present with symptoms of acute cholecystitis and malignancy may be incidentally found following a cholecystectomy [13]. Detection of gallbladder at an early stage is difficult because the symptoms often mimic benign conditions.

The major risk factors include being an elderly woman (over 60 years old, F:M ratio 3:1), cholelithiasis and gallstones (in 60–90% cases) [10]. Regarding our cases, five of them were female and one was male. Other risk factors include:

- ✓ chronic inflammation due to typhoid carrier state;
- ✓ gallbladder polyps (more than 10 mm);
- ✓ porcelain gallbladder;
- ✓ smoking and obesity [3,11];
- ✓ anomalous pancreaticobiliary ductal junction, which is a rare congenital anomaly [12].

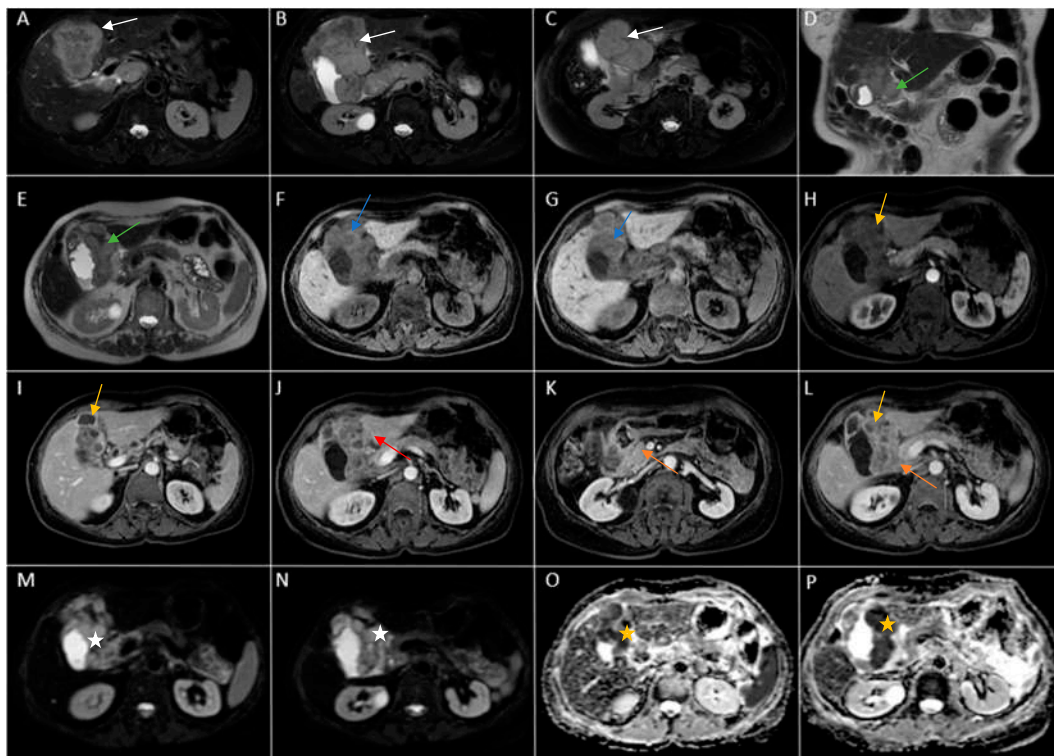


Figure 10. Abdominal MRI images vividly illustrating epithelial gallbladder carcinoma. (A–C). Axial T2-weighted FS showing inhomogeneous moderate hypointense heterogeneous tumoral parietal mass surrounding the gallbladder (white arrow). (D,E). Coronal and axial T2-weighted images showing hypointense heterogeneous tumoral gallbladder mass (green arrow). (F,G). Axial T1-weighted illustrating iso-hypointense tumoral mass (blue arrow). (H–L). Axial contrast-enhanced T1-weighted image (arterial phase followed by venous phase) showing a heterogeneous enhancement of the gallbladder mass with areas of necrosis (yellow arrows). The mass invades the adjacent liver ((J), red arrow) and duodenum II ((K,L), orange arrows). (M,N). Diffusion-weighted imaging (DWI B800) showing bright signal of the large gallbladder mass (white stars). (O,P). On ADC map, the large gallbladder mass is dark, illustrating diffusion restriction (yellow stars).

Gallbladder carcinoma might be found incidentally in 1–3% following a cholecystectomy [14]. Because of advanced disease at diagnosis, the typical 5-year survival is only 5% [15].

Imaging has a key role in the diagnosis, staging, characterization and planning management of gallbladder cancer.

Diagnostic imaging modalities for the gallbladder cancer include ultrasound, computerized tomography (CT) and magnetic resonance imaging (MRI). Ultrasound is frequently the initial imaging modality for evaluating gallbladder disease. In locally advanced gallbladder cancer, ultrasound has a sensitivity of 85% and a specificity of 80% in diagnosis. Moreover, ultrasound is limited to evaluate locoregional extension, nodal and metastatic disease. CT and MRI are commonly indicated for the comprehensive assessment of disease extension. Biphasic arterial phase (at 20 to 30 s) followed by venous phase (50 to 60 s) contrast-enhanced CT is useful to evaluate gallbladder cancer. CT demonstrates a sensitivity of 99% and a specificity of 76% in determining resectability. MRI is a noninvasive imaging method and demonstrates superior sensitivity compared to CT, providing superior soft-tissue characterization of the gallbladder and biliary tree [10].

Computed tomography (CT) and magnetic resonance imaging (MRI) reveal three major patterns of disease. Gallbladder carcinoma could present as a mass that completely replaces the gallbladder and invades the adjacent liver or as an intraluminal enhancement mass (in 25% of cases) arising from the fundus (60%) or body (30%) [15–18]. Regarding

our six patients, two of them presented with a mass that replaced a part of gallbladder and invaded the adjacent liver (Case 3 and 6) and one of them as a suspicious intraluminal gallbladder lesion localized in gallbladder fundus on CT and MRI (Case 5).

A third presentation of gallbladder carcinoma is either irregular focal or diffuse wall-thickening of the gallbladder [15,19]. Regarding our cases, three of them had presented with this imaging scenario (Cases 1, 2 and 4).

Tumor can spread to the liver (65%), colon (15%), duodenum (15%) and pancreas (6%) [12,15]. Regarding our cases, in Case 1 the tumor spread to the liver and duodenum and transvers colon and in Cases 4 and 6 metastatic spread to the liver and duodenum can be noted.

Tumor extending to biliary tract is associated with poor prognosis. This aspect was presented in Case 3. Also, in Cases 1, 3 and 6, local lymphatic tumoral spread was presented [15,20].

Associated findings include a checklist of:

- ✓ gallstones (Cases 1, 2);
- ✓ biliary dilatation (Case 3);
- ✓ metastases in the liver parenchyma (segments IV, V) (Cases 1, 3);
- ✓ peritoneum;
- ✓ bulky porta hepatis, adenopathy (Cases 1, 3, 5);
- ✓ invasion of the liver and bowel (Cases 1, 3, 4, 5, 6) [15,18].

Adenocarcinoma is the most common morphologic subtype of gallbladder cancer (over 90% of cases), followed by adenosquamous and squamous cell type (10–15%). Small cell carcinoma, neuroendocrine cell tumors and metastases are the rare types [10]. In our six cases, different subtypes of gallbladder cancer were observed, three of which were adenocarcinoma (Cases 1, 4 and 6). In two cases (Cases 3 and 5), the histopathology showed small cell neuroendocrine carcinoma. Neuroendocrine carcinoma of gallbladder is a rare entity and it tends to be more aggressive compared with gallbladder adenocarcinoma [21].

In our Case 5 report (Figure 7), the patient presented gallbladder carcinoma with endocrine manifestation. Gallbladder cancer associated with SIADH syndrome represents a very rare entity with few cases reported in the current literature. Hyponatremia (<135 mmol/L) is correlated with a negative prognosis and in some case is a predictive factor for cancer patients. Paraneoplastic syndrome of inappropriate antidiuretic hormone secretion (SIADH) is induced by the abnormal secretion of antidiuretic hormone by tumoral cells [21]. In our case, the final diagnosis was gallbladder carcinoma associated with SIADH as a paraneoplastic syndrome.

Moreover, the American Joint Committee on Cancer 8th edition gallbladder cancer staging system is staged by the depth of tumor invasion (T), presence of lymph node metastases (N) and presence of distant metastases (M) [1]. The T component describes the depth that the tumor has grown from the inside through the outer layers. The N component indicates invasion in lymph nodes. The M component describes distant metastases, the most common sites of metastases being represented by the peritoneum and liver parenchyma [10,22].

Furthermore, for the most important imaging part regarding differential diagnostic, imaging represents a helpful modality for distinguishing between benign and malign gallbladder diseases, in most cases [15,23]. Differential diagnosis includes a group of diseases, such as complicated or chronic cholecystitis, xanthogranulomatous cholecystitis, adenomyomatosis, adenoma, porcelain and metastases [15].

A gallbladder tumor is usually represented on imaging as focal or diffuse asymmetric mural thickening [10,24].

The presence of symmetric wall thickening often indicates a benign origin, such as acute or chronic cholecystitis or adenomyomatosis [24].

Acute cholecystitis complicated by pericholecystic abscess are frequently differentiated from gallbladder cancer due to their typically rapid and severe acute clinical presentation.

Also, acute cholecystitis on contrast-enhanced CT shows increased gallbladder wall enhancement associated with hyperemia, frequently associated with gallstones (Figure 11) [10].



Figure 11. A 67-year-old woman undergoing contrast-enhanced CT for suspected abdominal acute appendicitis. CT images show pericholecystic abscess (white arrow) and symmetric wall thickening suggestive of acalculous cholecystitis.

Moreover, the differential diagnosis between xanthogranulomatous cholecystitis (Figure 12) and gallbladder tumor, can be challenging, particularly in patients with proliferative fibrosis. Xanthogranulomatous cholecystitis is an uncommon form of chronic cholecystitis characterized by aggressive inflammatory changes, by intramural hypoattenuating nodules and by fat detection on MRI in thickened wall (Figure 13) [25–29].

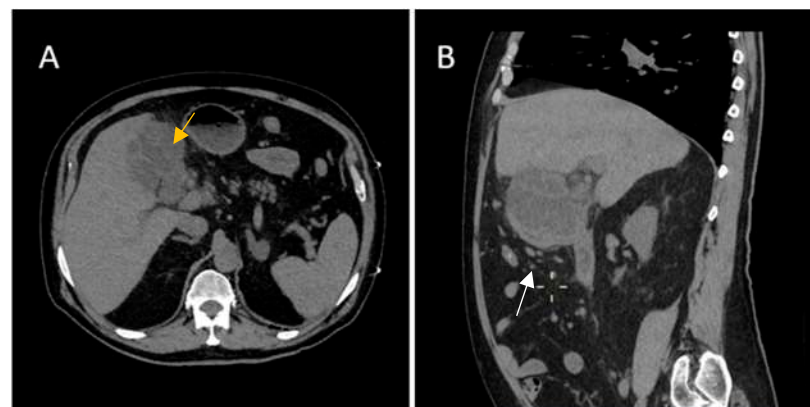


Figure 12. A 70-year-old male with a history of hypertension, type 2 diabetes, peripheral venous thrombosis, presented at our Emergency Department with abdominal pain accompanied by diarrhea, night sweats and fever. His laboratory findings showed elevated inflammatory markers. Computerized tomography (CT) revealed (B)—diffuse wall thickening with intramural low-density nodules and bands in thickened walls (white arrow) associated with (A) pericholecystic inflammatory change (yellow arrow).

Furthermore, gallbladder adenomyomatosis is a benign gallbladder lesion. Imaging shows a focal or diffuse gallbladder mural thickening, which can mimic cancer. The invaginations or diverticula are frequently called Rokitansky–Aschoff sinuses, which can be easily visualized on MRI imaging [19,20,30]. The differential diagnosis for intraluminal polypoid tumors includes both benign and malignant lesions: adenomatous polyp, cholesterol polyp, carcinoid tumor and metastasis from melanoma or renal cell carcinoma [31].

Metastases to the gallbladder are rare, usually with a late diagnosis and represent an end-stage of malignancy, being commonly associated with metastases to other tissues (patients with an established diagnosis of disseminated cancer) and usually presenting poor and unfavorable prognosis. The most common primary tumor metastasizing to the

gallbladder is melanoma (55% of cases) (Figures 14–16), followed by breast cancer (13%), hepatocellular carcinoma (13%) and renal cell carcinoma (7%) [32,33].

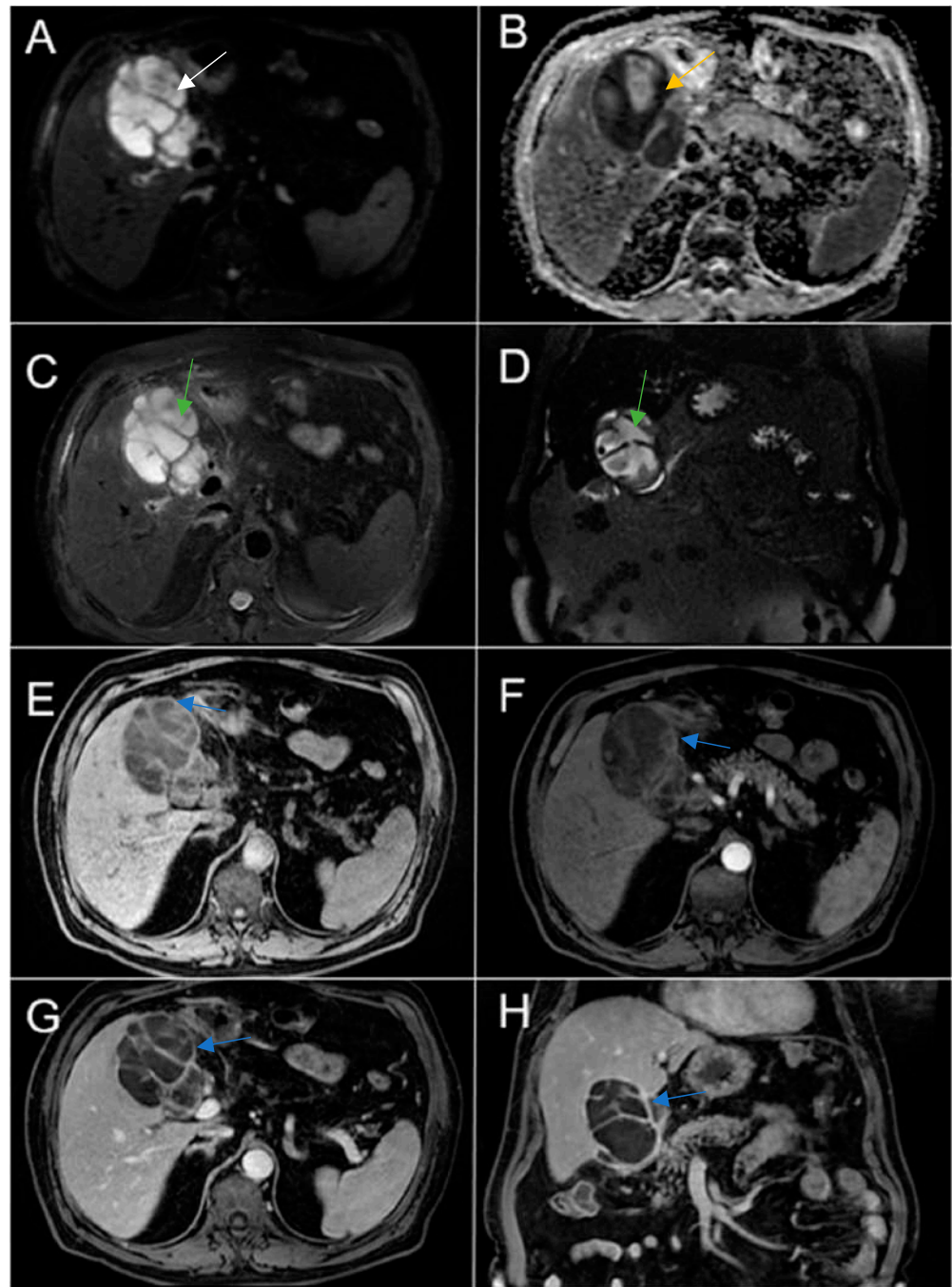


Figure 13. Abdominal MRI vividly illustrating Xanthogranulomatous Cholecystitis. (A) Diffusion-weighted imaging (DWI B800—bright high signal) demonstrated restricted diffusion (white arrow), but malignancy typically demonstrates lower ADC values. (B) On ADC map, the wall thickening is dark (yellow arrow). (C,D). Intramural areas of necrosis are high signal intensity on axial and coronal T2-weighted images (green arrows). (E–H). Axial unenhanced and contrast-enhanced T1-weighted images showing diffusely thickened wall, with multiple intramural nodules with peripheral contrast enhancement (blue arrows).

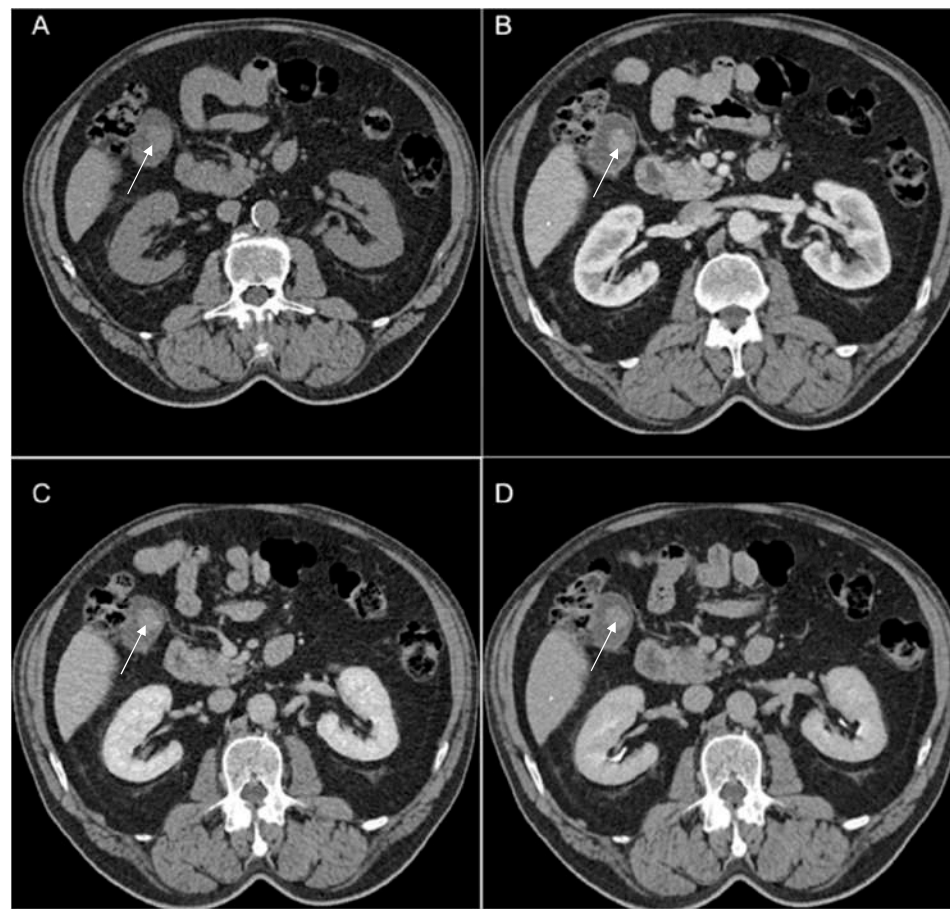


Figure 14. We present a rare and unusual case of a 67-year-old male with a medical history of cutaneous melanoma on right thorax stage IV. CT images fully illustrated a contrast-enhancing polypoid pseudonodular mass located in the gallbladder fundus measuring 21/20 mm (white arrows). (A) Native examination: 55–60 HU. (B) Arterial phase: 95–119 HU. (C) Venous phase: 80–100 HU. (D) Delayed phase (3 min): 75–80 HU. MRI was performed (Figure 15). Melanin is usually hyperdense on unenhanced CT images and hyperintense on T1-weighted MRI; this criterion plays an essential role in the differential diagnosis between primary or secondary gallbladder lesions. The patient followed immunotherapy.

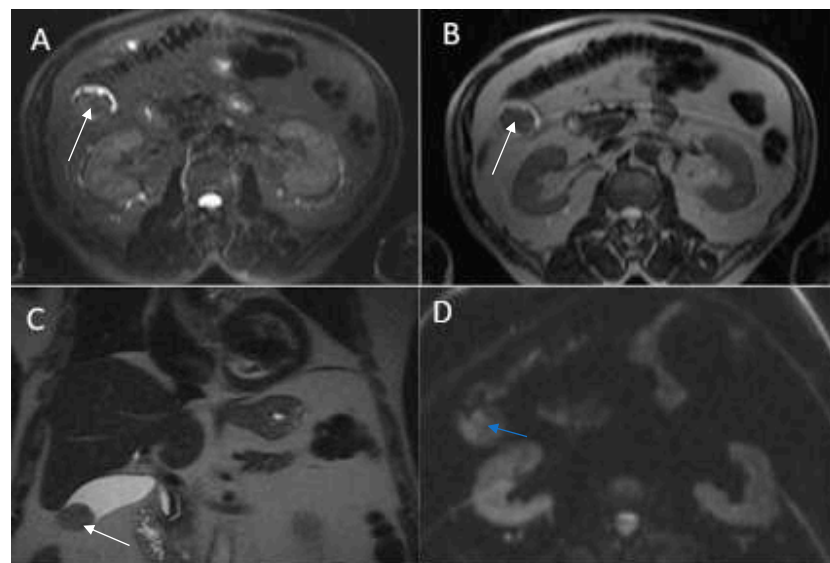


Figure 15. Cont.

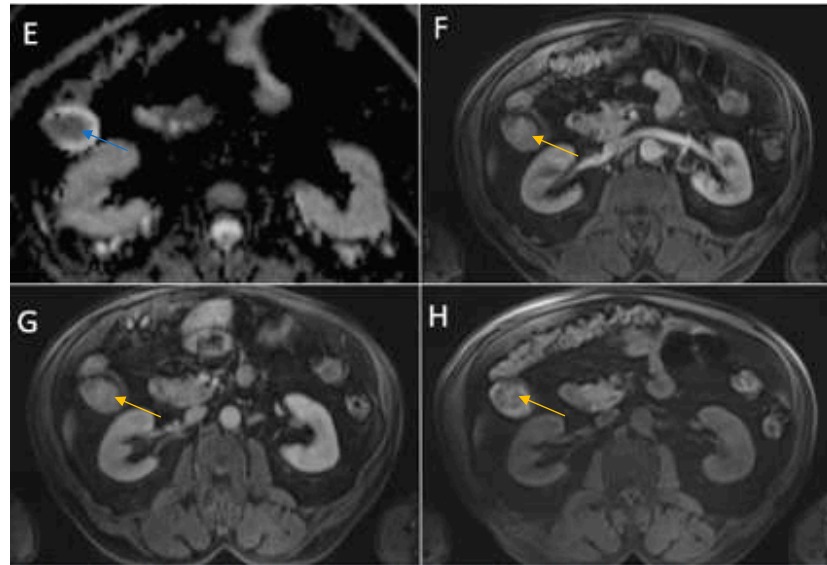


Figure 15. Abdominal MRI. (A) Axial T2-weighted FS showing markedly hypointense pseudonodular tumoral gallbladder lesion (white arrow). (B) Axial T2-weighted showing hypointense gallbladder lesion (white arrow). (C) Coronal T2-HASTE hypointense gallbladder lesion (white arrow). (D) Diffusion-weighted imaging (DWI B800) showing bright hypersignal of the lesion (blue arrow). (E) Restricted diffusion (blue arrow) on apparent diffusion coefficient (ADC) map. (F,G) Axial contrast-enhanced T1-weighted image showing a strongly enhancing polypoid pseudonodular mass in the gallbladder fundus. (H) Axial T1-weighted image FS showing hyperintense nodular lesion component (yellow arrows), highly suggestive of melanin.



Figure 16. Remarkable treatment response to immunotherapy; intracholecystic metastatic lesion from cutaneous melanoma after immunotherapy appears in remission (white arrow).

Author Contributions: All authors have worked on conception and design of the scientific paper, on the data collection and analysis and interpretation of data and images and on the revised article. All authors gave final approval of the version to be submitted. All authors have read and agreed to the published version of the manuscript.

Funding: This research received no external funding.

Institutional Review Board Statement: Ethical review and approval were waived for this study, due to being a retrospective case report series, which did not impact the management of the patients.

Informed Consent Statement: Informed written consent has been obtained from the patients.

Data Availability Statement: The data presented in this study are available on request from the corresponding author (N, L.C.).

Conflicts of Interest: The authors declare no conflicts of interest.

References

- Ramachandran, A.; Srivastava, D.N.; Madhusudhan, K.S. Gallbladder cancer revisited: The evolving role of a radiologist. *Br. J. Radiol.* **2021**, *94*, 20200726. [\[CrossRef\]](#)
- Rawla, P.; Sunkara, T.; Thandra, K.C.; Barsouk, A. Epidemiology of gallbladder cancer. *Clin. Exp. Hepatol.* **2019**, *5*, 93–102. [\[CrossRef\]](#)
- Halaseh, S.A.; Halaseh, S.A.; Halaseh, S.; Halaseh, S.; Shakman, R.; Shakman, R. A Review of the Etiology and Epidemiology of Gallbladder Cancer: What You Need to Know. *Cureus* **2022**, *14*, e28260. [\[CrossRef\]](#)
- Liu, Z.; Zhu, G.; Jiang, X.; Zhao, Y.; Zeng, H.; Jing, J.; Ma, X. Survival Prediction in Gallbladder Cancer Using CT Based Machine Learning. *Front. Oncol.* **2020**, *10*, 604288. [\[CrossRef\]](#)
- Hundal, R.; Shaffer, E.A. Gallbladder cancer: Epidemiology and outcome. *Clin. Epidemiol.* **2014**, *6*, 99–109. [\[CrossRef\]](#)
- Kalra, N.; Gupta, P.; Singhal, M.; Gupta, R.; Gupta, V.; Srinivasan, R.; Mittal, B.R.; Dhiman, R.K.; Khandelwal, N. Cross-sectional Imaging of Gallbladder Carcinoma: An Update. *J. Clin. Exp. Hepatol.* **2018**, *9*, 334–344. [\[CrossRef\]](#) [\[PubMed\]](#)
- John, S.; Moyana, T.; Shabana, W.; Walsh, C.; McInnes, M.D.F. Gallbladder Cancer: Imaging Appearance and Pitfalls in Diagnosis. *Can. Assoc. Radiol. J.* **2020**, *71*, 448–458. [\[CrossRef\]](#) [\[PubMed\]](#)
- Furlan, A.; Ferris, J.V.; Hosseinzadeh, K.; Borhani, A.A. Gallbladder carcinoma update: Multimodality imaging evaluation, staging, and treatment options. *Am. J. Roentgenol.* **2008**, *191*, 1440–1447. [\[CrossRef\]](#) [\[PubMed\]](#)
- Randi, G.; Malvezzi, M.; Levi, F.; Ferlay, J.; Negri, E.; Franceschi, S.; La Vecchia, C. Epidemiology of biliary tract cancers: An update. *Ann. Oncol.* **2009**, *20*, 146–159. [\[CrossRef\]](#) [\[PubMed\]](#)
- Lopes Vendrami, C.; Magnosta, M.J.; Mittal, P.K.; Moreno, C.C.; Miller, F.H. Gallbladder carcinoma and its differential diagnosis at MRI: What radiologists should know. *RadioGraphics* **2021**, *41*, 78–95. [\[CrossRef\]](#) [\[PubMed\]](#)
- Adam, K.M.; Abdelrahim, E.Y.; Doush, W.M.; Abdelaziz, M.S. Clinical presentation and management modalities of gallbladder cancer in Sudan: A single-center study. *JGH Open* **2023**, *7*, 365–371. [\[CrossRef\]](#)
- Gupta, P.; Meghashyam, K.; Marodia, Y.; Gupta, V.; Basher, R.; Das, C.K.; Yadav, T.D.; Irrinki, S.; Nada, R.; Dutta, U. Locally advanced gallbladder cancer: A review of the criteria and role of imaging. *Abdom. Imaging* **2020**, *46*, 998–1007. [\[CrossRef\]](#)
- Franco, N. Outcomes of Patients with Gallbladder Cancer Presenting with Acute Cholecystitis. *Researchsquare* **2023**. [\[CrossRef\]](#)
- Alkhayyat, M.; Saleh, M.A.; Qapaja, T.; Abureesh, M.; Almomani, A.; Mansoor, E.; Chahal, P. Epidemiology of gallbladder cancer in the United States: A population-based study. *Chin. Clin. Oncol.* **2021**, *10*, 25. [\[CrossRef\]](#) [\[PubMed\]](#)
- Zaheer, A.; Raman, S.P. *Diagnostic Imaging: Gastrointestinal*; Elsevier: Amsterdam, The Netherlands, 2015.
- Ganeshan, D.; Kambadakone, A.; Nikolaidis, P.; Subbiah, V.; Subbiah, I.M.; Devine, C. Current update on gallbladder carcinoma. *Abdom. Imaging* **2021**, *46*, 2474–2489. [\[CrossRef\]](#) [\[PubMed\]](#)
- Levy, A.D.; Murakata, L.A.; Rohrmann, C.A. Gallbladder carcinoma: Radiologic-pathologic correlation. *RadioGraphics* **2001**, *21*, 295–314. [\[CrossRef\]](#) [\[PubMed\]](#)
- George, R.; Godara, S.; Dhagat, P.; Som, P. Computed tomographic findings in 50 cases of gall bladder carcinoma. *Med. J. Armed Forces India* **2007**, *63*, 215–219. [\[CrossRef\]](#)
- Ratanaprasatporn, L.; Uyeda, J.W.; Wortman, J.R.; Richardson, I.; Sodickson, A.D. Multimodality imaging, including dual-energy CT, in the evaluation of gallbladder disease. *RadioGraphics* **2018**, *38*, 75–89. [\[CrossRef\]](#)
- Gourgoutis, S.; Kocher, H.M.; Solaini, L.; Yarollahi, A.; Tsiambas, E.; Salemis, N.S. Gallbladder cancer. *Am. J. Surg.* **2008**, *196*, 252–264. [\[CrossRef\]](#)
- Ng, E.S.; Venkateswaran, K.; Ganpathi, S.I.; Chuah, B.Y. Small cell gallbladder carcinoma complicated by paraneoplastic hyponatremia: A case report and literature review. *J. Gastrointest. Cancer* **2010**, *41*, 264–268. [\[CrossRef\]](#)
- Amin, M.B.; Greene, F.L.; Edge, S.B.; Compton, C.C.; Gershenwald, J.E.; Brookland, R.K.; Meyer, L.; Gress, D.M.; Byrd, D.R.; Winchester, D.P. The Eighth Edition AJCC Cancer Staging Manual: Continuing to build a bridge from a population-based to a more “personalized” approach to cancer staging. *CA Cancer J. Clin.* **2017**, *67*, 93–99. [\[CrossRef\]](#) [\[PubMed\]](#)
- Kitazume, Y.; Taura, S.-I.; Nakaminato, S.; Noguchi, O.; Masaki, Y.; Kasahara, I.; Kishino, M.; Tateishi, U. Diffusion-weighted magnetic resonance imaging to differentiate malignant from benign gallbladder disorders. *Eur. J. Radiol.* **2016**, *85*, 864–873. [\[CrossRef\]](#) [\[PubMed\]](#)
- Soundararajan, R.; Marodia, Y.; Gupta, P.; Rana, P.; Chhabra, M.; Kalage, D.; Dutta, U.; Sandhu, M. Imaging patterns of wall thickening type of gallbladder cancer. *Clin. Exp. Hepatol.* **2022**, *8*, 255–266. [\[CrossRef\]](#) [\[PubMed\]](#)
- Gri, J.; Hatahet, M.A.; Chopra, S. Xanthogranulomatous pyelonephritis: A rare case report of a 54 year old female (a potentially fatal infection). *Int. J. Surg. Case Rep.* **2021**, *85*, 106287. [\[CrossRef\]](#) [\[PubMed\]](#)
- Suzuki, H.; Wada, S.; Araki, K.; Kubo, N.; Watanabe, A.; Tsukagoshi, M.; Kuwano, H. Xanthogranulomatous cholecystitis: Difficulty in differentiating from gallbladder cancer. *World J. Gastroenterol.* **2015**, *21*, 10166–10173. [\[CrossRef\]](#)
- Kang, T.; Kim, S.; Park, H.; Lim, S.; Jang, K.; Choi, D.; Lee, S. Differentiating xanthogranulomatous cholecystitis from wall-thickening type of gallbladder cancer: Added value of diffusion-weighted MRI. *Clin. Radiol.* **2013**, *68*, 992–1001. [\[CrossRef\]](#)
- Xu, Z.; Cai, T.; Zhang, X.; Wu, J.; Liu, C. Xanthogranulomatous pyelonephritis infected with the *Providencia stuartii*: A case report and literature review. *BMC Nephrol.* **2021**, *22*, 356. [\[CrossRef\]](#)
- Chang, B.J.; Kim, S.H.; Park, H.Y.; Lim, S.W.; Kim, J.; Lee, K.H.; Lee, K.T.; Rhee, J.C.; Lim, J.H.; Lee, J.K. Distinguishing xanthogranulomatous cholecystitis from the wall-thickening type of early-stage gallbladder cancer. *Gut Liver* **2010**, *4*, 518–523. [\[CrossRef\]](#)

30. Bonatti, M.; Vezzali, N.; Lombardo, F.; Ferro, F.; Zamboni, G.; Tauber, M.; Bonatti, G. Gallbladder adenomyomatosis: Imaging findings, tricks and pitfalls. *Insights Imaging* **2017**, *8*, 243–253. [[CrossRef](#)]
31. Zemour, J.; Marty, M.; Lapuyade, B.; Collet, D.; Chiche, L. Gallbladder tumor and pseudotumor: Diagnosis and management. *J. Visc. Surg.* **2014**, *151*, 289–300. [[CrossRef](#)]
32. Cocco, G.; Pizzi, A.D.; Basilico, R.; Fabiani, S.; Taraschi, A.L.; Pascucci, L.; Bocatonda, A.; Catalano, O.; Schiavone, C. Imaging of gallbladder metastasis. *Insights Imaging* **2021**, *12*, 100. [[CrossRef](#)] [[PubMed](#)]
33. Christou, D.; Katodritis, N.; Decatris, M.P.; Katodritou, A.; Michaelides, I.; Nicolaou, N.; Kounoushis, M.; Hadjicostas, P. Melanoma of the gallbladder: Appropriate surgical management and review of the literature. *Clin. Case Rep.* **2014**, *2*, 313–318. [[CrossRef](#)] [[PubMed](#)]

Disclaimer/Publisher’s Note: The statements, opinions and data contained in all publications are solely those of the individual author(s) and contributor(s) and not of MDPI and/or the editor(s). MDPI and/or the editor(s) disclaim responsibility for any injury to people or property resulting from any ideas, methods, instructions or products referred to in the content.



Article

Gender Differences for His Bundle Pacing Long-Term Performance in the Elderly Population

Catalin Pestrea ^{1,*} , Ecaterina Cicala ¹, Dragos Lovin ¹, Adrian Gheorghe ¹, Florin Ortan ¹ and Rosana Manea ^{2,3}

¹ Department of Interventional Cardiology, Clinical County Emergency Hospital of Brasov, 500326 Brasov, Romania; cicalaecaterina@gmail.com (E.C.); dlovin94@gmail.com (D.L.); gheorghe.adrian9393@gmail.com (A.G.); ortan.florin@gmail.com (F.O.)

² Faculty of Medicine, “Transilvania” University of Brasov, 500019 Brasov, Romania; rosanamanea@gmail.com

³ Department of Radiology and Medical Imaging, Clinical County Emergency Hospital of Brasov, 500326 Brasov, Romania

* Correspondence: pestrea.catalin@gmail.com; Tel.: +40-745003637

Abstract: Background and aims: His bundle pacing (HBP) is considered the most physiological form of cardiac pacing. Although feasibility studies have included older patients, specific data for HBP in this population are scarce. This study aimed to evaluate gender differences in HBP long-term performance in elderly patients with atrioventricular (AV) block. Methods: This retrospective study included 73 patients aged over 65 years with successful HBP and at least 2 years of follow-up. The patients’ baseline and follow-up clinical and procedural characteristics were recorded. Results: The mean age of the cohort was 72.8 ± 6.3 years, with 43 males and 30 females. The paced QRS complex was significantly narrower than the baseline value for both genders. Females had a narrower-paced QRS complex without differences in detection, type of His bundle capture, impedance, or fluoroscopy time. The pacing threshold increased progressively, reaching statistical significance compared to the baseline values at the two-year follow-up. The pacing threshold increased by more than 1 V over the follow-up period in twenty-four patients (32.9%) and by more than 2 V in six patients (8.2%), with no significant difference between genders. The pacing threshold increase occurred within the first year for most patients, without gender differences. Multivariate Cox regression analysis demonstrated that the paced QRS duration, left ventricular ejection fraction, and ischemic cardiomyopathy were significantly associated with the pacing threshold increase over time. Conclusion: In elderly patients with AV block, HBP remains a feasible pacing method, without significant gender differences, over a long-term follow-up period. Pacing threshold increases are expected in up to one-third of the patients, requiring regular follow-ups to adjust the programmed parameters and optimize battery longevity.

Keywords: His bundle pacing; feasibility; elderly; long-term follow-up; gender differences



Academic Editor: Alexander Maass

Received: 24 January 2025

Revised: 16 February 2025

Accepted: 24 February 2025

Published: 26 February 2025

Citation: Pestrea, C.; Cicala, E.; Lovin, D.; Gheorghe, A.; Ortan, F.; Manea, R. Gender Differences for His Bundle Pacing Long-Term Performance in the Elderly Population. *J. Cardiovasc. Dev. Dis.* **2025**, *12*, 88. <https://doi.org/10.3390/jcdd12030088>

Copyright: © 2025 by the authors. Licensee MDPI, Basel, Switzerland. This article is an open access article distributed under the terms and conditions of the Creative Commons Attribution (CC BY) license (<https://creativecommons.org/licenses/by/4.0/>).

1. Introduction

Cardiac pacing is a life-saving procedure performed increasingly worldwide. The longer life expectancy in the general population due to better healthcare is partly responsible for this constantly growing number of devices implanted [1]. Consequently, the mean age of the patients subjected to pacemaker implantation has increased in the last decades. In a study by Matsubara et al., the mean age at initial pacemaker implantation increased by 12.1 years over the last 50 years, with the most significant increase in patients over 70 years [2]. Furthermore, several studies looked at gender differences in device

implantation, showing that males had a higher prevalence of atrioventricular disturbances and higher long-term mortality after the procedure [3]. In contrast, females were older at the time of the procedure and had a higher periprocedural morbidity [4].

Increasing evidence showed that conventional right ventricular pacing induces electrical and mechanical dyssynchrony. This translated into decreased left ventricular performance in a significant proportion of patients [5].

Consequently, almost two decades ago, His bundle pacing (HBP) was implemented as a more physiological pacing technique [6]. With time, several disadvantages, such as difficulty and procedural parameters, determined a shift towards left bundle branch area pacing (LBBAP), a more reproducible physiological pacing method with superior pacing parameters [7]. Nevertheless, in successful HBP cases, all studies have shown net clinical benefit in cardiac function and mortality, both for bradycardia and cardiac resynchronization indications [8,9]. Therefore, if not as a primary goal, HBP can still be useful as an alternative to failed LBBAP.

Although many observational HBP studies included elderly patients (65 years old and over) in their study groups, specific results for this category are scarce, especially in the long term. We have previously shown that the procedure was feasible in the elderly and the very elderly (over 80 years old), but gender-specific data are missing for these patients [10].

With the initial hypothesis that there are no significant differences, this study aimed to evaluate and compare gender-specific outcomes in HBP long-term performance in elderly patients with atrioventricular (AV) block.

2. Materials and Methods

2.1. Study Design

This was a retrospective, analytical, single-center study.

2.2. Patient Selection

All patients over 65 who underwent permanent HBP for second or third-degree AV block between August 2018 and December 2021 in the Cardiac Pacing Laboratory of the Braşov County Clinical Emergency Hospital in Romania were reviewed for inclusion in the study. Only patients with intraprocedural electrophysiological criteria for His bundle (HB) capture and a follow-up period of at least 2 years were accepted. In the end, 73 patients were included in the analysis. The baseline demographic and clinical characteristics of the patients were recorded.

2.3. Pacing Procedure

The physiological pacing procedure was performed using the C315 His catheter (Medtronic, Minneapolis, MN, USA) with the Select Secure 3830 lead (Medtronic, Minneapolis, MN, USA). The catheter was placed under fluoroscopic guidance at the superior part of the tricuspid valve, where unipolar mapping identified the HB signal. Pacing at decremental amplitude was performed to evaluate HB capture. In patients with a baseline narrow QRS complex, selective HBP was defined as a paced QRS complex and an ST-T interval identical to the baseline morphologies. Non-selective HBP was defined as a lack of an isoelectric line after the pacing artifact, with a “pseudo-delta” aspect at the beginning of the QRS complex and a transition with decremental pacing amplitude from non-selective HBP to either selective HBP or pure myocardial capture [11].

In patients with a baseline-wide QRS complex, the same criteria for selective/non-selective were applied as above, adding the correction of bundle-branch block if the paced QRS complex duration was lower than 130 ms. No ventricular back-up leads were implanted.

The pacing and sensing thresholds and the fluoroscopy time were recorded.

2.4. Follow-Up

The patients were followed in the outpatient clinic at 1, 3, 6, and 12 months after the procedure and then yearly. Sensing and pacing thresholds, as well as late complications, were recorded during follow-up. At each device interrogation, the pacing output was set at 1 V above the HB capture threshold.

2.5. Statistical Analysis

Continuous variables were presented as mean \pm one standard deviation. Categorical variables were presented as frequencies and percentages. A statistical comparison of means was performed using the t-test or the Mann–Whitney U test for independent groups and the t-test or Wilcoxon test for dependent groups according to the normality of distribution. The Chi-squared test evaluated the statistical difference between percentages. The Kaplan–Meier survival curve and the log-rank test were used to estimate event-free survival in the different pacing groups. Univariate and multivariate Cox proportional hazards regression analyses were performed to investigate the potential risk factors of pacing threshold increase during follow-up. A confidence interval of 95% was used for all tests, and a $p < 0.05$ was considered statistically significant.

Statistical analysis was performed using SPSS software version 26.0 (IBM, Armonk, NY, USA).

2.6. Ethical Considerations

The study complied with all aspects of the Declaration of Helsinki and was approved by the institutional ethics committee.

All patients provided written informed consent before the procedure.

3. Results

The mean age of the cohort was 72.8 ± 6.3 years, with 43 males and 30 females. Table 1 presents the baseline characteristics of the entire cohort and for each gender.

The two groups had no significant difference regarding baseline QRS duration and morphology, ejection fraction, comorbidities, or medical treatment taken. The only significant difference was a larger left atrial diameter recorded in the male group.

Table 1. Baseline patient characteristics.

Baseline Characteristics	All	Male	Female	<i>p</i>
Number of patients	73	43	30	
Age (years, mean \pm SD)	72.8 ± 6.3	71.8 ± 6.4	74.3 ± 5.9	0.10
e GFR (mL/min, mean \pm SD)	62.4 ± 19.5	60.4 ± 18.7	65.2 ± 20.5	0.32
BMI (kg/m ² , mean \pm SD)	28.8 ± 4.9	28.1 ± 4.5	29.2 ± 5.1	0.27
Baseline QRS				
QRS duration (ms, mean \pm SD)	108.6 ± 29.2	111.1 ± 29.8	105 ± 28.5	0.38
Normal QRS (<i>n</i> , %)	47 (64.4)	27 (62.8)	20 (66.7)	0.80
LBBB (<i>n</i> , %)	12 (16.4)	5 (11.6)	7 (23.3)	0.21
RBBB (<i>n</i> , %)	14 (19.2)	11 (25.6)	3 (10)	0.13
Echocardiography				
LVEF (% , mean \pm SD)	52.5 ± 11.8	51.6 ± 11.3	53.8 ± 12.6	0.43
LA diameter (mm, mean \pm SD)	41.1 ± 6.2	43.5 ± 5.9 *	36.8 ± 4.7 *	0.01
RA diameter (mm, mean \pm SD)	36.8 ± 6.2	$37.9.1 \pm 6.4$	34.9 ± 5.2	0.10

Table 1. Cont.

Baseline Characteristics	All	Male	Female	<i>p</i>
Comorbidities				
Hypertension (<i>n</i> , %)	65 (89)	37 (86)	28 (93.3)	0.46
Diabetes mellitus (<i>n</i> , %)	26 (35.6)	16 (37.2)	10 (33.3)	0.80
Ischemic disease (<i>n</i> , %)	19 (26)	11 (25.6)	8 (26.7)	1
Renal failure (<i>n</i> , %)	29 (39.7)	14 (32.6)	15 (50)	0.15
Persistent AF (<i>n</i> , %)	15 (20.5)	9 (20.9)	6 (20)	1
Treatment				
RAAS antagonists (<i>n</i> , %)	65 (89)	37 (86)	28 (93.3)	0.46
Beta-blockers (<i>n</i> , %)	54 (74)	33 (76.7)	21 (70)	0.59
MRAs (<i>n</i> , %)	13 (17.8)	9 (20.9)	4 (13.3)	0.54
Anticoagulants (<i>n</i> , %)	31 (42.5)	20 (46.5)	11 (36.7)	0.47

SD, standard deviation; eGFR, estimated glomerular filtration rate; BMI, body mass index; LBBB, left bundle branch block; RBBB, right bundle branch block; LVEF, left ventricular ejection fraction; LA, left atrium; RA, right atrium; RAAS, renin–angiotensin–aldosterone system; MRA, mineral receptors antagonist; *—significantly different from male/female.

3.1. Procedural Characteristics

All the procedural characteristics are presented in Table 2. The paced QRS complex was significantly narrower than the baseline value ($p < 0.001$ overall and for each gender group). The paced QRS duration was 98.9 ± 20.1 ms in males and 88.1 ± 16.6 ms in females ($p = 0.02$). There were no significant differences in detection times ($p = 0.94$), His bundle capture type ($p = 0.81$), impedance ($p = 0.79$), or fluoroscopy time ($p = 0.95$).

Table 2. Procedural characteristics.

Procedural Parameters	Overall	Male (<i>n</i> = 43)	Female (<i>n</i> = 30)	<i>p</i> -Value
Baseline QRS duration (ms)	108.6 ± 29.2	111 ± 29.8	105 ± 28.5	0.38
Paced QRS duration (ms)	94.5 ± 19.4	98.9 ± 20.1 *	88.1 ± 16.6 *	0.02
Detection (ms, mean \pm SD)	4.1 ± 2.5	4.1 ± 2.3	4.1 ± 2.9	0.94
Pacing threshold (V, mean \pm SD)	1.1 ± 0.8	1.1 ± 0.7	1.2 ± 0.9	0.50
Selective capture (<i>n</i> , %)	35 (47.9)	20 (46.5)	15 (50)	0.81
Impedance (Ohm, mean \pm SD)	465.4 ± 107.5	468.3 ± 104.8	461.3 ± 112.8	0.79
Fluoroscopy time (min, mean \pm SD)	8.9 ± 7.5	8.8 ± 7.7	8.9 ± 7.2	0.95

SD—standard deviation; *—significantly different from male/female.

3.2. Follow-Up

All patients reached the two-year follow-up, 63 patients the three-year follow-up, 33 patients the four-year follow-up, and 14 patients the five-year follow-up. There was one case of pocket infection that required reintervention and one case of a large pericardial effusion drained percutaneously without recurrences. No other complications, including lead dislodgements, that led to pacing interruption were noted.

Over the follow-up period, thirteen patients (17.8%) became completely pacemaker-dependent without an underlying escape rhythm. In the rest, the R wave sensing showed a non-statistically significant difference compared to the baseline (3.47 ± 2.35 mV vs. 3.81 ± 2.41 mV, $p = 0.24$).

The pacing threshold increased by more than 1 V over the follow-up period in twenty-four patients (32.9%, fifteen males and nine females, $p = 0.80$) and by more than 2 V in six patients (8.2%, four males and two females, $p = 1$). None of the patients had complete loss of HB capture. The 1 V increase occurred for sixteen patients (21.9%) in the first year of follow-up. For four patients (5.5%), there was an increase between the first and the second year, and for four patients (5.5%) after two years, without differences between genders.

The mean pacing thresholds at each visit are presented in Figure 1.

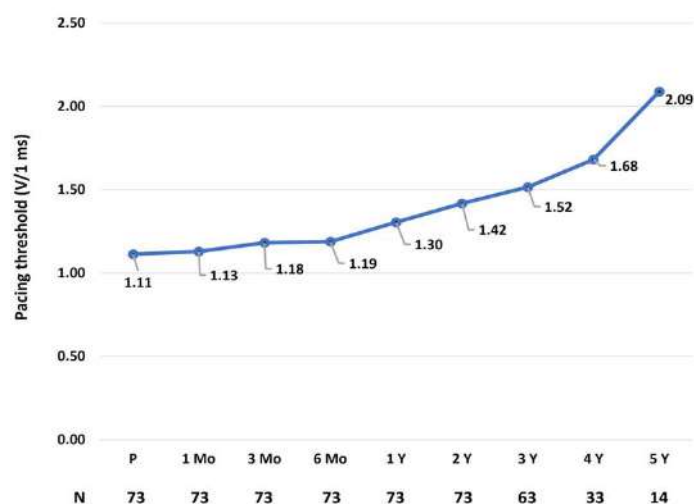


Figure 1. Mean pacing thresholds (V at 1 msec pulse duration) for the entire cohort at each visit. N, number of patients; P, procedural; Mo, months; Y, years.

As illustrated in the figure, the pacing threshold increased progressively, reaching statistical significance compared to the baseline values at the two-year follow-up ($p = 0.004$).

There was no significant difference between genders in the occurrence of pacing threshold increases by more than 1 V during follow-up (Figure 2).

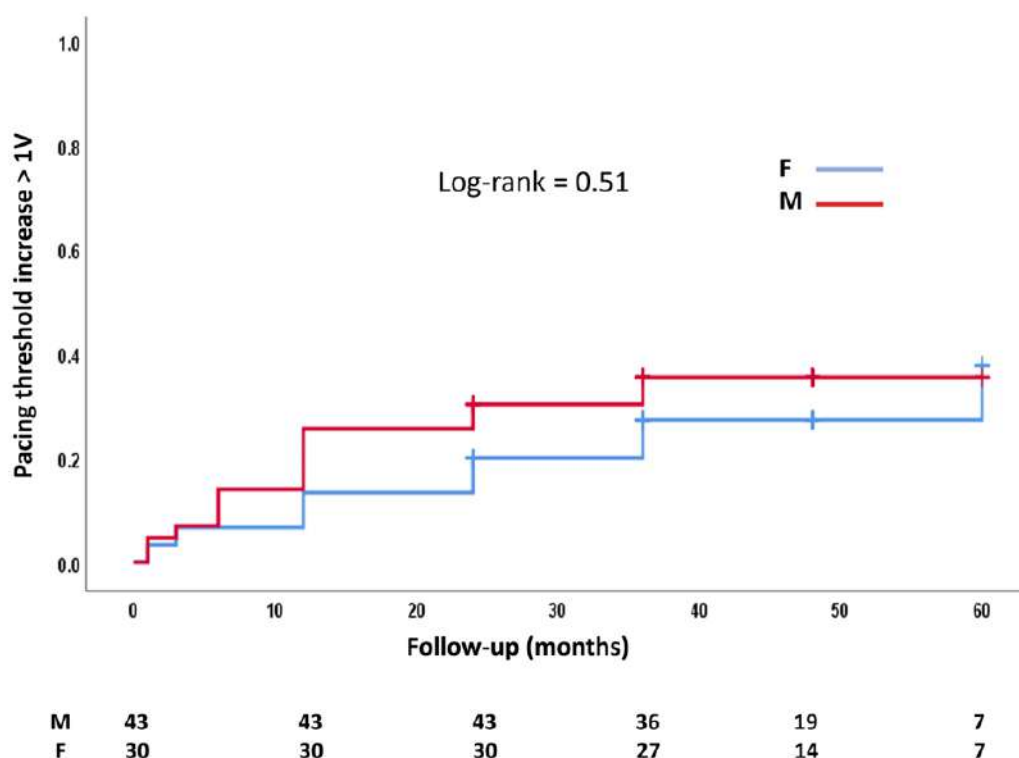


Figure 2. The Kaplan–Meier curve compares the pacing threshold increase of more than 1 V over time between gender groups. M, male; F, female.

Univariate Cox regression analysis of all possible risk factors demonstrated that the paced QRS duration, the left ventricular ejection fraction, and ischemic cardiomyopathy were significantly associated with pacing threshold increase over time (Table 3). The same

association was also confirmed by a subsequent multivariate Cox regression model in which we introduced all variables with a $p < 0.1$ in the univariate analyses.

Table 3. Uni/multivariate regression analysis of pacing threshold increase by at least 1 V after HBP.

Parameters	HR (95% CI)	<i>p</i> Value	HR (95% CI)	<i>p</i> Value
Sex	0.69 (0.27–1.77)	0.45		
Age (years)	0.96 (0.89–1.03)	0.26		
Baseline QRS duration (ms)	1.01 (0.99–1.02)	0.49		
Paced QRS duration (ms)	1.02 (1.00–1.04)	0.02	1.02 (1.00–1.05)	0.02
Type of capture	2.3 (0.86–6.00)	0.09	1.89 (0.69–5.20)	0.21
Procedural pacing threshold > 1.25 V	0.67 (0.24–1.86)	0.44		
LV ejection fraction (%)	1.08 (1.01–1.17)	0.03	1.08 (1.02–1.16)	0.01
LA volume (mL)	1.07 (0.96–1.19)	0.21		
RA volume (mL)	1.05 (0.94–1.18)	0.38		
Ischemic disease	0.38 (0.15–0.95)	0.04	0.26 (0.10–0.68)	0.01
Hypertension	0.71 (0.16–3.09)	0.65		
Diabetes Mellitus	1.99 (0.66–6.02)	0.22		
Atrial fibrillation	1.10 (0.72–1.68)	0.66		

HBP, His bundle pacing; HR, hazard ratio; LV, left ventricular; LA, left atrial; RA, right atrial.

At the last follow-up, most patients maintained the initial type of HB capture and the transition sequence at decremental pacing (32 non-selective HB to myocardial capture and 29 non-selective to selective HB capture). Five patients who initially transitioned from non-selective to myocardial capture developed a transition from non-selective to selective HB capture. Six patients who transitioned initially from non-selective to selective switched to a transition from non-selective HB to myocardial capture (Table 4). No significant differences in these transitions were recorded between genders.

Table 4. Type of capture and transition with decremental pacing over time.

Initial	Follow-Up	Overall	Male (<i>n</i> = 43)	Female (<i>n</i> = 30)	<i>p</i> -Value
NS-Myo	NS-Myo	32	20	12	0.34
NS-S	NS-S	29	19	10	0.46
NS-Myo	NS-S	5	2	3	0.39
NS-S	NS-Myo	6	1	5	0.07

NS, non-selective; Myo, myocardial; S, selective.

4. Discussion

The main findings of this study were as follows: (i) in the elderly population, HBP is a feasible pacing technique without significant long-term associated complications that lead to pacing failure; (ii) a pacing threshold increase of up to 2 V occurred in approximately a third of the cohort, but of more than 2 V in only 8% of the patients; (iii) there were no significant differences between genders for HBP performance both during the procedure and in the long-term.

HBP is supported by the strong physiological argument that it uses the entire infra-nodal conduction system to provide fast and synchronous biventricular activation. This explains the short QRS duration after HBP recorded in our cohort, which supports the existing data that HBP is associated with the narrowest paced QRS complex [12]. Also, it has been shown that HBP can correct infra-nodal conduction abnormalities, generating a narrower QRS complex than the baseline value [13].

An important issue related to HBP is the higher procedural pacing threshold compared to conventional right ventricular pacing [14]. This could be explained anatomically by

a deeper position in the septum and/or the fibrous sheath encapsulating the HB [15]. Nevertheless, initial studies have shown that the procedural pacing threshold depends on operator experience, with a trend of significant improvement during the learning curve [16]. The same argument applies to fluoroscopy times. In this regard, our procedural pacing thresholds of around 1 V at 1 ms pulse duration and fluoroscopy times of around 9 min align with the results published by other experienced and high-volume centers [17].

One of the main reasons for a shift towards LBBAP in laboratories worldwide is the risk of pacing threshold increase over time during HBP. Zanon et al. showed in a multicenter observational study that almost 25% of the patients had a follow-up threshold of more than 2.5 V, and 6% reached a threshold of more than 3.5 V [18]. On the other hand, Vijayaraman et al. reported that in 143 patients with AV block and HBP, there was a pacing threshold increase of more than 1 V in 5.6% over a two-year follow-up [17]. Possible mechanisms for the pacing threshold increase are lead slack and orientation to the HB, micro-dislodgements, local fibrosis, and the progression of conduction system disease [19]. In our data, although a third of the patients had a pacing threshold increase with more than 1 V, only 8.2% increased with more than 2 V. Moreover, the pacing threshold increase occurred mostly in the first year after the procedure, confirming the trend described in previous studies [19].

Because the HB lead is proximally placed in the conduction system, there is the concern of distal progression of the conduction disease, making HBP redundant. Therefore, in our population, these results and the fact that no patient completely lost the HB capture represent arguments against such significant distal progression.

Additionally, the pattern of HB capture during the procedure and at follow-up proves lead stability and lack of conduction system disease worsening, with 83.6% of the patients maintaining their initial transitions over time.

Previous studies looked at sex-based differences in outcomes in patients with HBP. For example, Wu et al. showed that females with left bundle branch block derive more benefits from HBP, with cardiac size and QRS duration contributing partially to these sex-based variations [20]. Also, Stangl et al. found no significant gender-based differences in the success of HBP implantations, measuring the threshold at implantation, one day after, and four weeks after implantation between 22 females and 39 males [21].

To our knowledge, this was the first study to evaluate gender differences in HBP performance over a mid- to long-term follow-up period in patients with AV block. Our results showed no significant difference in both acute results and the evolution of the pacing threshold values. Both genders displayed a constant trend of pacing threshold increases over time without reaching values that would necessitate lead revision. This finding is important since, in the elderly population (especially the very elderly), the decrease in battery longevity associated with higher pacing thresholds may not be a significant issue due to a lower life expectancy in this category.

An important finding was that the procedural pacing threshold was not a predictive factor for pacing threshold increase. This has been also shown in previous studies. Vijayaraman et al. found no association between clinical and procedural characteristics, except for the lead slack and pacing threshold increase over time in 294 HBP patients [19]. The same observation was made by Upadhyay et al. in 140 patients, proving that only a history of atrial fibrillation was predictive of pacing threshold increase [22]. Our observation that paced QRS duration was significantly associated with a subsequent rise in pacing thresholds could be explained by the more diffuse conduction system disease in patients with a wider paced QRS complex.

Given the long follow-up period, we believe the key message of this study is that irrespective of gender, in elderly patients, HBP is still a viable option for physiological

pacing, either as a first attempt or as a bailout after a failed attempt at left bundle branch area pacing.

Nevertheless, several limitations of the study should be mentioned. This was a retrospective, single-center study with a relatively small number of patients. Although the study included a theoretical follow-up of up to five years, only 14 patients were observed for this duration, limiting conclusions regarding long-term HBP stability. Future studies should aim for a more balanced follow-up duration across all participants. The procedures were performed using only one type of delivery system. With the current technological advances, the results may have been different. Finally, this was a procedural feasibility study that did not assess the clinical impact of HBP in the study group in the long term.

5. Conclusions

In elderly patients with AV block, HBP remains a feasible pacing method, without significant gender differences, over a long-term follow-up period. Pacing threshold increases are expected in up to one-third of the patients, requiring regular follow-ups to adjust the programmed parameters and optimize battery longevity.

Author Contributions: Conceptualization, C.P., E.C., D.L., A.G., F.O. and R.M.; methodology, C.P., F.O. and R.M.; software, C.P. and E.C.; validation, C.P., E.C., D.L., A.G., F.O. and R.M.; formal analysis, C.P., E.C., D.L. and A.G.; investigation, C.P., E.C., D.L. and A.G.; resources, C.P., F.O. and R.M.; data curation, C.P., E.C., D.L. and A.G.; writing—original draft, C.P.; writing—review and editing, C.P., F.O. and R.M.; visualization, C.P., E.C., D.L., A.G., F.O. and R.M.; supervision, C.P., F.O. and R.M.; funding acquisition, C.P., E.C., D.L., A.G. and F.O. All authors have read and agreed to the published version of the manuscript.

Funding: This research received no external funding.

Institutional Review Board Statement: The study was approved by the Ethics Committee of the Brasov County Emergency Clinical Hospital (Number 30/21.03.2022) and was conducted under all of the ethical principles of the Seventh Revision of the Helsinki Declaration from 2013.

Informed Consent Statement: Informed consent was obtained from all the subjects involved in the study before the cardiac pacing procedure.

Data Availability Statement: The datasets are available upon reasonable request to the corresponding author.

Conflicts of Interest: Catalin Pestrea has received proctorship and speaker fees from Medtronic. The other authors declare no conflict of interest.

References

1. de Vries, L.M.; Dijk, W.A.; Hooijschuur, C.A.M.; Leening, M.J.G.; Stricker, B.H.C.; van Hemel, N.M. Utilisation of cardiac pacemakers over a 20-year period: Results from a nationwide pacemaker registry. *Neth. Hear. J.* **2016**, *25*, 47–55. [[CrossRef](#)] [[PubMed](#)]
2. Matsubara, T.; Sumiyoshi, M.; Kimura, A.; Minami-Takano, A.; Maruyama, K.; Kimura, Y.; Tabuchi, H.; Hayashi, H.; Odagiri, F.; Sekita, G.; et al. Trend in Age at the Initial Pacemaker Implantation in Patients With Bradyarrhythmia—A 50-Year Analysis (1970–2019) in Japan. *Circ. J.* **2022**, *86*, 1292–1297. [[CrossRef](#)]
3. Pyatt, J.R.; Somauroo, J.D.; Jackson, M.; Grayson, A.D.; Osula, S.; Aggarwal, R.K.; Charles, R.G.; Connelly, D.T. Long-term survival after permanent pacemaker implantation: Analysis of predictors for increased mortality. *EP Europace* **2002**, *4*, 113–119. [[CrossRef](#)]
4. Nowak, B.; Misselwitz, B.; Erdogan, A.; Funck, R.; Irnich, W.; Israel, C.; Olbrich, H.-G.; Schmidt, H.; Sperzel, J.; Zegelman, M. Do gender differences exist in pacemaker implantation?—results of an obligatory external quality control program. *EP Europace* **2009**, *12*, 210–215. [[CrossRef](#)] [[PubMed](#)]
5. Kiehl, E.L.; Makki, T.; Kumar, R.; Gumber, D.; Kwon, D.H.; Rickard, J.W.; Kanj, M.; Wazni, O.M.; Saliba, W.I.; Varma, N.; et al. Incidence and predictors of right ventricular pacing-induced cardiomyopathy in patients with complete atrioventricular block and preserved left ventricular systolic function. *Hear. Rhythm. O2* **2016**, *13*, 2272–2278. [[CrossRef](#)] [[PubMed](#)]

6. Upadhyay, G.A.; Razminia, P.; Tung, R. His-bundle pacing is the best approach to physiological pacing. *Hear. Rhythm. O2* **2020**, *1*, 68–75. [\[CrossRef\]](#)
7. Keene, D.; Anselme, F.; Burri, H.; Pérez, Ó.C.; Čurila, K.; Derndorfer, M.; Foley, P.; Gellér, L.; Glikson, M.; Huybrechts, W.; et al. Conduction system pacing, a European survey: Insights from clinical practice. *EP Europace* **2023**, *25*, 1–9. [\[CrossRef\]](#)
8. Abdelrahman, M.; Subzposh, F.A.; Beer, D.; Durr, B.; Naperkowski, A.; Sun, H.; Oren, J.W.; Dandamudi, G.; Vijayaraman, P. Clinical Outcomes of His Bundle Pacing Compared to Right Ventricular Pacing. *J. Am. Coll. Cardiol.* **2018**, *71*, 2319–2330. [\[CrossRef\]](#)
9. Vinther, M.; Risum, N.; Svendsen, J.H.; Møgelvang, R.; Philbert, B.T. A Randomized Trial of His Pacing Versus Biventricular Pacing in Symptomatic HF Patients With Left Bundle Branch Block (His-Alternative). *JACC Clin. Electrophysiol.* **2021**, *7*, 1422–1432. [\[CrossRef\]](#) [\[PubMed\]](#)
10. Pestrea, C.; Cicala, E.; Gherghina, A.; Ortan, F.; Pop, D. Feasibility of Permanent His Bundle Pacing in the Elderly vs the Very Elderly. A Single-Center Mid-Term Follow-Up Study. *Clin. Interv. Aging* **2023**, *18*, 941–949. [\[CrossRef\]](#) [\[PubMed\]](#)
11. Burri, H.; Jastrzebski, M.; Cano, Ó.; Čurila, K.; de Pooter, J.; Huang, W.; Israel, C.; Joza, J.; Romero, J.; Vernoooy, K.; et al. EHRA clinical consensus statement on conduction system pacing implantation: Endorsed by the Asia Pacific Heart Rhythm Society (APHRS), Canadian Heart Rhythm Society (CHRS), and Latin American Heart Rhythm Society (LAHRS). *EP Europace* **2023**, *25*, 1208–1236. [\[CrossRef\]](#)
12. Tokavanich, N.; Prasitlumkum, N.; Mongkonsritragoon, W.; Cheungpasitporn, W.; Thongprayoon, C.; Vallabhajosyula, S.; Chokesuwattanaskul, R. A network meta-analysis and systematic review of change in QRS duration after left bundle branch pacing, His bundle pacing, biventricular pacing, or right ventricular pacing in patients requiring permanent pacemaker. *Sci. Rep.* **2021**, *11*, 1–8. [\[CrossRef\]](#)
13. Upadhyay, G.A.; Vijayaraman, P.; Nayak, H.M.; Verma, N.; Dandamudi, G.; Sharma, P.S.; Saleem, M.; Mandrola, J.; Genovese, D.; Oren, J.W.; et al. On-treatment comparison between corrective His bundle pacing and biventricular pacing for cardiac resynchronization: A secondary analysis of the His-SYNC Pilot Trial. *Hear. Rhythm. O2* **2019**, *16*, 1797–1807. [\[CrossRef\]](#) [\[PubMed\]](#)
14. Abdin, A.; Aktaa, S.; Vukadinović, D.; Arbelo, E.; Burri, H.; Glikson, M.; Meyer, C.; Munyombwe, T.; Nielsen, J.C.; Ukena, C.; et al. Outcomes of conduction system pacing compared to right ventricular pacing as a primary strategy for treating bradyarrhythmia: Systematic review and meta-analysis. *Clin. Res. Cardiol.* **2021**, *111*, 1198–1209. [\[CrossRef\]](#)
15. Kawashima, T.; Sasaki, H. A macroscopic anatomical investigation of atrioventricular bundle locational variation relative to the membranous part of the ventricular septum in elderly human hearts. *Surg. Radiol. Anat.* **2005**, *27*, 206–213. [\[CrossRef\]](#) [\[PubMed\]](#)
16. Keene, D.; Arnold, A.D.; Jastrzebski, M.; Burri, H.; Zweibel, S.; Crespo, E.; Chandrasekaran, B.; Bassi, S.; Joghetai, N.; Swift, M.; et al. His bundle pacing, learning curve, procedure characteristics, safety, and feasibility: Insights from a large international observational study. *J. Cardiovasc. Electrophysiol.* **2019**, *30*, 1984–1993. [\[CrossRef\]](#) [\[PubMed\]](#)
17. Vijayaraman, P.; Patel, N.; Colburn, S.; Beer, D.; Naperkowski, A.; Subzposh, F.A. His-Purkinje Conduction System Pacing in Atrioventricular Block: New Insights into Site of Conduction Block. *JACC Clin. Electrophysiol.* **2022**, *8*, 73–85. [\[CrossRef\]](#) [\[PubMed\]](#)
18. Zanon, F.; Abdelrahman, M.; Marcantoni, L.; Naperkowski, A.; A Subzposh, F.; Pastore, G.; Baracca, E.; Boaretto, G.; Raffagnato, P.; Tiribello, A.; et al. Long term performance and safety of His bundle pacing: A multicenter experience. *J. Cardiovasc. Electrophysiol.* **2019**, *30*, 1594–1601. [\[CrossRef\]](#)
19. Beer, D.; A Subzposh, F.; Colburn, S.; Naperkowski, A.; Vijayaraman, P. His bundle pacing capture threshold stability during long-term follow-up and correlation with lead slack. *EP Europace* **2020**, *23*, 757–766. [\[CrossRef\]](#) [\[PubMed\]](#)
20. Wu, S.; Shang, W.; Ye, Y.; Su, L.; Wang, S.; Cai, M.; Wang, D.; He, Y.; Zheng, R.; Fu, G.; et al. Sex differences outcomes in conduction system pacing for patients with typical left bundle branch block. *Int. J. Cardiol.* **2024**, *415*, 132475. [\[CrossRef\]](#)
21. Stangl, D.; Buia, V.; Walascheck, J.; Rittger, H.; Bastian, D.; Vitali-Serdoz, L. The pursuit of gender equality: A substudy of the PACE-CONDUCT trial on gender differences in His bundle pacing implantation. *EP Europace* **2024**, *26*, i899–i900. [\[CrossRef\]](#)
22. Upadhyay, G.A.; Sun, W.; Nayak, H.M.; Aziz, Z.; Beaser, A.D.; Ozcan, C.; Tung, R. B-PO01-040 Lead Stability in His Bundle Pacing—Incidence, Predictors, and Timing of Increased Pacing Thresholds. *Hear. Rhythm. O2* **2021**, *18*, S67. [\[CrossRef\]](#)

Disclaimer/Publisher’s Note: The statements, opinions and data contained in all publications are solely those of the individual author(s) and contributor(s) and not of MDPI and/or the editor(s). MDPI and/or the editor(s) disclaim responsibility for any injury to people or property resulting from any ideas, methods, instructions or products referred to in the content.